NASA CR-166129
VOLUME I

(G Hill)

A MATHEMATICAL MODEL FOR VERTICAL ATTITUDE TAKEOFF AND LANDING (VATOL) AIRCRAFT SIMULATION

VOLUME I MODEL DESCRIPTION AND APPLICATION

BY ROBERT L. FORTENBAUGH

DECEMBER 1980

PREPARED UNDER CONTRACT NAS2-10294 BY

VOUGHT CORPORATION
DALLAS, TX 75265

FOR

AMES RESEARCH CENTER
NATIONAL AERONAUTICS AND SPACE ADMINISTRATION

FOREWORD

This document is part of a three volume report prepared under NASA Ames Contract NAS2-10294, Mathematical Modeling for Vertical Attitude Take-Off and Landing (VATOL) Simulation. Volume I: Model Description and Application provides background and details of a generic mathematical model for simulation of VATOL aircraft concepts. A six-degree-of-freedom off-line (non-piloted) digital simulation program incorporating this model was developed and applied to the Vought SF-121 VATOL concept. Volume I gives results of this application which included development and demonstration of a control system for terminal VATOL operations. Volume II: Model Equations and Base Aircraft Data gives all the model equations and SF-121 aircraft data in a simulation data package format. This volume facilitated the development of a piloted VATOL simulation at NASA Ames. Volume III: Users Manual for VATOL Simulation Program provides a description of the six-degree-of-freedom off-line digital simulation program, instructions for its application, and examples of set-up decks and output for several of the SF-121 application runs.

Project Monitor for NASA Ames was Mr. Gary Hill. The Principal Investigator for the Vought Corporation was Robert L. Fortenbaugh.

TABLE OF CONTENTS

TABLE OF CONTENTS (Continued)

TABLE OF CONTENTS (Continued)

LIST OF FIGURES

LIST OF FIGURES (Continued)

LIST OF FIGURES (Continued)

LIST OF TABLES

LIST OF SYMBOLS

Axis System Symbols -

X_I, Y_I, Z_I	Reference inertial (earth) axis system with X_I axis pointed north and Z_I axis aligned with local gravity vector. (Section 2.1)
X_{I_R}, Y_{I_R}, Z_{I_R}	Rotated inertial axis system formed by rotating the X_I and Z_I axis about the Y_I axis. Y_I and Y_{I_R} are thus coincident. (Section 2.9)
X_B, Y_B, Z_B	Reference body axis system with origin at aircraft cg. Fixed orientation to aircraft. Oriented with respect to inertial axis system by Euler angle rotation through θ, ϕ and ψ. (Section 2.1)
X_w, Y_w, Z_w	Wind axis system with X_w axis always pointed into relative wind. (Section 2.1)
X_s, Y_s, Z_s	Stability axis system with X_s axis pointed into component of relative wind in the X_B - Z_B plane. X_s is oriented by a rotation by α above the Y_B axis. Thus Y_s and Y_B are coincident. (Section 2.1)
X_{sw}, Y_{sw}, Z_{sw}	Axis system with origin at the engine nozzle swivel location and X_{sw}, Y_{sw}, Z_{sw} parallel to X_B, Y_B, Z_B, respectively. (Section 2.3)

LIST OF SYMBOLS (Continued)

Axis System Symbols -

X_{AP}, Y_{AP}, Z_{AP}	Axis system with origin at application point of inlet ram force and X_{AP}, Y_{AP}, Z_{AP} parallel to X_B, Y_B, Z_B respectively. (Section 2.4)
X_{JET}, Y_{JET}, Z_{JET}	Axis system with origin at application point of RCS jet and X_{JET}, Y_{JET}, Z_{JET} parallel to X_B, Y_B, Z_B respectively. (Section 2.5)
X_D, Y_D, Z_D	Duct axis system with X_D aligned parallel to centerline of engine. (Section 2.6)

Aircraft Kinematic Variables -

$a_{x_{cg}}$, $a_{y_{cg}}$, $a_{z_{cg}}$	Aircraft accelerations in reference body axis system measured at cg (ft/sec^2)
d_{11}, d_{12}, etc	Direction cosines
M_N	Mach number
$n_{x_{cg}}$, $n_{y_{cg}}$, $n_{z_{cg}}$	$a_{x_{cg}}$, $a_{y_{cg}}$, $a_{z_{cg}}$ expressed in units of g
p, q, r	Component of aircraft rotation rate vector ($\overline{\omega}_A$) in reference body axis system. (rad/sec)

LIST OF SYMBOLS (Continued)

Aircraft Kinematic Variables -

p_s, q_s, r_s	Components of aircraft rotation rate vector ($\overline{\omega}_A$) in stability axis system. (rad/sec)
p_{INT}, q_{INT}, r_{INT}	Integrals of p, q, r respectively (rad)
q	Dynamic pressure = $\frac{\rho}{2} V_A^2$(lb/ft^2)
u, v, w	Components of inertial velocity vector ($\overline{V}_e$) in reference body axis system (ft/sec)
u_{AS}, u_{AS}, w_{AS}	Components of airspeed vector ($\overline{V}_A$) in reference body axis system (ft/sec)
$\overline{V}_e$	Inertial velocity vector
$\overline{V}_A$	Airspeed vector
V_A	Airspeed, the magnitude of V_A (ft/sec)
V_∞	Used interchangeably with V_A, particularly in Section 2.4 (ft/sec)
X_e, Y_e, Z_e	Aircraft cg position in inertial axis system (ft)
α	Angle of attack = $\tan^{-1}(w_{AS}/u_{AS})$ (rad)

LIST OF SYMBOLS (Continued)

Aircraft Kinematic Variables -

β	Sideslip angle = $\sin^{-1}(v_{AS}/V_A)$ (rad)	
$\hat{\beta}$	Pseudo-$\dot{\beta}$ = $(g/V_A)\,\phi - r_s$ (rad/sec)	
γ	Flight path angle (rad)	
θ	Euler pitch angle (rad)	Define relative orientation between reference inertial axis system and reference body axis system.
ϕ	Euler roll angle (rad)	
ψ	Euler yaw angle (rad)	
θ_R	Euler pitch angle referred to rotated inertial axis system (rad)	
ρ	Air density (slugs/ft^3)	
$\bar{\omega}_A$	Aircraft rotation rate vector	

Aerodynamics Model Symbols (Section 2.2) -

b	Reference wingspan (ft)
C_D, C_L, C_m	Drag, lift, and pitch moment coefficients, respectively. Referenced to stability axis system.
C_{L_q}, C_{m_q}	Change in lift and pitch moment coefficient per unit change in $qc/2V_A$. Referenced to stability axis system.

LIST OF SYMBOLS (Continued)

Aerodynamics Model Symbols (Section 2.2) -

c	Mean aerodynamic chord (ft)
cp	Center of pressure
C_{Y_β}, C_{l_β}, C_{n_β}	Change in side force, roll moment, and yaw moment coefficients respectively, per unit change in β. Referenced to stability axis system.
$C_{t_{\delta_r}}$, $C_{l_{\delta_r}}$, $C_{n_{\delta_r}}$	Change in side force, roll moment, and yaw moment coefficients per unit change in δ_r. Referenced to stability axis system.
$C_{y_{\delta_a}}$, $C_{l_{\delta_a}}$, $C_{n_{\delta_a}}$	Change in side force, roll moment, and yaw moment coefficients per unit change in δ_a. Referenced to stability axis system.
C_{y_p}, C_{l_p}, C_{n_p}	Change in side force, roll moment, and yaw moment coefficients per unit change in $(pb/2V_A)$. Referenced to stability axis system.
C_{y_r}, C_{l_r}, C_{n_r}	Change in side force, roll moment, and yaw moment coefficients per unit change in $(rb/2V_A)$. Referenced to stability axis system.
$C_{y_{\beta_{C_L2}}}$	Change in C_{y_β} per unit change in C_L2

LIST OF SYMBOLS (Continued)

Propulsion System Model Symbols (Section 2.3) -

A_{FT}	Geometric thrust turning angle (rad)
B_{REF}	Reference RCS bleed level (%)
B_{AVL}	Bleed available for RCS (%)
$\overline{BLD}$	Actual bleed used for RCS (%)
$F_{G_{IDL}}$	Gross thrust level at idle throttle (lb)
$F_{G_{MIN}}$	Gross thrust level at maximum rpm and minimum afterburner setting (lb)
$F_{G_{MAX}}$	Gross thrust level at maximum rpm and maximum afterburner setting (lb)
F_{RPM}	Fractional engine rpm
FS_{TAP}, BL_{TAP}, WL_{TAP}	Location of the thrust application point in aircraft coordinates (ft)
FS_{SW}, BL_{SW}, WL_{SW}	Location of the nozzle swivel point in aircraft coordinates (ft)
ΔFS_{SW}, ΔBL_{SW}, ΔWL_{SW}	Distance from nozzle swivel point to thrust application point in aircraft coordintes (ft)
$K_{A_{FT}}$	Flow turning correction coefficient for thrust

LIST OF SYMBOLS (Continued)

Propulsion System Model Symbols (Section 2.3) -

$K_{A_{FT_1}}$, $K_{A_{FT_2}}$	Constants used to calculate $K_{A_{FT}}$
K_{BT}	Adjusts commanded thrust level for reference RCS bleed
K_{BT}'	Adjusts output thrust level for actual RCS bleed
$K_{\dot{m}}$	Ratio of currently available RCS bleed air to maximum available.
l_{NOZ}	Length of engine nozzle (ft)
$\dot{m}_I$	Inlet mass flow rate to engine (lb/sec)
$\dot{m}_{MAX}$	Maximum inlet mass flow rate (lb/sec)
T_{APPL}	Thrust corrected for RCS effects only (lb)
T_{AB}	Afterburner thrust level normalized to $F_{G_{MIN}}$
$\dot{T}_{AB_{MAX}}$, $\dot{T}_{AB_{MIN}}$	Maximum and minimum rates of change of normalized afterburner thrust (lb/sec)
T_c	Commanded thrust level (lb)
T_{COR}	Thrust applied to aircraft after corrections for RCS effects and flow turning (lb)

LIST OF SYMBOLS (Continued)

Propulsion System Model Symbols (Section 2.3) -

T_F	Non-afterburning thrust level normalized to $F_{G_{MIN}}$
$\dot{T}_{F_{MAX}}, \dot{T}_{F_{MIN}}$	Maximum and minimum rates of change of normalized non-afterburning thrust level (lb/sec)
T_o	Thrust level before RCS and flow turning corrections (lb)
$\Delta X_T, \Delta Y_T, \Delta Z_T$	Body axis components of direct thrust (lb)
θ_T	Pitch thrust deflection angle, positive for thrust deflected below engine centerline (rad)
σ_y	Engine installation angle, positive for engine inlet above nozzle swivel point (rad)
τ_{AB}	Time constant for afterburner dynamics (sec)
τ_{ENG}	Time constant for non-afterburning thrust dynamics (sec)
ψ_T	Yaw thrust deflection angle, positive for thrust deflected left of engine centeline (rad)
$\Omega_{E_{MAX}}$	Maximum engine spool rotational speed (rad/sec)

LIST OF SYMBOLS (Continued)

Inlet Ram Model Symbols (Section 2.4) -

A_{INLET}	Inlet area seen by approaching air flow. In propulsion nomenclature this is the capture or highlight plane area (ft^2).
A_{TURN_O}	Geometric turning angle of the inlet flow defined by the angle that $\bar{V}_A$ makes with the inlet centerline (rad)
A_{TURN}	Effective turning angle of the inlet flow (rad)
B_{TURN}	Angle between the $\bar{V}_A$ - engine centerline plane and the aircraft plane of symmetry (rad)
D_{IN}	Equivalent inlet diameter (ft)
$\bar{F}_{RAM_I}$	Additional inlet ram force vector produced by rotation of the inlet relative to the incoming air stream (lb)
$\bar{F}_{RAM_O}$	Basic inlet ram force vector defined as $\dot{m}_I \bar{V}_A$ (lb)
$\bar{F}_{RAM}$	Effective inlet ram force vector = $\bar{F}_{RAM_O} R_M$ (lb)

LIST OF SYMBOLS (Continued)

Inlet Ram Model Symbols (Section 2.4) -

L_{RAM_O}, M_{RAM_O}, M_{RAM_O}	X, Y, and Z body axis components, respectively, of $\overline{M}_{RAM_O}$ (ft lb)
L_{RAM_I}, M_{RAM_I}, N_{RAM_I}	X, Y, and Z body axis components, respectively, of $\overline{M}_{RAM_I}$ (ft lb)
L_{RAM}, M_{RAM}, N_{RAM}	Total roll, pitch, and yaw moments in the body axis system due to inlet ram effects (ft lb)
$\overline{M}_{RAM_O}$	Moment vector about the cg produced by $\overline{F}_{RAM_O}$ acting at a point located by the vector $\overline{r}_{AP}$ relative to the cg (ft lb)
$\overline{M}_{RAM_I}$	Moment vector about the cg produced by $\overline{F}_{RAM_I}$ acting at the center of the inlet (ft lb)
$\overline{r}_{AP}$	Vector from the cg to the basic inlet ram force application point (ft)
$\overline{r}_{IN}$	Vector from the cg to the center of the inlet (ft)
R_M	Ram effectiveness factor
V_I	Inlet air mass velocity (ft/sec)
X_{APPL}	Distance from inlet face to F_{RAM_O} application point along inlet centerline, positive for application point upstream of inlet (ft)

LIST OF SYMBOLS (Continued)

Inlet Ram Model Symbols (Section 2.4) -

X_{IN}, Y_{IN}, Z_{IN}	X, Y, and Z body axis coordinates, respectively, of $\bar{r}_{IN}$ (ft)
ΔA_{TURN}	Difference between effective and geometric flow turning angles (rad)
ΔX_{R_O}, ΔY_{R_O}, ΔZ_{R_O}	X, Y, and Z body axis components, respectively, of $\bar{F}_{RAM_O}$ (lb)
ΔX_{R_I}, ΔY_{R_I}, ΔZ_{R_I}	X, Y, and Z body axis components, respectively of $\bar{F}_{RAM_I}$ (lb)
X_{RAM}, Y_{RAM}, Z_{RAM}	Total X, Y, and Z forces in the body axis system due to inlet ram effects (lb)

Reaction Control System Model Symbols (Section 2.5) -

$\overline{BLDM}$	The bleed more parameter. Indicates whether a demand bleed jet can command RCS bleed in excess of the reference bleed level.
$\overline{DMD}(I)$	The demand parameter. If = 1, indicates jet I is a demand bleed jet. If = 0 indicates jet I is a continuous bleed jet.
$F_{RCS}(I)$	Commanded force at RCS jet I uncorrected for propulsion system interactions or demands of other jets (lb)

LIST OF SYMBOLS (Continued)

Reaction Control System Model Symbols (Section 2.5) -

$F_{RCS_C}(I)$	Commanded force for RCS jet I after correction for propulsion system interactions and demands of other jets. Input to RCS force dynamics model (lb)
$F_{RCS_A}(I)$	Actual force at RCS jet I. Output of RCS force dynamics model (lb)
$F_{RCS_{MX}}(I)$	Maximum force of jet I (lb)
$F_{RCS_{AL}}$	Total RCS force available for distribution among all jets. Includes correction for actual bleed level (lb)
$F_{RCS_{SUM}}$	Sum of the commanded uncorrected (for propulsion system interactions and demands of other jets) forces of all RCS jets $\left(= \sum_{I=1}^{n_{JET}} F_{RCS}(I)\right)$ (lb)
$\Delta F_{RCS_{DMD}}$	Total uncorrected force commanded by demand bleed jets (lb)
$FS_{JET}(I)$, $BL_{JET}(I)$, $WL_{JET}(I)$	Location of RCS jet I in aircraft coordinates (ft)
L_{RCS}, M_{RCS}, N_{RCS}	Total roll, pitch, and yaw moments in the body axis system contributed by the RCS (ft lb)

LIST OF SYMBOLS (Continued)

Reaction Control System Model Symbols (Section 2.5) -

n_{JET}	Total number of RCS jets
$X_{JET}(I)$, $Y_{JET}(I)$, $Z_{JET}(I)$	X, Y, and Z body axis components, respectively, of the vector between the aircraft cg and the location of jet I (ft)
$\Delta X_{RCS}(I)$, $\Delta Y_{RCS}(I)$, $\Delta Z_{RCS}(I)$	X, Y, and Z body axis components, respectively, of the force produced by jet I (lb)
X_{RCS}, Y_{RCS}, Z_{RCS}	Total X, Y, and Z forces in the body axis system contributed by the RCS (lb)
$\delta_{RCS}(I)$	Normalized area of jet I
$\theta_{JET}(I)$	Installed pitch angle of jet I. Used along with $\psi_{JET}(I)$ to orient thrust direction of the jet (rad)
$\psi_{JET}(I)$	Installed yaw angle of jet I. Used along with $\theta_{JET}(I)$ to orient thrust direction of the jet (rad)

Coriolis Model Symbols (Section 2.6) -

a	Perpendicular distance from cg to the X_D-Y_D plane (ft)
$\bar{a}_{COR}$	Coriolis acceleration (ft/sec^2)

LIST OF SYMBOLS (Continued)

Coriolis Model Symbols (Section 2.6) -

$\bar{F}_{COR}$	Coriolis force (lb)
l	Distance along X_D axis from inlet to origin of the duct axis system (ft)
l_{DUCT}	Length of the engine duct (ft)
$\bar{M}_{COR}$	Coriolis moment about the cg (ft lb)
$\bar{R}$	Vector from cg to any point along the X_D axis (ft)
$\dot{\bar{R}}$	Rate of change of R (ft/sec)
ζ_D	Integration variable along X_D axis (ft)

Actuation System Model Symbols (Section 2.7 and 3.5) -

$K_{TEF_{H1}}$, $K_{TEF_{H2}}$	Constants which define programming of horizontal stabilizer trailing edge flap as a function of angle of attack
$K_{LEF_{W1}}$, $K_{LEF_{W2}}$	Constants which define programming of wing leading edge flap as a function of angle of attack
K_{δ_a}	Aileron command per unit δ_{ROLL} deflection (rad)
K_{δ_e}	Elevator command per unit δ_{PITCH} deflection (rad)

LIST OF SYMBOLS (Continued)

Actuation System Model Symbols (Section 2.7 and 3.5) -

K_{δ_y}	Rudder command per unit δ_{YAW} deflection (rad)
$K_{\delta_y \delta_r}$	Rudder command per unit δ_{ROLL} deflection (rad)
$K_{\theta_T \delta_p}$	Pitch thrust deflection command per unit δ_{PITCH} deflection (rad)
$K_{\theta_T \delta_r}$	Pitch thrust deflection command per unit δ_{ROLL} deflection (rad)
$K_{\psi_T \delta_r}$	Yaw thrust deflection command per unit δ_{ROLL} deflection (rad)
$K_{\psi_T \delta_y}$	Yaw thrust deflection command per unit δ_{YAW} deflection (rad)
$\delta_{a_{MAX}}$, $\delta_{a_{MIN}}$	Maximum and minimum aileron command limits (rad)
$\delta_{e_{MAX}}$, $\delta_{e_{MIN}}$	Maximum and minimum elevator command limits (rad)
δ_{c_v} or δ_r	Rudder deflection (rad)
δ_I	Input to generic actuator model
$\delta_{LEF_W}(I)$	Deflection of leading edge flap of I wing half. I = 1 for left and 2 for right (rad)

LIST OF SYMBOLS (Continued)

Actuation System Model Symbols (Section 2.7 and 3.5) -

δ_{MIN}, δ_{MAX}	Minimum and maximum position limits of generic actuator model
$\dot{\delta}_{MIN}$, $\dot{\delta}_{MAX}$	Minimum and maximum rate limits of generic actuator model
δ_O	Output of generic actuator model
$\dot{\delta}_O$	Rate of change of generic actuator model output
δ_{TEF_H}	Deflection of trailing edge flap of horizontal stabilizer (rad)
$\delta_{TEF_W}(I)$	Deflection of trailing edge flap of I wing half. I = 1 for left and 2 for right (rad)
τ_{ACT}	Time constant of generic actuator model (sec)

Subscript:

c	Indicates commanded value (i.e. input to actuator)

Flight Control System Model Symbols (Sections 2.8 and 3.7) -

CS_{SW}	Control system switch

LIST OF SYMBOLS (Continued)

Flight Control System Model Symbols (Sections 2.8 and 3.7) -

N^{x}_{y}	Numerator of x to y transfer function where y is the input variable and x is the output variable
s	Laplace transform variable ($s = \sigma + j\omega$) (rad/sec)
T_{CMD}	Thrust commanded by throttle and/or heave control system (lb)
$\frac{x}{y}\Big\|_{a,b \to c}$	Indicates x to y transfer function with the a and b to c loops closed where a and b are feedback variables and c is a control variable
Δ	Indicates denominator (characteristic equation) of the aircraft transfer functions.
ΔT	Incremental change in thrust (lb)
δ_{HEAVE}	Cockpit heave controller deflection
δ_{LATSTK}	Left-right deflection of the cockpit control stick
δ_{LNGSTK}	Fore-aft deflection of the cockpit control stick

LIST OF SYMBOLS (Continued)

Flight Control System Model Symbols (Sections 2.8 and 3.7) -

δ_{PED}	Cockpit pedal deflection
$\delta_{p_{BUT}}$	Trim button for left-right control stick deflection
$\delta_{q_{BUT}}$	Trim button for fore-aft control stick deflection
$\delta_{r_{BUT}}$	Pedal deflection trimmer
δ_{THROT}	Cockpit manual throttle deflection
ζ	Damping ratio of complex root
σ	Real part of Laplace variable (rad/sec)
ω	Imaginary part of Laplace variable (rad/sec)
ω_n	Undamped natural frequency of complex root (rad/sec)

Roll Control System Symbols (Figure 2-27):

$K_{P_{ATT}}$	Roll attitude feedback gain (rad/rad or rad/sec/rad)
K_{p_B}	Roll rate feedback selector gain

LIST OF SYMBOLS (Continued)

Roll Control System Symbols (Figure 2-27):

K_{p_c}	Roll input proportional gain (rad/unit cockpit controller deflection or rad/sec/unit cockpit controller deflection)
$K_{p_{CI}}$	Roll input integral gain (rad/sec/P_{CMD} or rad/sec^2/P_{CMD})
K_{p_e}	Roll control system proportional error gain (δ_{ROLL}/rad or δ_{ROLL}/rad/sec)
$K_{p_{e_{I1}}}$	Roll control system error integral gain (rad/sec or rad/sec^2)
K_{p_p}	Roll rate feedback gain (rad/rad/sec or rad/sec/rad/sec)
$K_{p_{TRM_1}}$	Lateral stick trim input gain (rad/sec^2/unit input or rad/sec/unit input)
$K_{r_{TRM_1}}$	Pedal trim input gain (rad/sec^2/unit input or rad/sec/unit input)
K_ϕ	Roll attitude feedback selector gain
$K_{\int p}$	Integral of roll rate feedback selector gain
P_{CMD}	Cockpit controller deflection, either pedals or right-left stick motion

LIST OF SYMBOLS (Continued)

Roll Control System Symbols (Figure 2-27):

p_c	Input to command filter (rad or rad/sec)
p_c'	Output of command filter (rad or rad/sec)
$p_{c_{TRM}}$	Output of input integrator path (rad or rad/sec)
p_e	Roll control system error signal (rad or rad/sec)
$p_{e_{LIM}}$	Limiter on error integrator (units of δ_{ROLL})
$p_{e_{TRM}}$	Output of error integrator path (units of δ_{ROLL})
p_{INT_c}	Alternate name for p_c' when the roll attitude feedback signal is p_{INT}. (i.e. the system controls p_{INT}) (rad)
p_{TRM}	Trim input from pedal trim or lateral stick trim (rad or rad/sec)
δ_{ROLL}	Normalized control output of roll control system; roll control input for actuation system
τ_{ROLL}	Time constant of command filter (sec)
ϕ_{SW}	Logic switch related to CS_{SW} required to insure proper initialization of roll rate integrator and system trim input.

LIST OF SYMBOLS (Continued)

Pitch Control System Symbols (Figure 2-28):

$K_{q_{ATT}}$	Pitch attitude feedback gain (rad/rad or rad/sec/rad)
K_{q_c}	Pitch input proportional gain (rad/δ_{LNGSTK} or rad/sec/δ_{LNGSTK})
$K_{q_{CI}}$	Pitch input integral gain (rad/sec/δ_{LNGSTK} or rad/sec^2/δ_{LNGSTK})
K_{q_e}	Pitch control system proportional error gain (δ_{PITCH}/rad/sec or δ_{PITCH}/rad)
$K_{q_{e_{I1}}}$	Pitch control system error integral gain (rad/sec or rad/sec^2)
K_{q_q}	Pitch rate feedback gain (rad/rad/sec or rad/sec/rad/sec)
$K_{q_{TRM_1}}$, $K_{q_{TRM_2}}$	Longitudinal stick trim input gains (rad/sec/unit input or rad/sec^2/unit input)
K_θ	Pitch attitude feedback selector gain
$K_{\int q}$	Integral of pitch rate feedback selector gain
q_c	Input to command filter (rad or rad/sec)
q_c'	Output of command filter (rad or rad/sec)
$q_{c_{TRM}}$	Output of input integrator path (rad or rad/sec)

LIST OF SYMBOLS (Continued)

Pitch Control System Symbols (Figure 2-28):

q_e	Pitch control system error signal (rad or rad/sec)
$q_{e_{LIM}}$	Limiter on error integrator (units of δ_{PITCH})
$q_{e_{TRM}}$	Output of error integrator path (units of δ_{PITCH})
q_{INT_c}	Alternate name for q_c' when the pitch attitude feedback signal is q_{INT} (i.e. the system controls q_{INT}) (rad)
q_{TRM}	Trim input from longitudinal stick trim (rad or rad/sec)
δ_{PITCH}	Normalized control output of pitch control system; pitch control input for actuation system
τ_{PITCH}	Time constant of command filter (sec)
θ_{SW}	Logic switch related to CS_{SW} required to insure proper initialization of pitch rate integrator and system trim input.

Yaw Control System Symbols (Figure 2-29):

K_{a_y}	Lateral acceleration feedback gain (δ_{YAW}/ft/sec^2)

LIST OF SYMBOLS (Continued)

Yaw Control System Symbols (Figure 2-29):

$K_{r_{ATT}}$	Yaw attitude feedback gain (rad/rad or rad/sec/rad)
K_{r_3}	Yaw rate feedback selector gain
K_{r_c}	Yaw input proportional gain (rad/unit cockpit controller deflection or rad/sec/unit cockpit controller deflection)
$K_{r_{CI}}$	Yaw input integral gain (rad/sec/R_{CMD} or rad/sec^2/R_{CMD})
K_{r_e}	Yaw control system proportional error gain (δ_{YAW}/rad or δ_{YAW}/rad/sec)
$K_{r_{e_{I1}}}$	Yaw control system error integral gain (rad/sec or rad/sec^2)
K_{r_r}	Yaw rate feedback gain (rad/rad/sec or rad/sec/rad/sec)
$K_{r_{TRM_2}}$	Pedal trim input gain (rad/sec^2/unit input or rad/sec/unit input)
$K_{p_{TRM_2}}$	Lateral stick trim input gain (rad/sec^2/unit input or rad/sec/unit input)
$K_{\phi_{r_s}}$	Roll attitude feedback gain to yaw control system (rad sec/rad or rad/rad)

LIST OF SYMBOLS (Continued)

Yaw Control System Symbols (Figure 2-29):

K_{ψ}	Yaw attitude feedback selector gain
$K_{\int r}$	Integral of yaw rate feedback selector gain
R_{CMD}	Cockpit controller deflection, either pedals or right-left stick motion.
r_c	Input to command filter (rad or rad/sec)
r_c'	Output of command filter (rad or rad/sec)
$r_{c_{TRM}}$	Output of input integrator path (rad or rad/sec)
r_e	Yaw control system error signal (rad or rad/sec)
$r_{e_{LIM}}$	Limiter on error integrator (units of δ_{YAW})
$r_{e_{TRM}}$	Output of error integrator path (units of δ_{YAW})
r_{TRM}	Trim input from pedal trim or lateral stick trim (rad or rad/sec)
r_{INT_c}	Alternate name for r_c' when the yaw attitude feedback signal is r_{INT} (i.e. the system controls r_{INT}) (rad)

LIST OF SYMBOLS (Continued)

Yaw Control System Symbols (Figure 2-29):

r_{s_c}, $\hat{\beta}_c$	Alternate names for r_c' when $\hat{\beta}$ feedback is used (i.e. the system is a control for $\hat{\beta}$ or r_s) (rad/sec)
δ_{YAW}	Normalized control output of yaw control system; yaw control input for actuation system
τ_{YAW}	Time constant of command filter (sec)
ψ_{SW}	Logic switch related to CS_{SW} required to insure proper initialization of yaw rate integrator and system trim input.

Heave Control System Symbols (Figure 2-30):

K_{THROT}	Manual throttle input gain (lb/unit input)
K_{z_e}	Heave control system proportional error gain (lb/ft/sec)
$K_{\dot{z}_{e_c}}$	Heave rate command lever input gain (ft/sec/unit input)
$K_{z_{e_{I1}}}$	Heave control system error integral gain (1/sec)
$T_{e_{LIM}}$	Limiter on error integrator path (lb)
$T_{e_{TRM}}$	Output of error integrator path (lb)

LIST OF SYMBOLS (Continued)

Heave Control System Symbols (Figure 2-30):

$\dot{Z}_{e_c}$	Heave rate command input (ft/sec)
$\dot{Z}_{e_e}$	Heave control system error signal (ft/sec)

Pseudo-Pilot Model Symbols (Section 2.10)

K_u, K_v, K_w	Velocity feedback gains for control along the X_B, Y_B, and Z_B axes, respectively (ft/ft/sec)
$K_{x_{e_s}}$, $K_{y_{e_s}}$, $K_{z_{e_s}}$	Position error gains for control along the X_B, Y_B, and Z_B axes, respectively (units of appropriate cockpit controller/ft)
X_{e_s}, Y_{e_s}, Z_{e_s}	Position errors along X_B, Y_B, and Z_B axes, respectively (ft)
$V_{e_{EST}}$	Estimated inertial speed at next computer update (ft/sec)
ΔT	Computer iteration time (sec)
θ_{c_1}	Pitch angle command at current time based on V_e (rad)
θ_{c_2}	Pitch angle command at next computer update based on $V_{e_{EST}}$ (rad)
$\dot{\theta}_c$	Pitch rate command required to go from θ_{c_1} to θ_{c_2} by next computer update $(=(\theta_{c_2} - \theta_{c_1})/\Delta T)$ (rad/sec)

ACRONYMS

DATCOM	Data Compendium
FCS	Flight Control System
IOC	Initial Operational Capability
LINA	Vought Linear Analysis Program
NASA	National Aeronautics and Space Administration
PIO	Pilot Induced Oscillation
RCS	Reaction Control System
VAPE	V/STOL Aircraft Propulsive Effects
VATOL	Vertical Attitude Takeoff and Landing
VATLAS	Vertical Attitude Takeoff and Landing Aircraft Simulation
VL	Vertical Landing
VTO	Vertical Takeoff

SUMMARY

Vought Corporation has developed under contract NAS2-10294 for NASA-Ames Research Center a mathematical model of a high performance airplane capable of vertical attitude takeoff and landing (VATOL). The model is to be applied in piloted simulation studies at Ames of the flying qualities of VATOL aircraft in terminal area operations. An off-line (non-piloted) digital simulation program incorporating this model has been developed to provide trim conditions and dynamic check runs for the piloted simulation studies and support dynamic analyses of proposed VATOL configuration and flight control concepts. The final report for this contract is contained in three volumes. Volume I provides development details for the various simulation component models and describes the application of the off-line simulation program, VATLAS (Vertical Attitude Take-Off and Landing Simulation), to develop a baseline control system for the Vought SF-121 VATOL airplane concept. Volume II contains the simulation math model equations and baseline SF-121 data provided to Ames for the piloted simulation studies. The equations are the same as those implemented in VATLAS. Volume III is a users manual for VATLAS. It describes input data for each program option, contains several illustrative example runs, and includes complete program listings.

The component models for VATLAS were assembled from various sources. Several are "off the shelf". For example, the aerodynamics model is a modified version of a deterministic, high angle of attack, and large sideslip angle model developed at the Naval Air Development Center for application to low speed flight of V/STOL airplanes. Likewise, the propulsion system dynamics, generalized flight control system, and actuator models were applied in the simulation for the recent Lift/Cruise Fan V/STOL Flight Control/Flying Qualities Program. Other models are new or highly modified versions of existing models. Examples of these are the inlet ram effects, Coriolis effects and propulsion system-Reaction Control System interactions models. In the aircraft equations of motion, the standard Euler rate equations were replaced with a direction cosine formulation to avoid the singularity in the Euler equations when pitch angle equals 90 degrees. A collection of "pseudo-pilot" functions was developed to enable the VATLAS user to impose open loop time varying inputs (e.g. steps, doublets) on each cockpit controller and/or specify pilot-controlled (closed-loop) stationkeeping and transitions.

The application of VATLAS to develop a baseline FCS (flight control system) for the SF-121 airplane follows a general FCS design procedure. The inputs to this procedure include basic aircraft geometry, mass, inertia, lifting surface and fuselage aerodynamics, and propulsion system data; operational considerations for the airplane; and a preliminary FCS configuration. The operational consideration having most impact on the FCS design was that a tilted cockpit (similar to the "nutcracker" concept) would be used during hover. This required reversing of the conventional lateral stick and pedal roles for hover flight.

With all inputs defined, a candidate interface between FCS control variables and SF-121 actuators was defined. The acceptability of this interface was established by evaluation of six degrees of freedom trims of wings level transitions and of hovers in 35 kt winds from any direction. Next the FCS gains and control laws were developed by applying linear system analysis techniques to the preliminary FCS configuration. Complete design analyses were performed at six airspeeds between 0 and 200 kt. Features of the FCS thus developed include:

- Two modes - conventional mode above 60 kt airspeed, hover mode below 60 kt
- Three controlled degrees of freedom in conventional mode - roll, pitch, yaw; four in hover mode - roll, pitch, yaw, heave
- Gains are functions of airspeed
- Attitude stabilization in the rotational degrees of freedom; rate stabilization in heave
- Rate command/attitude hold type system in roll for both modes
- Rate command/attitude hold type system in pitch conventional mode; attitude command in hover mode
- Automatic turn coordination in yaw conventional mode; attitude command in hover mode
- Rate command in heave in hover mode

To evaluate the SF-121 FCS performance, nonlinear time histories were calculated by VATLAS for ten different test cases. The cases included longitudinal stick doublet, lateral stick pulse, and pedal step at 120 kt; longitudinal and lateral stick doublets, pedal pulse, and heave rate controller doublet at 10 kt; mode switching transient; and pseudo-pilot controlled transition and stationkeeping. The response traces are examined and discussed in some detail and support the conclusion that the baseline FCS provides an adequate starting point for piloted simulation studies and does not have to be iterated to correct unanticipated control deficiencies. The most distinguishing flying qualities characteristic of the SF-121 in hover is the non-minimum phase response of the airplane (i.e. it initially accelerates in the wrong direction) produced by the use of aft end thrust deflection for surge or sway control. This characteristic has the potential for producing pilot-induced oscillations when the pilot attempts tight control of surge or sway position.

1.0 INTRODUCTION

Aircraft capable of vertical attitude takeoff and landing (VATOL) may result from application of certain emerging fighter performance - enhancing technologies. These technologies include thrust vectoring, post stall controllability, and reliable high authority fly-by-wire control systems. VATOL aircraft have many unique handling characteristics, control system and display requirements, and pilot-cockpit interface requirements, particularly during terminal area operations. A simulation capability is required to evaluate and develop these characteristics and requirements prior to a large scale commitment of funds for VATOL aircraft development. This capability must therefore be available early in the design process as a medium for comparing VATOL concepts. Detailed data bases will generally not be available for these comparisons. Thus the simulation must be capable of generating appliable data sufficiently detailed to emphasize differences and trends among several competing concepts. Under contract NAS2-10294 with NASA - Ames Research Center, Vought Corporation has developed a generic VATOL simulation math model which provides this capability.

This math model has been implemented at NASA - Ames for piloted simulation studies and in an off-line digital program named VATLAS (Vertical Attitude Takeoff and Landing Simulation). VATLAS provides trim conditions and dynamic check runs for the piloted simulation studies and supports nonlinear dynamic analyses of proposed VATOL configuration and flight control concepts. Development details of the aerodynamics, propulsion system, flight control system, inlet ram, and Coriolis effects models and results of a VATLAS application to the Vought SF-121 VATOL concept are described in this volume which is the first of a three volume final report. Volume II details the model equations and baseline data for the NASA - Ames simulation studies. Volume III is a user manual for VATLAS.

Section 2.0 of this volume details the component models and axis systems employed in the complete VATOL model. Interfacing of the models for simulation is depicted in figure 1-1. Also described in Section 2.0 is a collection of "pseudo-pilot" functions which was developed to enhance the

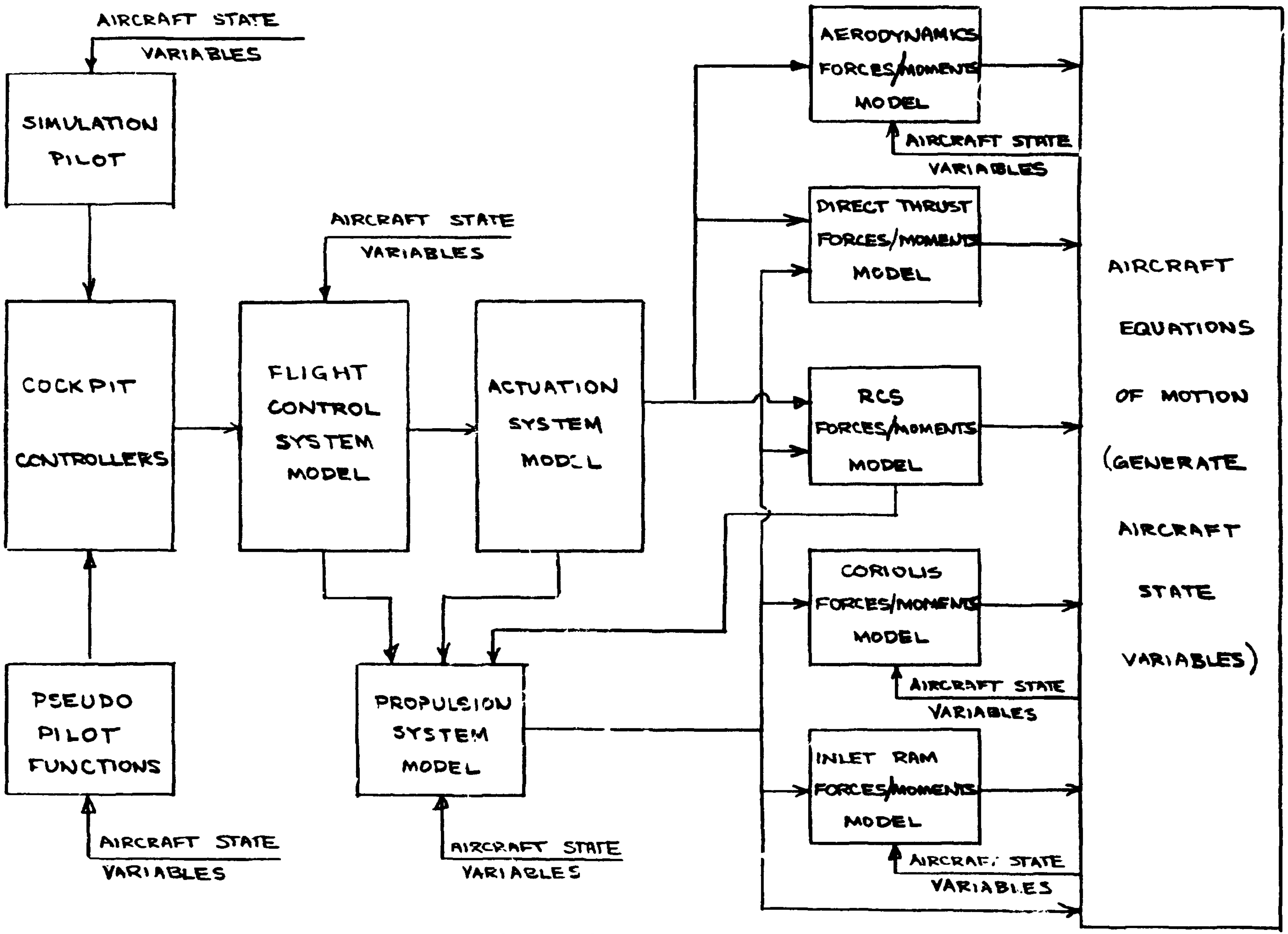

Figure 1-1. VATOL Simulation Math Model General Arrangement

utility of VATLAS. These functions enable the VATLAS user to impose open loop time varying inputs (e.g. steps, doublets, etc.) on each cockpit controller and/or specify pilot controlled (closed loop) stationkeeping and transitions.

Section 3.0 details the VATLAS application to the Vought SF-121 VATOL airplane depicted in figures 1-2 and 1-3. This application is the development of a baseline flight control system for the SF-121 beginning with a definition of the basic airplane data and proceeding through actuator input specification and trim characteristics evalution to specification and evaluation of the baseline system gains and control laws.

Conclusions and recommendations established during the model development and application are incorporated in Section 4.0.

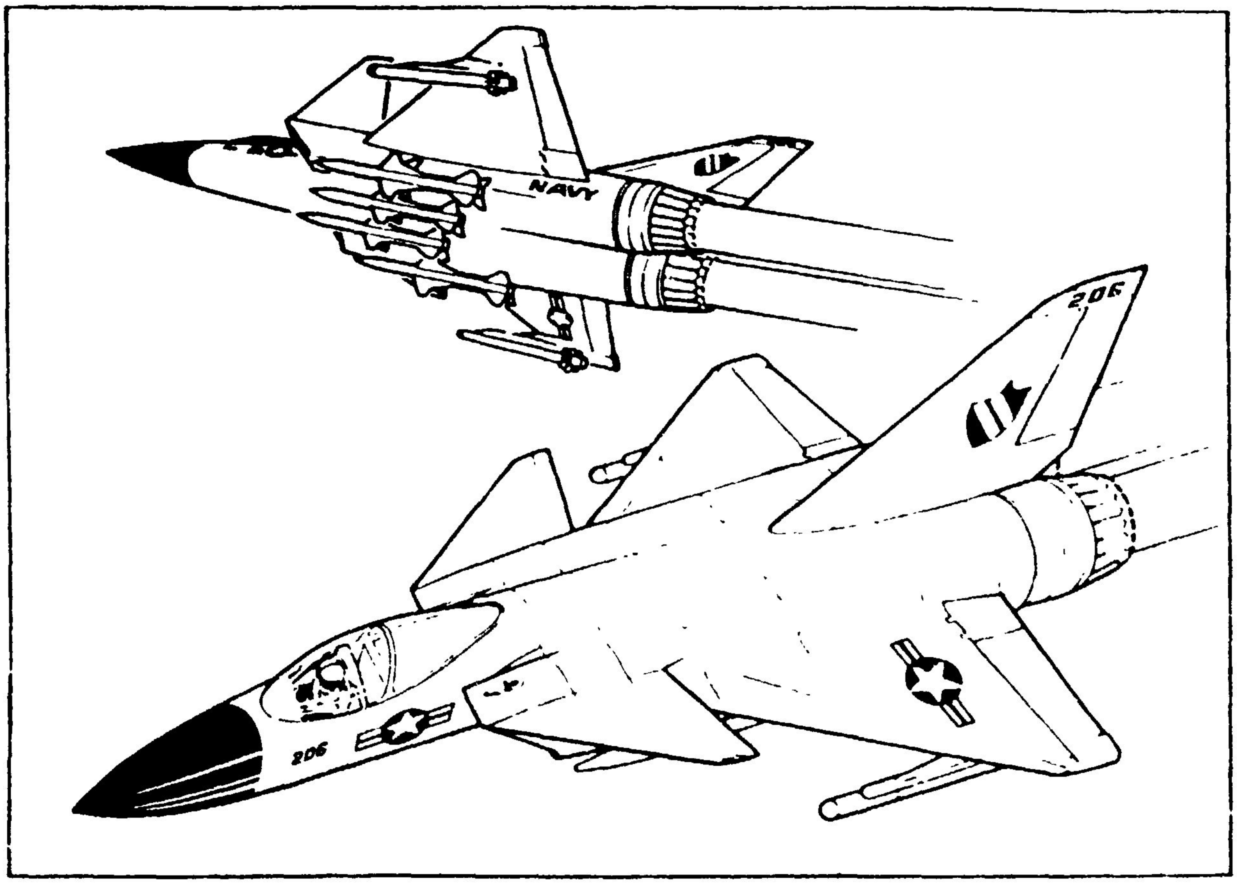

Figure 1-2. SF-121 Series Superfly VATOL Fighter

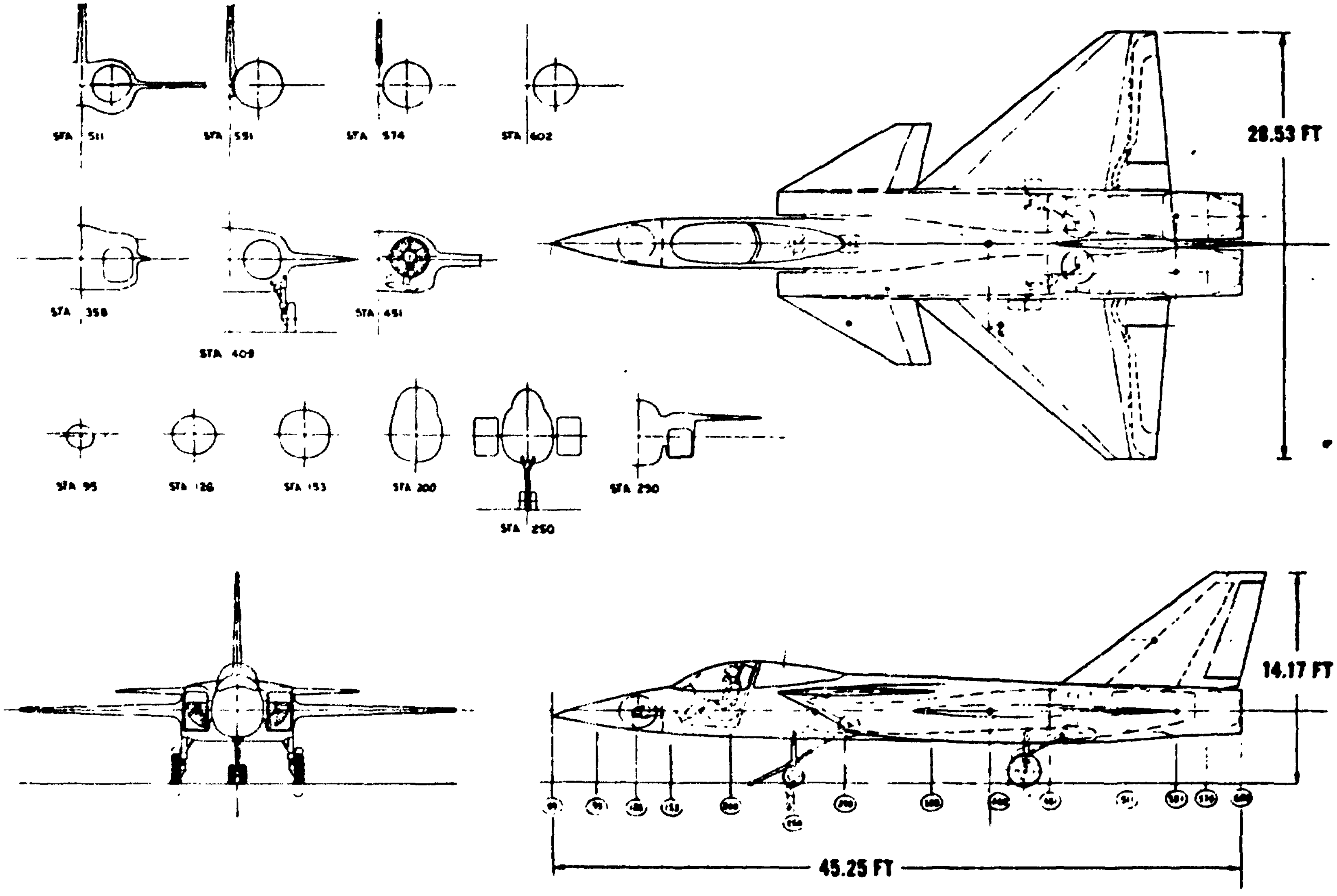

Figure 1-3. SF-121 General Arrangement

2.0 VATOL SIMULATION MATH MODEL

This chapter provides background and details for the six component models of the VATOL simulation math model. The component models and applicable report sections are as follows:

- o Aerodynamic Forces and Moments - Section 2.2
- o Propulsion System Model including dynamics, forces and moments, and RCS (Reaction Control System) interactions - Section 2.3.
- o Inlet Ram Forces and Moments - Section 2.4
- o RCS Forces and Moments - Section 2.5
- o Coriolis Forces and Moments - Section 2.6
- o Actuation System - Section 2.7
- o Flight Control System - Section 2.8

The model discussions are preceded by a description in Section 2.1 of the primary axis systems used in the simulation.

Since VATOL airplanes routinely maneuver at pitch angles approaching 90 degrees where the standard Euler angle transformation has a singularity, the airplane equations of motions were formulated with direction cosines. This formulation and other possible alternatives to avoid the singularity are discussed in Section 2.9. Section 2.10 details the pseudo-pilot functions which were incorporated into VATLAS to simulate pilot control of the aircraft.

2.1 Primary Axis Systems

Four primary axis systems are employed in the VATOL simulation math model. These include a North oriented inertial or earth axis system, the vehicle-referenced body axis system, the wind axis system, and the stability axis system. The relation between earth axes (X_I, Y_I, Z_I) and body axes (X_B, Y_B, Z_B) is depicted in figure 2-1. The orientation of the body axes with respect to earth axes is determined by an ordered rotation through the standard Euler angles - first, yaw (ψ) around the Z_I axis, then pitch (θ) around the Y_1 axis, and finally roll (ϕ) around the X_B axis. Aircraft cg position ($\vec{r}_{cg}$) is measured in earth axes and has components X_e, Y_e, and Z_e along the X_I, Y_I, and Z_I axes respectively. Similarly, aircraft cg velocity ($\dot{\vec{r}}_{cg}$) is measured in earth axes and has components $\dot{X}_e$, $\dot{Y}_e$, and $\dot{Z}_e$. In the body axis system, aircraft velocity has components u, v, and w along the X_B, Y_B, and Z_B axes respectively. $\dot{X}_e$, $\dot{Y}_e$, $\dot{Z}_e$ and u, v, w are related by the Euler transformation matrix:

$$\begin{bmatrix} u \\ v \\ w \end{bmatrix} = \begin{bmatrix} \cos\theta\cos\psi & \cos\theta\sin\psi & -\sin\theta \\ \sin\phi\sin\theta\cos\psi - \sin\psi\cos\phi & \sin\psi\sin\theta\sin\phi + \cos\psi\cos\phi & \sin\theta\cos\theta \\ \cos\psi\cos\phi\sin\theta + \sin\psi\sin\phi & \sin\psi\cos\phi\sin\theta - \cos\psi\sin\phi & \cos\phi\cos\theta \end{bmatrix} \begin{bmatrix} \dot{X}_e \\ \dot{Y}_e \\ \dot{Z}_e \end{bmatrix}$$

$$= \begin{bmatrix} d_{11} & d_{21} & d_{31} \\ d_{12} & d_{22} & d_{32} \\ d_{13} & d_{23} & d_{33} \end{bmatrix} \begin{bmatrix} \dot{X}_e \\ \dot{Y}_e \\ \dot{Z}_e \end{bmatrix}$$

where the d_{ij}'s are direction cosines.

The body axis system is oriented in the aircraft as follows (figure 2-2): The origin is at the aircraft cg. The X_B axis is parallel to the fuselage reference line and positive forward. The Y_B axis is perpendicular to the aircraft plane of symmetry and is positive to the right. The Z_B axis is in the plane of symmetry, perpendicular to the X_B and Y_B axes, and positive downward. This orientation remains fixed in the aircraft for all time. Locations of aircraft features of interest (e.g. engine inlets

NOTE:

X_B, Y_B, Z_B - AIRPLANE BODY AXES

X_I, Y_I, Z_I - INERTIAL AXES (NORTH-ORIENTED)

θ, ϕ, ψ - EULER ANGLES

$\dot{\theta}, \dot{\phi}, \dot{\psi}$ - RATES OF CHANGE OF EULER ANGLES

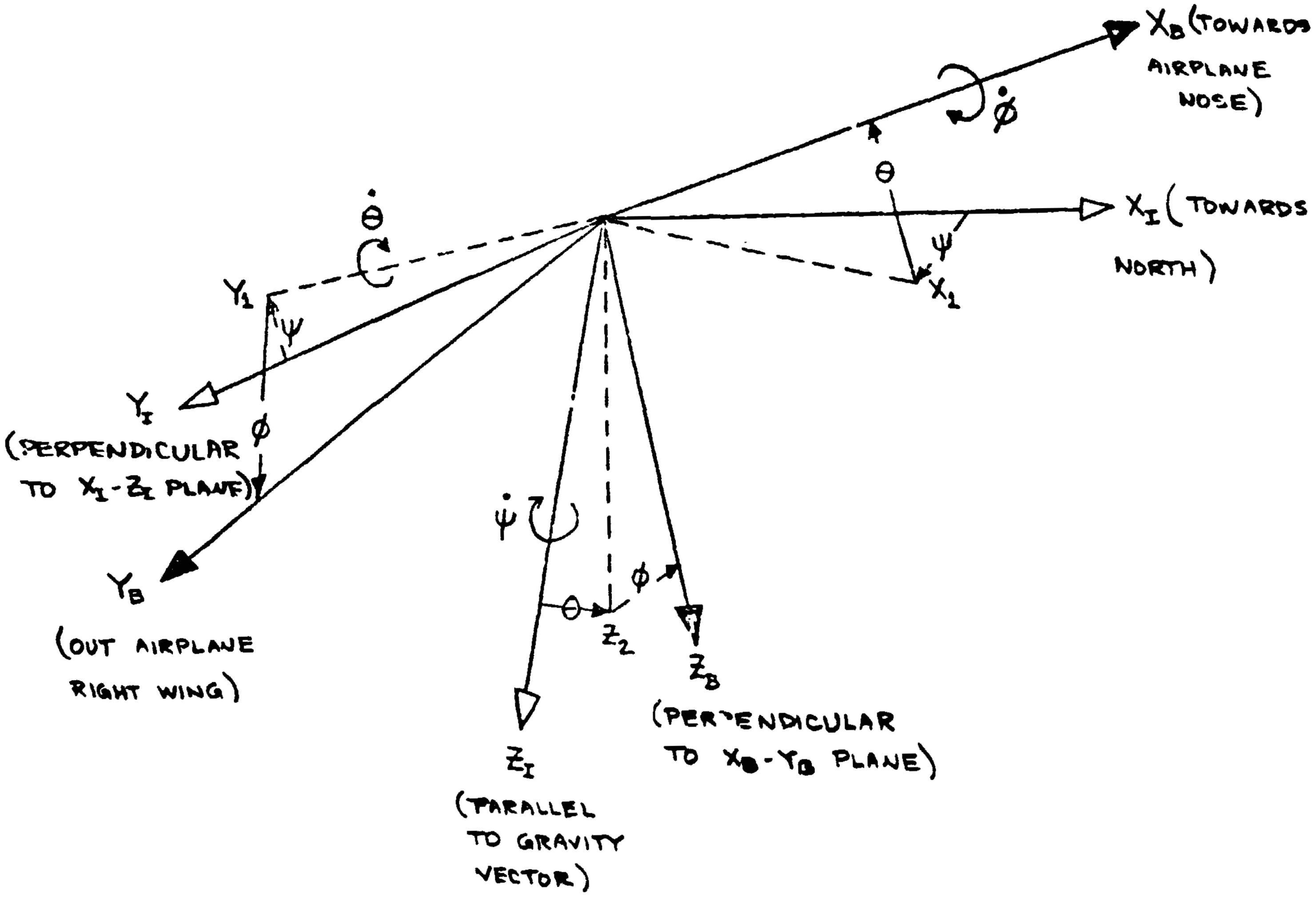

Figure 2-1. Systems of Inertial and Vehicle Body Axes

NOTE:

X_B, Y_B, Z_B – AIRPLANE BODY AXES
FS – FUSELAGE STATION
BL – BUTT LINE
WL – WATER LINE

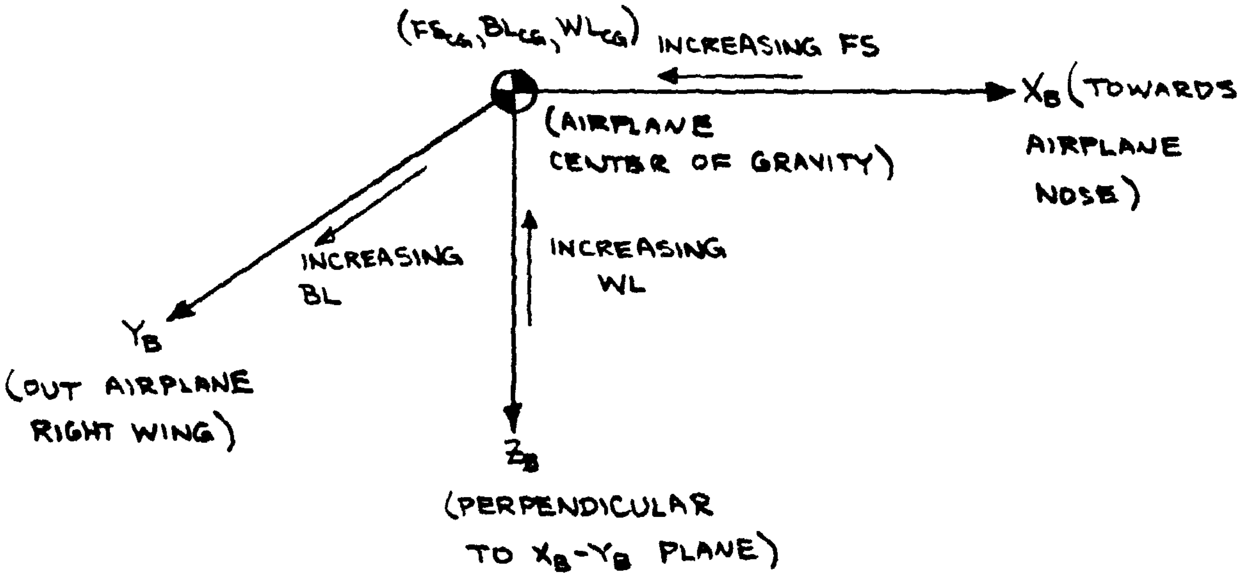

Figure 2-2. Relation of Aircraft Coordinates to Vehicle Body Axes

and exits, lifting surface centers of pressure) in the body axis system are expressed in aircraft coordinates - fuselage station (FS), butt line (BL), and waterline (WL). The directions of increasing aircraft coordinates are indicated on figure 2-2.

Unlike the body axis system, the wind and stability systems do not maintain fixed orientation to the aircraft. The relations between wind, stability, and body axes are depicted in figure 2-3. The X wind axis (X_W always points into the relative wind. Note that if angle of attack (α) and sideslip angle (β) are both zero, the wind, stability, and body axis systems are coincident. Similarly if $\alpha = 0$ and $\beta \neq 0$, the body and stability axes are coincident and, if $\alpha \neq 0$ and $\beta = 0$, the stability and wind axes are coincident.

The VATOL math model uses several axis systems of convenience for force and moment producing elements of the aircraft. These systems are introduced as required in the model development. Examples include the inlet and Coriolis force and moment axis systems. Regardless of the axis system adopted for a component model, all forces and moments are resolved eventually into body axes.

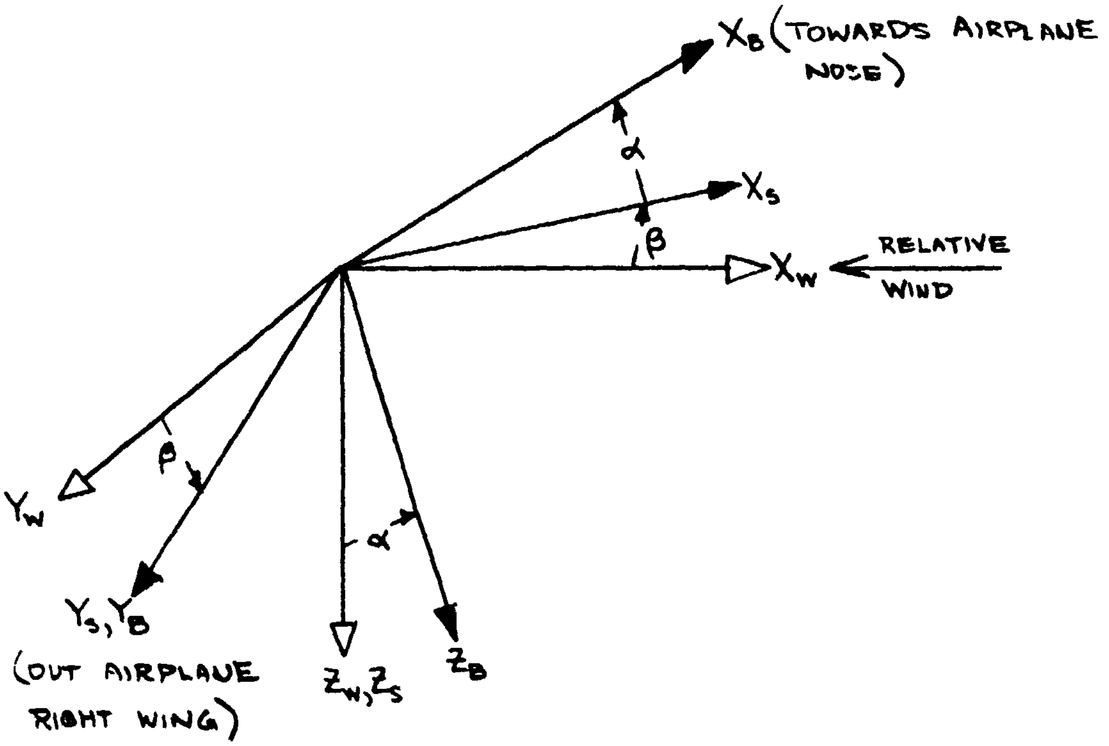

NOTE:

X_E, Y_B, Z_B – AIRPLANE BODY AXES

X_W, Y_W, Z_W – WIND AXES

X_S, Y_S, Z_S – STABILITY AXES

X_S POINTS INTO COMPONENT OF RELATIVE WIND IN X_B-Z_B PLANE (X_S, Y_S, Z_S RELATED TO X_B, Y_B, Z_B BY AN α ROTATION ABOUT Y_B AXIS)

X_W POINTS INTO RELATIVE WIND (X_W, Y_W, Z_B RELATED TO X_S, Y_S, Z_S BY A β ROTATION ABOUT Z_S AXIS)

Figure 2-3. Systems of Wind, Stability, and Vehicle Body Axes

2.2 Aerodynamics Model

Operating with the guideline to produce an easily modified model, the NASA contract requirement to produce a componentized aerodynamics model, and the fact that VATOL aircraft will experience large angles of attack and sideslip; Clark's model (reference (a)) was adopted as a base for the VATLAS aerodynamics model. This model "builds" the total airplane aerodynamics from fuselage and lifting surface contributions i.e., it is componentized. The model provides continuous aerodynamics functions for all α's and β's i.e., $-180 \leq \alpha \leq 180$ degrees and $-90 \leq \beta \leq 90$ degrees. The model is based on DATCOM (reference (b)) techniques and thus requires only a modicum of data (e.g. lifting surface geometry, linear lift curve slopes, stall angles, etc) to completely model airplane aerodynamics i.e., it is easily modified to represent a range of VATOL concepts. In recognition of the limitations of DATCOM in predicting aerodynamic characteristics at high α's and β's, the reader is reminded that, in terminal operations, large α's and β's are encountered only at low speeds where aerodynamics do not affect significantly the aircraft flying qualities.

Adapting Clark's model to current purposes was guided by a self-imposed requirement to obtain reasonable fits of the published Vought SF-121 aerodynamics data in reference (c). Obviously these published data could have been loaded directly into the math model, but at the sacrifice of overall VATOL model flexibility and timeliness. The strength of Clark's approach is its inherent ability to produce consistent aerodynamic estimates for aircraft concepts not yet possessing wind tunnel data bases.

The procedure outlined below was followed in applying and eventually modifying Clark's model for VATOL simulation:

1. Model parameter data were developed for the SF-121 either from the data in reference (c) or from DATCOM. DATCOM was used if the data could not be extracted from reference (c).
2. Clark's model as published was applied to the SF-121 using the model parameter data determined in step 1.

3. Calculated and published SF-121 data were compared to indicate what model modifications might be necessary to improve its predictive capability.
4. The candidate model modifications were made, evaluated, and incorporated as required.

Equations for the aerodynamics model which evolved from this procedure are given in Section 2.0.1 of Volume II of this report. Model parameter data for the SF-121 are given in Section 3.3 of Volume II. Results of the published and calculated SF-121 aerodynamics data comparisons and the modifications made to Clark's model to produce the VATLAS model are presented and discussed in the next section.

2.2.1 Data Comparison and Aero Model Modifications

Figures 2-4 through 2-10 compare the published SF-121 data (reference (c)) with the "initial" and "final" aero models. The SF-121 data are a composite of results from various Vought and NASA wind tunnel tests on similar configurations. The "initial aero model" results represent Clark's model applied to model parameter data developed from references (b) and (c). The "final aero model" results represent a modified version of Clark's model applied to the initial aero model parameter data base augmented by the additional data required by the modifications.

Comparison with SF-121 data of the results of applying the initial model to the SF-121 led to the following observations:

1. Predicted and SF-121 lift coefficient (figure 2-4) data are in good agreement for all $\alpha \leq 90$ degrees.
2. Predicted and SF-121 drag coefficient (figure 2-5) are in good agreement below $\alpha = 50$ degrees. Predicted drag coefficients are considerably higher than SF-121 data for $\alpha > 50$ degrees.
3. For $\alpha < 20$ to 30 degrees, the model provides reasonable predictions of SF-121 pitch moment coefficient (figure 2-6) data. For $\alpha > 30$ degrees the model predictions and data have

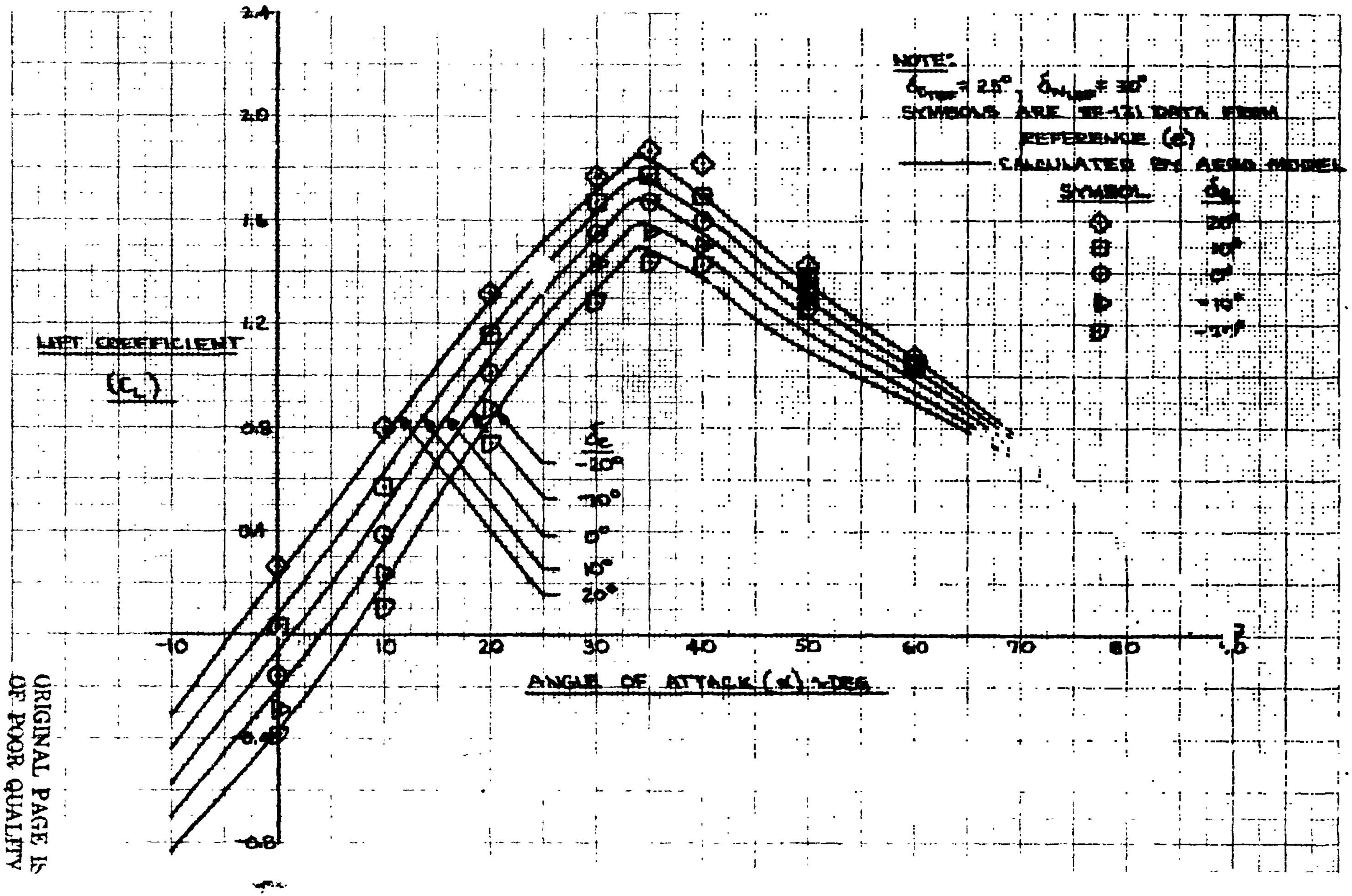

Figure 2-4. Comparison of SF-121 Lift Coefficient Published Data With That Calculated by Aero Model

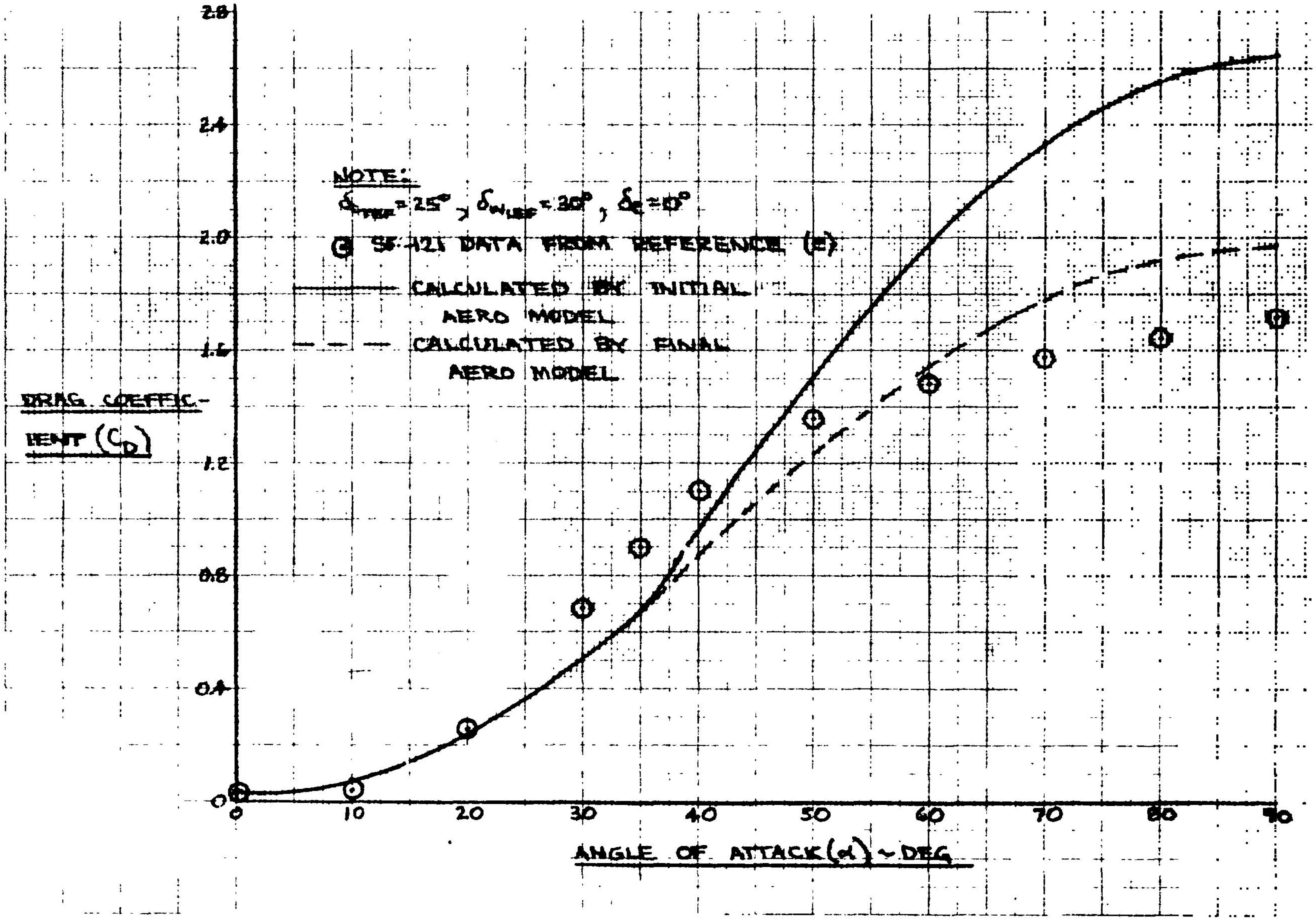

Figure 2-5. Comparison of SF-121 Drag Coefficient Published Data With That Calculated by Aero Model

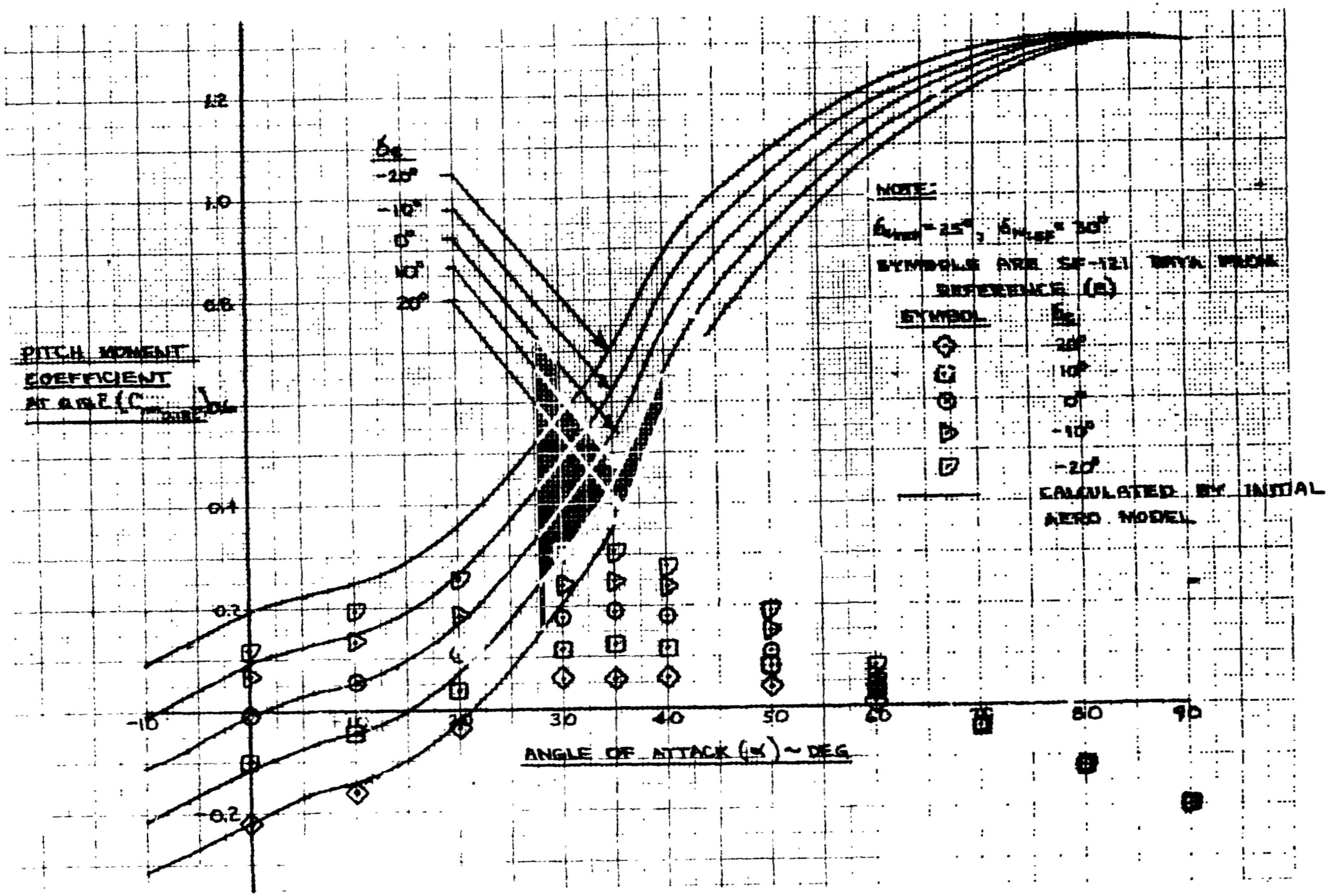

Figure 2-6. Comparison of SF-121 Pitch Moment Coefficient Published Data With That Calculated by Initial Aero Model

opposite trends; the model predicts an increasing (unstable) pitch moment as α increases while the data show a decreasing (stable) pitch moment with increasing α. The apparent cause and resolution of this discrepancy are discussed in the next paragraph.

4. Predicted and SF-121 C_{l_β} and C_{Y_β} (figure 2-7) data are in reasonable agreement for all $\alpha \leq 90$ degrees.
5. Predicted and SF-121 C_{n_β} (figure 2-7) data are in good agreement for $\alpha < 20$ to 25 degrees. For $\alpha > 25$ to 30 degrees, the SF-121 data are considerabley more negative than the model predictions.
6. Below $\alpha = 25$ degrees, the predicted and SF-121 rudder derivatives (figure 2-8) are in reasonable agreement. The $C_{l_{\delta_r}}$ prediction is reasonable to $\alpha = 90$ degrees. $C_{n_{\delta_r}}$ and $C_{Y_{\delta_r}}$ predictions are not good in the $\alpha = 30$ to 60 degrees range; the data fall off faster than the predictions. Beyond $\alpha = 60$ degrees, the $C_{n_{\delta_r}}$ and $C_{Y_{\delta_r}}$ predictions are reasonable; data and predictions indicate small values of the derivatives.
7. SF-121 $C_{l_{\delta_a}}$ data (figure 2-9) are reasonably predicted for $\alpha < 30$ degrees. At high α, the data indicate aileron reversal which is not predicted by the model.
8. SF-121 $C_{n_{\delta_a}}$ data (figure 2-9) indicate a proverse yaw tendency for $\alpha < 15$ to 20 degrees which is not predicted by the model. The data trend toward adverse yaw with increasing α (for $\alpha < 35$ degrees) is predicted by the model. With the exception of more adverse yaw displayed by the data for $\alpha = 55$ to 70 degrees, the model predictions and data have reasonable agreement for $\alpha > 35$ degrees.

The result of most concern from the initial aero model evaluation is the poor prediction of pitch moment coefficient for $\alpha > 30$ degrees. Based on the good agreement in lift coefficient data and predictions, it is obvious that some, if not all, the pitch moment discrepancies could be resolved by allowing an aft shift of the center of pressure (cp) of the aerodynamic components with increasing α. Clark's model has no provision for a cp shift

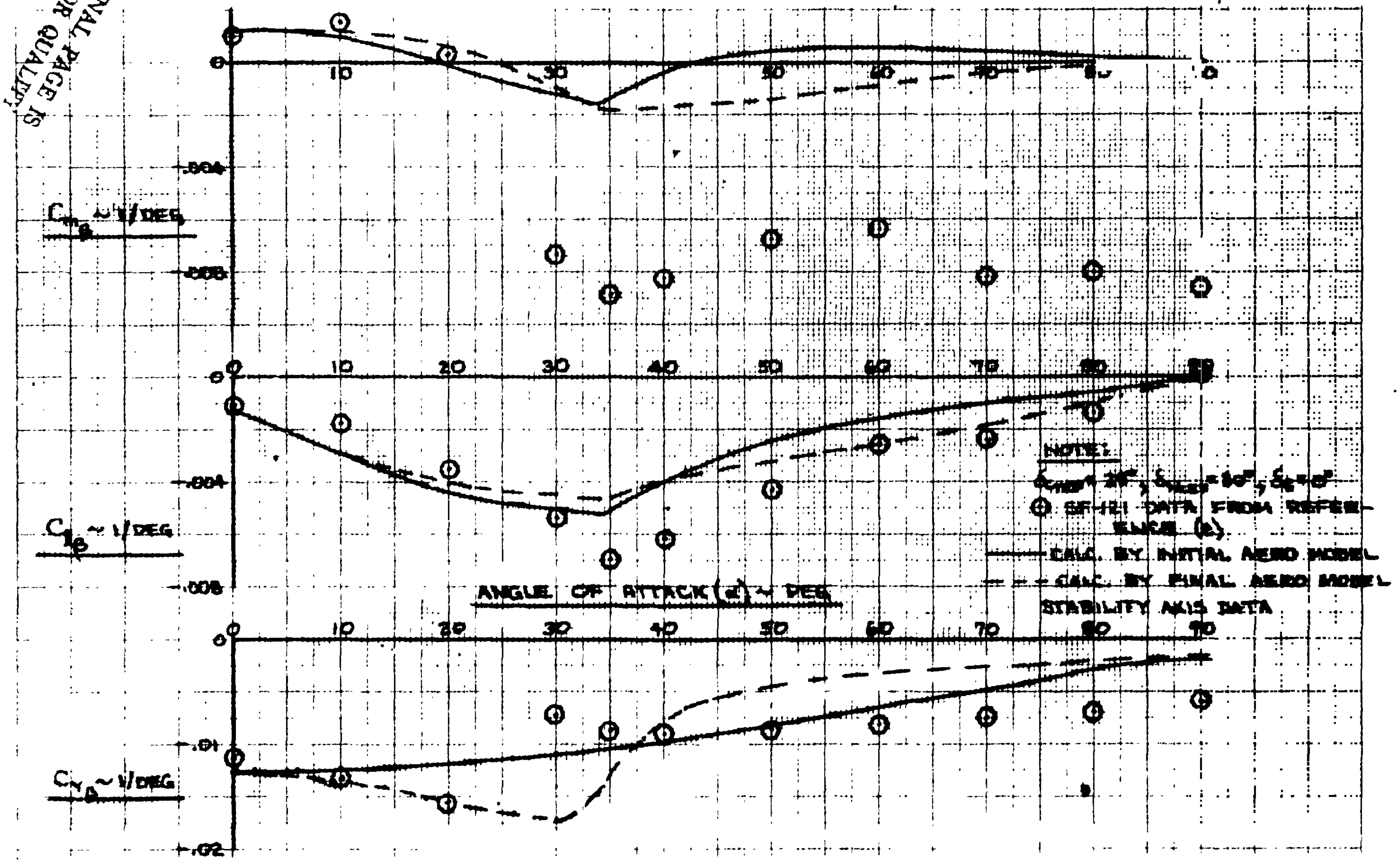

Figure 2-7. Comparison of SF-121 Static Lateral Stability Derivatives Published Data With That Calculated by Aero Model

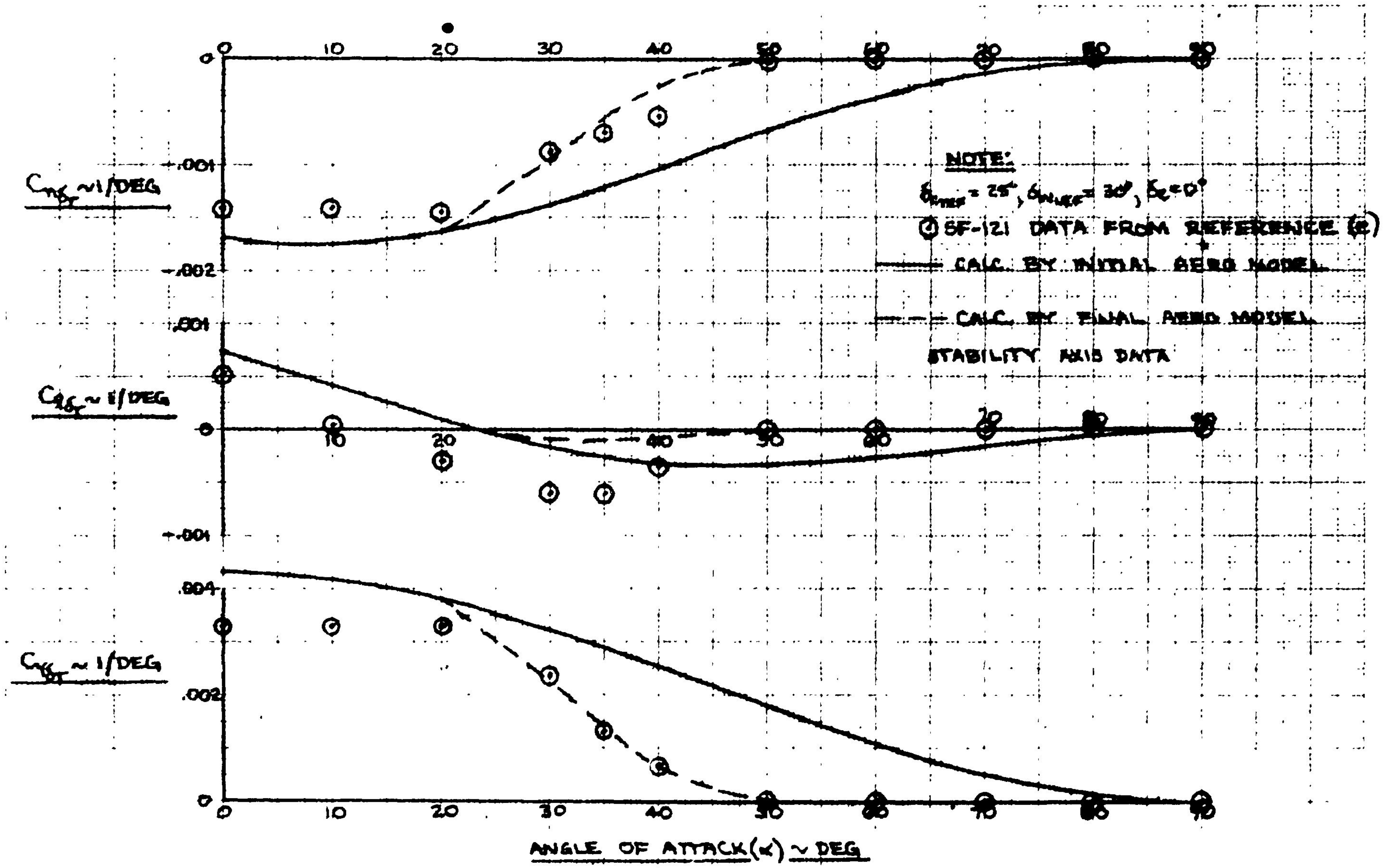

Figure 2-8. Comparison of SF-121 Rudder Derivatives Published Data With That Calculated by Aero Model

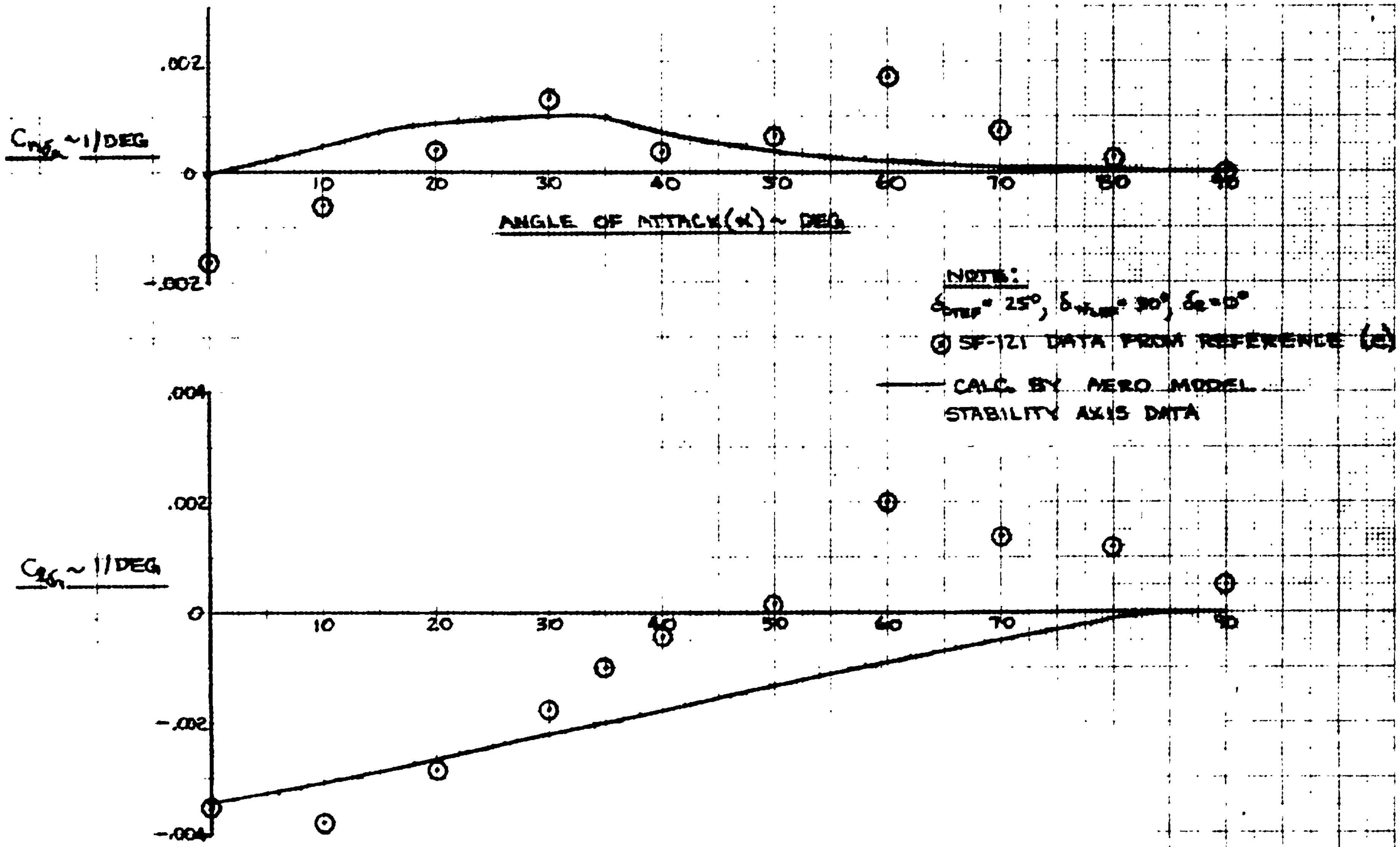

Figure 2-9. Comparison of SF-121 Aileron Derivatives Published Data With That Calculated by Aero Model

with α. Section 4.1.4.3 in DATCOM describes a model for the cp shift of lifting surfaces. This model was appended to Clark's basic equations. Equations were also added to allow the cp of the fuselage to change with α. This fuselage cp shift is not covered in DATCOM but was added to compensate for residual pitch moment discrepancies between model and data after the effect of lifting surface cp shifts are included. In the absence of a data base, the fuselage cp shift would not be implemented. Figure 2-10 presents the data comparison obtained with the final pitch moment model i.e., Clark's model modified to include cp shifts with α for both fuselasge and lifting surfaces. The agreement between pitch moment coefficient data and prediction is now almost as good as that for the lift coefficient.

Examination of the difference between drag coefficient data and prediction for $\alpha > 50$ degrees led to a modification in the calculation of high α lifting surface drag. Clark's high α drag model fairs lifting surface drag coefficient to 1.2 at $\alpha = 90$ degrees. This limiting value of drag coefficient is based on the reference area of the surface. It seems reasonable that, in consonance with other calculations in Clark's model the limit drag should be based on exposed surface rather than reference area. This modification (i.e. multiply 1.2 times the ratio of exposed area to reference area in the high α drag equation) was made in Clark's model and produced the much improved high α drag coefficient prediction shown in figure 2-5.

The differences between $C_{n_{\delta_r}}$ and $C_{Y_{\delta_r}}$ predictions and data in the $\alpha = 30$ to 60 degrees range (figure 2-8) are attributed to a gradual, and eventually total, loss of vertical tail effectiveness due to masking by the wing and fuselage (refer to SF-121 3-view on figure 1-3). Since Clark's model has no provision for this phenomenon, it was incorporated in a table format of vertical tail effectiveness as a function of α. The table was quantified using $C_{Y_{\delta_r}}$ data which, unlike other side force derivatives, have only a vertical tail contribution. For aircraft not possessing a data base, reasonable estimates of vertical tail effectiveness can be made by scutinizing relative locations of the vertical tail and other aerodynamic contributors of the aircraft as a function of α. The much improved predictions of $C_{Y_{\delta_r}}$ and $C_{n_{\delta_r}}$ with the modified model are shown on figure 2-8. Note that the prediction of $C_{l_{\delta_r}}$ is only slightly affected by this modification.

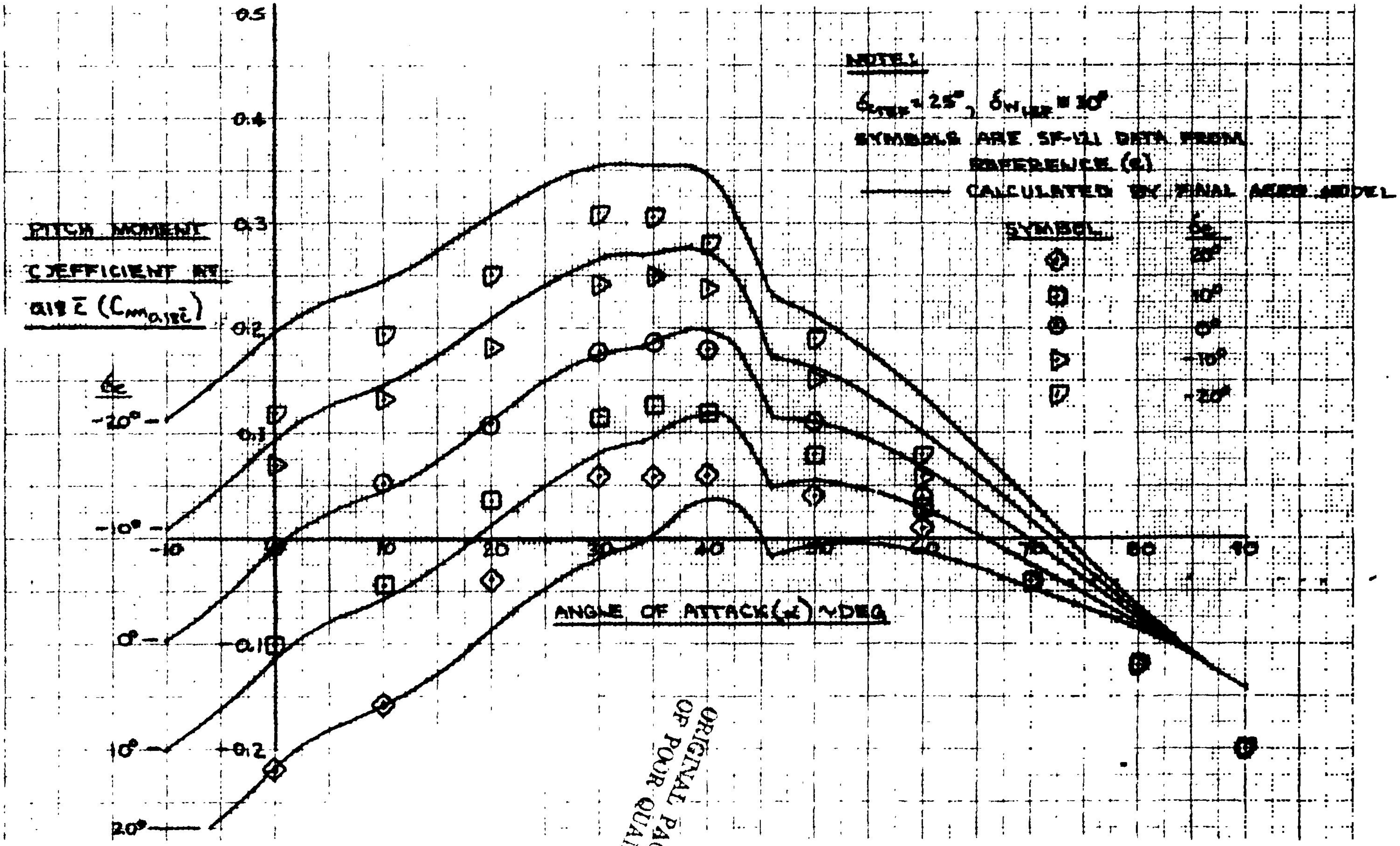

Figure 2-10. Comparison of SF-121 Pitch Moment Coefficient Published Data With That Calculated by Final Aero Model

The modification of vertical tail effectiveness also affects the sideslip derivatives. The dashed curves for C_{n_β} and C_{l_β} on figure 2-7 reflect this modification. The C_{Y_β} dashed curve includes this plus another modification to be discussed below. The C_{l_β} prediction is improved at high α with little change in the already good low α prediction. The C_{n_β} prediction is improved only in that, like the data with increasing α, the aircraft does not reacquire a positive C_{n_β} once it becomes negative. To predict the large C_{n_β} shown by the data for $\alpha > 30$ degrees would require modifications to the model which are highly configuration specific and are thus beyond the scope of intended model application. The required changes were not made for the SF-121 application reported herein.

The other modification reflected in the dashed C_{Y_β} curve on figure 2-7 is the addition of a $C_{Y_{\beta C_L^2}}$ term in the wing contribution to C_{y_β}. Calculations of C_{y_β} with only the vertical tail effectiveness modification showed a degraded predicton capability from that of the basic Clark model. This indicated a need for further model refinement. Examination of unpublished wing-body C_{Y_β} data for the SF-121 justified the inclusion of a $C_{Y_{\beta C_L^2}}$ term in the model and allowed its value to be estimated. Section 5.1.1.1 of DATCOM has a methodology to determine its value in the absence of data. The term was incorporated into the aero model and C_{Y_β} was recalculated. As indicated by the dashed C_{Y_β} curve on figure 2-7 the model prediction capability has not been enhanced significantly over that of the basic Clark model. The modified model is, however, consistent with DATCOM methodology and the vertical tail effectiveness change with α.

Similar to sideslip derivatives, the highly configuration specific nature of high α lateral control derivatives of plain flapped elevons (used on the SF-121) precludes reliable predictions. Thus the prediction of Clark's model for $C_{n_{\delta_a}}$ and $C_{l_{\delta_a}}$ (figure 2-9) cannot be improved without data.

The "final aero model" was used to generate all SF-121 aero data for the application described in Section 3.0 of this volume. The major discrepancies remaining between data and model predictions are high α C_{n_β} and $C_{l_{\delta_a}}$. It is postulated that the effects of these discrepancies on aircraft flying qualities will be minimal because, in SF-121 terminal operations, high α's are encountered only at low airspeeds and low dynamic pressures. To prove this contention is beyond the scope of the contract.

The modifications to the "initial aero model" to produce the "final aero model" are reiterated below:

1. Incorporation of DATCOM method to calculate cp shift of lifting surface as a function of α. Also a fuselage cp shift has been incorporated to fine tune the pitch moment coefficient prediction if supporting data are available.
2. The $\alpha = 90$ degrees lifting surface drag coefficient ($= 1.2$) has been referenced to exposed surface area.
3. A table to incorporate vertical tail effectiveness as a function of α has been made available.
4. A $C_{Y_{\beta C_L^2}}$ term has been added in the wing contribution to sideforce calculations.

The equations for the final model are given in Section 2.0.1 of Volume II while model parameter data for the SF-121 are given in Section 3.3 of the same volume.

2.1.2 Aerodynamic Rotary Derivatives

The aero model calculates rotary derivatives. Reference (c) has no rotary derivative data for the SF-121, thus a comparison of model predictions and data is not possible. For completeness, a sampling of calculated SF-121 rotary derivatives is given in figures 2-11 through 2-13. These were, of course, used in the SF-121 application described in Section 3.0 of this volume.

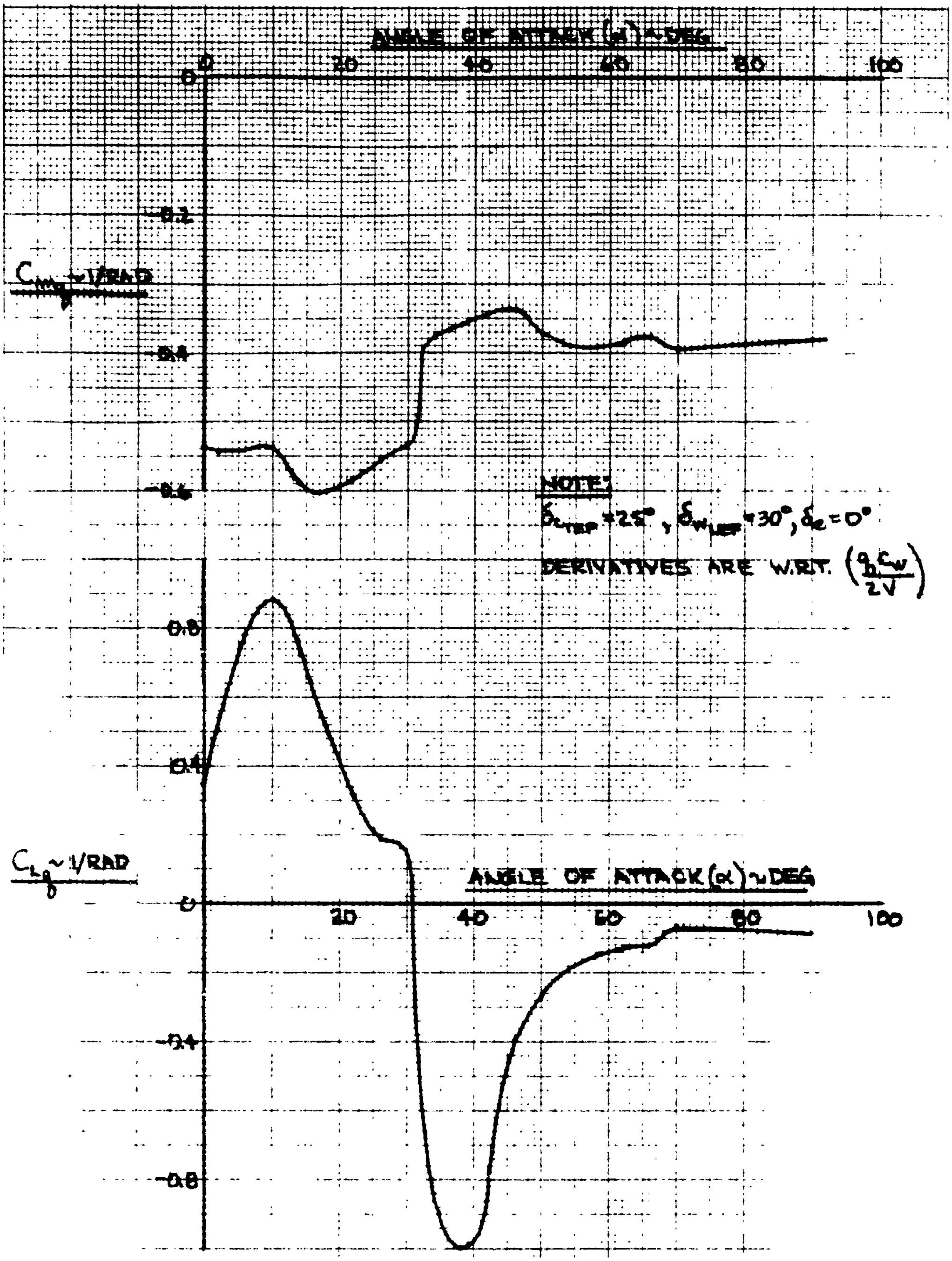

Figure 2-11. SF-121 Pitch Rate Derivatives Calculated by Aero Model

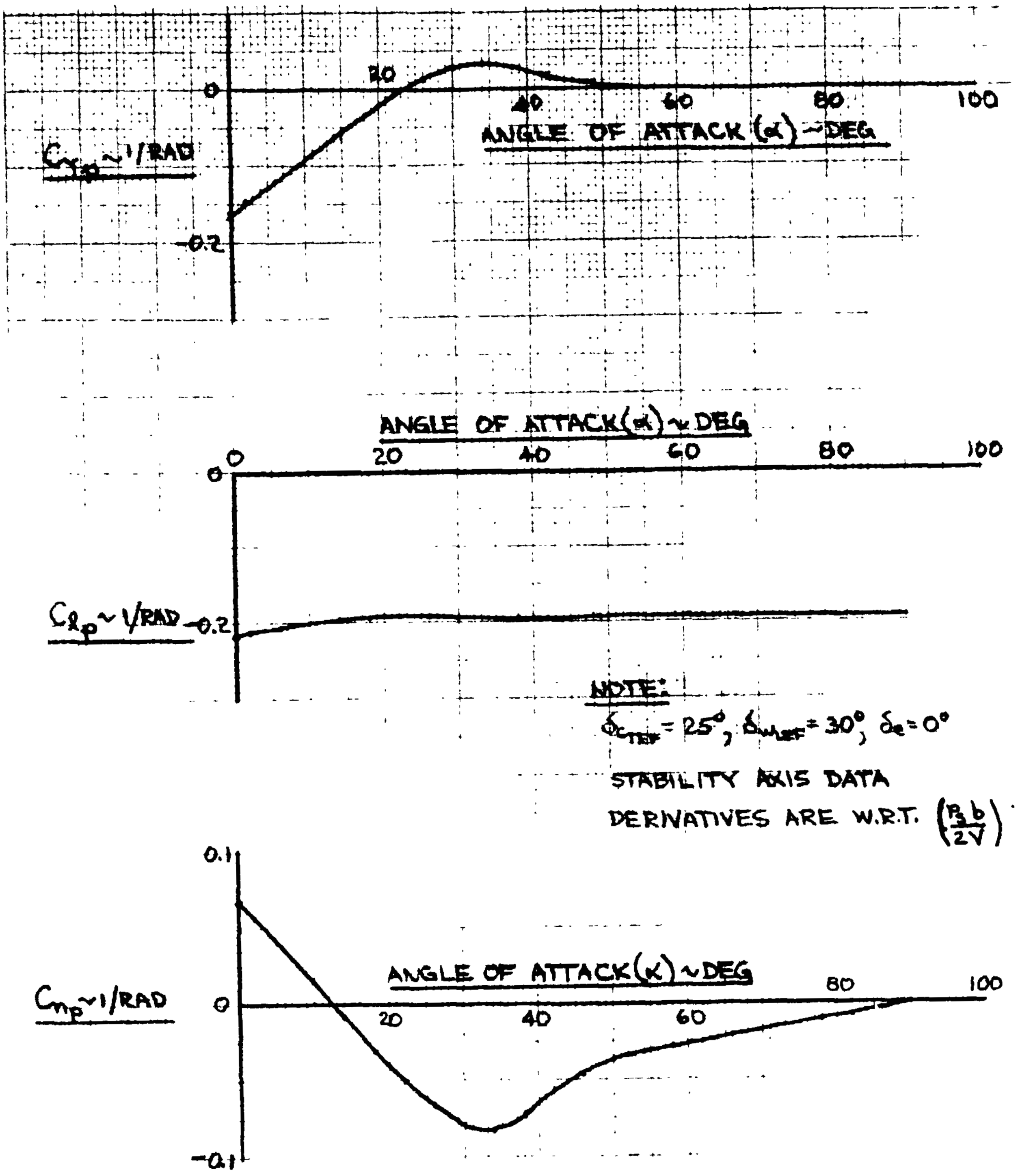

NOTE:

$\delta_{C_{TEF}} = 25°$, $\delta_{WLEF} = 30°$, $\delta_e = 0°$

STABILITY AXIS DATA

DERIVATIVES ARE W.R.T. $\left(\frac{P_s b}{2V}\right)$

Figure 2-12. SF-121 Roll Rate Derivatives Calculated by Aero Model

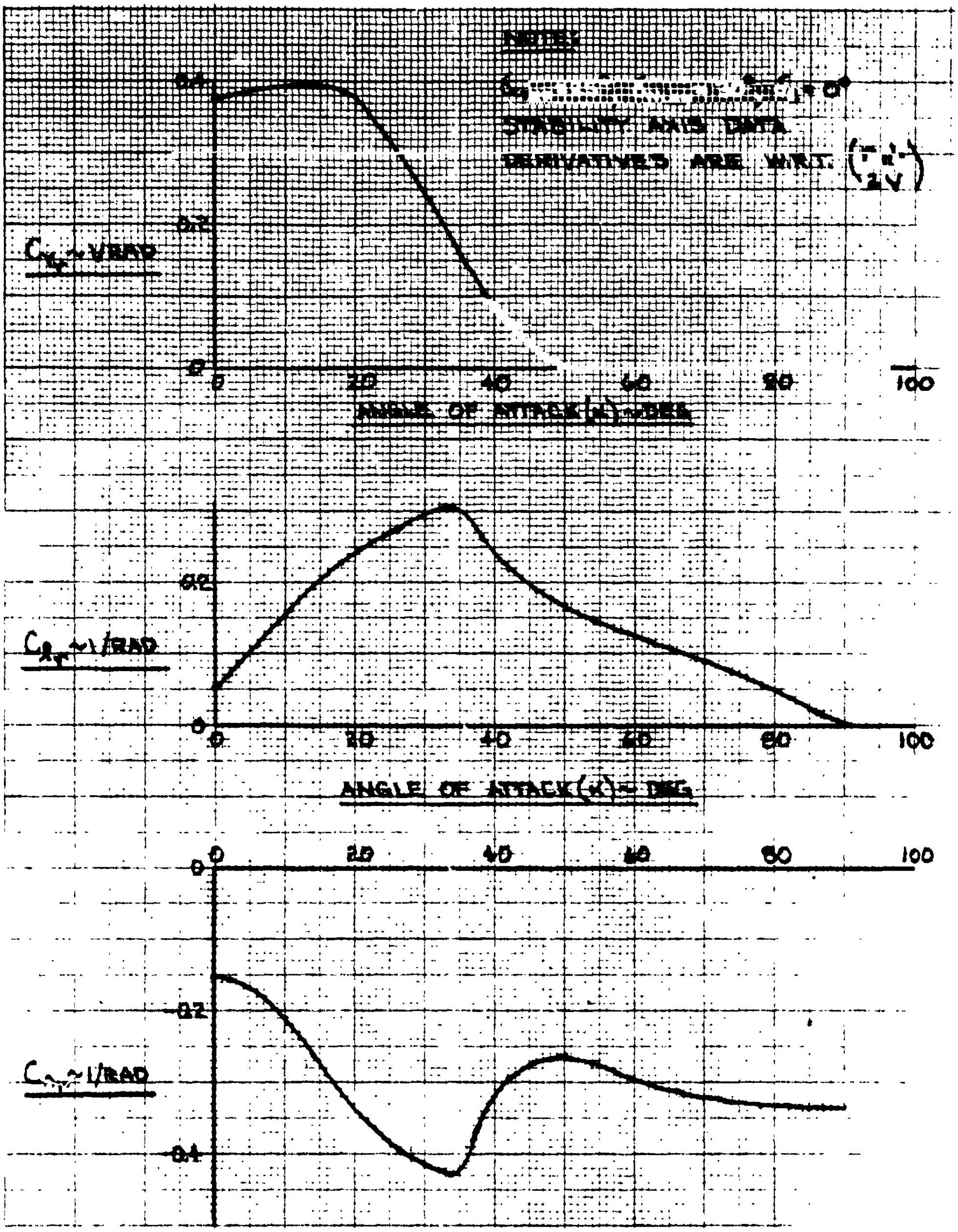

Figure 2-13. SF-121 Yaw Rate Derivatives Calculated by Aero Model

2.3 Propulsion System Model

The basic propulsion system model for VATOL simulation has six primary distinguishing features:

- o Thrust deflection in two directions via a gimballed nozzle arrangement
- o Engine installation angle
- o Nonlinear dynamics - time constant and rate limits vary with thrust level
- o Continuously modulated afterburner which can be lit at any throttle setting
- o RCS bleed capability
- o One or two engines

The model is presented as three submodels: The relations for resolving individual engine thrusts into body axis forces and moments are developed in Section 2.3.1. The engine performance and dynamics model is discussed in Section 2.3.2. The modeling of RCS effects on engine performance is discussed in Section 2.3.3.

Data for the SF-121 airplane propulsion system are provided in Section 3.4 of Volume II. The SF-121 uses two scaled MFTF-2800-25-1 engines whose performance and physical characteristics are described in reference (d). The characteristics of these "paper" engines were developed by Vought from a Pratt and Whitney parametric cycle analysis computer program and are believed to be attainable for a 1995 IOC (Initial Operational Capability). The engine dynamics time constant and rate limits data are the same as used in the core engine model of the reference (c) study.

2.3.1 Direct Thrust Forces and Moments Model

Figure 2-14 depicts the geometry for resolving the thrust of one engine into body axis forces and moments. The thrust is assumed to act at the center of the nozzle exit face parallel to the nozzzle centerline. To

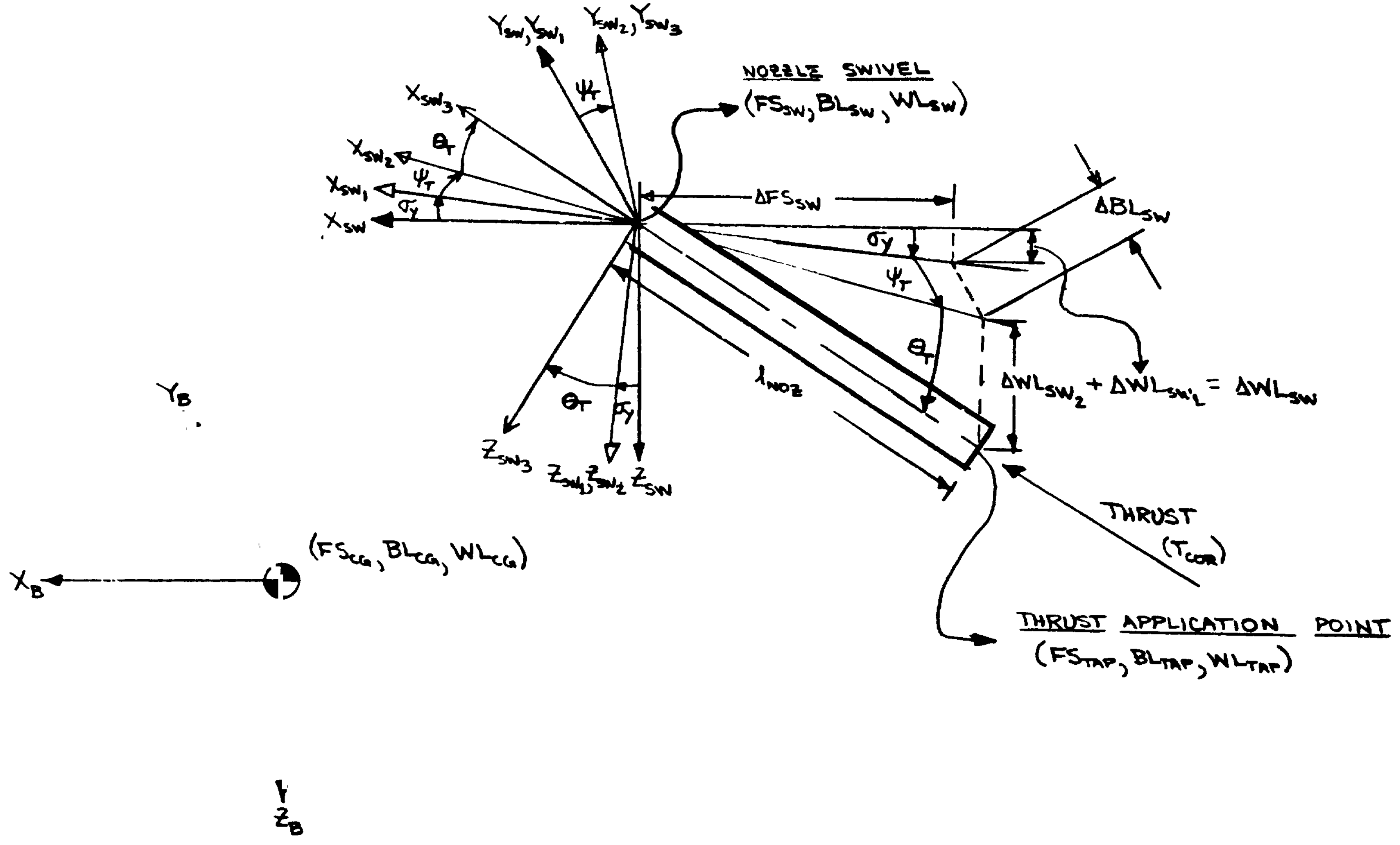

Figure 2-14. Geometry for Resolving Engine Thrust into Body Axis Forces and Moments

determine the direct thrust forces and moments requires that the aircraft coordinates of the thrust application point and the thrust components in the body axis system are known. The thrust application point coordinates will be developed first.

The VATOL simulation model provides for nozzle rotation (i.e. thrust deflection) in two directions about the swivel point and for an engine installation angle (σ_y) relative to the X_B axis. The nozzle rotaions provide yaw (ψ_T) and pitch (θ_T) thrust deflections. Since the nozzle swivel point remains fixed in the body axis system, it is convenient and necessary to determine the aircraft coordinates (ΔFS_{sw}, ΔBL_{sw}, ΔWL_{sw}) of the thrust applicaton point relative to the swivel point. All three angles - σ_y, ψ_T, θ_T - and the nozzle length (l_{NOZ}) influence these coordinates. Starting with the engine and nozzle centerline coincident and parallel to the X_B axis, the following rotation sequence orients the nozzle relative to the body axis system (see figure 2-14). First rotate by σ_y about the Y_{sw} axis which is parallel to the Y_B axis, then rotate by ψ_T about the Z_{sw_1} axis, and finally, rotate by θ_T about the Y_{sw_2} axis. The relation which describes this sequence and defines ΔFS_{sw}, ΔBL_{sw}, and ΔWL_{sw} is as follows:

$$\begin{bmatrix} \Delta FS_{sw} \\ \Delta BL_{sw} \\ \Delta WL_{sw} \end{bmatrix} = \begin{bmatrix} \cos\sigma_y & 0 & \sin\sigma_y \\ 0 & 1 & 0 \\ -\sin\sigma_y & 0 & \cos\sigma_y \end{bmatrix} \begin{bmatrix} \cos\psi_T & \sin\psi_T & 0 \\ -\sin\psi_T & \cos\psi_T & 0 \\ 0 & 0 & 1 \end{bmatrix} \begin{bmatrix} \cos\theta_T & 0 & \sin\theta_T \\ 0 & 1 & 0 \\ -\sin\theta_T & 0 & \cos\theta_T \end{bmatrix} \begin{bmatrix} l_{NOZ} \\ 0 \\ 0 \end{bmatrix} \quad (2.1)$$

The coordinates of the thrust application point are thus defined as:

$$\begin{aligned} FS_{TAP} &= FS_{SW} + \Delta FS_{SW} \\ BL_{TAP} &= BL_{SW} + \Delta BL_{SW} \\ WL_{TAP} &= WL_{SW} + \Delta WL_{SW} \end{aligned} \quad (2.2)$$

To complete the development, the body axis components of thrust must be determined. This resolution is essentially the same as that of equation

(2.1) except that the sense of ψ_T rotation is reversed to reflect the sign reversal between the direction of increasing WL and that of the Z_B axis:

$$\begin{bmatrix} \Delta X_T \\ \Delta Y_T \\ \Delta Z_T \end{bmatrix} = \begin{bmatrix} \cos\sigma_y & 0 & \sin\sigma_y \\ 0 & 1 & 0 \\ -\sin\sigma_y & 0 & \cos\sigma_y \end{bmatrix} \begin{bmatrix} \cos\psi_T & -\sin\psi_T & 0 \\ \sin\psi_T & \cos\psi_T & 0 \\ 0 & 0 & 1 \end{bmatrix} \begin{bmatrix} \cos\theta_T & 0 & \sin\theta_T \\ 0 & 1 & 0 \\ -\sin\theta_T & 0 & \cos\theta_T \end{bmatrix} \begin{bmatrix} T_{COR} \\ 0 \\ 0 \end{bmatrix} \qquad (2.3)$$

where

ΔX_T, ΔY_T, ΔZ_T are the body axis components of direct thrust

T_{COR} is gross thrust corrected for RCS interactions as described in Section 2.3.3 and flow turning effects as described below.

The equations for the flow turning correction to thrust are as follows:

$$T_{COR} = T_{APPL}\, K_{AFT} \qquad (2.4)$$

$$K_{A_{FT}} = K_{A_{FT_1}}\, A_{FT} + K_{A_{FT_2}} \qquad (2.5)$$

$$A_{FT} = \cos^{-1}\left[\cos\theta_T \cos\psi_T\right] \qquad (2.6)$$

where

T_{APPL} is gross thrust corrected for RCS interactions only

$K_{A_{FT_1}}$ and $K_{A_{FT_2}}$ are constants.

A_{FT} is the geometric thrust turning angle defined as the angle between the engine centerline and nozzle centerline.

Equations (2.1) through (2.6) are the basic relations for the direct thrust forces and moments model. They are expanded in full in Section 2.0.2 of Volume II.

2.3.2 Engine Performance and Dynamics Model

The engine performance and dynamics model is depicted in figure 2-15. Engine performance is represented by the following model parameters:

1. $F_{G_{IDL}}$ is the gross thrust level at idle throttle and is a function of Mach number (M_N).
2. $F_{G_{MIN}}$ is the gross thrust level at maximum rpm at minimum afterburner setting and is a function of M_N. There is an assumption here that the thrust at maximum rpm with no afterburner is the same as the thrust at maximum rpm at minimum afterburner; actually there is a finite but generally negligible difference between these two thrust levels.
3. $F_{G_{MAX}}$ is the gross thrust level at maximum rpm at maximum afterburner setting and is a function of M_N.
4. $\Omega_{E_{MAX}}$ is maximum engine rpm.
5. F_{RPM} is fractional engine rpm and is a function of fractional non-afterburning thrust level (T_F). T_F, a model dynamic parameter, is the thrust produced by changing spool rpm normalized to $F_{G_{MIN}}$.
6. $\dot{m}_{MAX}$ is the inlet mass flow rate when $T_F = 1$ and is a function of M_N. Inlet mass flow rate is assumed to be a function of T_F only; thus, by inference, inlet mass flow rate is not a function of afterburner setting.
7. K_{BT} adjusts the commanded thrust level (T_C) for the reference RCS bleed (B_{REF}) level. Thus when model output thrust (T_O) is adjusted for actual bleed ($\overline{BLD}$) level and $\overline{BLD} = B_{REF}$, the thrust applied to the aircraft will equal T_C. The use of this parameter assumes that engine controls will be able to compensate for known reference RCS bleed. If the controls are not this sophisticated then K_{BT} can be set to 1.0.

These parameters are quantified from steady state engine data. Data for the SF-121 engines, which are scaled versions of the MFTF-2800-25-1 engines described in reference (d), are provided in Section 3.4 of Volume II.

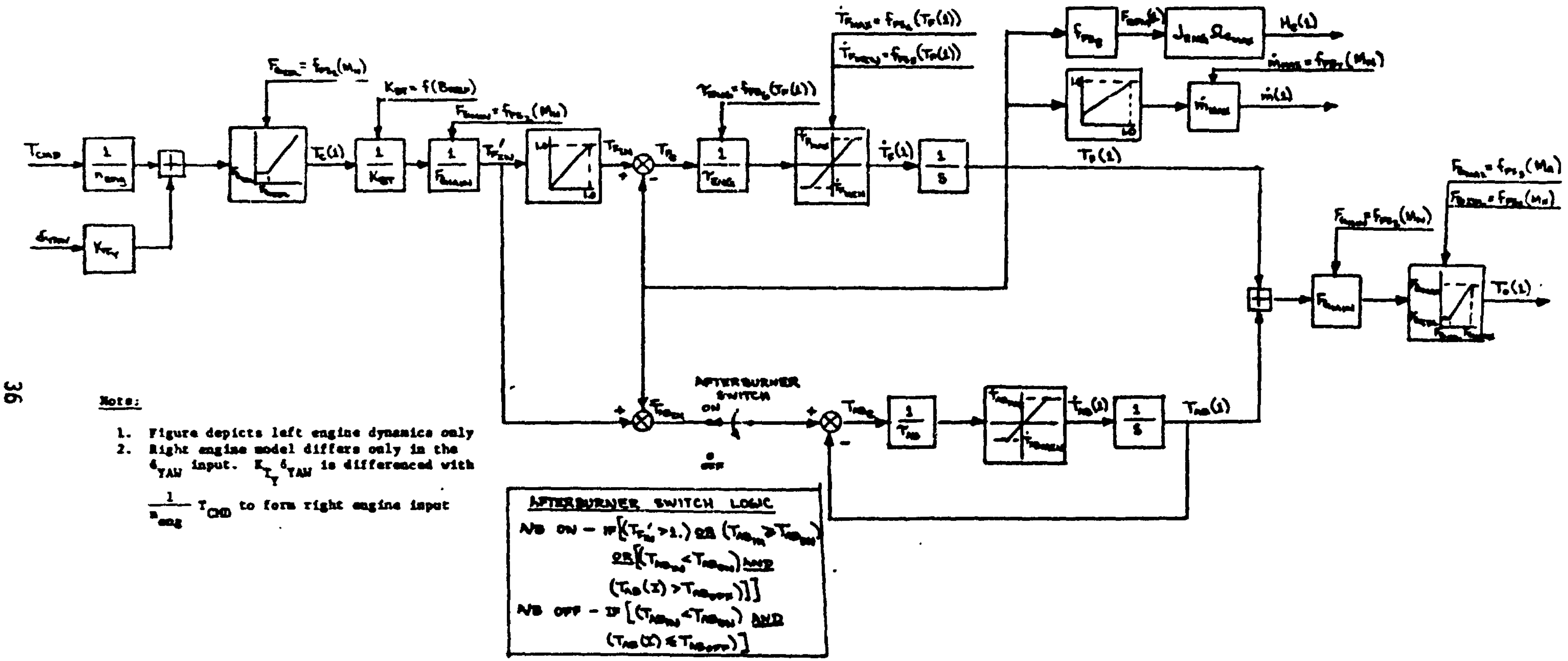

Note:

1. Figure depicts left engine dynamics only
2. Right engine model differs only in the δ_{YAW} input. $K_{T_Y}\delta_{YAW}$ is differenced with $\frac{1}{n_{eng}} T_{CMD}$ to form right engine input

Figure 2-15. Propulsion Syst m Dynamics and Performance Model

The engine dynamics model for non-afterburning thrust (output is T_F) indicated on figure 2-15 is nonlinear and was defined by Pratt and Whitney for use by Vought in preliminary Type A V/STOL airplane design studies. For the current application a model of afterburner thrust dynamics (output is T_{AB}) has been placed in parallel with the basic model. The afterburner can be lit according to the logic indicated in the figure. With the afterburner lit the more rapid afterburner thrust response will enhance the slower non-afterburning thrust response which is influenced by the engine spool inertia. The equations indicated by figure 2-15 are expanded to full detail in Section 2.1 of Volume II.

The engine dynamics model is particularly suited for parametric variations to establish propulsion system requirements and control system interface. It is also computationally efficient for real-time simulation. The application and validity of the non-afterburning thrust model (in essence, the spool dynamics model) has been demonstrated in the simulator studies of references (e) and (f). Thus, as a baseline, the same values used in reference (e) for the nonlinear time constant (τ_{ENG}) and rate limits ($\dot{T}_{F_{MAX}}$ and $\dot{T}_{F_{MIN}}$) of the non-afterburning thrust model used in reference (e) have been adopted for the analyses presented herein. In lieu of definitive data, the time constant of the afterburner thrust model (τ_{AB}) has been set at 0.05 sec to simulate the dynamics of fuel delivery to the afterburner. Similarly the afterburner thrust rate limits ($\dot{T}_{AB_{MAX}}$ and $\dot{T}_{AB_{MIN}}$) have been set high (= ± 20.) to simulate a non-rate limited afterburner. Also $T_{AB_{ON}}$ has been set at 0.10 and $T_{AB_{OF}}$ at 0.001; this establishes that the afterburner will be lit when exceeds $T_F(I)$ by 0.10 (10% of $F_{G_{MIN}}$) or when $T_{F_{IN}}$ exceeds 1. The burner will remain lit until $T_{AB}(I)$ has dropped to 0.001 (0.1% of $F_{G_{MIN}}$) and $T_{F_{IN}}$ is not more than 0.10 larger than $T_F(I)$.

2.3.3 RCS Effects on Engine Performance

The RCS-propulsion system interactions model is depicted on figure 2-16. Model inputs are T_F and the output thrust (T_0) of the engine performance and dynamics model. T_0 is to be corrected for RCS effects.

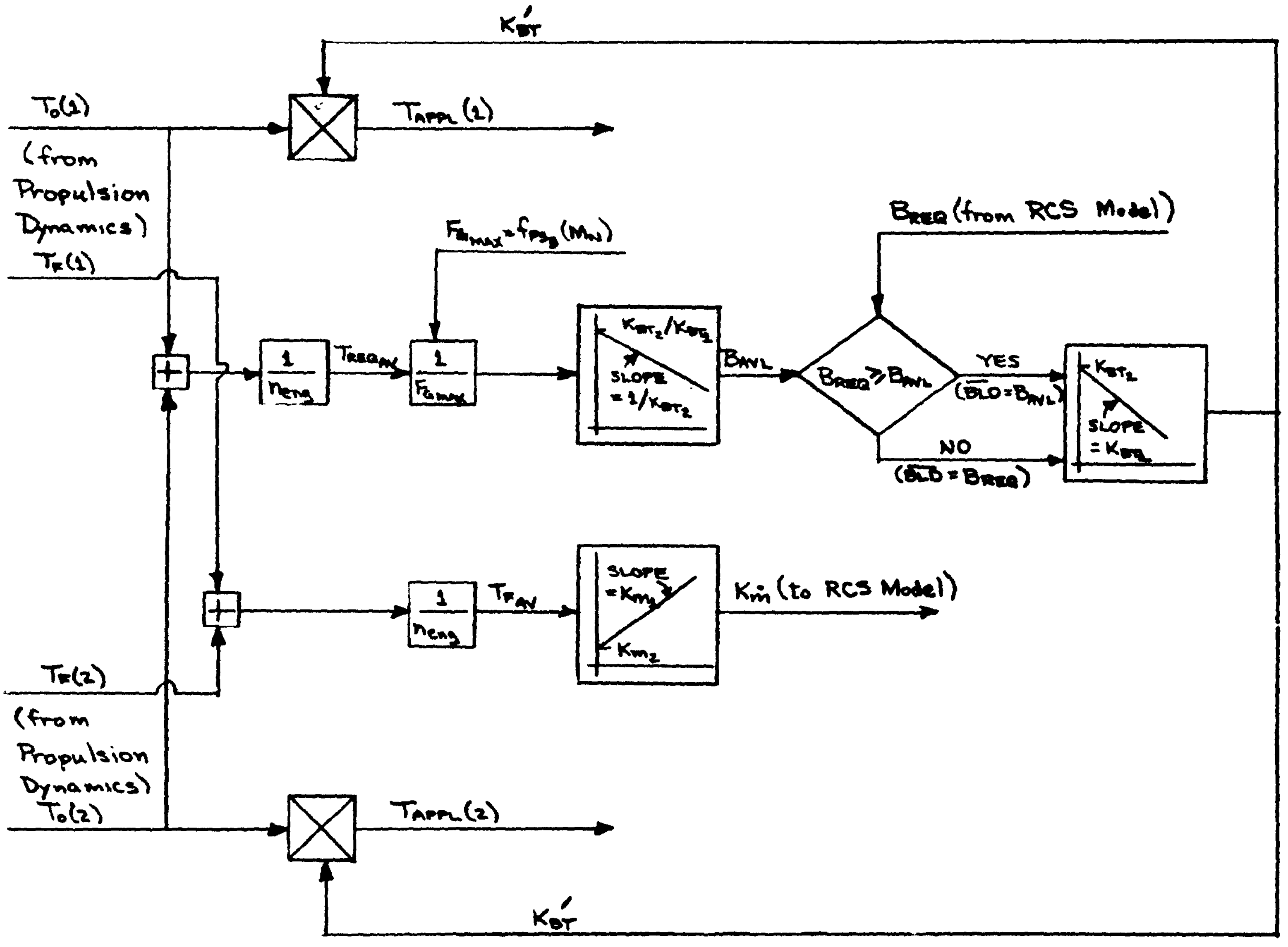

Figure 2-16. RCS–Propulsion System Interactions Model

Model outputs are the corrected thrust (T_{APPL}) applied to the aircraft and the ratio of RCS bleed air currently available to the maximum available ($K_{\dot{m}}$). The maximum RCS bleed air is available when the inlet mass flow rate is maximum which occurs when $T_F = 1$. As will be shown in Section 2.5, the RCS model applies multiplicative factors to scale down the maximum RCS capability; $K_{\dot{m}}$ is one of these factors. The data for $K_{\dot{m}}$ for the SF-121 were taken from reference (d).

Corrected thrust (T_{APPL}) is formed by multiplying T_0 by a correction factor (K'_{BT}) which is based on actual bleed ($\overline{BLD}$) and $F_{G_{MAX}}$. The first step to determine K'_{BT} is to calculate the bleed available (B_{AVL}) at the current uncorrected thrust level. B_{AVL} is then compared with RCS bleed required (B_{REQ}) which is generated by the RCS model. If $B_{REQ} \geq B_{AVL}$ then $\overline{BLD}$ is set equal to B_{AVL}; thus in this case K'_{BT} will be set by T_0 and the RCS is saturated. If, on the other hand, $B_{REQ} < B_{AVL}$ then $\overline{BLD}$ is set equal to B_{REQ}; thus K'_{BT} will be set by RCS requirements and excess RCS capability proportional to ($B_{AVL} - B_{REQ}$) is available. Note also that if $B_{REQ} = B_{REF}$ (the reference bleed) then K'_{BT} will equal K_{BT} (figure 2-16) and T_{APPL} will equal commanded thrust (T_C). The data to define K_{BT} for the SF-121 were also taken from reference (d).

The relations and logic indicated by figure 2-16 are expanded to full detail in Section 2.1 of Volume II.

2.4 Inlet Ram Forces and Moments Model

The development of the inlet ram forces and moments model is presented in two steps. First the relatively simple, standard model is given. This model is phenomenologically correct but lacks experimental and/or theoretical guidance to define the ram force application point. This aspect of the model is normally left to user whim. A recent Vought contracted effort (reference (g)), undertaken to remedy this situation, resulted in a series of inlet force and moment design charts intended for preliminary design application. The standard model was expanded and modified to incorporate these results. This is the second step of the model development.

2.4.1 The Standard Model

Figure 2-17 depicts the geometry of the standard ram forces and moments model in the aircraft plane of symmetry. The forces and moments have contributions from two sources:

1. The forces and moments imposed on the inlet by the captured stream of air which enters it.
2. The additional forces and moments imposed on the inlet when, because of aircraft rotation, it moves relative to the captured stream of air.

The model of the first contribution assumes a ram force ($\overline{F}_{RAM_0}$) parallel but opposite to the relative airspeed vector ($\overline{V}_A$) acting at an application point (AP). The ram force is defined as

$$\overline{F}_{RAM_0} = - \dot{m}_I \overline{V}_A$$

where $\dot{m}_I$ is the inlet mass flow rate determined by the propulsion system model and $\overline{V}_A$ has the components u_{AS}, v_{AS}, and w_{AS} along the X_B, Y_B, and Z_B axes, respectively. Thus the body axis components of $\overline{F}_{RAM_0}$ are

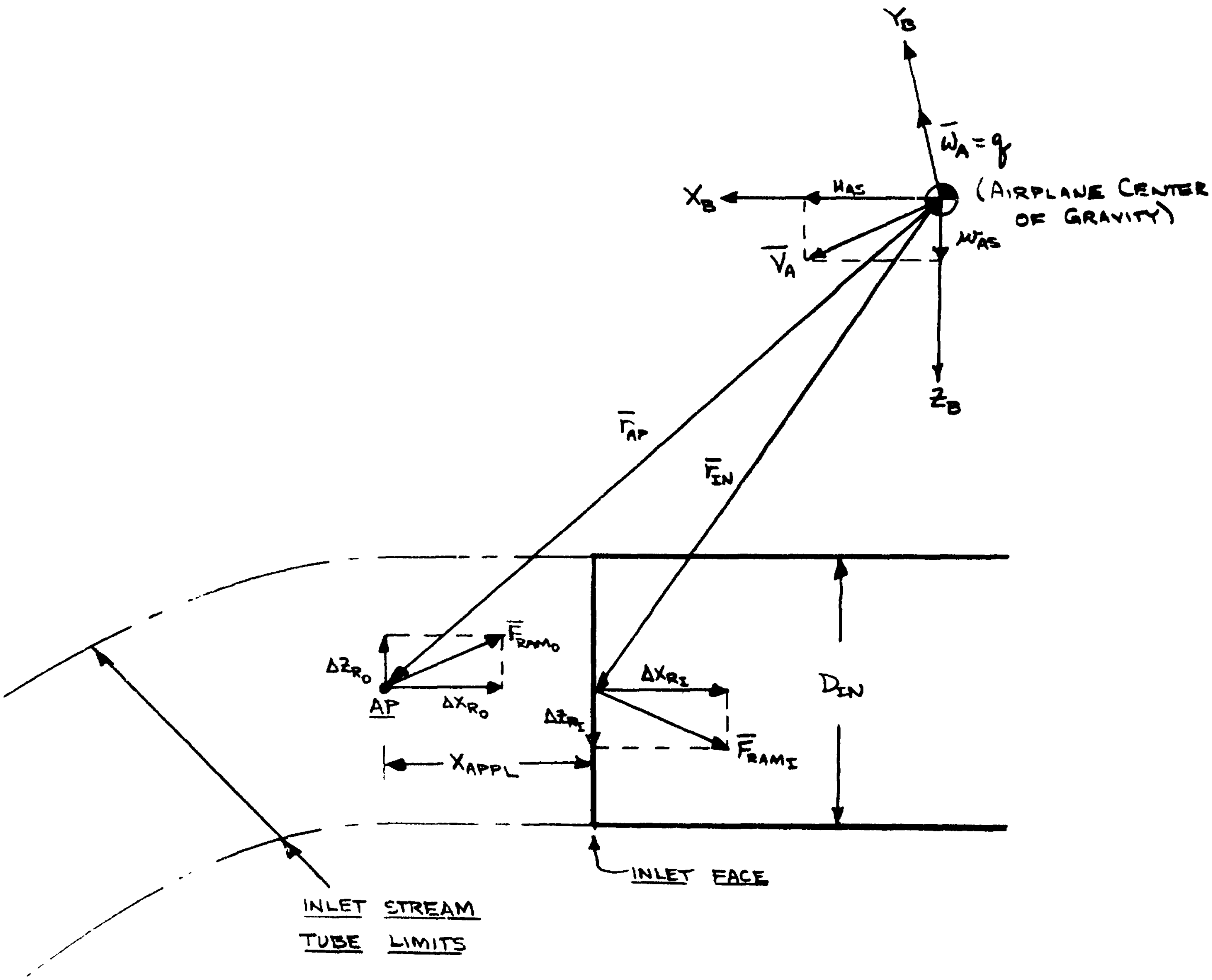

Figure 2-17. Geometry of Standard Inlet Ram Forces and Moments Model

$$\begin{aligned} \Delta X_{R_o} &= -\dot{m}_I \, u_{AS} \\ \Delta Y_{R_o} &= -\dot{m}_I \, v_{AS} \\ \Delta Z_{R_o} &= -\dot{m}_I \, w_{AS} \end{aligned} \qquad (2.4.1)$$

Anticipating the modifications to the standard model to incorporate the recent Vought results, an alternate formulation of ΔX_{R_o}, ΔY_{R_o}, and ΔZ_{R_o} is now introduced. The angles A_{TURN_o} and B_{TURN} are required for this purpose (figure 2-18). A_{TURN_o} is defined as the geometric inlet flow turning angle and is equal to the angle $\bar{V}_A$ makes with the inlet centerline. B_{TURN} is defined as the angle between the $\bar{V}_A$-engine centerline plane and the aircraft plane of symmetry. Using A_{TURN_o}, B_{TURN}, and the ram force magnitude (i.e. $|F_{RAM_o}| = \dot{m}_I |V_A| = \dot{m}_I V_\infty$), equations (2.4.1) can be recast as

$$\begin{aligned} \Delta X_{R_o} &= -\dot{m}_I \, V_\infty \cos A_{TURN_o} \\ \Delta Y_{R_o} &= -\dot{m}_I \, V_\infty \sin A_{TURN_o} \sin B_{TURN} \\ \Delta Z_{R_o} &= -\dot{m}_I \, V_\infty \sin A_{TURN_o} \cos B_{TURN} \end{aligned} \qquad (2.4.2)$$

where

$$\begin{aligned} A_{TURN_o} &= \cos^{-1} [u_{AS}/V_\infty] \\ B_{TURN} &= \tan^{-1} [v_{AS}/w_{AS}] \end{aligned}$$

As noted above, guidance on where to place AP is lacking. It is generally agreed that it should lie on the centerline of the engine. There is no agreement, however, in where it should lie relative to the inlet face. It has been placed by various researchers from $X_{APPL} = 0.$ upstream to $X_{APPL} = D_{IN}$ and beyond. Since information now exists to quantify X_{APPL} (reference (g)), the derivation of the standard model continues with X_{APPL} unspecified. The moments about the aircraft cg due to F_{RAM_o} are

$$\bar{M}_{RAM_o} = (\bar{r}_{AP} \times \bar{F}_{RAM_o})$$

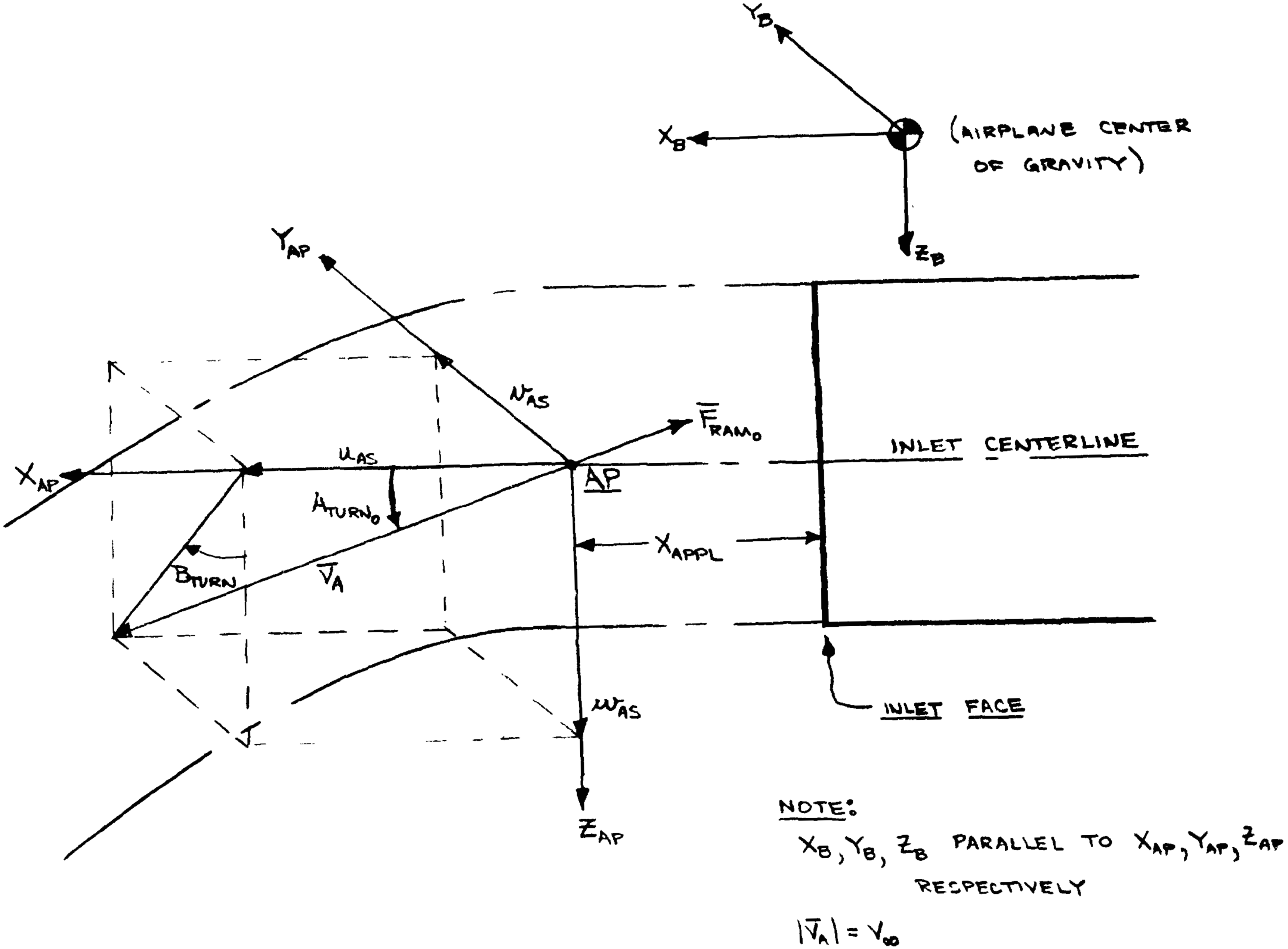

NOTE:
X_B, Y_B, Z_B PARALLEL TO X_{AP}, Y_{AP}, Z_{AP} RESPECTIVELY

$|\overline{V}_A| = V_\infty$

Figure 2-18. Geometry of Inlet Ram Forces and Moments Model Showing Flow Turning Angles

$$\begin{bmatrix} L_{RAM_O} \\ M_{RAM_O} \\ N_{RAM_O} \end{bmatrix} = \begin{bmatrix} \Delta Z_{R_O} Y_{IN} - \Delta Y_{R_O} Z_{IN} \\ \Delta X_{R_O} Z_{IN} - \Delta Z_{R_O} (X_{IN} + X_{APPL}) \\ \Delta Y_{R_O} (X_{IN} + X_{APPL}) - \Delta X_{R_O} Y_{IN} \end{bmatrix} \qquad (2.4.3)$$

where $\bar{M}_{RAM_O}$ is the moment vector of $\bar{F}_{RAM_O}$

$\bar{r}_{AP}$ is the vector location of the AP relative to the cg.

X_{IN}, Y_{IN}, Z_{IN} are the coordinates of the inlet in aircraft body axes.

L_{RAM_O}, M_{RAM_O}, N_{RAM_O} are the components of $\bar{M}_{RAM_O}$ along the aircraft body axes.

The second contribution to the inlet ram forces originates in the velocity, produced by aircraft rotation, of the inlet relative to the incoming stream of air. The defining relation is

$$\bar{F}_{RAM_I} = -\dot{m}_I (\bar{\omega}_A \times \bar{r}_{IN})$$

$$\begin{bmatrix} \Delta X_{R_I} \\ \Delta Y_{R_I} \\ \Delta Z_{R_I} \end{bmatrix} = \begin{bmatrix} -\dot{m}_I(qZ_{IN} - rY_{IN}) \\ -\dot{m}_I(rX_{IN} - pZ_{IN}) \\ -\dot{m}_I(pY_{IN} - qX_{IN}) \end{bmatrix} \qquad (2.4.4)$$

where

ΔX_{R_I}, ΔY_{R_I}, ΔZ_{R_I} are the body axis components of $\bar{F}_{RAM_I}$

p, q, r are the body axis roll, pitch, and yaw rates and are also the components of $\bar{\omega}_A$.

$\bar{F}_{RAM_I}$ acts at the inlet face. The moments due to $\bar{F}_{RAM_I}$ are thus defined as

$$\overline{M}_{RAM_I} = (\overline{r}_{IN} \times \overline{F}_{RAM_I})$$

$$\begin{bmatrix} L_{RAM_I} \\ M_{RAM_I} \\ N_{RAM_I} \end{bmatrix} = \begin{bmatrix} \Delta Z_{R_I} \; Y_{IN} - \Delta Y_{R_I} \; Z_{IN} \\ \Delta X_{R_I} \; Z_{IN} - \Delta Z_{R_I} \; X_{IN} \\ \Delta Y_{R_I} \; X_{IN} - \Delta X_{R_I} \; Y_{IN} \end{bmatrix} \qquad (2.4.5)$$

where

L_{RAM_I}, M_{RAM_I}, N_{RAM_I} are the body axis components of $\overline{M}_{RAM_I}$

Combining the two contributions represented by equations 2.4.2 through 2.4.5 gives the standard model form for the body axis forces and moments produced by inlet ram effects:

$$X_{RAM} = \Delta X_{R_O} + \Delta X_{R_I} = -\dot{m}_I(V_\infty \cos A_{TURN_O} + qZ_{IN} - rY_{IN})$$

$$Y_{RAM} = \Delta Y_{R_O} + \Delta Y_{R_I} = -\dot{m}_I(V_\infty \sin A_{TURN_O} \sin B_{TURN} + rX_{IN} - pZ_{IN})$$

$$Z_{RAM} = \Delta Z_{R_O} + \Delta Z_{R_I} = -\dot{m}_I(V_\infty \sin A_{TURN_O} \cos B_{TURN} + pY_{IN} - qX_{IN})$$

$$L_{RAM} = L_{RAM_O} + L_{RAM_I} = Y_{IN} \; Z_{RAM} - Z_{IN} \; Y_{RAM} \qquad (2.4.6)$$

$$M_{RAM} = M_{RAM_O} + M_{RAM_I} = Z_{IN} \; Y_{RAM} - X_{IN} \; Z_{RAM} + X_{APPL} \; \dot{m}_I \; V_\infty \sin A_{TURN_O} \cos B_{TURN}$$

$$N_{RAM} = N_{RAM_O} + N_{RAM_I} = X_{IN} \; Y_{RAM} - X_{APPL} \; \dot{m}_I \; V_\infty \sin A_{TURN_O} \sin B_{TURN} - X_{RAM} \; Y_{IN}$$

Recall that the standard model makes the following assumptions about the ram force ($\overline{F}_{RAM_O}$):

1. $|\bar{F}_{RAM_0}|$ is equal to $\dot{m}_I V_\infty$ (where $V_\infty = |V_A|$) for all values of A_{TURN_0}.

2. $\bar{F}_{RAM_0}$ acts parallel and opposite to $\bar{V}_A$

Vought's recent efforts (reference (g)) to apply sophisticated inlet modeling techniques to determine the ram force application point determined that not only the application point but also the actual inlet flow turning angle and magnitude of the ram force vary with A_{TURN_0}, ratio of ambient airspeed to inlet air speed (V_∞ / V_I), and inlet geometry. The next section will describe the modification and expansion of the standard model to incorporate these effects.

2.4.2 Expansion and Modification of the Standard Model

A brief synopsis of the work performed by Vought in reference (g) is required as background for the development in this section: Under contract to Naval Air Development Center, Vought has developed a computerized prediction method for propulsive induced forces and moments in transition and STOL flight. This method is based on Vought's V/STOL Aircraft Propulsive Effects (VAPE) program. One of the VAPE options provides for the calculation of inlet forces and moments. This option combines a highly modified Stockman inlet flow model with a program which integrates the inlet pressures determined by the inlet model to produce inlet forces and moments. Arbitrary axisymmetric inlet geometries are accepted by the program. The bulk of the program applications in reference (g) is to the NASA QCSEE GE2 inlet. Being a subsonic inlet, it has relatively thick lips. To determine the effects of thinner supersonic lips, a limited program application was made to a thin lipped configuration. The force and moment differences were minor at low values of V_∞ / V_I (< 0.3 to 0.4) and negligible at higher values of V_∞ / V_I. Model results designated for preliminary design application can be presented as the difference between the geometric and effective flow turning angles (ΔA_{TURN}), the ram effectiveness factor (R_M), and normalized (to equivalent inlet diameter) ram moment arm (X_{APPL}/D_{IN}) as functions of A_{TURN_0} and V_∞ / V_I (figures 2-19 to 2-21).

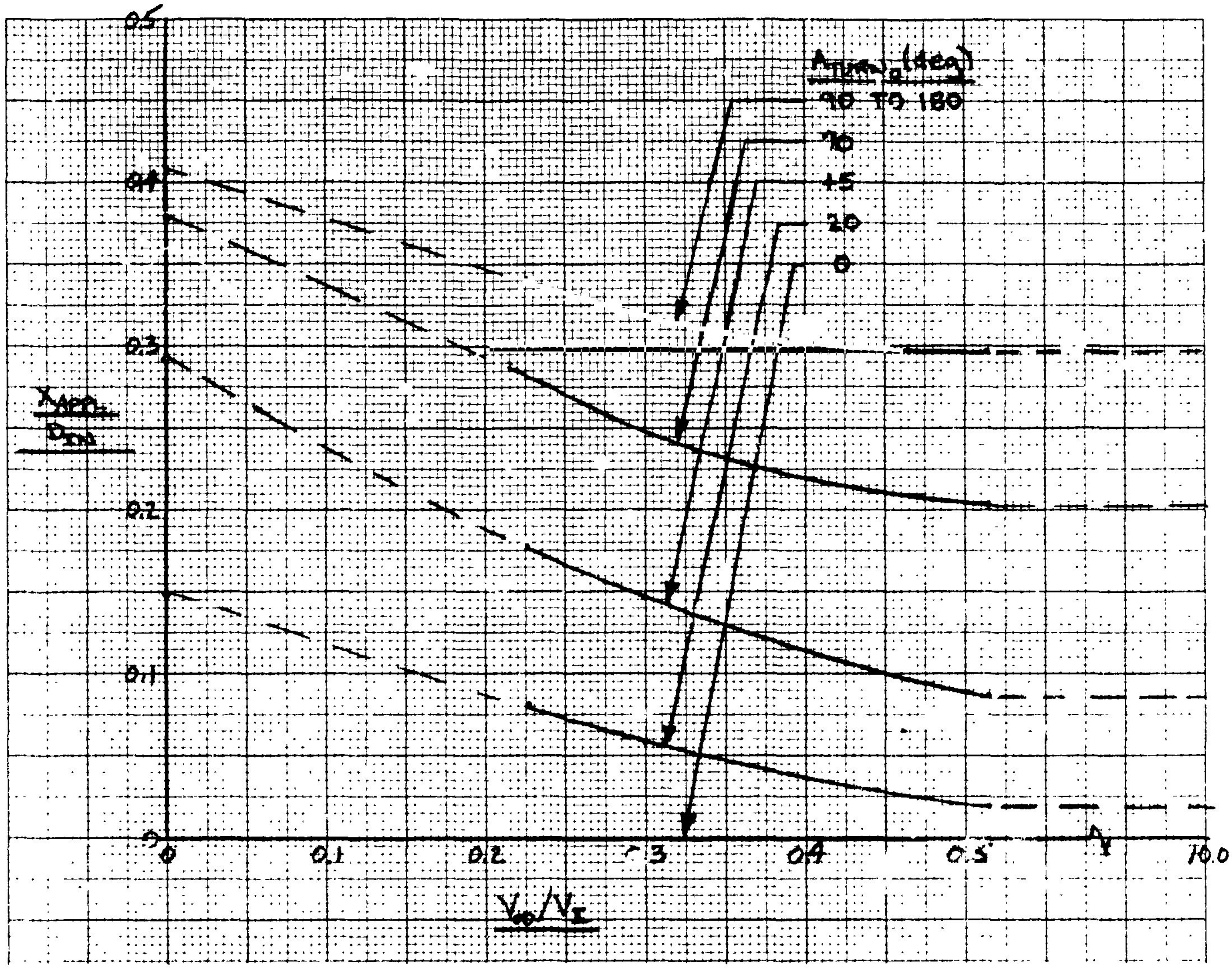

NOTE:

——— SUPPORTED BY REF (9) CALCULATIONS

– – – EXTRAPOLATED FOR COMPUTERIZED MODEL

Figure 2-19. Effect of Velocity Ratio and Geometric Flow Turning Angle on Inlet Moment Arm

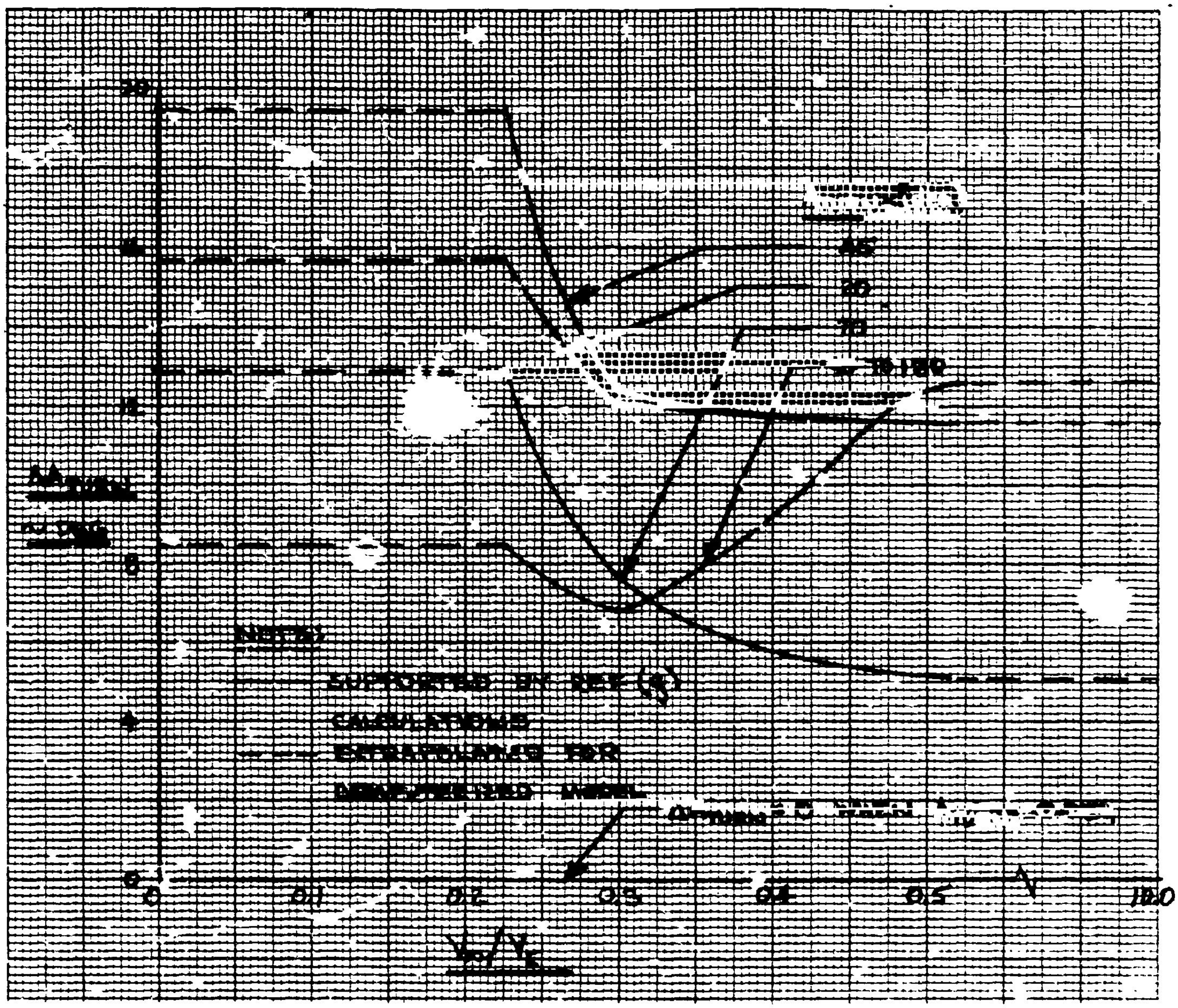

Figure 2-20. Effect of Velocity Ratio and Geometric Flow Turning Angle on the Difference Between Effective and Geometric Flow Turning Angle (ΔA_{TURN})

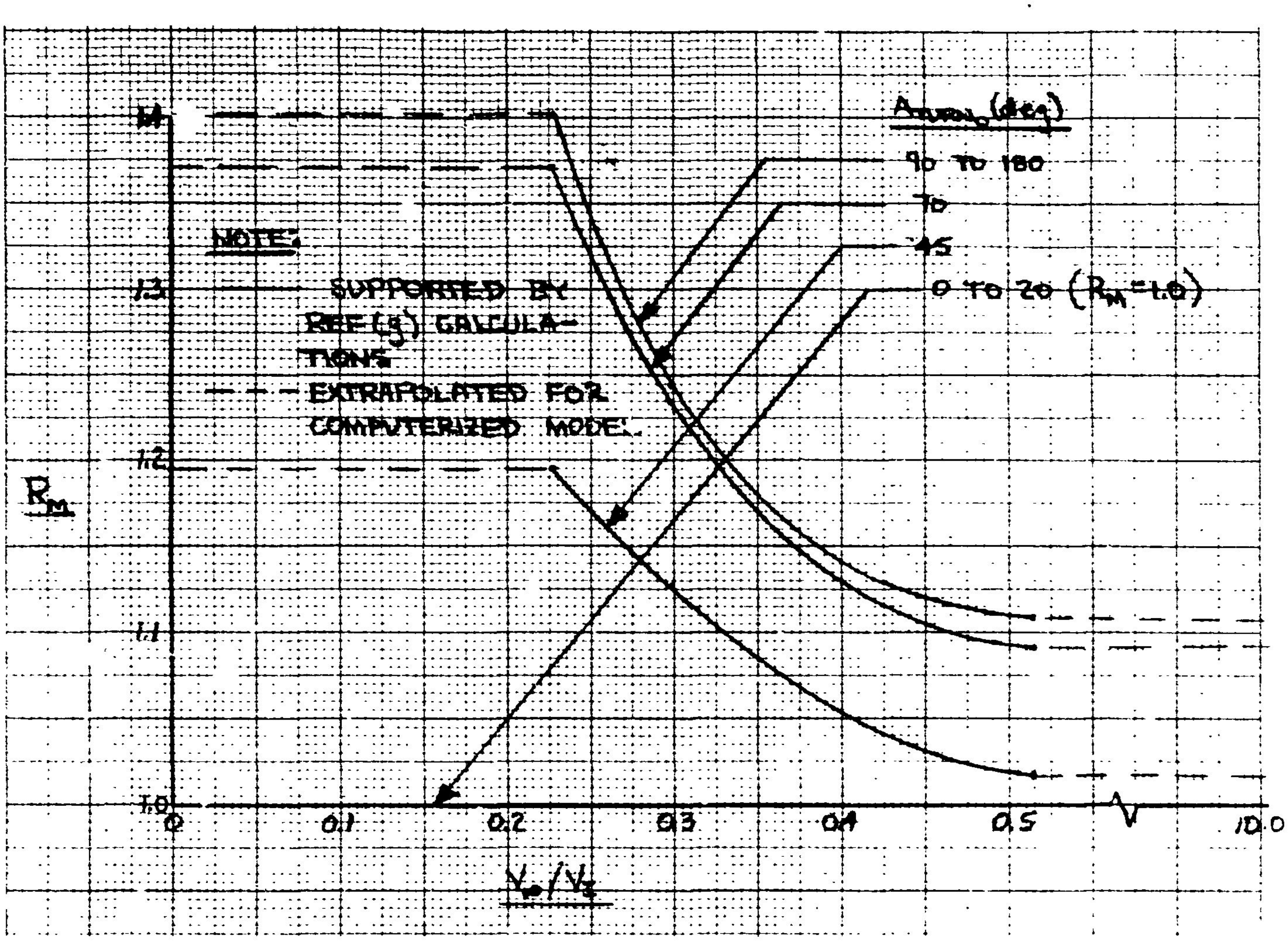

Figure 2-21. Effect of Velocity Ratio and Geometric Flow Turning Angle on Ram Effectiveness Factor (R_M)

There is no provision in the Vought VAPE program for rectangular inlets, thus data equivalent to that of figures 2-19 to 2-21 cannot be generated for rectangular inlets. For application of the VATOL simulation model, it is assumed that the data for axisymmetric inlets can be applied to rectangular inlets by replacing them with equivalent circular inlets. The equivalent circular inlets have the same area as the rectangular inlets; the inlet diameter (D_{IN}) specified in the simulation model is the diameter of the equivalent circular inlet. The validity of this approximation cannot be readily assessed. It is believed that the inlet forces and moments calculated by the simulation model will provide reasonable estimates of actual ram effects and will certainly be adequate for comparing inlet ram effects on various VATOL aircraft concepts.

Introducing the data and terminology of figures 2-19 to 2-21 into the standard model (equation (2.4.6)) gives the following set of equations:

$$A_{TURN_0} = \cos^{-1}(u_{as}/V_\infty) \tag{2.4.7}$$

$$\Delta A_{TURN} = f_{1_{RAM}}[A_{TURN_0}, (V_\infty/V_I)] \tag{2.4.8}$$

$$R_M = f_{2_{RAM}}[A_{TURN_0}, (V_\infty/V_I)] \tag{2.4.9}$$

$$X_{APPL}/D_{IN} = f_{3RAM}[A_{TURN_0}, (V_\infty/V_I)] \tag{2.4.10}$$

$$F_{RAM} = \dot{m}_I V_\infty R_M \tag{2.4.11}$$

$$A_{TURN} = A_{TURN_0} + \Delta A_{TURN} \tag{2.4.12}$$

$$X_{RAM} = -F_{RAM} \cos A_{TURN} - \dot{m}_I\ (q\ Z_{IN} - r\ Y_{IN}) \tag{2.4.13}$$

$$Y_{RAM} = -F_{RAM} \sin A_{TURN} \sin B_{TURN} - \dot{m}_I (rX_{IN} - pZ_{IN}) \tag{2.4.14}$$

$$Z_{RAM} = -F_{RAM} \sin A_{TURN} \cos B_{TURN} - \dot{m}_I (pY_{IN} - qX_{IN}) \tag{2.4.15}$$

$$L_{RAM} = Z_{RAM}\ Y_{IN} - \text{[illegible]}_{RAM} \tag{2.4.16}$$

$$M_{RAM} = X_{RAM} Z_{IN} - Z_{RAM} X_{IN} - (X_{APPL}/D_{IN}) D_{IN} F_{RAM} \sin A_{TURN} \cos B_{TURN} \qquad (2.4.17)$$

$$N_{RAM} = Y_{RAM} X_{IN} - X_{RAM} Y_{IN} + (X_{APPL}/D_{IN}) D_{IN} F_{RAM} \sin A_{TURN} \sin B_{TURN} \qquad (2.4.18)$$

where A_{TURN} is the effective inlet flow turning angle
F_{RAM} is the effective magnitude of the ram force

Equations (2.4.7) through 2.4.18) are the basic relations of the VATOL simulation inlet ram forces and moments model. The functional relations indicated by equations (2.4.8) through (2.4.10) are the data of figures 2-19 to 2-21 extrapolated as indicated to $(V_{\infty}/V_I) = 0$ and $A_{TURN} = 0$ and 180 degrees. The detailed equations actually programmed in the VATOL math model are given in Section 2.0.3 of Volume II. These Volume II equations include the effect of engine tilt angle (σ_y) which was not introduced here for reasons of brevity and clarity.

2.5 Reaction Control System Forces and Moments

The features of the RCS forces and moments model are as follows:

- o Up to ten jets locatable anywhere in the airplane and at any angle relative to aircraft axes.
- o Jets can be specified as demand or continuous bleed. Demand bleed jets can be further specified to demand more bleed than the RCS reference bleed.
- o Jets thrust in one direction only.
- o The bleed required by the RCS is monitored and limited, if necessary, by the bleed available from the engines.
- o Continuous jet forces follow RCS actuator outputs with no lag. Demand jet forces are lagged relative to actuator outputs to simulate bleed flow dynamics.

The model is presented in three sections: the procedure for locating and specifying the type of jet is described in Section 2.5.1, calculation of individual jet forces is developed in Section 2.5.2, resolution of jet forces into body axis forces and moments is developed in Section 2.5.3. Data for the SF-121 RCS are presented in Section 3.6 of Volume II while detailed equations are given in Section 2.0.4 of the same volume.

The overall approach to RCS modeling is to calculate an ideal force demanded at each jet based on an ideal maximum. This maximum is based on the maximum inlet mass flow rate of the engines. The ideal force is then corrected for actual inlet mass flow rate, bleed available for the RCS, and demand for thrust at the other jets. This modeling approach has evolved primarily from the author's experience with the math model and background data of the VAK-191B airplane (reference (h)). The procedure for locating jets is based on reference (a).

2.5.1 RCS Jet Parameters

The parameters involved in locating or orienting RCS jets are depicted in figure 2-22. The application point (i.e. location) of a jet force

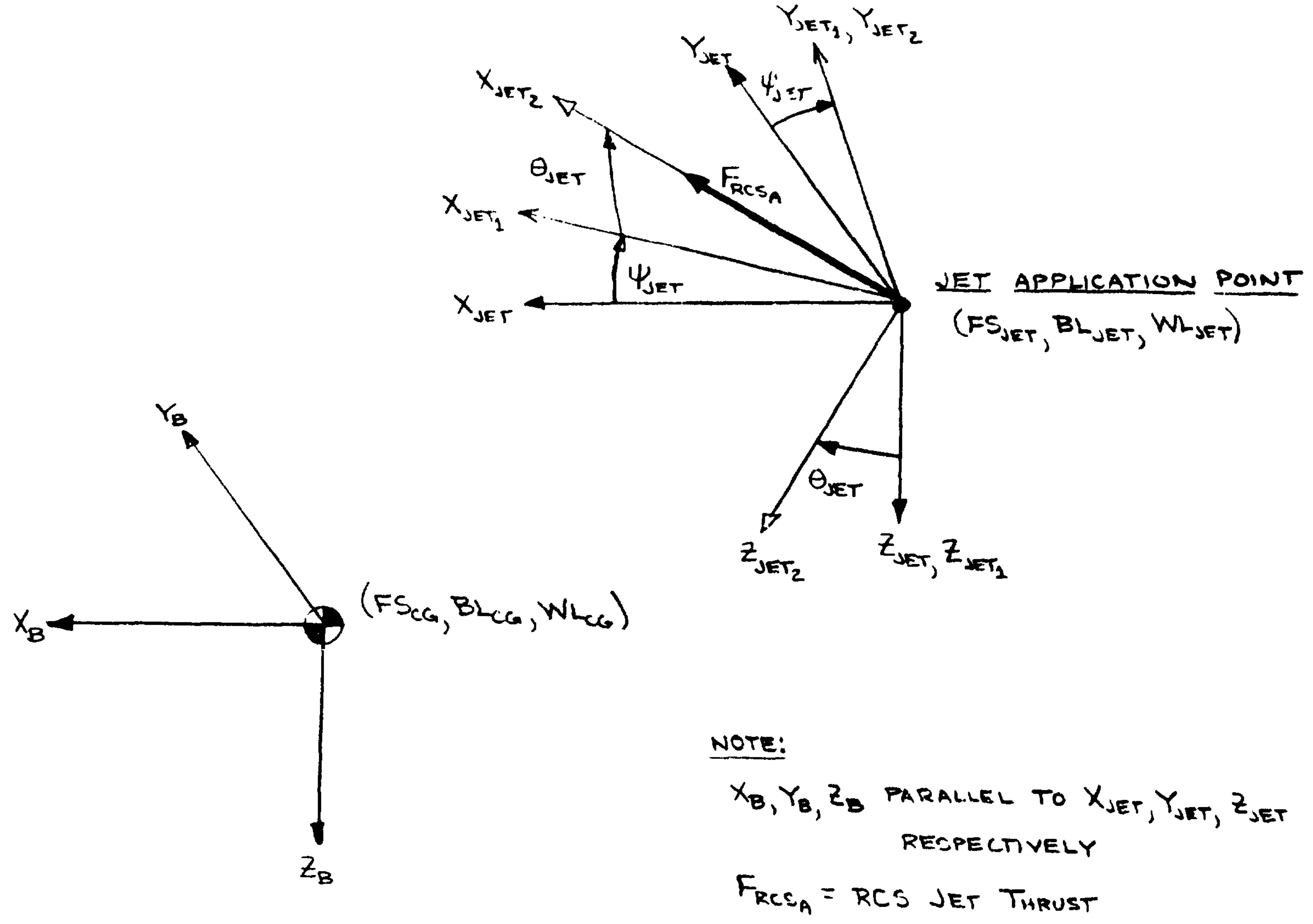

Figure 2-22. Geometry for Locating and Orienting RCS Jets

is defined in airplane coordinates. The orientation is defined by the ordered rotation required to align a jet force initially along the positive X_B axis with its final installed force direction. The ordered rotation proceeds as follows: first, rotate around the Z_B axis by the jet yaw angle (ψ_{JET}), then, rotate around the rotated Y axis by the jet pitch angle (θ_{JET}). Five parameters are therefore associated with the location and orientation of each jet:

- Fuselage Station (FS_{JET}), Butt Line (BL_{JET}), and Waterline (WL_{JET}) of the force application point.
- Jet yaw and pitch angles (ψ_{JET} and θ_{JET})

Three more parameters are required to completely specify each jet. These are $\overline{DMD}$, the demand parameter, $\overline{BLDM}$, the bleed more parameter, and $F_{RCS_{MX}}$, the maximum force of the jet. A demand bleed jet is designated by setting $\overline{DMD} = 1.$; for a continuous bleed jet, $\overline{DMD} = 0$. If the jet is demand bleed, then $\overline{BLDM}$ must be specified; if $\overline{BLDM} = 1.$ the RCS bleed can be increased beyond the reference level if the additional bleed capability is required and available; if $\overline{BLDM} = 0.$, RCS bleed cannot exceed the reference level. ($\overline{BLDM}$ can be set to 0.0 for continuous bleed jets). The SF-121 has two RCS demand bleed jets for roll control and has a 3.5% reference bleed level (which is the bleed required for non-RCS uses). Therefore $\overline{DMD} = \overline{BLDM} = 1.$ for both SF-121 RCS jets.

The maximum force of the jet is the thrust produced if the jet area is maximum and bleed required is less than bleed available, the engine is operating with maximum inlet mass flow rate, and there is no thrust loss due to other operating jets. For the SF-121, $F_{RCS_{MX}}$ of each jet was set at 1500 lb.

2.5.2 Calculation of Individual RCS Jet Forces

Figure 2-23 outlines the calculation of individual jet forces. The inputs to the process are the individual normalized jet areas ($\delta_{RCS}(I)$). These are processed by the standard demand bleed or continuous bleed force

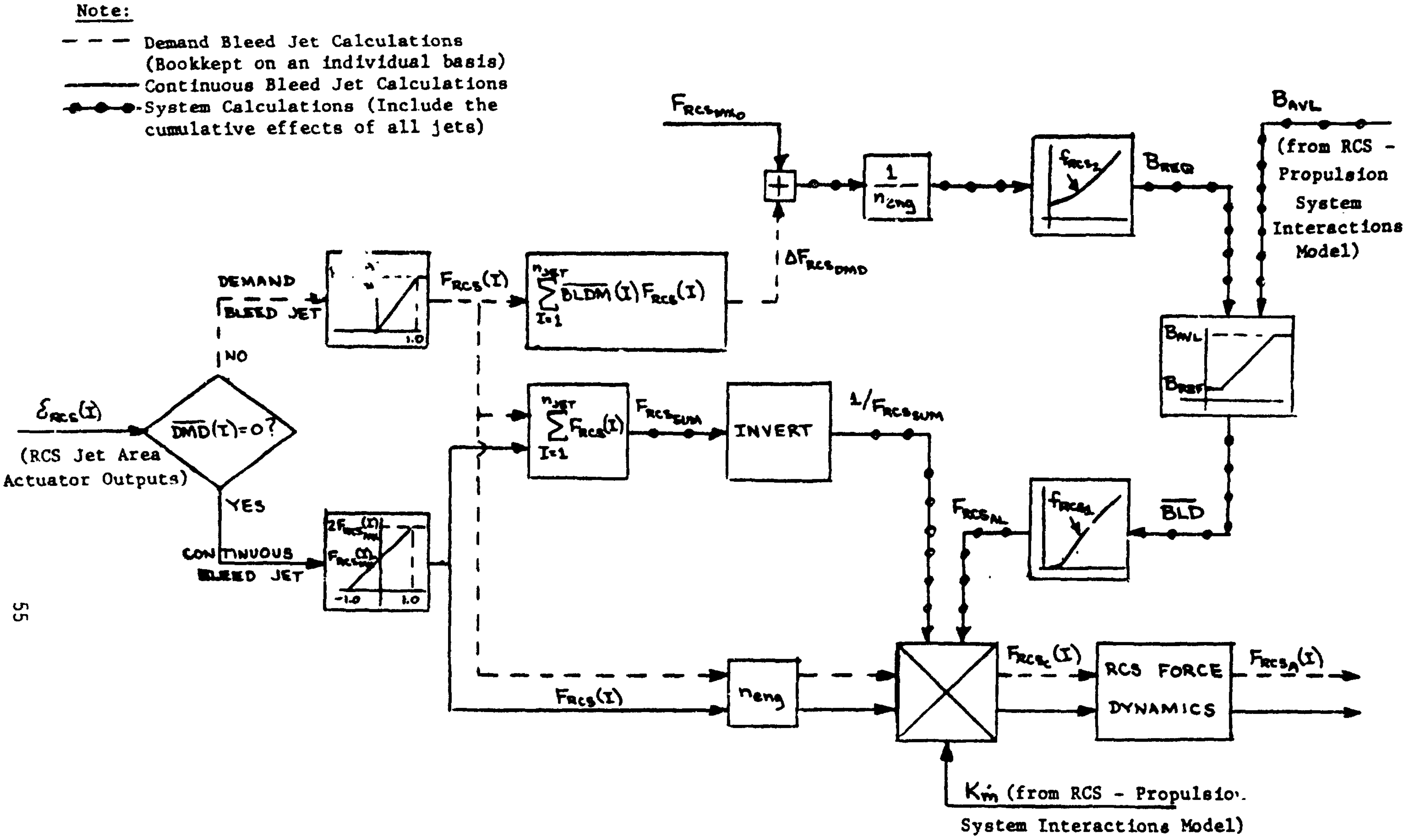

Figure 2-23. Calculation of Individual RCS Jet Forces

shaping functions to produce commanded forces. The demand bleed shaping function is as follows:

$$F_{RCS}(I) = \begin{cases} F_{RCS_{MX}}(I)\ \delta_{RCS}(I) & \delta_{RCS}(I) > 0. \\ 0 & \delta_{RCS}(I) < 0. \end{cases}$$

The continuous bleed shaping function is as follows:

$$F_{RCS}(I) = F_{RCS_{MX}}(I)\ (1 + \delta_{RCS}(I))$$

Continuous bleed jets are assumed to act in pairs. The total jet flow area is constant for these jet pairs; differential control forces are produced by increasing one jet area at the same rate as the other is decreased. Thus when $\delta_{RCS}(I) = 0$, the jet areas are equal and both jets command $F_{RCS_{MX}}(I)$. When $\delta_{RCS}(I) = 1.0$, the one jet area is double its value at $\delta_{RCS}(I) = 0$, and commands 2 $F_{RCS_{MX}}(I)$ while the other jet area is zero and commands zero force.

The demand jet commanded force takes three paths (figure 2-23): one path determines whether more bleed should be allowed to handle the additional RCS force requirement. This additional bleed, if any, is reflected in the variable $\Delta F_{RCS_{DMD}}$. The second path combines the force into the commanded force summation ($F_{RCS_{SUM}}$). When all jets have been processed, $F_{RCS_{SUM}}$ represents the total exit flow area of the RCS. The third path adjusts the commanded jet force for various thrust-loss contributors (such as available bleed less than required and less than maximum inlet mass flow rate) before applying it to the aircraft. The continuous jet commanded force is also combined into $F_{RCS_{SUM}}$ and adjusted for thrust losses before being applied to the airplane.

Bleed required by the RCS (B_{REQ}) is generated from the sum of the RCS force required at the reference bleed level ($F_{RCS_{MX_0}}$) and

$\Delta F_{RCS_{DMD}}$. Note that if the RCS is totally demand bleed, $F_{RCS_{MX_0}} = 0$.

B_{REQ} is compared with bleed available (B_{AVL}) to establish the actual RCS bleed level ($\overline{BLD}$). Bleed available is generated by the propulsion system model. The relation between RCS force and engine bleed denoted by $f_{RCS_{?}}$ is a function of the engine installation and bleed capability. The variable $F_{RCS_{AL}}$ represents the total RCS force available and is less than or equal to $F_{RCS_{SUM}}$. $K_{\dot{m}}$ is generated by the propulsion system model and is the ratio of actual inlet mass flow rate to the maximum available. Thus the relation for adjusting the individual jet command forces to the force applied to the aircraft can be shown to be:

$$F_{RCS_C}(I) = F_{RCS}(I)\,K_{\dot{m}}F_{RCS_{AL}}/F_{RCS_{SUM}}$$

This relation assumes each jet is affected proportionally the same by inlet mass flow rates and bleed capability.

$F_{RCS_C}(I)$ is processed by the RCS force dynamics to incorporate the effects of demand or continuous bleeding on the force applied to the aircraft. Continuous bleed jets are assumed to have no lag and $F_{RCS_C}(I)$ is applied immediately to the aircraft. Demand bleed jets are assumed to have first order lag dynamics to represent the delay between jet area changes and the appropriate force changes. Thus, for demand bleed jets, $F_{RCS_C}(I)$ is sent through a first order lag before being applied to the aircraft.

2.5.3 Resolution of RCS Forces into Body Axis Forces and Moments

Body axis RCS forces are the summation over the number of jets of the body axis components of the individual jet forces ($F_{RCS_A}(I)$):

$$X_{RCS} = \sum_{I=1}^{n_{JET}} F_{RCS_A}(I)\cos(\psi_{JET}(I))\cos(\theta_{JET}(I)) = \sum_{I=1}^{n_{JET}} \Delta X_{RCS}(I)$$

$$Y_{RCS} = \sum_{I=1}^{n_{JET}} F_{RCS_A}(I)\sin(\psi_{JET}(I))\cos(\theta_{JET}(I)) = \sum_{I=1}^{n_{JET}} \Delta Y_{RCS}(I)$$

$$Z_{RCS} = \sum_{I=1}^{n_{JET}} -F_{RCS_A}(I)\,\sin(\theta_{Jet}(I)) = \sum_{I=1}^{n_{JET}} \Delta Z_{RCS}(I)$$

where X_{RCS}, Y_{RCS}, Z_{RCS} are the total body axis RCS forces
$\Delta X_{RCS}(I)$, $\Delta Y_{RCS}(I)$, $\Delta Z_{RCS}(I)$ are the body axis RCS forces due to jet I
n_{JET} is the number of RCS jets.

Body axis moments are the summation of the moments produced by each jet:

$$L_{RCS} = \sum_{I=1}^{n_{JET}} [\Delta Z_{RCS}(I)Y_{JET}(I)-\Delta Y_{RCS}(I)Z_{JET}(I)]$$

$$M_{RCS} = \sum_{I=1}^{n_{JET}} [\Delta X_{RCS}(I)Z_{JET}(I)-\Delta Z_{RCS}(I)X_{JET}(I)]$$

$$N_{RCS} = \sum_{I=1}^{n_{JET}} [\Delta Y_{RCS}(I)X_{JET}(I)-\Delta X_{RCS}(I)Y_{JET}(I)]$$

where L_{RCS}, M_{RCS}, N_{RCS} are the total body axis RCS moments
$X_{JET}(I)$, $Y_{JET}(I)$, $Z_{JET}(I)$ are the body axis components of the position vector between the aircraft cg and the application point of jet I.

2.6 Coriolis Forces and Moments

Forces and moments are generated when the aicraft rotates and produces a change in the direction of the mass flow passing through the propulsion system. These forces and moments are due to the Coriolis acceleration imposed on the aircraft - $\bar{a}_{cor} \propto m(\bar{\omega}_A \times \bar{V})$ where $\bar{\omega}_A$ is the aircraft rotation vector and $m\bar{V}$ is proportional to the mass flow rate. Although Coriolis forces and moments are not large in magnitude and are generally not influential contributors to aircraft dynamics, a model of the effect was incorporated for completeness in the VATOL simulation.

The model is derived from the straight through propulsion system representaion shown in figure 2-24. This is an assumption in that the flow through actual propulsion systems may have several turns to traverse before exiting. The model also assumes that the amount of mass within the propulsion system is proportional to the inlet mass flow rate, thus the effect of fuel mass flow added within the propulsion system is neglected. This is reasonable since fuel mass flow rarely exceeds 10% of the inlet mass flow and is typically 5% or less.

The development of the Coriolis force and moment model equations is based on reference (i) and proceeds from the definitions of Coriolis moment about the cg ($\bar{M}_{COR}$) and force ($\bar{F}_{COR}$) vectors:

$$\bar{F}_{COR} = -2\int_{-(l_{DUCT}-1)}^{1} (\bar{\omega}_A \times \dot{\bar{R}})\, \rho A\, d\zeta_D \qquad (2.6.1)$$

$$\bar{M}_{COR} = -2\int_{-(l_{DUCT}-1)}^{1} (\bar{R} \times (\bar{\omega}_A \times \dot{\bar{R}}))\, \rho A\, d\zeta_D \qquad (2.6.2)$$

where

ζ_D is the integration variable which moves along the propulsion system centerline (figure 2-24) i.e. along the X_D axis.

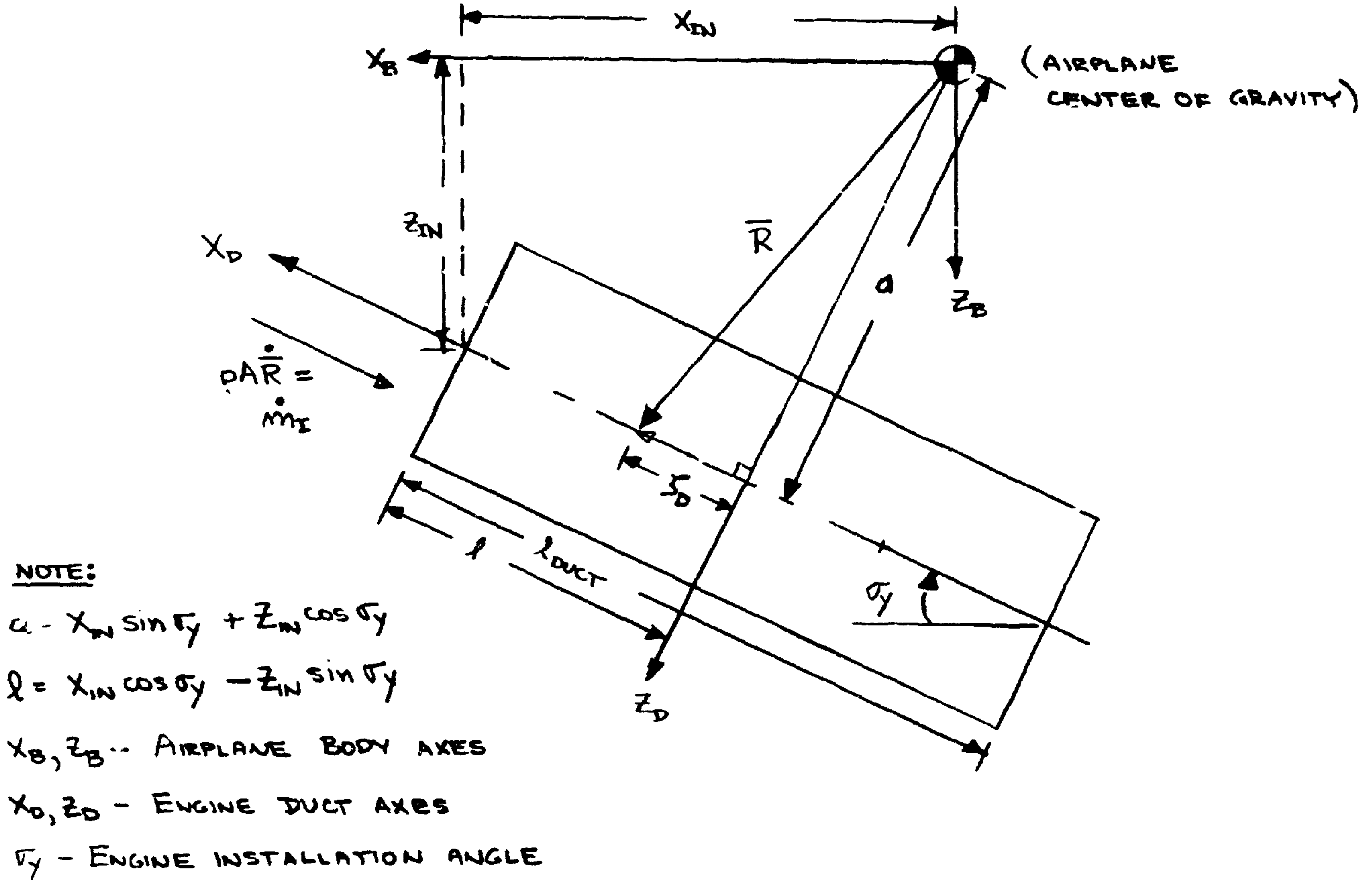

NOTE:

$a - X_{IN} \sin\sigma_y + Z_{IN} \cos\sigma_y$

$\ell = X_{IN} \cos\sigma_y - Z_{IN} \sin\sigma_y$

X_B, Z_B -- AIRPLANE BODY AXES

X_D, Z_D - ENGINE DUCT AXES

σ_y - ENGINE INSTALLATION ANGLE

Figure 2-24. Geometry ıor Coriolis Forces and Moments Model

l_{DUCT} is the length along the centerline from inlet face to exit plane with no nozzle deflection.

$\dot{\rho A \bar{R}}$ is the mass flow rate through the propulsion system

$\bar{R}$ is the vector from the aircraft cg to point ζ_D

In terms of propulsion system and aircraft variables, the vector quantities in equations (2.6.1) and (2.6.2) can be written as

$$\dot{\rho A \bar{R}} = -\dot{m}_I \bar{i} + 0\ \bar{j} + 0\ \bar{k} \tag{2.6.3}$$

$$\bar{\omega}_A = (p \cos \sigma_y - r \sin \sigma_y)\ \bar{i} + q\bar{j} + (r \cos \sigma_y + p \sin \sigma_y)\bar{k} \tag{2.6.4}$$

$$\bar{R} = \zeta_D \bar{i} + Y_I\ \bar{j} - a\ \bar{k} \tag{2.6.5}$$

where $\bar{i}$, $\bar{j}$, $\bar{k}$ are unit vectors along the propulsion system X_D, Y_D, Z_D axes.

Substituting equations (2.6.3) through (2.6.5) into equations (2.6.1) and 2.6.2) gives:

$$\bar{F}_{COR} = 2\dot{m}_I \int_{-(l_{DUCT}-l)}^{l} [(r \cos \sigma y + p \sin \sigma_y)\bar{j} + q\ \bar{k}]\ d\zeta_D \tag{2.6.6}$$

$$\bar{M}_{COR} = -2\dot{m}_I \int_{-(l_{DUCT}-l)}^{l} [Y_I\ q - a(r \cos \sigma_y + p \sin \sigma_y)]\bar{i} - q\bar{j} - (r\cos\sigma_y + p \sin\sigma_y)\bar{k}\ d\zeta_D \tag{2.6.7}$$

The Coriolis force and moment equations which result when equations (2.6.6) and (2.6.7) are integrated are detailed in Secton 2.0.5 of Volume II.

2.7 Actuation System Model

The VATOL simulation models for the actuation and flight control systems are perceived to interface as shown in figure 2-25. The purpose of the flight control system (FCS) model is to combine cockpit controller and motion sensor inputs through various control laws to generate control commands for the aircraft degrees of freedom. These control commands direct the application of body axis control moments and forces to the airplane. The actuation system model converts the control commands into commands for the actuators of the control force and moment generators and provides dynamic models for the actuators. The propulsion system is shown on figure 2-25 because one of its functions is to serve as the actuator for thrust commands.

The four FCS submodels - roll, pitch, yaw, and heave control systems - are justified and presented in Section 2.8. The actuation system actuator input submodel is discussed in Section 2.7.1 while the actuator dynamics submodel is discussed in Section 2.7.2.

2.7.1 Actuator Input Model

The VATOL simulation model has remained generic to this point: Insofar as a proposed configuration has no more than four lifting surfaces (i.e. left and right wing halves, horizontal stabilizing surface, and vertical stabilizing surface), one fuselage, ten RCS jets, and two jet engines with the capability to deflect thrust in two directions, it can be simulated without changing the force and moment models for any arrangement of these components. The futility of maintaining generality in the actuator input model and the need for this model to be more configuration specific become apparent in the following discussion: The VATOL force and moment models accept inputs from twenty eight control force and moment generators. As a minimum, the actuator input model, to maintain generality, must provide paths from each FCS control command to each actuator. Generally the gains in these paths must be programmed as functions of aircraft state or control variables to accommodate controls blending and/or nonlinear gearings for optimum flying qualities during transition. Crossfeeds between actuator inputs are also generally

C-2

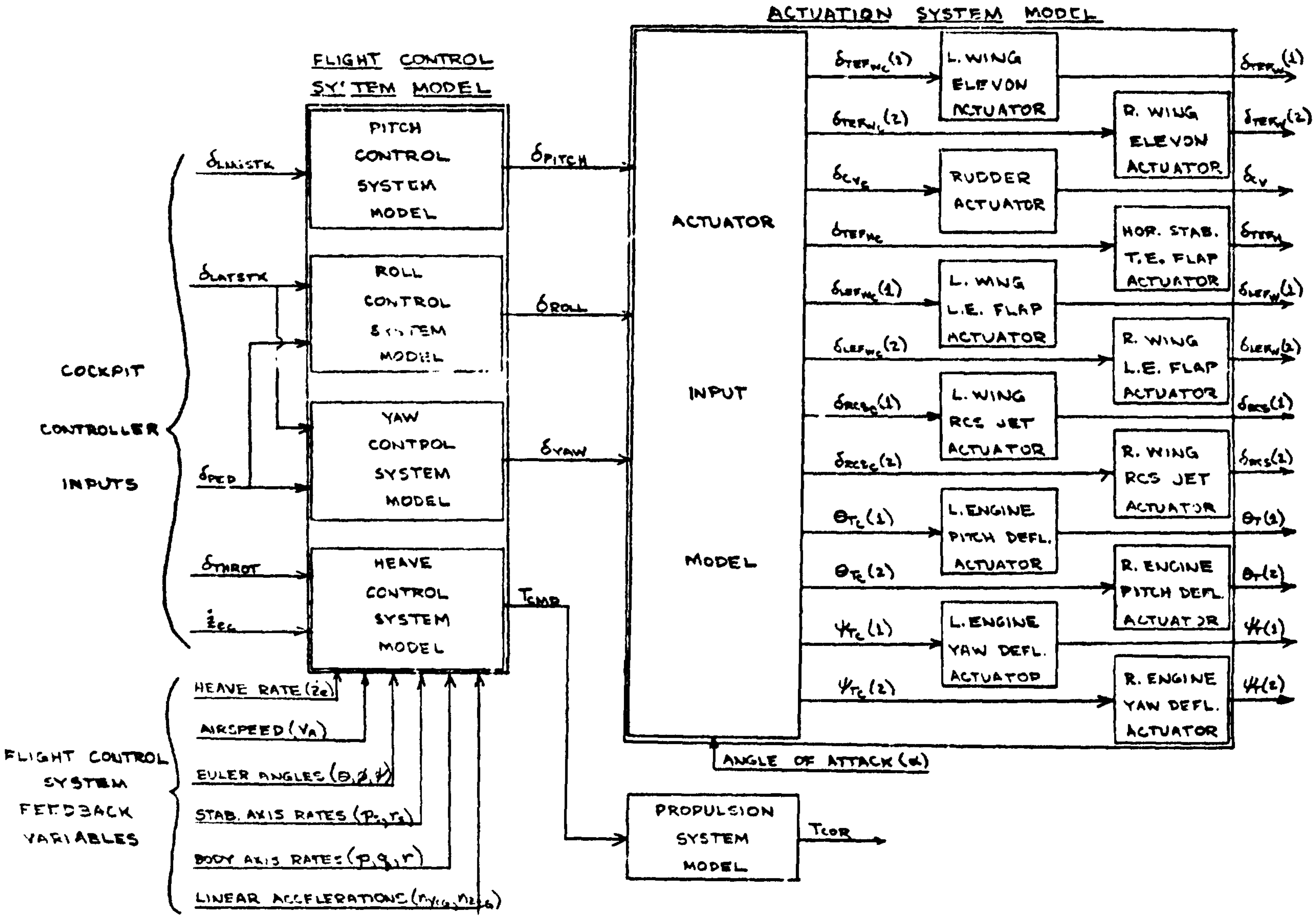

Figure 2-25. Interface of Flight Control System and Actuation System Models

required to minimize control couplings. An actuator input model which provides a priori for all these contingencies would be so large as to preclude real time manned simulation. In a practical application, only a small portion of the general model would ever be required and specification of that portion would be guided by a control system analysis of the simulated aircraft concept. Thus, the actuator input model is constrained to be more configuration specific than any of the other simulation component models and must be developed by off line analyses.

The development of the SF-121 actuator input model is described in Section 3.5 of this volume. The model is depicted in figure 3-2 and detailed by the equations of Section 2.2.1 of Volume II.

2.7.2 Generic Actuator Dynamics Model

With the exception of propulsion system thrust dynamics, the dynamics of all actuators in the VATOL simulation model are represented by the position and rate limited first order model shown in figure 2-26. The position and rate limits and time constants for the SF-121 actuators are specified in Section 3.7.2 of Volume II. The model equations are detailed in Section 2.2.2 of Volume II.

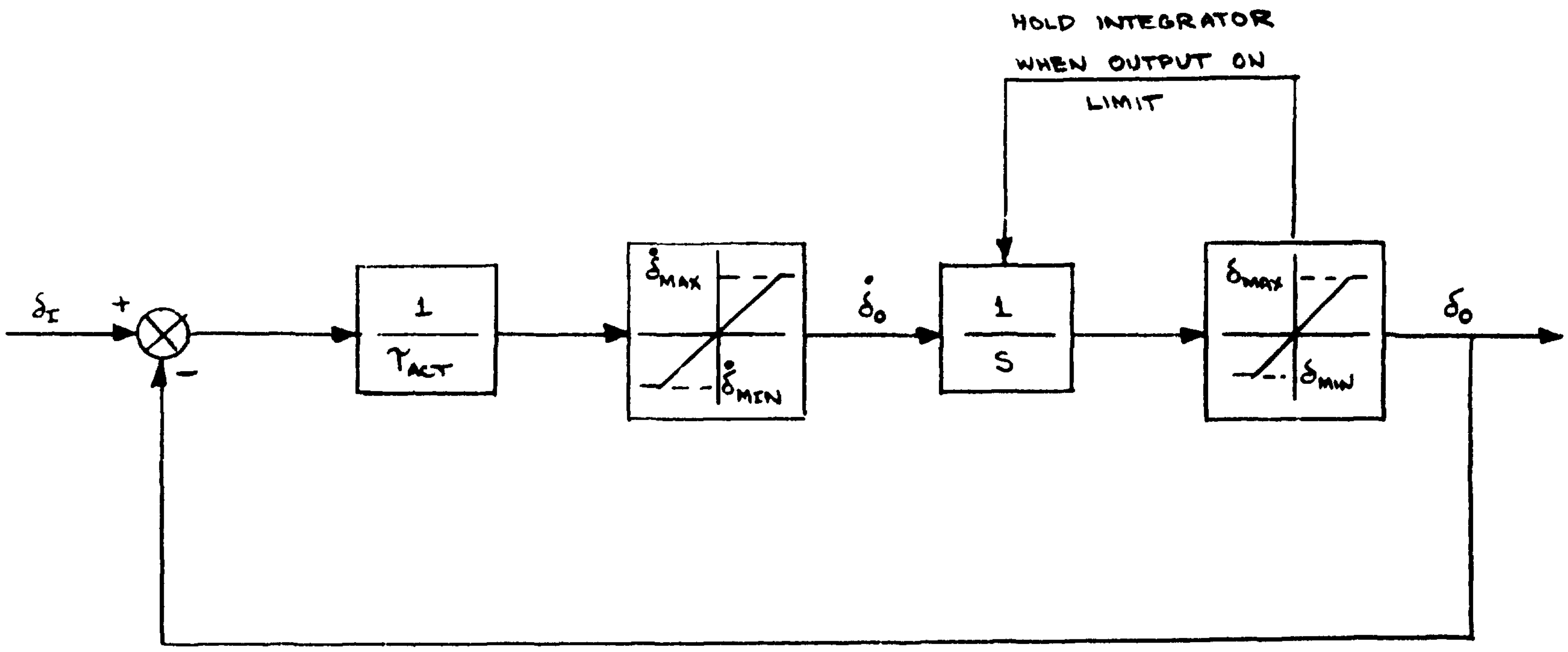

Figure 2-26. Generic Actuator Model

2.8 Flight Control System Model

As indicated by figure 2-25, the FCS model has four submodels. These are the roll, pitch, yaw and heave* control system models and correspond to the four degrees of freedom which normally require some level of automatic control or augmentation in VATOL airplanes. The roll, pitch, and yaw degrees of freedom are augmented in all flight regimes while heave is augmented only in the low speed (hover) regime. Surge and sway control at all speeds and high speed heave control are not modeled because these are totally manual modes utilizing throttle commands and/or aircraft attitude as the means to generate control forces. Generic roll, pitch, yaw, and heave control systems are depicted on figures 2-27 through 2-30 and are discussed in Sections 2.8.1 through 2.8.4

The FCS model receives inputs (figure 2-25) from three conventional cockpit controllers - pedals, control stick with right-left and fore-aft degrees of freedom, and manual throttles - plus one additional controller for heave. The pedals and both control stick degrees of freedom can be trimmed. Motion variables assumed available for FCS control law formulation include body axis roll, pitch, and yaw rates (p, q, r), stability axis yaw and roll rates (r_s and p_s), airspeed (V_A), Euler angles (θ, ϕ, ψ), aircraft lateral and normal accelerations at the cg ($n_{y_{cg}}$ and $n_{z_{cg}}$), and heave rate (Z_e).

---

*As used herein, heave, surge, and sway degrees of freedom are referenced to earth axes; heave is motion along the Z_I axis, surge is motion along the X_I axis, and sway is along the Y_I axis.

The FCS submodels are similar in several respects: All feature the option to switch control laws and cockpit controller function as a function of the control system switch (CS_{SW}) value. The value of CS_{SW} is determined by V_A; CS_{SW} = 0. for high speeds, = 1. for hover. Most of the system gains are programmable as functions of V_A. The forward loops can be set up as proportional or proportional-plus - integral controllers. The cockpit controller commands can be input through pure or shaped (by a lag filter) gains (for rate or attitude command systems) or through proportional-plus-integral arrangements (for rate command-attitude hold or acceleration command-rate hold systems).

Most of the feedbacks provided for the various FCS submodels are fairly conventional: For example, body and stability axis roll rates (p and p_s) and Euler roll angle (ϕ) are available in the roll control system; body and stability axis yaw rates (r and r_s) and Euler roll and yaw angles (ϕ and ψ) are available in the yaw control system; body axis pitch rate (q) and Euler pitch angle (θ) are available in the pitch control system; heave rate ($\dot{Z}_e$) is used in the heave control system. Several unconventional feedbacks have also been provided: For example, to avoid the high sensitivity of ϕ and ψ to aircraft rotations when $\theta > 80$ to 85 degrees and provide a feedback proportional to attitude, the integrals of roll and yaw rates (p_{INT} and r_{INT}) have been made available in the roll and yaw control systems. Also to avoid problems with the range of θ ($-90 < \theta < 90$ degrees) and provide a feedback proportional to pitch attitude, the integral of pitch rate (q_{INT}) has been made available in the pitch control system.

Two areas of concern in VATOL terminal operations which will be studied extensively via manned simulation are cockpit controller function switching and control mode switching. Cockpit controller function switching is required to avoid pilot confusion with VATOL concepts which rotate the cockpit as the aircraft approaches hover. The requirement for control mode switching should be obvious - the aircraft flies differently in aerodynamic force - supported flight than it does in thrust - supported flight. As specified in the FCS model, both cockpit controller function switching and control mode switching are controlled by the control system switch (CS_{SW}).

It is asumed that the function and mode switchings occur simultaneously and that CS_{SW} changes from 0 to 1 or vice versa in one sample period or one computer time frame. Logic is provided for reinitializing any input or feedback integrators when CS_{SW} changes value. This helps to avoid large switching transients, particularly when switching between Euler angle and integrated rate feedbacks. This switching scenario is rudimentary and should provide a "worst case" starting point. Many switching functions will be explored in evolving VATOL design guidelines; each of these will require reprogramming of the simulation model.

2.8.1 Roll Control System Model

The roll control system model is depicted on figure 2-27. Table 2-1 gives the parameter values required to implement several common combinations of roll control system types and forward loop controllers. Feedback variable selection is controlled by the three selector gains; K_{p_B} for roll rate, K_ϕ for ϕ, and $K_{\int p}$ for p_{INT}; which are functions of CS_{SW} and generally assume values of 0. or 1.. Those gains which can assume any value are indicated in Table 2-1 as being $\neq 0$. The exact values of these gains must be established by off-line control system analyses.

Figure 2-27 represents the roll control system for a VATOL airplane in which the cockpit rotates as hover is approached. cockpit control of roll is switched from lateral stick to pedals and roll trim function switches from lateral stick trim controller to pedal trim controller. This feature can be eliminated from the model by removing the CS_{SW} dependence from the cockpit controller inputs to the system.

Equations for the roll control system model are given in Section 2.3.2 of Volume II. Parameter values for the SF-121 roll control system are given in Section 3.8.2 of Volume II. These parameter values were established by the control system analyses described in Section 3.7 of this volume.

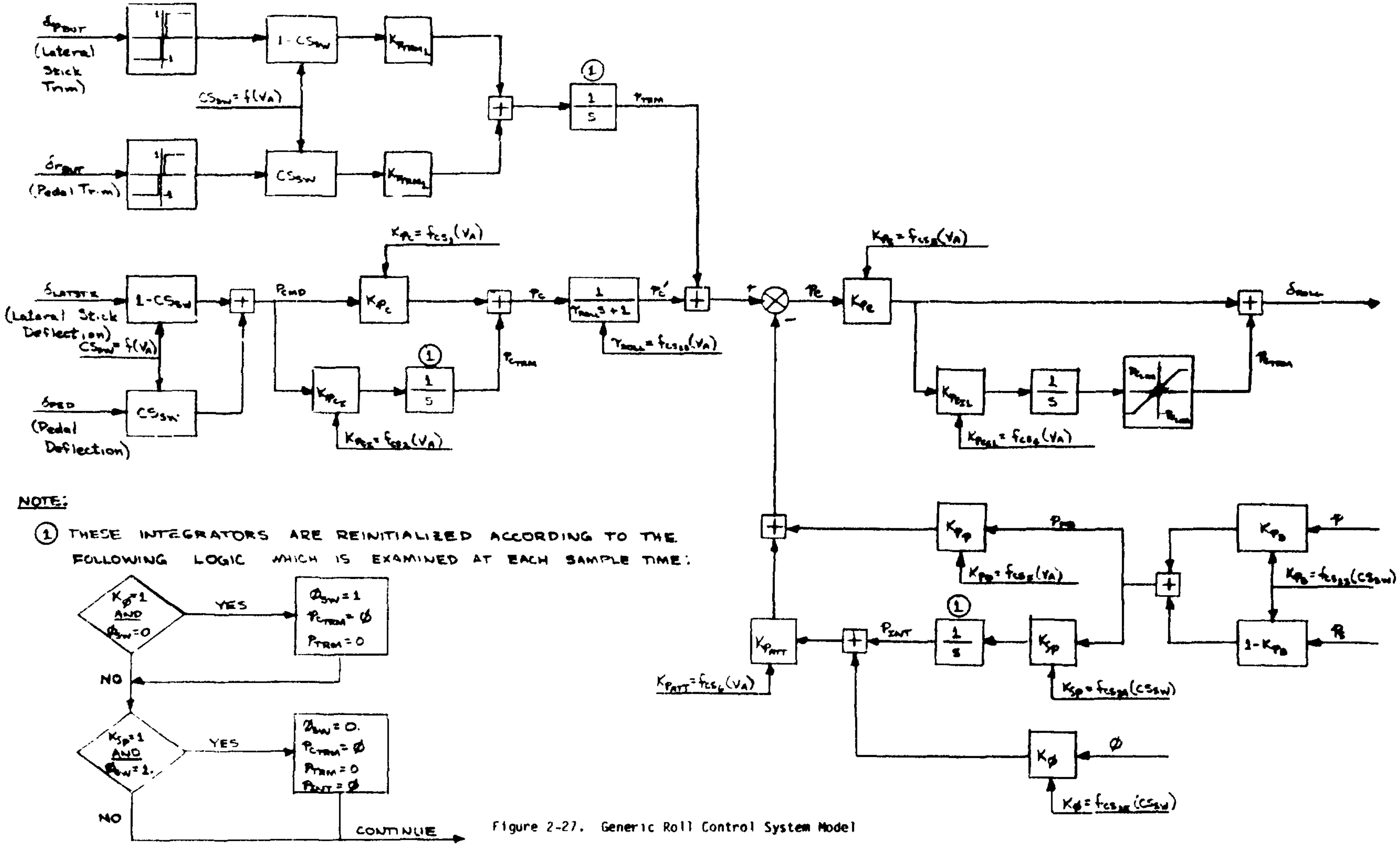

NOTE:

① THESE INTEGRATORS ARE REINITIALIZED ACCORDING TO THE FOLLOWING LOGIC WHICH IS EXAMINED AT EACH SAMPLE TIME:

Figure 2-27. Generic Roll Control System Model

TABLE 2-1

ROLL CONTROL SYSTEM MODEL PARAMETERS REQUIRED TO IMPLEMENT VARIOUS COMBINATIONS OF CONTROL SYSTEM TYPE AND FORWARD PATH CONTROLLER

CONTROL SYSTEM TYPE	FORWARD PATH CONTROLLER	ROLL CONTROL SYSTEM MODEL PARAMETERS									
		K_{p_c}	$K_{p_{c_I}}$	τ_{ROLL}	K_{p_e}	$K_{p_{e_{II}}}$	K_{p_p}	$K_{p_{ATT}}$	K_{ϕ}	K_{ψ}	K_{p_B}
ACCELERATION COMMAND	PROPORTIONAL	$\neq$ 0.*	0.	$\neq$ 0.	$\neq$ 0.	0.	0.	0.	NA**	NA	NA
RATE COMMAND	PROPORTIONAL	$\neq$ 0.	0.	$\neq$ 0.	$\neq$ 0.	0.	$\neq$ 0.	0.	NA	NA	NA
	PROPORTIONAL + INTEGRAL	$\neq$ 0.	0.	$\neq$ 0.	$\neq$ 0.	$\neq$ 0.	$\neq$ 0.	0.	NA	NA	NA
ATTITUDE COMMAND	PROPORTIONAL	$\neq$ 0.	0.	$\neq$ 0.	$\neq$ 0.	0.	$\neq$ 0.	1.	0. if K_{ψ}=1. 1. if K_{ψ}=0.	1. if K_{ϕ}=0. 0. if K_{ϕ}=1.	NA
	PROPORTIONAL + INTEGRAL	$\neq$ 0.	0.	$\neq$ 0.	$\neq$ 0.	$\neq$ 0.	$\neq$ 0.	1.	0. if K_{ψ}=1. 1. if K_{ψ}=0.	1. if K_{ϕ}=0. 0. if K_{ϕ}=1.	NA
RATE COMMAND - ATTITUDE HOLD	PROPORTIONAL	$\neq$ 0.	$\neq$ 0.	0.	$\neq$ 0.	0.	$\neq$ 0.	1.	0. if K_{ψ}=1. 1. if K_{ψ}=0.	1. if K_{ϕ}=0. 0. if K_{ϕ}=1.	NA
	PROPORTIONAL + INTEGRAL	$\neq$ 0.	$\neq$ 0.	0.	$\neq$ 0.	$\neq$ 0.	$\neq$ 0.	1.	0. if K_{ψ}=1. 1. if K_{ψ}=0.	1. if K_{ϕ}=0. 0. if k_{ϕ}=1.	NA

* $\neq$ 0. means gain value must be established by off-line control system analysis

** NA = not applicable, i.e., the control system type and forward path controller are independent of this parameter.

2.8.2 Pitch Control System Model

The pitch control system model is depicted on figure 2-28. Table 2-2 gives the parameter values required to implement several common combinations of pitch control system types and forward loop controllers. Feedback variable selection is controlled by the two selector gains; $K_{\int q}$ for q_{INT} and K_{θ} for θ; which are functions of CS_{SW} and generally assume values of 0. or 1.. Those gains which can assume any value are indicated in Table 2-2 as being $\neq 0$. The exact values of these gains must be established by off-line control system analyses.

Equations for the pitch control system model are given in Section 2.3.3 of Volume II. Parameter values for the SF-121 pitch control system are given in Section 3.8.3 of Volume II. These parameter values were established by the control system analyses described in Section 3.7 of this volume.

2.8.3 Yaw Control System Model

The yaw control system model is depicted on figure 2-29. Table 2-3 gives the parameter values required to implement several common combinations of yaw control system types and forward loop controllers. Feedback variable selection is controlled by the four selector gains; $K_{\phi_{r_s}}$ for ϕ, K_{r_B} for yaw rate, K_{ψ} for ψ, and $K_{\int r}$ for r_{INT}; which are functions of CS_{SW} and generally assume values of 0. or 1. Those gains which can assume any value are indicated in Table 2-3 as being $\neq 0$. The exact values of these gains must be established by off-line control system analyses.

Figure 2-29 represents the yaw control system for a VATOL airplane in which the cockpit rotates as hover is approached: cockpit control of yaw is switched from pedals to lateral stick and the yaw trim function switches from pedal trim controller to lateral stick trim controller. This feature can be eliminated from the model by removing the CS_{SW} dependence from the cockpit controller inputs to the system.

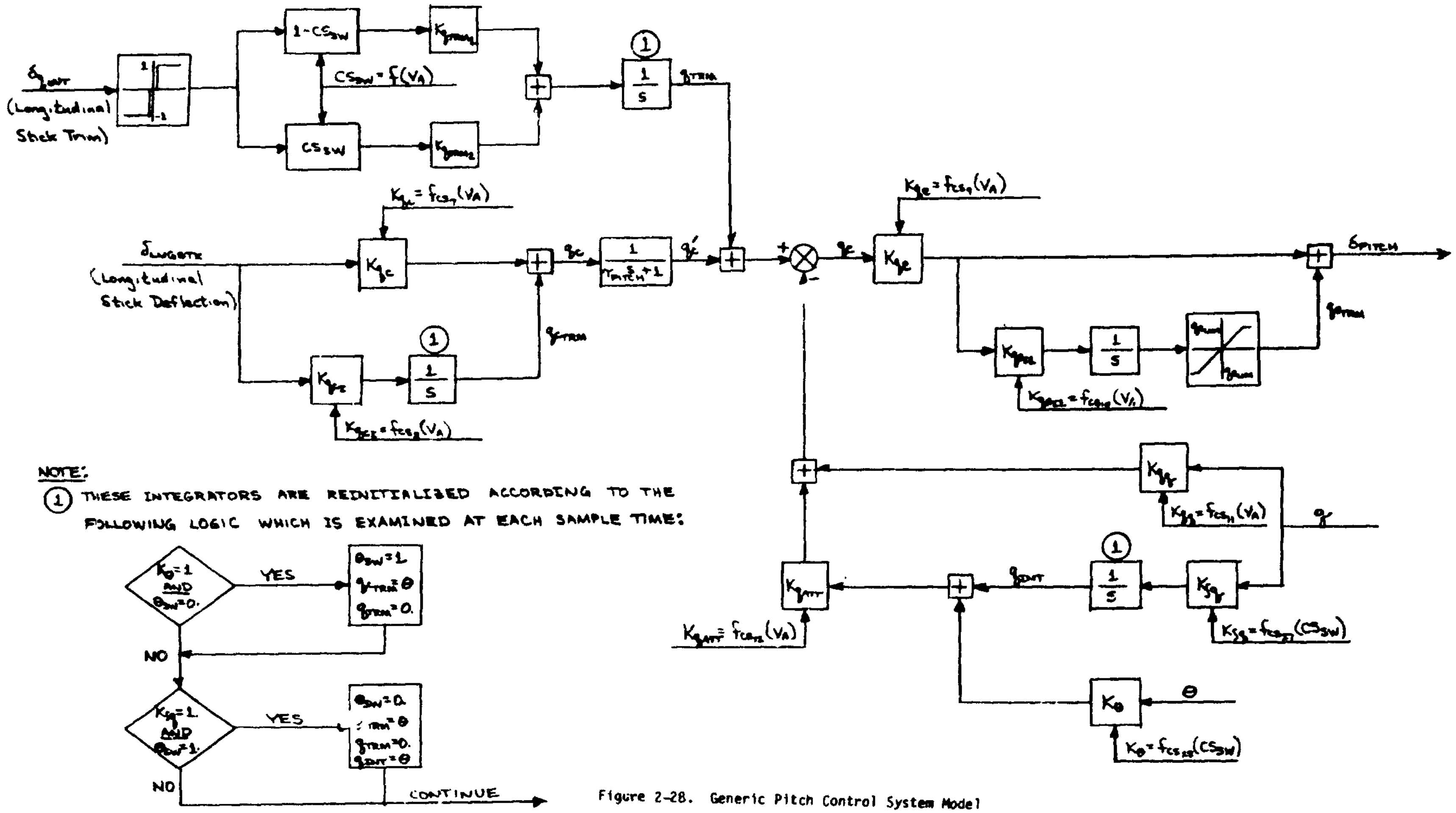

NOTE:

① THESE INTEGRATORS ARE REINITIALIZED ACCORDING TO THE FOLLOWING LOGIC WHICH IS EXAMINED AT EACH SAMPLE TIME:

Figure 2-28. Generic Pitch Control System Model

TABLE 2-2

PITCH CONTROL SYSTEM MODEL PARAMETERS REQURED TO IMPLEMENT VARIOUS COMBINATIONS OF CONTROL SYSTEM TYPE AND FORWARD PATH CONTROLLER

CONTROL SYSTEM TYPE	FORWARD PATH CONTROLLER	PITCH CONTROL SYSTEM MODEL PARAMETERS								
		K_{q_c}	$K_{q_{c_I}}$	τ_{PITCH}	K_{q_e}	$K_{q_{e_{I1}}}$	K_{q_q}	$K_{q_{ATT}}$	K_{θ}	K_{γ}
ACCELERATION COMMAND	PROPORTIONAL	≠ 0.*	0.	≠ 0.	≠ 0.	0.	0.	0.	NA**	NA
RATE COMMAND	PROPORTIONAL	≠ 0.	0.	≠ 0.	≠ 0.	0.	≠ 0.	0.	NA	NA
	PROPORTIONAL + INTEGRAL	≠ 0.	0.	≠ 0.	≠ 0.	≠ 0.	≠ 0.	0.	NA	NA
ATTITUDE COMMAND	PROPORTIONAL	≠ 0.	0.	≠ 0.	≠ 0.	0.	≠ 0.	1.	0. if K_{γ}=1. 1. if K_{γ}=0.	0. if K_{θ}=1. 1. if K_{θ}=0.
	PROPORTIONAL + INTEGRAL	≠ 0.	0.	≠ 0.	≠ 0.	≠ 0.	≠ 0.	1.	0. if K_{γ}=1. 1. if K_{γ}=0.	0. if K_{θ}=1. 1. if K_{θ}=0.
RATE COMMAND ATTITUDE HOLD	PROPORTIONAL	≠ 0.	≠ 0.	0.	≠ 0.	0.	≠ 0.	1.	0. if K_{γ}=1. 1. if K_{γ}=C.	0. if K_{θ}=1. 1. if K_{θ}=0.
	PROPORTIONAL + INTEGRAL	≠ 0.	≠ 0.	0.	≠ 0.	≠ 0.	≠ 0.	1.	0. if K_{γ}=1. 1. if K_{γ}=0.	0. if K_{θ}=1. 1. if K_{θ}=0.

* ≠ 0. means gain value must be established by off-line control system analysis

** NA = Not applicable; i.e., the control system type and forward path controller are independent of this parameter

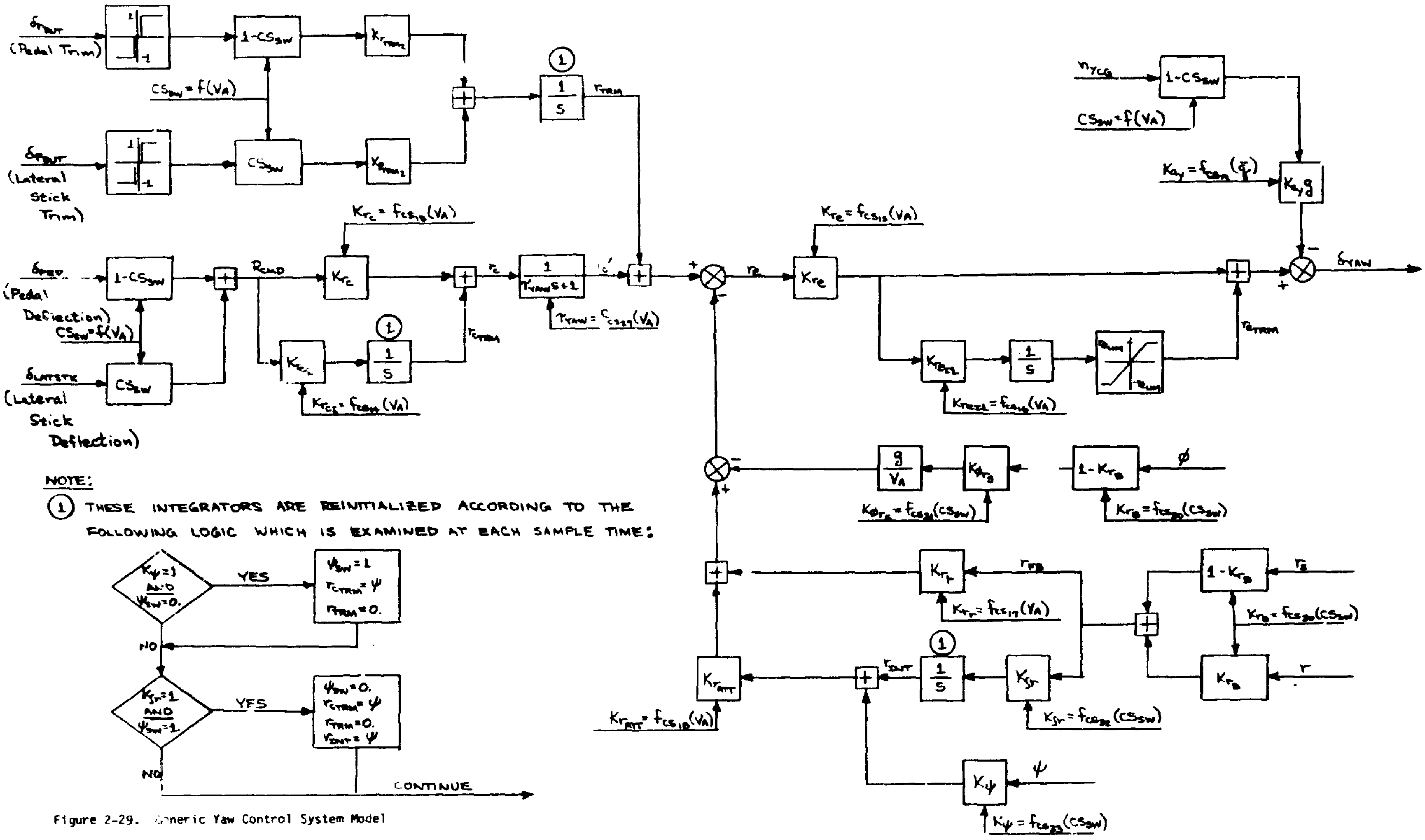

Figure 2-29. Generic Yaw Control System Model

TABLE 2-3

YAW CONTROL SYSTEM MODEL PARAMETERS PEQUIRED TO IMPLEMENT VARIOUS COMBINATIONS OF CONTROL SYSTEM TYPE AND FORWARD PATH CONTROLLER

CONTROL SYSTEM TYPE	FORWARD PATH CONTROLLER	YAW CONTROL SYSTEM MODEL PARAMETERS										
		K_{r_C}	$K_{r_{C_I}}$	τ_{YAW}	K_{r_e}	$K_{r_{e_I}}$	K_{r_r}	$K_{r_{ATT}}$	$K_{\phi r_S}$	K_{ψ}	$K_{\dot\psi}$	K_{r_B}
ACCELERATION COMMAND	PROPORTIONAL	$\neq$ 0.*	0.	$\neq$ 0.	$\neq$ 0.	0.	0.	0.	0.	NA**	NA	NA
TURN COORDINATION	PROPORTIONAL	$\neq$ 0.	0.	$\neq$ 0.	$\neq$ 0.	0.	$\neq$ 0.	0.	1.	NA	NA	0.
	PROPORTIONAL + INTEGRAL	$\neq$ 0.	0.	$\neq$ 0.	$\neq$ 0.	$\neq$ 0.	$\neq$ 0.	0.	1.	NA	NA	0.
RATE COMMAND	PROPORTIONAL	$\neq$ 0.	0.	$\neq$ 0.	$\neq$ 0.	0.	$\neq$ 0.	0.	0.	NA	NA	NA
	PROPORTIONAL + INTEGRAL	$\neq$ 0.	0.	$\neq$ 0.	$\neq$ 0.	$\neq$ 0.	$\neq$ 0.	0.	0.	NA	NA	NA
ATTITUDE COMMAND	PROPORTIONAL	$\neq$ 0.	0.	$\neq$ 0.	$\neq$ 0.	0.	$\neq$ 0.	0.	0.	1. if $K_{\dot\psi}$=0. 0. if $K_{\dot\psi}$=1.	1. if K_{ψ}=0. 0. if K_{ψ}=1.	NA
	PROPORTIONAL + INTEGRAL	$\neq$ 0.	0.	$\neq$ 0.	$\neq$ 0.	$\neq$ 0.	$\neq$ 0.	1.	0.	1. if $K_{\dot\psi}$=0. 0. if $K_{\dot\psi}$=1.	1. if K_{ψ}=0. 0. if K_{ψ}=1.	NA
RATE COMMAND ATTITUDE HOLD	PROPORTIONAL	$\neq$ 0.	$\neq$ 0.	0.	$\neq$ 0.	0.	$\neq$ 0.	1.	0.	1. if $K_{\dot\psi}$=0. 0. if $K_{\dot\psi}$=1.	1. if K_{ψ}=0. 0. if K_{ψ}=1.	NA
	PROPORTIONAL + INTEGRAL	$\neq$ 0.	$\neq$ 0.	0.	$\neq$ 0.	$\neq$ 0.	$\neq$ 0.	1.	0.	1. if $K_{\dot\psi}$=0. 0. if $K_{\dot\psi}$=1.	1. if K_{ψ}=0. 0. if K_{ψ}=1.	NA

* $\neq$ 0. means gain value must be established by off-line control system analysis

** NA = Not applicable, i.e. the control system type and forward path controller are independent of this parameter.

The lateral acceleration ($n_{y_{cg}}$) to FCS yaw control command (δ_{YAW}) feedback was added to decouple a coupled roll-spiral mode which appeared in the SF-121 in the speed range of 60 to 200 kt. (See Section 3.7 in this volume). The feedback can be removed simply by zeroing the lateral acceleration gain (K_{a_y}).

Equations for the yaw control system model are given in Section 2.3.4 of Volume II. Parameter values for the SF-121 yaw control system are given in Section 3.8.4 of Volume II. These parameter values were established by the control system analyses described in Section 3.7 of this volume.

2.8.4 Heave Control System Model

The heave control system model is depicted on figure 2-30. It receives input rate commands from the heave rate cockpit controller, compares these inputs with a heave rate feedback, and adjusts thrust to reduce the error according to a proportional ($K_{Z_{e_I}} = 0.$) or proportional plus integral ($K_{Z_{e_I}} \neq 0.$) forward loop control law. The heave control system operates only at low speed ($CS_{SW} = 1.$). The error gain (K_{Z_e}) and error integral gain ($K_{Z_{e_I}}$) must be determined by off-line control system analyses.

Equations for the heave control system model are given in Section 2.3.5 of Volume II. Parameter values for the SF-121 heave control system are given in Section 3.8.5 of Volume II. These parameter values were established by the control system analyses described in Section 3.7 of this volume.

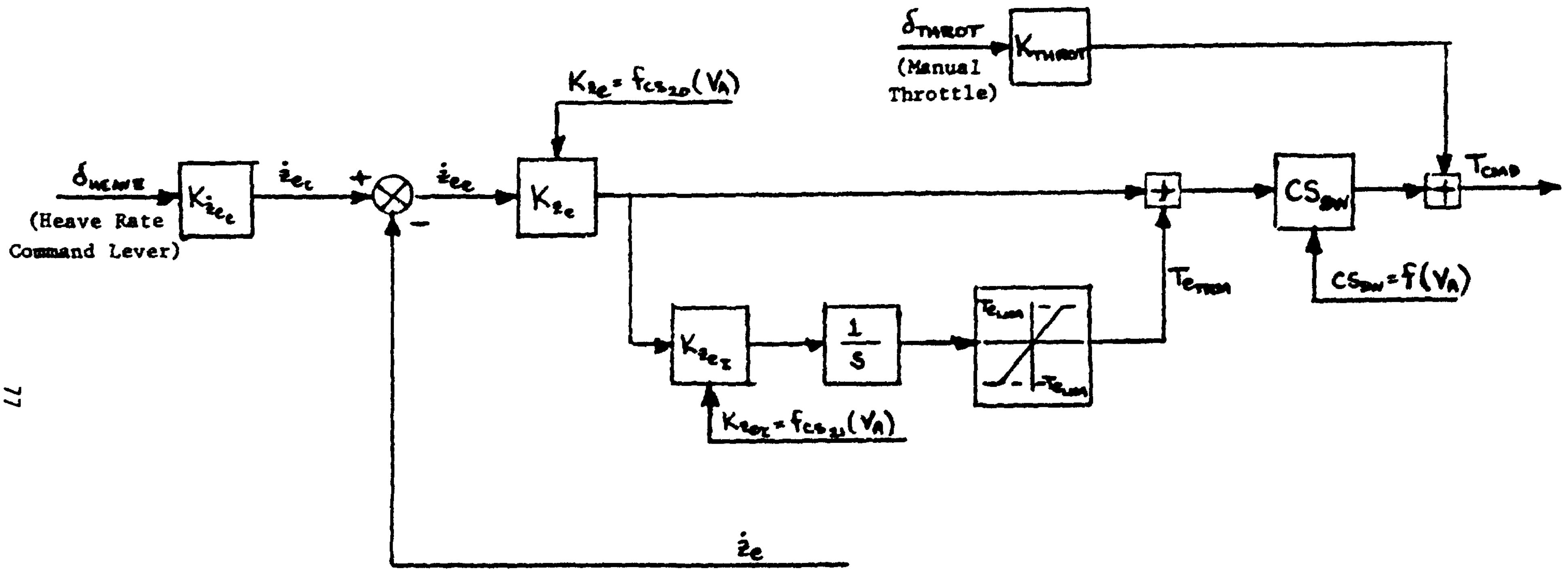

Figure 2-30. Generic Heave Control System Model

2.9 Relative Orientation of Aircraft Body Axes and Inertial Axes

Most simulations involving vehicle dynamics require a transformation to define the orientation of a set of vehicle-fixed body axes relative to an earth-fixed or inertial axis system. There are two basic formulations of this transformation: Euler rate equations and direction cosines. Because of their simplicity and almost universal applicability, the Euler rate equations are used for most aircraft simulations. Their one drawback is a singularity at $\theta = 90$ degrees. Even in aircraft simulations, such as air to air combat, where rapid large angle maneuvers are involved, the Euler rate equations are used by introducing approximate continuous forms of the equations when θ is close to 90 degrees. These approximations work well and have tolerably small errors as long as $\theta = 90$ degrees occurs only momentarily. It would be impossible to trim the aircraft at $\theta = 90$ degrees with the approximations present. VATOL aircraft routinely maneuver for long periods with θ close to 90 degrees. In addition they must be trimmed near 90 degrees for initiating hover analyses. For these reasons, the direction cosines formulation was adopted for the VATOL simulation math model since it is continuous everywhere. Because nine (vice three Euler rate equations) equations are involved, a slightly increased computation load is imposed on the simulation computer. Reference (j) quantified this increase to be 0.04 millisecond per integration using an Adams 2nd order integration algorithm; the Euler rate equations used 70 milliseconds per integration while the direction cosines used 0.74 milliseconds. In real time manned simulation activities to date using this VATOL model and requiring a frame time of approximately 50 milliseconds, this increased load has not been noticed. Neither has it noticeably increased expected run times in applications of VATLAS to generate dynamic check cases for the manned simulation.

Alternatives to the direction cosines formulation which have not been explored are as follows:

1. Rotated Inertial Axis System - Choose an inertial axis system in which the X_I and Z_I axes are rotated relative to the standard inertial system in which the Z_I axis is aligned with gravity.

The Euler rates and angles would then be applied to the rotated axis system. For example, figure 2-31 shows that, with the inertial axis system rotated 45 degrees, VATOL hover occurs at $\theta_R = 45$ degrees (where θ_R is pitch angle referenced to the rotated axes) and the singularity will not occur until the aircraft rotates another 45 degrees off the vertical. Similarly, straight and level flight in the rotated axes will occur with $\theta_R = -45$ degrees.

2. Quaternions - Computational speed and universal applicability are cited as advantages of quaternions. A limited investigation by Vought of these claims (ref (j)) found that quaternions are slightly faster than both Euler rate equations and direction cosines (0.66 milliseconds per iteration vs 0.70 milliseconds for Euler rate equations and 0.74 milliseconds for direction cosines) and are continuous everywhere. This speed improvement is "down in the noise" of real time manned simulations which operate in the 40 to 60 millisecond range.

The equations for the direction cosine formulation are detailed along with the aircraft equations of motion in Section 2.4 of Volume II. This formulation incorporates relations developed in reference (k) which maintain the orthonormality of the transformation by correcting the direction cosines for integration errors.

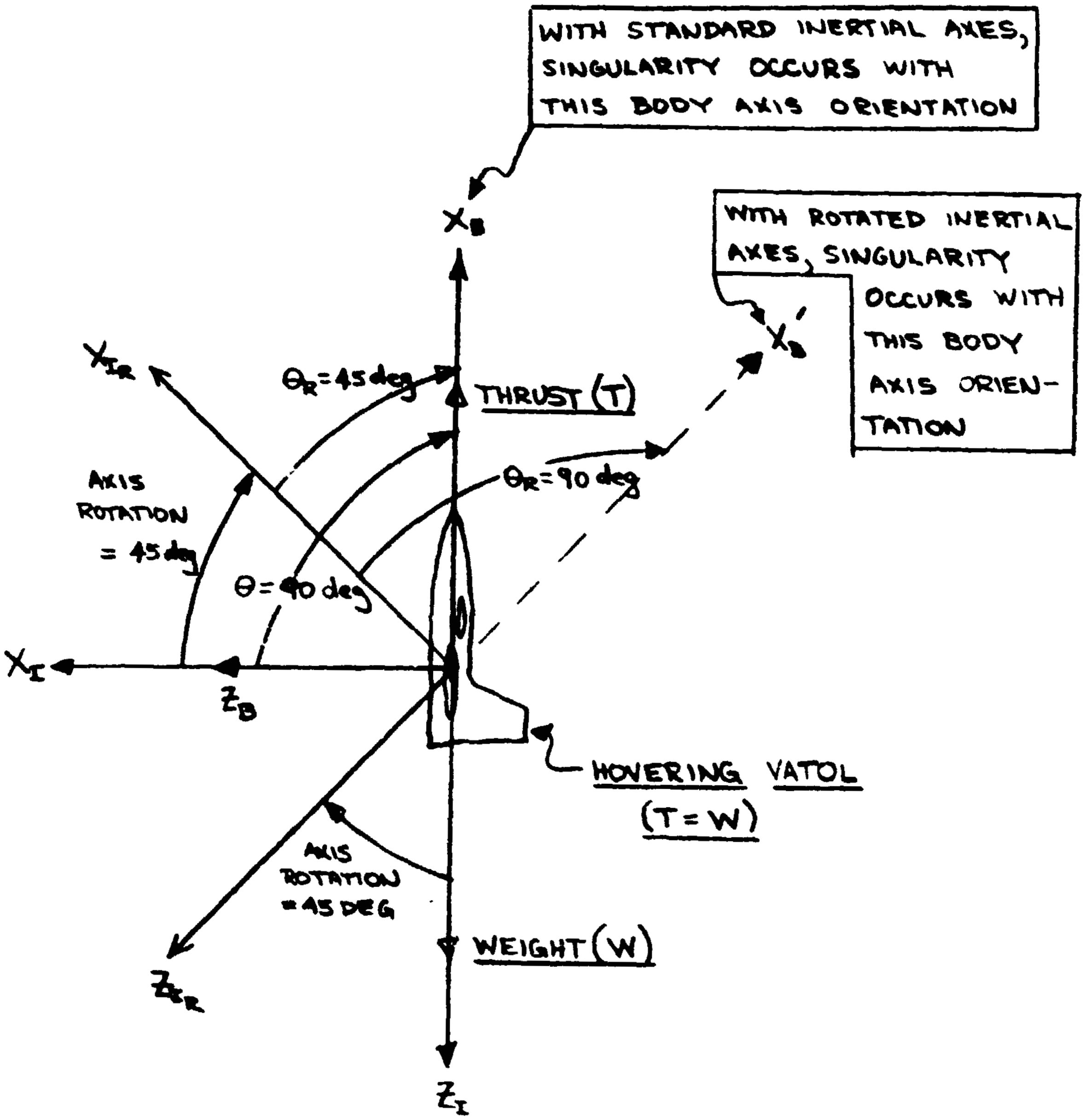

Figure 2-31. Relation of Standard and Rotated Inertial Axis Systems

2.10 Pseudo-Pilot Functions

To effectively apply the VATOL simulation model in an off-line mode required the incorporation of pilot-like (or pseudo-pilot) logic and inputs into VATLAS. These pseudo-pilot options include:

1. Apply open-loop inputs to any combination of cockpit controllers using data tables.
2. Equations for pilot-flown transition
3. Equations for pilot-flown stationkeeping

The table input functions can be applied in parallel with pilot-flown transitions or stationkeeping. Since the pseudo-pilot functions are not required for the VATOL manned simulation, they are not detailed in Volume II. Instead they will be presented here.

2.10.1 Open-Loop Cockpit Controller Inputs

The equations for the open loop cockpit controller inputs are quite simple:

$$\delta_{LNGSTK} = f_{PP_1}(t)$$

$$\delta_{LATSTK} = f_{PP_2}(t)$$

$$\delta_{PED} = f_{PP_3}(t)$$

$$\dot{Z}_{e_c} = f_{PP_4}(t)$$

$$\delta_{THROT} = f_{PP_5}(t)$$

where the f_{PP}'s are user defined tables

δ_{LNGSTK} is fore-aft motion of the control stick

δ_{LATSTK} is left-right motion of the control stick

δ_{PED} is pedals motion

$\dot{Z}_{e_c}$ is heave rate commanded by the heave rate controller

δ_{THROT} is throttle motion

Ordinarily the input functions are arranged to be steps, doublets, pulses, and other test inputs but, because of their table input format, can be made completely random. VATLAS is arranged so that inputs can be applied to any and all of the controllers simultaneously. In addition, the inputs can be different for each controller since each controller has its own function table.

2.10.2 Pseudo-Pilot Transition Equations

The pilot-flown transition equations require tables of trim pitch angles and throttle settings as a function of ground speed. Thus an analysis of transition trims is required before the pseudo-pilot can "fly" the transition. The equations assume that the pitch control system is rate command-attitude hold at high speeds ($CS_{SW} = 0.$) and attitude command at low speeds ($CS_{SW} = 1.$) The equations are given below:

1. $V_e = \sqrt{u^2 + v^2 + w^2}$
2. $\dot{V}_e = (u\dot{u} + v\dot{v} + w\dot{w})/V_e$
3. $(V_{e_{EST}}) = V_e + \dot{V}_e \, \Delta T$
4. $\Theta_{C_1} = f_{PP_6}(V_e)$
5. $\Theta_{C_2} = f_{PP_6}(V_{e_{EST}})$

6. $\dot{\theta}_C = (\theta_{C_2} - \theta_{C_1})/\Delta T$

7. $\delta_{LNGSTK} = \dot{\theta}_C(1 - CS_{SW}) + (\theta_{C_1} - q_{C_{TRM}})\ CS_{SW}$

8. $\delta_{THROT} = f_{PP_7}(V_e)$

where V_e is inertial speed

$\dot{V}_e$ is rate of change of inertial speed

$V_{e_{EST}}$ is estimated inertial speed at the next update assuming $\dot{V}_e$ is constant

ΔT is the time between updates

$\dot{u}$, $\dot{v}$, $\dot{w}$ are the rates of change of the body axis components of inertial speed

θ_{C_1} is the trim pitch angle at speed V_e

θ_{C_2} is the trim pitch angle at speed $V_{e_{EST}}$

$\dot{\theta}_C$ is the pitch rate required over the next ΔT seconds to reach θ_{C_2} at the next update

$q_{C_{TRM}}$ is the value of the input integrator when CS_{SW} changes from 0. to 1.0 (i.e. when the pitch control system switches from rate command-attitude hold to attitude command).

To initiate a transition δ_{THROT} is retarded below trim to start a deceleration, then as the speed decreases to 80 to 100 kt, the throttle is advanced to the proper trim setting. These throttle changes are controlled by the values in $f_{PP_7}(V_e)$. When CS_{SW} changes to 1.0, the heave control system is engaged and adjusts the thrust level to maintain the preset heave rate (normally = 0 ft/sec.). A sample pilot-flown transition is shown in figure 3-32 and discussed in Section 3.8.9.

2.10.3 Pseudo-Pilot Stationkeeping Equations

The development of the stationkeeping control equations assumed that the aircraft pitch and yaw control systems are attitude hold and that the heave rate command system was operative. It also assumed that the three inertial position loops are closed by the pilot who has both inertial rate and position available. The stationkeeping control laws are depicted in figure 2-32. The pseudo-pilot's goal is to maintain aircraft position at $X_e = Y_e = 0$ and Z_e at some desired altitude. Since δ_{LNGSTK} controls pitch attitude which in turn controls fore-aft motion along the Z body axis (recall $\theta \approx 90$ degrees while stationkeeping) and δ_{LATSTK} controls yaw attitude which in turn controls right-left motion along the Y body axis, the X_e and Y_e rate and position data are resolved into the body axis system. Longitudinal and lateral stick commands are then made proportional to Z and Y body axis errors respectively. Similarly, the heave rate commands are made proportional to heave and heave rate errors or, equivalently (with $\theta = 90$ degrees), X body axis position and rate. By reference to figure 2-32, the pilot-flown stationkeeping equations can be written as follows:

1. $Z_{e_s} = -d_{13}(X_e + K_W\dot{X}_e) - d_{23}(Y_e + K_w\dot{Y}_e) \cong -\int_0^t w\,dt - K_w W$

2. $Y_{e_s} = -d_{12}(X_e + K_v\dot{X}_e) - d_{22}(Y_e + K_v\dot{Y}_e) \cong -\int_0^t v\,dt - K_v v$

3. $X_{e_s} = (Z_{e_o} - Z_e - K_u\dot{Z}_e) \cong -\int_0^t u\,dt - K_u u$

4. $\delta_{LNGSTK} = K_{Z_{e_s}} Z_{e_s}$

5. $\delta_{LATSTK} = K_{Y_{e_s}} Y_{e_s}$

6. $\dot{Z}_{e_c} = K_{X_{e_s}} X_{e_s}$

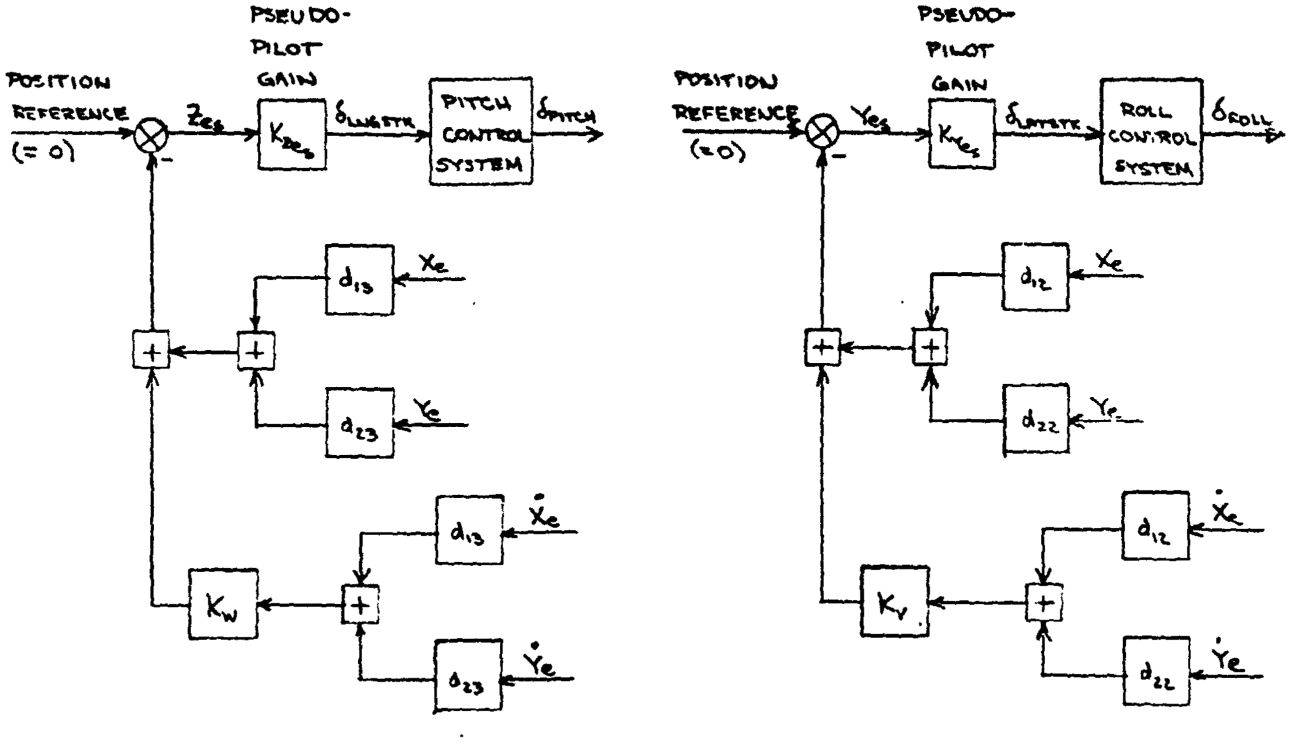

(a) Control Along Z_B Axis

(b) Control Along Y_B Axis

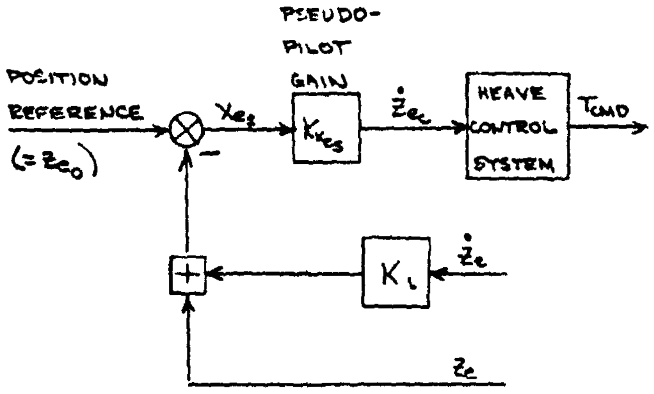

(c) Control Along X_B Axis

Figure 2-32. Stationkeeping Control Laws where

X_{e_s}, Y_{e_s}, Z_{e_s} are the error quantities along the X, Y, Z body axes assuming $\theta = 90$ degrees. The position contributions (i.e. $\int w dt$, $\int v dt$, $\int u dt$) in the expressions at the far right of equations 1, 2, and 3 are exact only if d_{13}, d_{23}, d_{12}, and d_{22} are constants (i.e. the relative orientation of the body and inertial axes does not change).

K_u, K_v, K_w are the rate feedback gains and must be determined by off-line control system analyses.

$K_{X_{e_s}}$, $K_{Y_{e_s}}$, $K_{Z_{e_s}}$ are the error gains and must also

be determined by off-line control system analyses.

A sample pilot-flown turn over a spot in a 35 kt wind at a commanded 20 degrees/sec turn rate is shown in figure 3-33 and discussed in Section 3.8.10. This maneuver combined the pseudo-pilot stationkeeping equations with an open loop pedal input.

3.0 APPLICATION OF VATLAS TO THE VOUGHT SF-121 AIRPLANE

This section describes the application of VATLAS to develop and demonstrate a FCS for terminal operations of the Vought SF-121 airplane. The general FCS design procedure depicted on figure 3-1 was followed for this application. The primary outputs of this iterative process are specification of actuator inputs and FCS laws and gains. Required inputs include aircraft data, operational conditions, desired FCS configuration, and inputs for testing FCS performance. Also required are an initial set of actuator input specifications and FCS laws and gains. Each step in the procedure (denoted by the blocks in figure 3-1) is discussed in detail below. Cal[illegible]ions are performed by VATLAS, which is used to generate 6DOF nonline[illegible]rs and response time histories to test inputs, and LINA, Vought's li[illegible] analysis routine.

The purpose of this VATLAS application to the SF-121 was to develop a baseline FCS which would enable a pilot to perform transition and hover flight tasks in a moving base simulation of the airplane. This FCS is to be capable of trimming the aircraft anywhere in the transition corridor and of meeting the maneuver requirements of MIL-F-83300 and AGARD 577. There are no requirements that this FCS be optimized with regard to pilot workload, augmentation level required to accomplish terminal operations, ride qualities, and similar items which can be considered when defining a baseline FCS but can not be completely evaluated without simulator studies and flight tests.

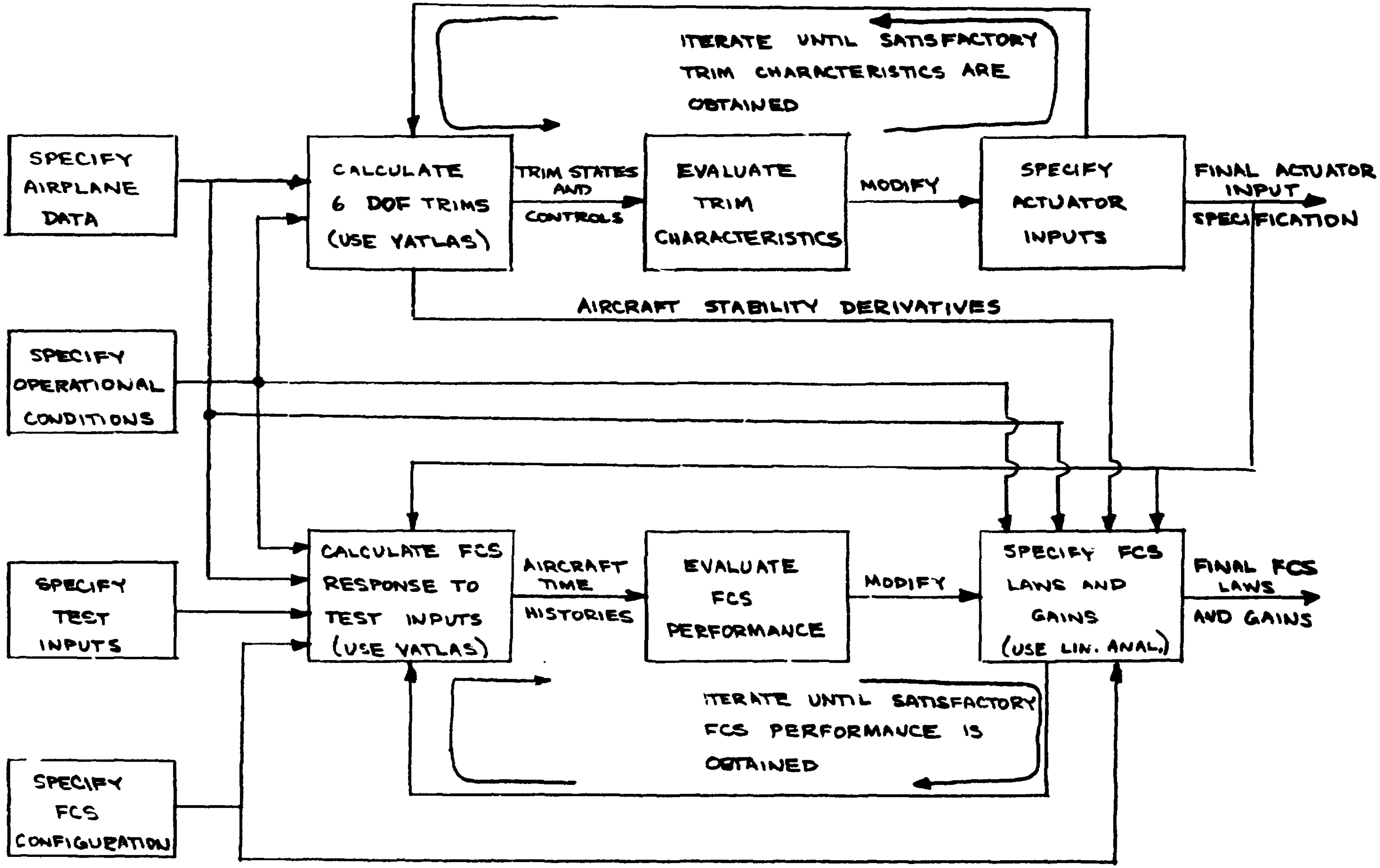

Figure 3-1. Flight Control System Design Procedure

3.1 SF-121 Airplane Data

The data required by VATLAS to model an airplane have been discussed in Secton 2.0 of this volume. Requisite SF-121 data have been incorporated in Volume II of this report as follows:

- Mass Properties Data - Section 3.1
- Geometry Data - Section 3.2
- Aerodynamic Data - Section 3.3
- Propulsion System Data - Section 3.4
- Inlet Ram Forces and Moments Data - Section 3.5
- Reaction Control System Data - Section 3.6
- Actuation System Data - Section 3.7

The mass properties data in Volume II represent only one SF-121 loading - design mission stores (2 Sidewinder and 2 Sparrow missiles and gun plus 400 rounds of ammunition), gear down, 1000 lb. fuel. This is a landing condition and served as the loading for the baseline FCS design. Tables 3-1 through 3-4, taken from reference (c), provide more extensive mass properties data for design mission stores on and off and gear up and gear down.

SF-121 control system data are given in Section 3.8 of Volume II. These data are outputs of the FCS design procedure; they were not required or available at initiation of the design process described herein.

TABLE 3-1

SF-121 MASS AND INERTIA DATA: DESIGN MISSION STORES, GEAR UP

FUEL STATE	WEIGHT	CENTER OF GRAVITY			MOMENT OF INERTIA~SLUG FT^2			
		F.S.	MAC	W.L.	I_X	I_Y	I_Z	I_{XZ}
Full	23,375	401.0	17.9	101.6	10,388	57,289	65,693	-498
7,000 lb.	22,299	401.1	18.0	100.9	9,195	56,194	63,515	-271
6,000 lb.	21,299	401.1	18.0	100.8	8,538	55,210	61,905	-160
COMBAT 4,845 lb.	20,144	401.2	18.0	100.8	8,032	54,091	60,283	-157
4,000 lb.	19,299	401.3	18.1	100.0	7,840	53,615	59,718	-208
3,000 lb.	18,299	401.3	18.1	99.7	7,686	53,184	59,185	-309
2,000 lb.	17,299	401.4	18.1	99.8	7,550	52,772	58,652	-307
1,000 lb.	16,299	401.5	18.2	99.9	7,383	52,382	58,167	-305
EMPTY	15,299	401.6	18.2	100.1	7,188	52,127	57,826	-253

TABLE 3-2

SF-121 MASS AND INERTIA DATA: DESIGN MISSION STORES, GEAR DOWN

FUEL STATE	WEIGHT	CENTER OF GRAVITY			MOMENT OF INERTIA~SLUG FT^2			
		F.S.	MAC	W.L.	I_X	I_Y	I_Z	I_{XZ}
FULL	23,375	400.5	17.6	101.0	10,744	57,526	65,862	-386
7,000 lb.	22,299	400.5	17.6	100.2	9,545	56,426	63,684	-162
6,000 lb.	21,299	400.5	17.6	100.0	8,886	55,441	62,075	-53.2
COMBAT	20,144	400.5	17.6	100.0	8,392	54,355	60,497	-52.1
4,000 lb.	19,299	400.5	17.6	99.2	8,184	53,842	59,888	-103
3,000 lb.	18,299	400.6	17.7	98.9	8,028	53,410	59,355	-154
2,000 lb.	17,299	400.6	17.7	98.9	7,892	52,998	58,823	-204
1,000 lb.	16,299	400.6	17.7	99.0	7,726	52,609	58,338	-202
EMPTY	15,299	400.7	17.7	99.1	7,532	52,356	57,998	-101

TABLE 3-3

SF-121 MASS AND INERTIA DATA: DESIGN MISSION STORES OFF, GEAR UP, SIDEWINDER LAUNCHERS AND PYLONS ON

FUEL STATE	WEIGHT	CENTER OF GRAVITY			MOMENT OF INERTIA~SLUG FT^2			
		F.S.	MAC	W.L.	I_X	I_Y	I_Z	I_{XZ}
FULL	21,738	401.7	18.3	102.8	8,559	55,909	62,802	-651
7,000 lb.	20,662	401.8	18.4	102.1	7,373	54,821	60,624	-426
6,000 lb.	19,662	401.9	18.4	101.9	6,718	53,838	59,014	-314
COMBAT 4,845 lb.	18,506	402.0	18.5	102.0	6,212	52,719	57,392	-307
4,000 lb.	17,662	402.1	18.5	101.3	6,028	52,250	56,825	-356
3,000 lb.	16,662	402.2	18.6	101.0	5,876	51,821	56,292	-454
2,000 lb.	15,662	402.4	18.7	101.2	5,739	51,407	55,759	-450
1,000 lb.	14,662	402.5	18.8	101.4	5,571	51,015	55,273	-447
EMPTY	13,662	402.7	18.9	101.8	5,373	50,756	54,932	-396

TABLE 3-4

SF-121 MASS AND INERTIA DATA DESIGN MISSION STORES OFF, GEAR DOWN, SIDEWINDER LAUNCHERS AND PYLONS ON

FUEL STATE	WEIGHT	CENTER OF GRAVITY			MOMENT OF INERTIA SLUG FT^2			
		F.S.	MAC	W.L.	I_X	I_Y	I_Z	I_{XZ}
FULL	21,738	401.1	18.0	102.1	8,922	56,158	62,975	-541
7,000 lb.	20,662	401.1	18.0	101.3	7,731	55,065	60,797	-318
6,000 lb.	19,662	401.2	18.0	101.2	7,075	54,082	59,188	-208
COMBAT 4,845 lb.	18,506	401.2	18.0	101.2	6,569	52,964	57,566	-153
4,000 lb.	17,662	401.3	18.1	100.4	6,381	52,490	56,467	-253
3,000 lb.	16,662	401.4	18.1	100.1	6,227	52,060	56,467	-301
2,000 lb.	15,662	401.5	18.2	100.2	6,090	51,647	55,935	-349
1,000 lb.	14,662	401.6	18.2	100.4	5,923	51,257	55,450	-347
EMPTY	13,662	401.7	18.3	100.6	5,728	51,001	55,109	-247

3.2 SF-121 Operational Conditions

As stated above, the baseline FCS development was to consider only terminal operations of the SF-121. Terminal operations include approach to transition, transition or reconversion, and hover flight conditions. It is assumed that these operations occur at low altitude in a speed range of 0 to 200 kt. At 200 kt, the SF-121 cruises in aerodynamically supported (conventional) flight at $\alpha \gtrsim 9.5$ degrees while at hover the airplane is fully thrust supported at $\alpha \gtrsim 90$ deg. The specific operational conditions selected for linear analysis and design of the baseline FCS were $V_A = 0, 10, 40, 60, 80, 120,$ and 200 kt. in level flight at VL (Vertical Landing) weight and inertias. The closely spaced conditions at $V_A = 40, 60,$ and 80 kt emphasize that portion of the SF-121 transition where the aircraft trim characteristics change most rapidly with speed. (See Section 3.6 for the SF-121 trim data.) Landing was considered more critical to the design since VL trim thrust (thus control power) is lower than VTO (Vertical Takeoff) thrust and VL is a more demanding piloting task than VTO.

Another operational condition imposed by the NASA-Ames S.01 simulator limitation on cockpit pitch angle but certainly within the realm of VATOL possibilities was that, in hover, the cockpit centerline will be approximately perpendicular to the fuselage centerline; i.e. the pilot looks out the airplane Z body axis during hover. This cockpit (pilot) orientation is similar to that of the "nutcracker" aircraft concept. To maintain harmony between cockpit controller inputs and pilot - perceived aircraft motions, the baseline FCS has to provide for swapping pedals and lateral stick functions during transition. Thus, lateral stick always commands cockpit roll and pedals always command cockpit yaw.

3.3 Baseline FCS Configuration Selection

It was immediately obvious that at least two modes were required for the SF-121 baseline FCS configuration; one mode for hover or thrust-supported flight and one for conventional or aerodynamically-supported flight. A switch point or blending region between these modes has to be established. Sections 3.6 and 3.7 detail the development of this mode changing.

The next step in FCS configuration selection was to consider how control forces and moments are produced for the SF-121 airplane. Table 3-5 summarizes this information for each of the airplane six degrees of freedom and for hover and conventional flight modes. The table specifies the primary force or moment generator and cockpit controller, if available, for each degree of freedom. The cockpit heave controller in hover flight is a separate controller if closed loop heave or heave rate control is adopted; otherwise it is the throttle. With the exception of the role reversal of pedals and left-right stick motion and the possible addition of a heave controller in hover flight, the functions of the cockpit controllers are fairly standard.

The dual-mode requirement for the FCS and similarity in number and function of the cockpit controllers led to adoption for the SF-121 of the augmentation levels and functions of the baseline FCS of the lift/cruise fan V/STOL airplane studied in reference (e). The selection of these levels and functions for the lift/cruise fan airplane FCS was based on an extensive foundation of analysis, simulation, and flight testing of terminal operations of V/STOL airplanes. These levels and functions were demonstrated in reference (e) to be adequate for launch and recovery operations on a DD963 type ship. There was no reason to doubt that the same FCS concept would suffice as a baseline FCS for terminal operations the SF-121 airplane.

The SF-121 baseline FCS configuration is summarized by degrees of freedom controlled, system type, cockpit controller, and flight mode in Table 3-6. The only deviation from the lift/cruise fan V/STOL baseline FCS is the substitution of a rate command-attitude hold system for an attitude command system in the pitch axis for the conventional flight mode. The pitch angle changes required during VATOL transition are large (50-60 degrees). With an

TABLE 3-5

CONTROL FORCE AND MOMENT GENERATION ON THE SF-121

CONTROL FORCE OR MOMENT	HOVER MODE		CONVENTIONAL MODE	
	GENERATED BY	ASSOCIATED COCKPIT CONTROL	GENERATED BY	ASSOCIATED COCKPIT CONTROL
ROLL MOMENT (ABOUT X_B AXIS)	REACTION CONTROL SYSTEM	PEDALS	DIFFERENTIAL ELEVON DEFLECTION	LEFT-RIGHT STICK DEFLECTION
PITCH MOMENT (ABOUT Y_B AXIS)	PITCH THRUST DEFLECTION	FORE-AFT STICK DEFLECTION	SYMMETRICAL ELEVON DEFLECTION	FORE-AFT STICK DEFLECTION
YAW MOMENT (ABOUT Z_B AXIS)	YAW THRUST DEFLECTION	LEFT-RIGHT STICK DEFLECTION	RUDDER	PEDALS
SURGE FORCE (ALONG X_I AXIS)	FUSELAGE PITCH ANGLE	-	THRUST AT HIGH SPEED THEN FUSELAGE PITCH ANGLE AT LOW SPEED	THROTTLE FOR THRUST
SWAY FORCE (ALONG Y_I AXIS)	FUSELAGE YAW ANGLE	-	FUSELAGE ROLL ANGLE	-
HEAVE FORCE THROTTLE FOR (ALONG Z_I AXIS)	THRUST	HEAVE CONTROLLER	FUSELAGE PITCH ANGLE AT HIGH SPEED THEN THRUST AT LOW SPEED	THRUST

TABLE 3-6

SF-121 BASELINE FCS CONFIGURATION

DEGREE OF FREEDOM	SYSTEM TYPE		COCKPIT CONTROLLER	
	HOVER MODE	CONVENTIONAL MODE	HOVER MODE	CONVENTIONAL MODE
ROLL (MOMENT ABOUT X_B AXIS)	RATE COMMAND-ATTITUDE HOLD	RATE COMMAND-ATTITUDE HOLD	PEDALS	LEFT-RIGHT STICK STICK DEFLECTION
PITCH (MOMENT ABOUT Y_B AXIS)	ATTITUDE COMMAND	RATE COMMAND-ATTITUDE HOLD	FORE-AFT STICK DEFLECTION	FORE-AFT STICK DEFLECTION
YAW (MOMENT ABOUT Z_B AXIS)	ATTITUDE COMMAND	RATE COMMAND WITH TURN COORDINATION	LEFT-RIGHT STICK DEFLECTION	PEDALS
HEAVE (FORCE ALONG Z_I AXIS)	RATE COMMAND	NO AUGMENTATION (i.e. ACCELERATION COMMAND)	HEAVE CONTROLLER	THROTTLE

attitude command system limited to 15 or 20 degrees pitch command authority for the stick, the pilot has to spend considerable time on the trim button to keep the stick in a desirable range of travel. The rate command-attitude hold system eliminates the requirement for trim button inputs and maintains the attitude stability supplied by the attitude command system.

3.4 Test Cases to Evaluate FCS Performance

The test cases selected to demonstrate and evaluate FCS performance are as follows:

- Steps, doublets, and/or pulses imposed on various cockpit controllers in both hover and conventional modes and in the mode switching flight regime.
- Pseudo-pilot flown transition
- Pseudo-pilot flown turn over a spot in a 35 kt wind

Since these runs will be produced by the full nonlinear simulation program (VATLAS), they should highlight any problems due to actuator position or rate limits, nonlinear aerodynamics, thrust dynamics, kinematic coupling, and similar nonlinearities. The pseudo-pilot transition and stationkeeping runs will indicate potential piloting problems in attempting to perform transition and hover tasks.

3.5 Actuator Input Specification

The SF-121 has fourteen actuators which are to be linked with four FCS variables. The FCS variables are commanded thrust and roll, pitch, and yaw control commands. The roll, pitch, and yaw commands are normalized such that ±1. commands all available control power in the appropriate direction. The fourteen actuators are as follows:

- Left and right wing trailing edge flaps (elevons)
- Vertical stabilizer control surface (rudder)
- Left and right engines pitch thrust deflection
- Left and right engines yaw thrust deflection
- Left and right engines thrust (i.e. propulsion system)
- Left and right wing tip RCS jets
- Canard trailing edge flap
- Left and right wing leading edge flaps

The inputs to the left and right wing leading edge flap actuators and to the trailing edge flap of the canard are specified in reference (c) to be functions of angle of attack. Inputs for each of the other actuators except the propulsion system were formed by multiplying the appropriate normalized roll, pitch, or yaw command by the maximum deflection controlled by that actuator. For example, the normalized pitch control (δ_{PITCH}) was linked to the right and left wing elevon actuators (which are the primary generator of pitch control power during conventional flight) and to the left and right engines pitch thrust deflection actutators (which are the primary generator of pitch control power during hover flight). All actuators were assumed to be driven full time. The gains for the elevon actuator inputs were 25 degrees, the maximum symmetric elevon deflection, and the gains for the pitch thrust deflection actuators were 15 degrees, the maximum pitch thrust deflection.

The actuator inputs are depicted in figure 3-2. This arrangement is the initial and, as will be shown, the only actuator input specification required. Note that, in addition to the basic links, the arrangement anticipates use of differential left-right pitch thrust deflection for roll control (gain

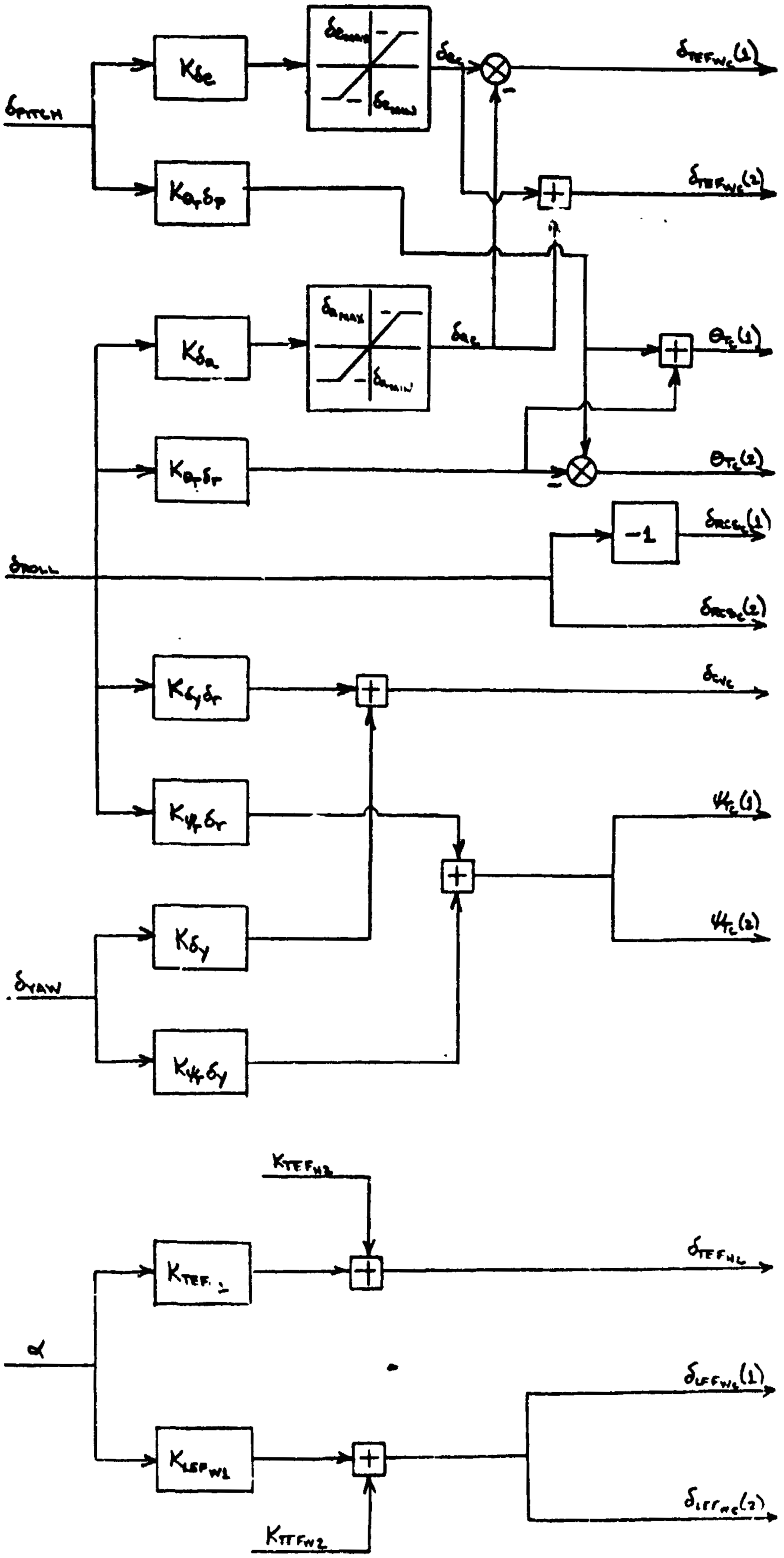

Figure 3-2. SF-121 Actuator Input Specification

$K_{\theta_T \delta_r}$) and a crossfeed of roll control to rudder (gain $K_{\delta_y \delta_r}$) and yaw thrust deflection (gain $K_{\psi_T \delta_r}$). As will be shown, these additions were not required. The actuator input gains are specified in Section 3.7.1 of Volume II.

3.6 Trim Characteristics Evaluation

Once the actuator inputs were specified, the airplane could be trimmed using FCS control variables. Two types of trim were calculated by VATLAS: hover trims in a 35 kt wind whose direction varied from head wind to tail wind and transition trims. Transition trims assumed straight ($\phi = 0$) and level ($\gamma = 0$) flight and were calculated for three deceleration levels ($V_A = 0$, -0.1, -0.2 g) along the flight path for a speed range of 0 to 200 kt. The primary transition trim variables - pitch angle, thrust level, and normalized pitch control (δ_{PITCH}) - are shown on figure 3-3. Similarly the primary hover trim variables - pitch and bank angles, thrust level, angles of attack and sideslip, and normalized roll, pitch, and yaw controls - are shown on figure 3-4.

Figures 3-3 and 3-4 indicate that the SF-121 has sufficient control power for trim in 35 kt winds and along reasonable reference trajectories in the airplane's transition corridor. The maximum percentage use of available pitch control power to trim is 74% which occurs at 80 kt in a 0.2g decelerating transition. The maximum percentage use of available roll control power to trim is 9% which occurs in a 35 kt crosswind ($\psi_{WIND} = -90$ degrees) while that for yaw control power is 17% which occurs in a 35 kt wind oriented 75 deg to port or starboard.

Figure 3-5 compares pitch, roll, and yaw control power available with trim (for a 0.2g decelerating transition) and flying qualities specification requirements. Because of the rotated SF-121 cockpit in hover the flying qualities roll (yaw) control power requirements are compared with SF-121 yaw (roll) control power. AGARD 577 requirements are assumed to be applicable from 0 to 35 kt, which is the range for hover and low speed flight specified in MIL-F-83300. The AGARD 577 requirements indicated on figure 3-5 show the control power range designated to be typical for attitude stabilized V/STOL aircraft for maneuvering, trim, and gust regulation functions. The control power available for maneuvering and gust regulation is also compared with the flying qualities requirements on figure 3-5. As can be seen the SF-121 has adequate control power for meeting the trim and maneuvering specification requirements with some margin left for gust regulation.

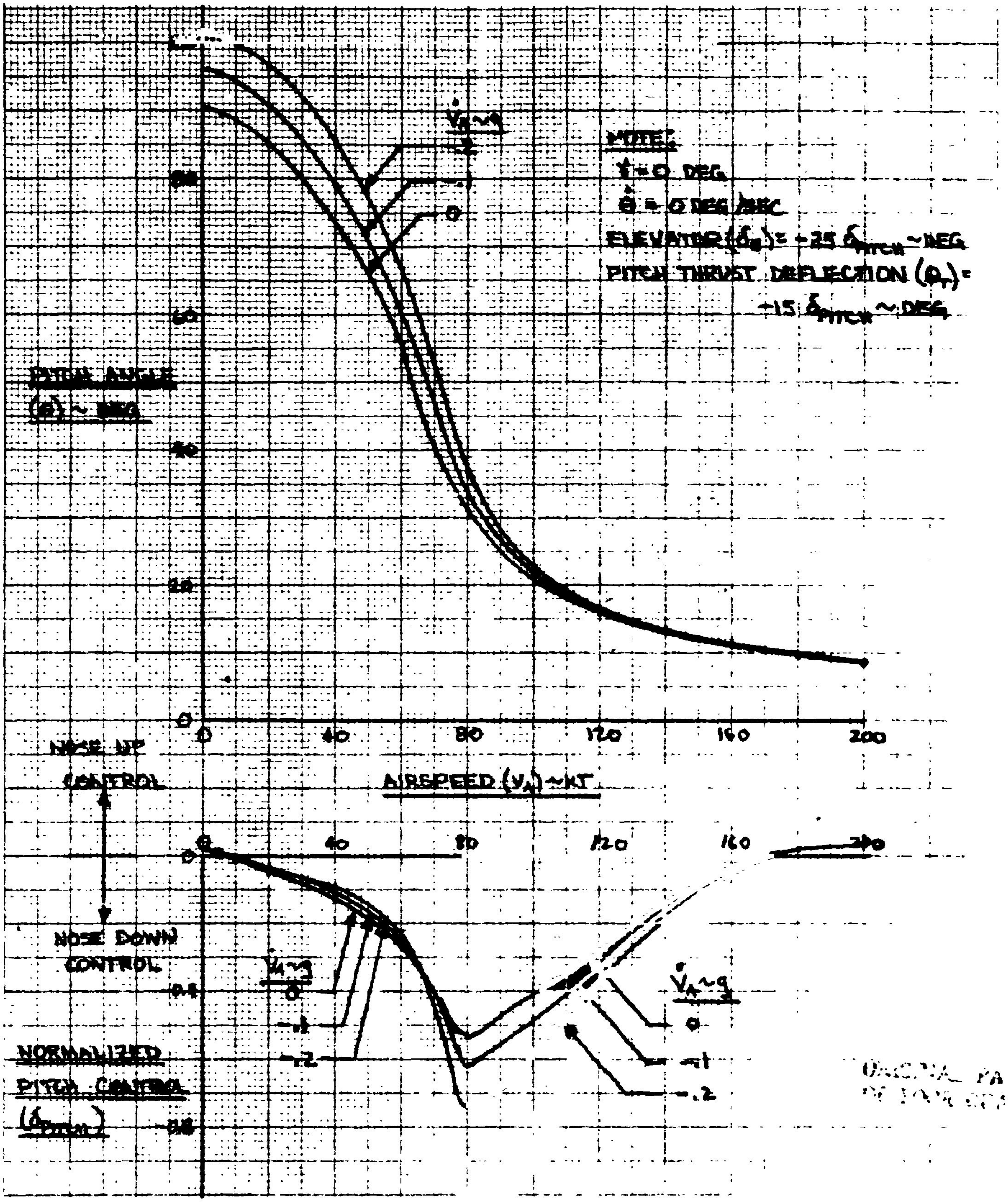

Figure 3-3. SF-121 Trim Requirements for Level Flight Decelerations (Sheet 1 of 2)

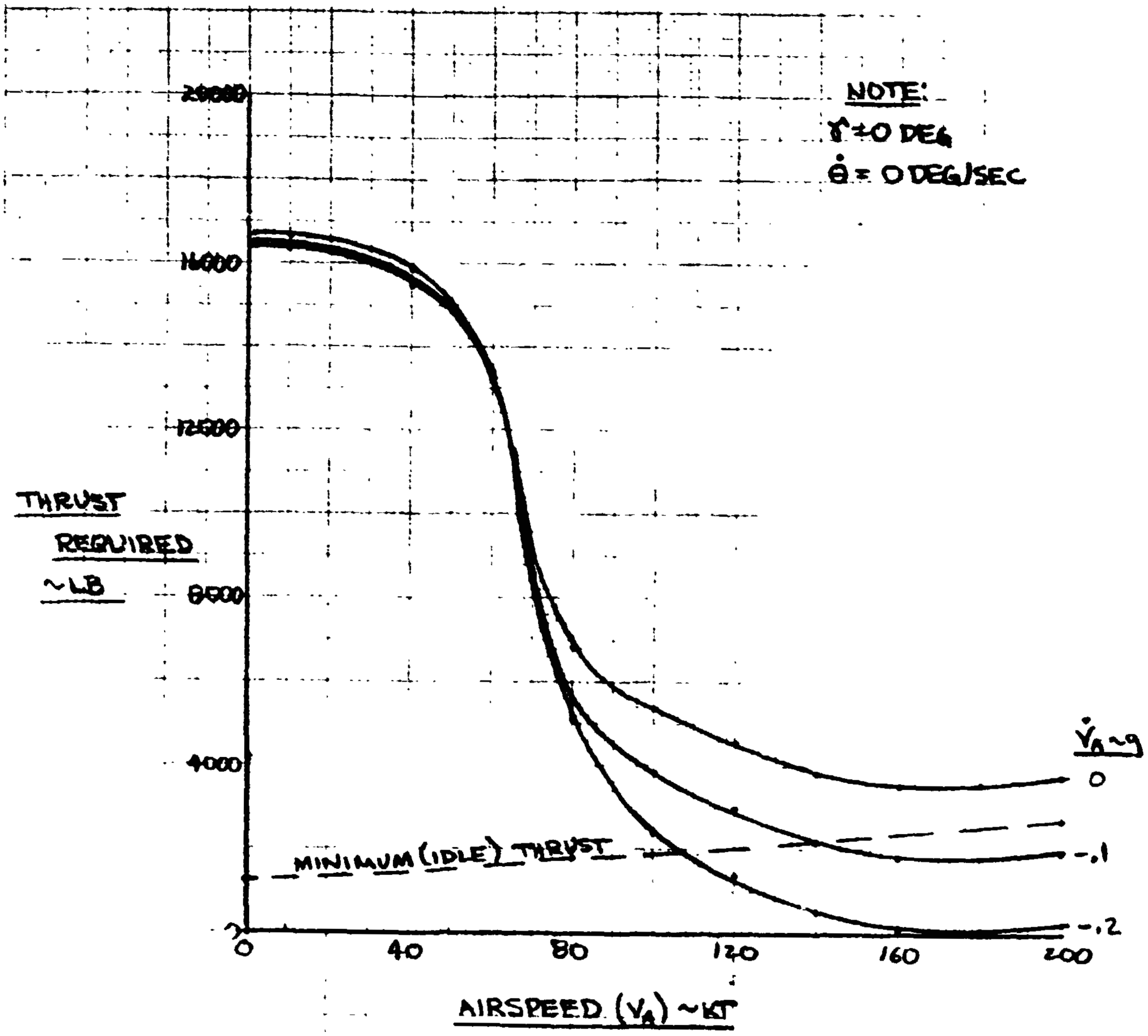

Figure 3-3. SF-121 Trim Requirements for Level Flight Decelerations (Sheet 2 of 2)

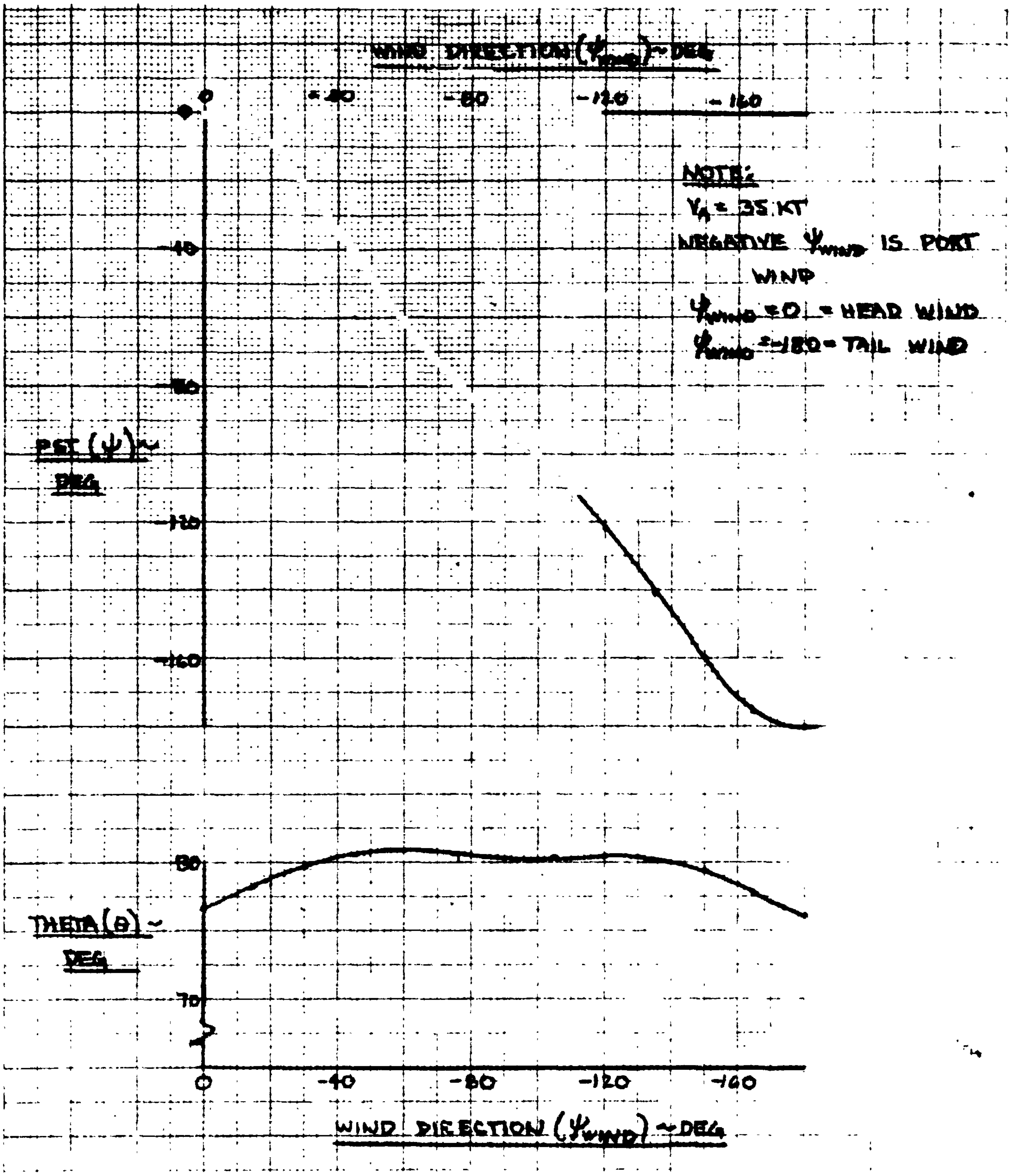

Figure 3-4. SF-121 Trim Requirements for Stationkeeping in a 35 kt Wind (Sheet 1 of 4)

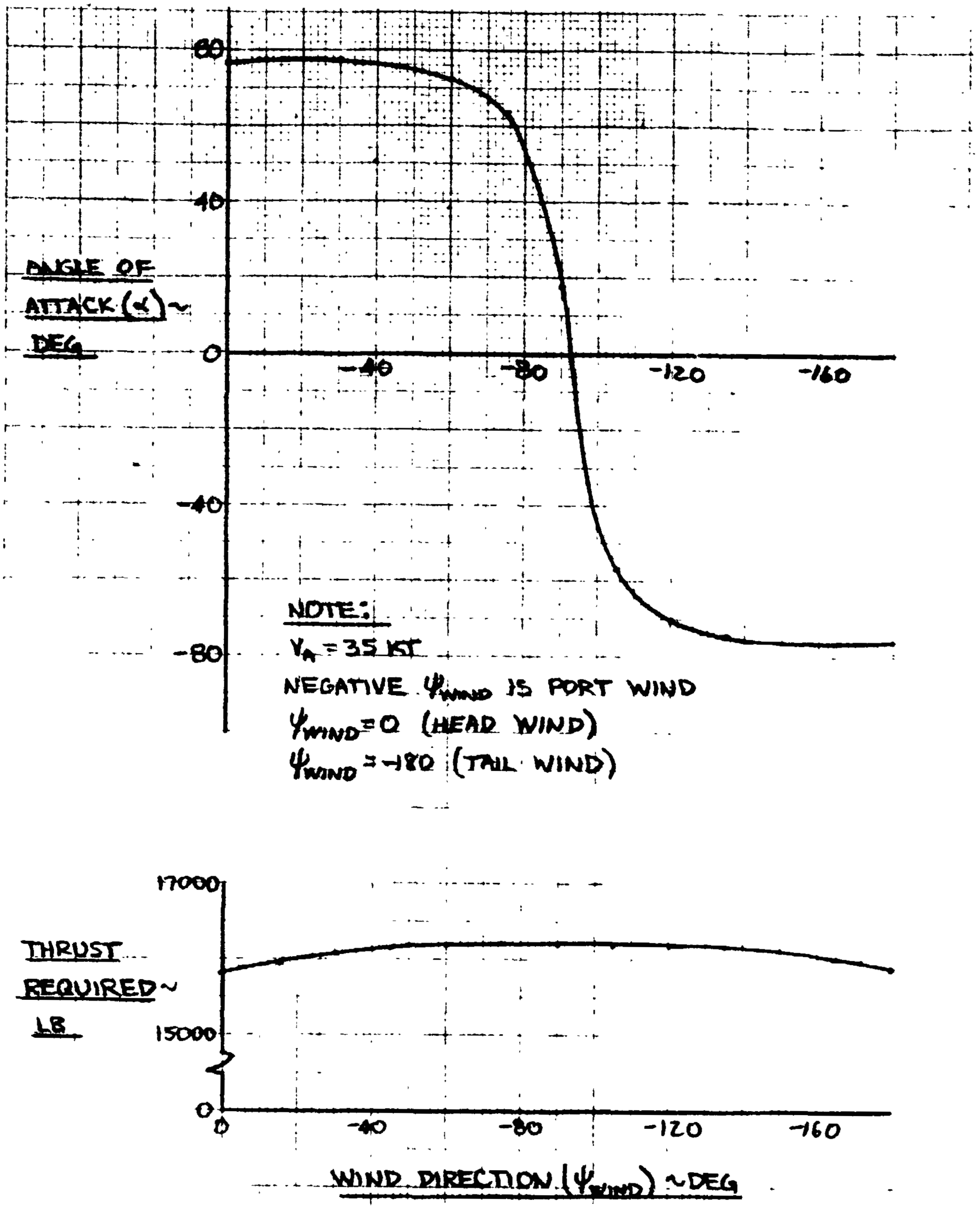

NOTE:
$V_A = 35$ KT
NEGATIVE ψ_{WIND} IS PORT WIND
$\psi_{WIND} = 0$ (HEAD WIND)
$\psi_{WIND} = -180$ (TAIL WIND)

Figure 3-4. SF-121 Trim Requirements for Stationkeeping in a 35 kt Wind (Sheet 2 of 4)

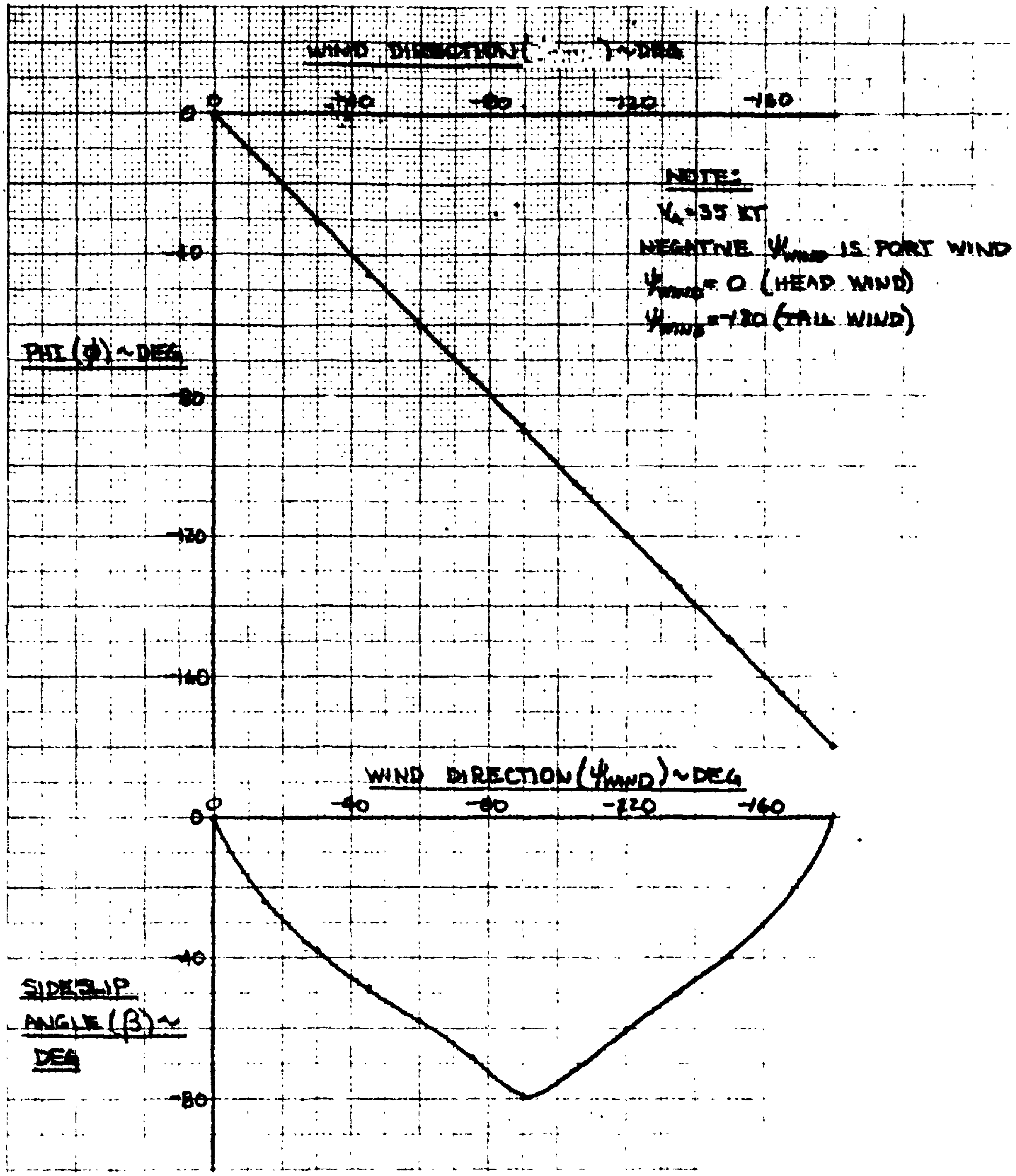

Figure 3-4. SF-121 Trim Requirements for Stationkeeping in a 35 kt Wind (Sheet 3 of 4)

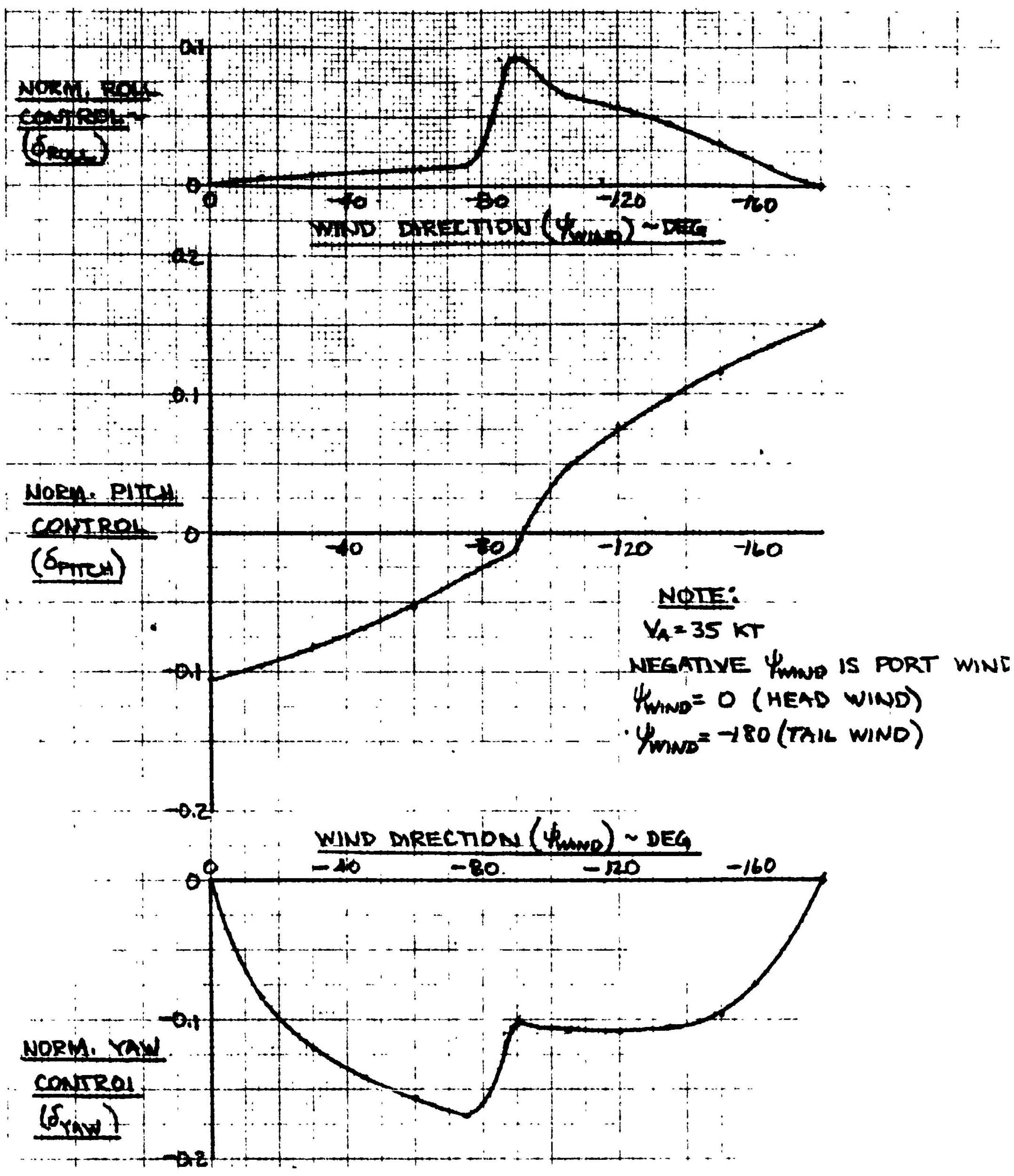

Figure 3-4. SF-121 Trim Requirements for Stationkeeping in a 35 kt Wind (Sheet 4 of 4)

The results of the trim characteristics evaluation have shown that the SF-121 has sufficient control power and that the actuator input specification of Section 3.5 is adequate. Thus no iterations were required of the actuator input specification design loop shown in figure 3-1. A more comprehensive trim analysis might have indicated a nonlinear blending of the elevon and pitch thrust deflections is better than the linear blending which has been adopted. For example, the elevon could be programmed to provide all the trim control power to as low speeds as possible. This would save thrust deflection for the maneuvering and gust regulation functions.

Another result of the trim characteristics evaluation was the selection of 60 kt as the switch point between the hover and conventional modes of the FCS. To obtain this result the transition trim data of figures 3-3 and 3-4 were examined using the following criteria:

- More than 50% of the aircraft weight supported by thrust (i.e. transition more than 50% complete). This occurs at approximately 65 kt.
- Since surge and sway control in hover are generically the same for the SF-121, similar capabilities and characteristics are desirable in the paired pitch/surge and yaw/sway degrees of freedom. Thus it was decided that pitch control margin and yaw control power should be approximately equal at and below the switch point. As shown by figure 3-5 this criterion is first met near 60 kt when the two control powers equal 0.7 rad/sec^2.

The final result of the trim characteristics evaluation was the provision of dimensional stability derivatives for developing the FCS laws and gains. These derivatives are an important by-product of VATLAS trim calculations; they are automatically generated at each trim point. Tables 3-7 and 3-8 summarize SF-121 derivatives at the speeds selected for FCS development. The derivatives are based on a transition trim along an unaccelerated straight and level flight path.

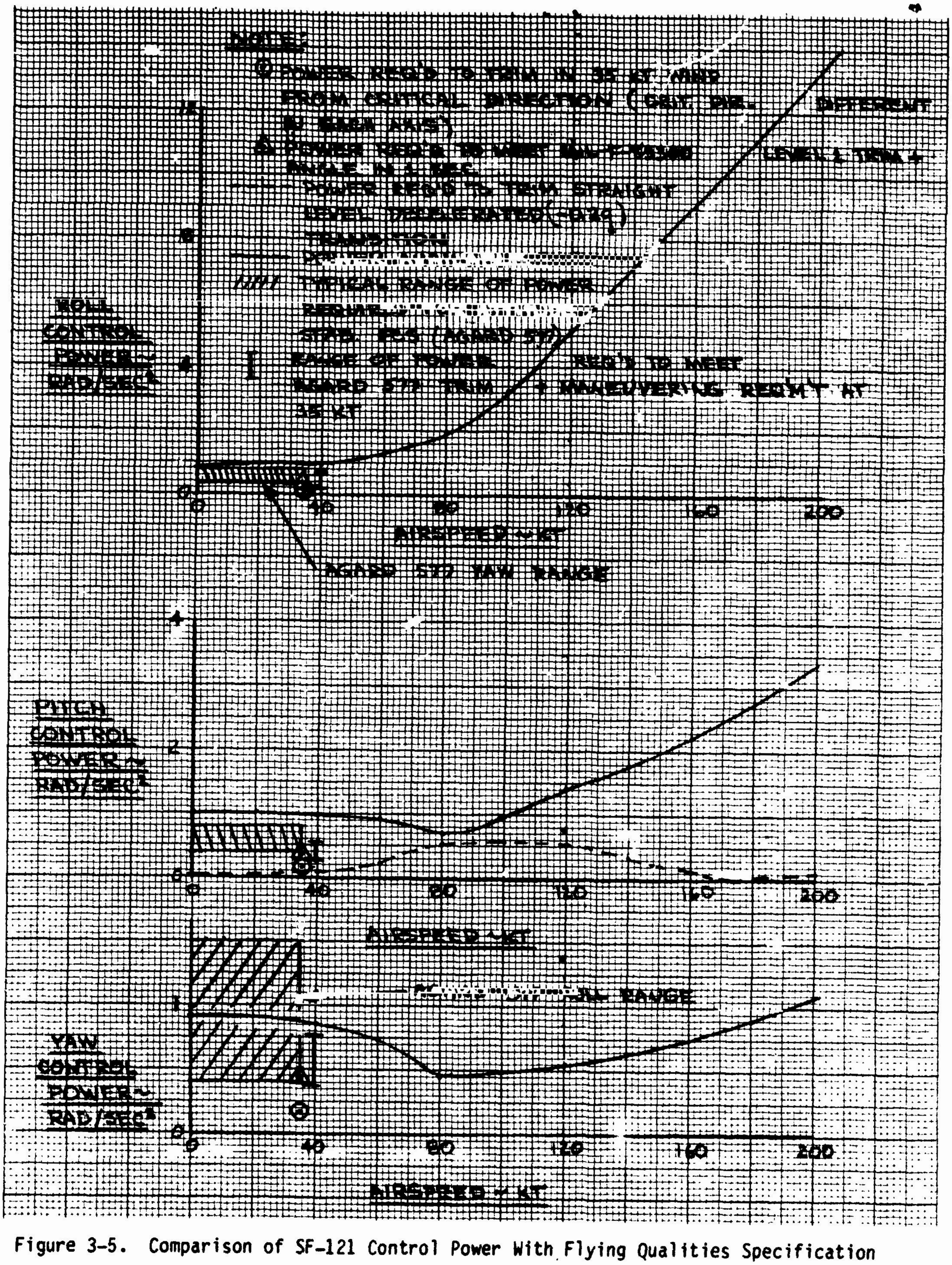

Figure 3-5. Comparison of SF-121 Control Power With Flying Qualities Specification Requirements

TABLE 3-7

SF-121 LONGITUDINAL STABILITY DERIVATIVES AT FLIGHT CONTROL SYSTEM DESIGN CONDITIONS

(Landing Weight, Level Flight)

TRIM AIRSPEED ~ KT / DERIVATIVE	200	120	80	60	40	10	0
-X derivatives							
X_u - ft/sec^2/ft/sec	-0.0222	-0.0253	-0.0243	0.0134	0.00035	-0.00869	-0.0168
X_w - ft/sec^2/ft/sec	0.1033	0.1202	0.1577	0.0204	0.0154	0.00412	0.00121
X_q - ft/sec^2/rad/sec	0.2936	0.3306	0.4900	-0.0464	-0.00558	0.0330	0.0413
X_{δ_e} - ft/sec^2/rad	13.75	-6.269	-1.136	1.141	0.34	0.0	0.0
X_{θ_T} - ft/sec^2/rad	0.539	-1.819	-3.558	-5.190	-5.008	-0.963	1.514
$X_{\Delta T}$ - ft/sec^2/lb	0.0036	0.0037	0.0038	0.0038	0.0039	0.0040	0.0040
-Z derivatives							
Z_u - ft/sec^2/ft/sec	-0.0597	-0.1377	-0.1871	-0.1294	-0.0565	-0.00265	0.00327
Z_w - ft/sec^2/ft/sec	-0.8944	-0.6039	-0.4148	-0.2805	-0.2181	-0.0730	-0.0303
Z_q - ft/sec^2/rad/sec	1.299	2.312	3.421	4.397	4.648	4.805	4.831
Z_{δ_e} - ft/sec^2/rad	-73.17	-24.65	-5.664	-2.573	-0.3221	0.0	0.0
Z_{θ_T} - ft/sec^2/rad	-7.332	-8.706	-12.842	-25.460	-30.16	-32.04	-32.10
$Z_{\Delta T}$ - ft/sec^2/lb	0.0	-0.0004	-0.0006	-0.0004	-0.0002	0.0	0.0
-M derivatives							
M_u - rad/sec^2/ft/sec	-0.00147	-0.00215	0.0001	0.00238	0.00291	0.00039	-0.00035
M_w - rad/sec^2/ft/sec	0.00881	0.0107	0.0050	0.00163	0.00116	0.00208	0.00252
M_q - rad/sec^2/rad/sec	-0.5245	-0.5002	-0.5100	-0.6151	-0.6507	-0.6513	-0.6471
M_{δ_e} - rad/sec^2/rad	-7.115	-2.569	-0.6576	-0.3082	-0.0500	0.0	0.0
M_{θ_T} - rad/sec^2/rad	-0.8842	-1.0478	-1.545	-3.064	-3.632	-3.860	-3.870
$M_{\Delta T}$ - rad/sec^2/lb	0.0	0.0	-0.0001	0.0	0.0	0.0	0.0

TABLE 3-8

SF-121 LATERAL DIRECTIONAL STABILITY DERIVATIVES AT FLIGHT CONTROL SYSTEM DESIGN CONDITIONS

(Landing Weight, Level Flight)

TRIM AIRSPEED ~ KT / DERIVATIVE	200	120	80	60	40	10	0
-Y derivatives							
Y_v - ft/sec^2/ft/sec	-0.2085	-0.1726	-0.1537	-0.0419	-0.0293	-0.0259	-0.0259
Y_p - ft/sec^2/rad/sec	-0.6127	-0.3692	-0.1619	-0.0380	-0.0411	-0.0421	-0.0422
Y_r - ft/sec^2/rad/sec	-1.603	-2.235	-3.059	-4.358	-4.708	-4.831	-4.834
Y_{δ_a} - ft/sec^2/rad	0.0	0.0	0.0	0.0	0.0	0.0	0.0
$Y_{\delta_{RCS}}$ - ft/sec^2/lb	0.0	0.0	0.0	0.0	0.0	0.0	0.0
Y_{δ_r} - ft/sec^2/rad	20.36	6.936	1.589	0.0	0.0	0.0	0.0
Y_{ψ_T} - ft/sec^2/rad	7.336	8.792	13.082	25.68	30.28	32.04	32.12
-L derivatives							
L_v - rad/sec^2/ft/sec	-0.0717	-0.0658	-0.0362	-0.00573	-0.00099	-0.00012	-0.00012
L_p - rad/sec^2/rad/sec	-1.658	-1.196	-1.198	-0.8609	-0.6870	-0.3575	-0.2561
L_r - rad/sec^2/rad/sec	0.8224	1.008	1.061	0.2168	0.0562	-0.0238	-0.0258
L_{δ_a} - rad/sec^2/rad	-28.73	-9.899	-2.348	-0.9328	-0.1115	0.0	0.0
$L_{\delta_{RCS}}$ - rad/sec^2/lb	-0.00090	-0.00095	-0.00107	-0.00139	-0.00151	-0.00156	-0.00156
L_{δ_r} - rad/sec^2/rad	6.293	2.144	0.4911	0.0	0.0	0.0	0.0
L_{ψ_T} - rad/sec^2/rad	0.0391	0.0474	0.0746	0.1392	0.1616	0.1708	0.1711
-N derivatives							
N_v - rad/sec^2/ft/sec	0.00099	-0.00384	-0.00976	-0.00578	-0.00365	-0.00238	-0.00235
N_p - ras/sec^2/rad/sec	0.0152	-0.00492	-0.00696	-0.0213	-0.0104	-0.00432	-0.00415
N_r - rad/sec^2/rad/sec	-0.5324	-0.5324	-0.5464	-0.6025	-0.6344	-0.6248	-0.6174
N_{δ_a} - rad/sec^2/rad	-0.7174	0.3077	0.0563	-0.0618	-0.1714	0.0	0.0
$N_{\delta_{RCS}}$ - rad/sec^2/lb	0.0	0.0	0.0	0.0	0.0	0.0	0.0
N_{δ_r} - rad/sec^2/rad	-1.990	-0.6781	-0.1553	0.0	0.0	0.0	0.0
N_{ψ_T} - rad/sec^2/rad	-0.7972	-0.9546	-1.417	-2.790	-3.292	-3.482	-3.490

3.7 Specification of Baseline FCS Laws and Gains

Linear analysis, supported by LINA, was applied to quantify the baseline FCS configuraton described in Section 3.3 and Table 3-6. Design analyses were performed at each of the speeds specified in Tables 3-7 and 3-8. The first step in these analyses was to calculate the unaugmented or bare airframe transfer functions using the stability derivatives in the tables. These airframe functions are given in Tables 3-9, 3-10, and 3-11.

Longitudinal (pitch and heave) FCS development will be discussed in Section 3.7.1 followed by lateral directional (roll and yaw) development in Section 3.7.2. Discussion of the hover FCS design details are focused on the $V_A = 10$ kt case while conventional FCS details are focused on the $V_A = 120$ kt case. The FCS for other speeds differs only in gain from the representative 10 and 120 kt cases.

Before the baseline FCS configuration (Table 3-6) could be quantified, several issues having general applicability to the design process had to be resolved. These were:

- How should FCS gains be scheduled
- What attitude signal should be fedback for attitude stabilization in the hover mode
- What are desirable bandwidths for the attitude stabilization and heave rate loops

The first issue was resolved in favor of gain scheduling as a function of airspeed. Pitch angle scheduling was considered but quickly eliminated; a wide range of pitch attitudes can be attained at any speed, thus a high probability of incompatible FCS gains exists with possibly disastrous consequences.

The issue of attitude feedback signals for hover stems from the discontinuity at $\theta = 90$ degrees in the Euler angle transformation. If the aircraft body axes are aligned with standard North-oriented inertial axes at $\theta = \phi = \psi = 0$ deg. then ϕ and ψ must change by 180 degrees to maintain the

TABLE 3-9

SF-121 UNAUGMENTED AIRCRAFT LONGITUDINAL TRANSFER FUNCTIONS

QUANTITY	AIRSPEED (V_A) ~ KT		
	200	120	80
Δ	1. (1.065)(-2.455) [-2.44, .148j; .163, .15]	1. (.985)(-2.037) [-.389, .203j; .188, .207]	1. (.339)(-1.239) [-.0246, .230j; .106, .231]
$N^{q}_{\delta_{PITCH}}$	3.336 (0)(-.0305)(-.978)	1.395 (0)(-.0372)(-.687)	.691 (0)(-.103)(-.379)
$N^{\dot{x}_e}_{\delta_{PITCH}}$	1.22 (-.822) [.0575, 10.21j; -.00563, 10.2]	6.62 (28.33)(-3.608)(-.430)	4.23 (2.048)(-2.921)(-.284)
$N^{\dot{z}_e}_{\delta_{PITCH}}$	34.37 (-6.00)(-.0128)(5.32)	11.68 (-4.329)(3.631)(.325)	4.26 (2.264)(-3.151)(.150)
$N^{q}_{\delta_{HEAV}}$	$7.79\mathrm{x}10^{-6}$ (0)(.810)(-1.017)	$-3.08\mathrm{x}10^{-5}$ (0) [-.506, .328j; .839, .603]	$-5.76\mathrm{x}10^{-5}$ (0) [-.243, .198j; .775, .314]
$N^{\dot{x}_e}_{\delta_{HEAV}}$	.00355 (1.073)(-2.477) (-.00695)	.00345 (.676)(-1.960)(.224)	.00286 (-.904) [.0669, .581j; -.114, .585]
$N^{\dot{z}_e}_{\delta_{HEAV}}$	$-5.42\mathrm{x}10^{-6}$ (.928) [-1.34, 1.62j; .638, 2.10]	-.00135 (1.708)(-2.758) (-.307)	-.00245 (.669)(-1.826) (.0310)

NOTE: δ_{PITCH} is dimensionless, δ_{HEAV} has units of lb

$(-\alpha)$ means 1st order root as $s = -\alpha$

$[-\zeta\omega_n, \omega_n\sqrt{1-\zeta^2}\ j;\ \zeta,\ \omega_n]$ means 2nd order root at $s = -\zeta\omega_n + \omega_n\sqrt{1-\zeta^2}\ j$

First number in box is root locus gain of tranfser function

TABLE 3-9 (CONTINUED)

SF-121 UNAUGMENTED AIRCRAFT LONGITUDINAL TRANSFER FUNCTIONS

QUANTITY	AIRSPEED (V_A) ~ KT		
	40	10	0
Δ	1. (-.610)(-.0845) [-.0868, .350j; .241, .369]	1. (-.780)(-.00969) [.0283, .293j; -.0961, .294]	1. (-.797)(-.0166) [.0596, .314j; -.187, .319]
$N^{q}_{\delta_{PITCH}}$	.973 (0)(-.223)(-.00828)	1.011 (0)(-.0899)(-.00905)	1.013 (0)(-.0166)(-.0515)
$N^{\dot{x}_e}_{\delta_{PITCH}}$	8.03 (1.442)(-2.633)(-.00377)	8.392 (1.445)(-2.675)(-.00880)	8.405 (1.449)(-2.678)(-.0169)
$N^{\dot{z}_e}_{\delta_{PITCH}}$	1.23 (-2.086) [.335, .919j; -.343, .978]	-.0105 (1.116) [1.763, 3.497j; -.450, 3.92]	.361 (-.858) [.190, 419j; -.413, .460]
$N^{q}_{\delta_{HEAV}}$	-8.23×10^{-6} (0)(-.201)(1.331)	-1.99×10^{-6} (0)(-.0623)(.718)	-2.44×10^{-7} (0)(-.00660) (-5.52)
$N^{\dot{x}_e}_{\delta_{HEAV}}$	9.18×10^{-4} (.361) [-.506, .801j; .534, .947]	7.53×10^{-5} (.424) [-.457, 1.046j; .401, 1.14]	2.96×10^{-6} (-4.533) [.00165, 1.799j; -.000916, 1.800]
$N^{\dot{z}_e}_{\delta_{HEAV}}$	-.00380 (-.670) [-.107, .386j; .267, .401]	-.00393 (-.780) [.0230, .293j; -.0951, .294]	-.00303 (-.797) [.0596, .313j; -.187, .319]

NOTE: δ_{PITCH} is dimensionless, δ_{HEAV} has units of lb

$(-a)$ means 1st order root as $s = -a$

$[-\zeta\omega_n, \omega_n\sqrt{1-\zeta^2}\,j; \zeta, \omega_n]$ means 2nd order root at $s = -\zeta\omega_n + \omega_n\sqrt{1-\zeta^2}\,j$

First number in box is root locus gain of tranfser function

TABLE 3-10

SF-121 UNAUGMENTED AIRCRAFT LATERAL DIRECTIONAL TRANSFER FUNCTIONS (V_A = 60, 80, 120 and 200 kt)

QUANTITY	AIRSPEED (V_A) ~ KT			
	200	120	80	60
Δ	1. [-.592, .0519j; .999, .593] [-.609, 1.735j; .331, 1.84]	1. [-.628, .322j; .89, .706] [-.324, 1.545j; .205, 1.58]	1. [-.878, .450j; .89, .986] [-.073, 1.020j; .0714, 1.020]	1. (-.836)(-.858) [.0941, .539j; -.172, .547]
$N^{p_s}_{\delta_{YAW}}$	-2.600 (0)(3.118)(-3.157)	-.777 (0)(3.563)(-3.010)	.0171 (0)(-37.27)(-4.242)	.573 (0) [-.589, .755j; .615, .958]
$N^{r_s}_{\delta_{YAW}}$	1.474 (-1.772) (.211, .934j; -.220, .958]	.789 (-1.526) [.332, .973j; -3.23, 1.030]	.503 (-1.312) [.346, .873j; -.368, .939]	.457 (-.936) [.192, .542j; -.334, .575]
$N^{\phi}_{\delta_{YAW}}$	-2.626 (3.118)(-3.157)	-.808 (3.563)(-3.010)	.0200 (-37.27)(-4.24	1.016 [-.589, .755j; .615, .958]
$N^{\hat{\beta}}_{\delta_{YAW}}$	-1.474 (.124)(-.280)(-1.366)	-.789 (.330)(-.436)(-.919)	-.503 (.693) [-.653, .248j; .935, .698]	-.457 (1.156) [-.500, .209j; .923, .542]
$N^{a_y}_{\delta_{YAW}}$	-10.81 (-2.882)(-1.416)(1.933) (.167)	-5.330 (-2.311)(-.949) [.682, .656j; -.721, .946]	-4.116 (-2.233)(-.827) [.498, .929j; -.472, 1.050]	-6.724 (-1.572)(-.639) [.137, .604j; -.221, .619]
$N^{p_s}_{\delta_{ROLL}}$	13.78 (0) [-.383, .928j; .382, 1.00]	5.489 (0)(-1.422)(.748)	2.233 (0)(-1.634)(.951)	1.419 (0)(-1.367)(.744)
$N^{r_s}_{\delta_{ROLL}}$	-1.728 (.72[illegible]) [-.581, .7[illegible]j; .607, .957]	-1.704 (-1.129) [.193, .692j; -.268, .719]	-1.385 (-1.138) [.215, .704j; -.292, .736]	-2.046 (-.921) [.132, .475j; -.267, .493]
$N^{\phi}_{\delta_{ROLL}}$	13.92 [-.383, .928j; .382, 1.00]	5.702 (0)(-1.422)(.748)	2.607 (-1.634)(.951)	2.517 (-1.367)(.744)
$N^{\hat{\beta}}_{\delta_{ROLL}}$	1.728 (-.235) [.479, .442j; .735, .652]	1.704 (-.0438) [-.616, .0853j; .991, .622]	1.385 (.146) [-.651, .352j; .880, .740]	2.046 (.281) [-.665, .419j; .846, .786]
$N^{a_y}_{\delta_{ROLL}}$	-9.003 (-13.12) [-.529, .413j; .788, .671]	-1.540 (-37.93)(-.636)(-.358)	-.158 (-180.7)(-.422)(-.305)	-.466 (-18.37)(-.238) (5.21×10^{-5})

NOTE: δ_{YAW} and δ_{ROLL} are dimensionless

(-a) means 1st order root at s = -a

[$-\zeta\omega_n$, $\omega_n\sqrt{1-\zeta^2}$ j; ζ, ω_n] means 2nd order root at $s = -\zeta\omega_n + \omega_n\sqrt{1-\zeta^2}\, j$

First number in box is root locus gain of transfer function

TABLE 3-11

SF-121 UNAUGMENTED AIRCRAFT LATERAL DIRECTIONAL TRANSFER FUNCTIONS (V_A = 60, 40, 10 and 0 kt)

QUANTITY	AIRSPEED (V_A) - KT			
	60	40	10	0
Δ	1. (-.836)(-.858)(0) [.0941, .539j; -.172, .547]	1. (-.893)(-.637)(0) [.0893, .375j; -.231, .386]	1. (-.357)(-.773)(0) [.0611, .309j; -.194, .315]	1. (-.256)(-.766)(0) [.0163, .308j; -.195, .314]
$N^{p}_{\delta_{YAW}}$	-.0548 (.327)(4.321)(-1.511) (0)	-.0643 (-.844)(0) [.631, .416j; -.835, .755]	-.0679 (-.880)(0) [.0354, .333j; -.193, .339]	-.0681 (-.894)(0) [.0609, .329j; -.182, .334]
$N^{r}_{\delta_{YAW}}$	.731 (-.275)(0) [-.341, .529j; .542, .629]	.862 (-.578)(0) [-.0860, .107j; .625, .138]	.912 (-.347)(-.0140) (-.0448)(0)	.914 (-.254)(.00236) (-.0522)(0)
$N^{\dot{Y}_e}_{\delta_{YAW}}$	-6.724 (-2.441)(1.435) [-.466, .625j; .598, .780]	-7.930 (-2.508)(-.556) (1.374)(-.144)	-8.39 (-2.531)(-.346) (1.382)(-.0114)	-8.41 (-2.527)(-.255) (1.385)(-.00153)
$N^{p}_{\delta_{ROLL}}$	2.492 (-1.080)(0) [.216, .307j; -.576, .375]	2.309 (-.886)(0) [.111, .338j; -.312, .356]	2.334 (-.774)(0) [.0616, .308j; -.196, .314]	2.340 (-.766)(0) [.0613, .308j -.195, .314]
$N^{r}_{\delta_{ROLL}}$	.0208 (-.218)(-7.283) (7.841)(0)	.00362 (-.146)(0) [-5.097, 11.11j; .417, 12.2]	-.00819 (-.0652)(0) [-.603, 3.316j; .179, 3.37]	-.00821 (.0738)(0) [-.642, .902j; .589, 1.11]
$N^{\dot{Y}_e}_{\delta_{ROLL}}$	-.127 (-1.525)(.820) (92.82)	-.203 (-1.461)(.721) (85.42)	-.0588 (-2.210)(1.499) (15.47)	-.0590 (-11.05) [-.384, .558j; .567, .677]

NOTE: δ_{YAW} and δ_{ROLL} are dimensionless

$(-a)$ means 1st order root at $s = -a$

$[-\zeta\omega_n,\ \omega_n\sqrt{1-\zeta^2}\,j;\ \zeta,\ \omega_n]$ means 2nd order root at $s = -\zeta\omega_n + \omega_n\sqrt{1-\zeta^2}\,j$

First number in box is root locus gain of transfer function consistency of the transformation as the aircraft X_B axis goes through vertical. These large angle changes would be imposed in the appropriate feedback paths and produce cockpit motions which are disorienting to the pilot: For example, to slow down in surge the pilot simply pulls back on the stick to bring the aircraft nose through vertical. He doesn't command or expect cockpit roll or yaw motions during this maneuver. With Euler angle feedbacks based on the standard North-oriented inertial axes the pilot will experience uncommanded cockpit yaw and roll motions which (if control isn't lost and/or the pilot doesn't punch out) will place him in the orientation he expects. Analysis of this problem indicated that uncommanded cockpit motions could be avoided in hover by feeding back the integrals of body axis roll, pitch, and yaw rates as attitude feedbacks. (Also, the rotated inertial axis system discussed in Section 2.9 could be applied.) Thus the attitude feedback issue was resolved as follows: feedback the integrals of body rates in the FCS hover mode and standard Euler angles in the FCS conventional mode. In addition, the body rate integrators must be initialized to equal Euler angles upon switching to hover mode. Similarly, upon switching to conventional mode, the trim systems must be reinitialized to avoid discontinuities in attitude feedbacks.

Desired attitude loop bandwidth was set at 3.0 rad/sec. This selection was based on experimental evidence (references (l) and (m)) that pilots strive for closed loop bandwidths of approximately 3.0 rad/sec when they manually close the loop. This provides adequate separation between the flight path and attitude modes of the aircraft and allows the pilot to attain reasonable manual closures of the flight path control loops. In addition to reducing pilot workload, a 3.0 rad/sec attitude bandwidth also provides good regulation against distrubances.

Desired heave rate bandwidth was set at 1.5 rad/sec. Similar to the attitude bandwidth selection, this rate bandwidth allows the pilot to easily close the manual heave position loop in the desired bandwidth range of 0.7 to 1.0 rad/sec.

An issue of lesser importance to quantifying the baseline FCS was the specification of parameter values for the pilot input shaping networks in the rate command-attitude hold and attitude command systems. Even though these parameter values will be established via the piloted simulator studies, initial "guess" values are required at this point in the design process. Therefore the first order lag in the attitude command system input shaping network was set at 4.0 rad/sec in accordance with Vought experience while the breakpoint of the lead term in the rate command-attitude hold systems input shaping network was set at 3.0 rad/sec which was used in reference (e). Also in accordance with reference (e) input command authority was set to ± 15 deg. for the attitude command systems and ± 20 deg/sec for the rate command-attitude hold systems.

3.7.1 Longitudinal FCS Development

The baseline configuration for the pitch control system is shown in figure 3-6. The values adopted for many of the generic pitch control system parameters are evident in a comparison of figures 2-28 and 3-6. The baseline heave control system is essentially the same as the generic system shown in figure 2-30. Most features of these configurations have already been discussed in Sections 3.3 and 3.7. The functional descriptions which follow are intended as a review but provide additional details where required.

The forward path of the pitch FCS consists of a straight gain (K_{q_e}) and a parallel integrator (gain = $K_{q_{e_{I1}}}$) that provides automatic trim and boosts the low frequency gain of the loop. K_{q_e} is programmed as a function of airspeed. The feedbacks in the hover mode include pitch rate through a gain (K_{q_q}) in parallel with the integral of pitch rate (q_{INT}). In the conventional mode the feedbacks include pitch rate through K_{q_q} in parallel with pitch angle (θ). The pitch FCS has two pilot inputs, the longitudinal stick trim button ($\delta_{q_{BUT}}$) and longitudinal stick deflection (δ_{LNGSTK}). In the hover mode, δ_{LNGSTK} is input through a gain (K_{q_c}) and first order shaping network (time constant = τ_{PITCH}). In the conventional mode, δ_{LNGSTK} is input through K_{q_c} and a parallel integrator (gain = $K_{q_{c_I}}$);

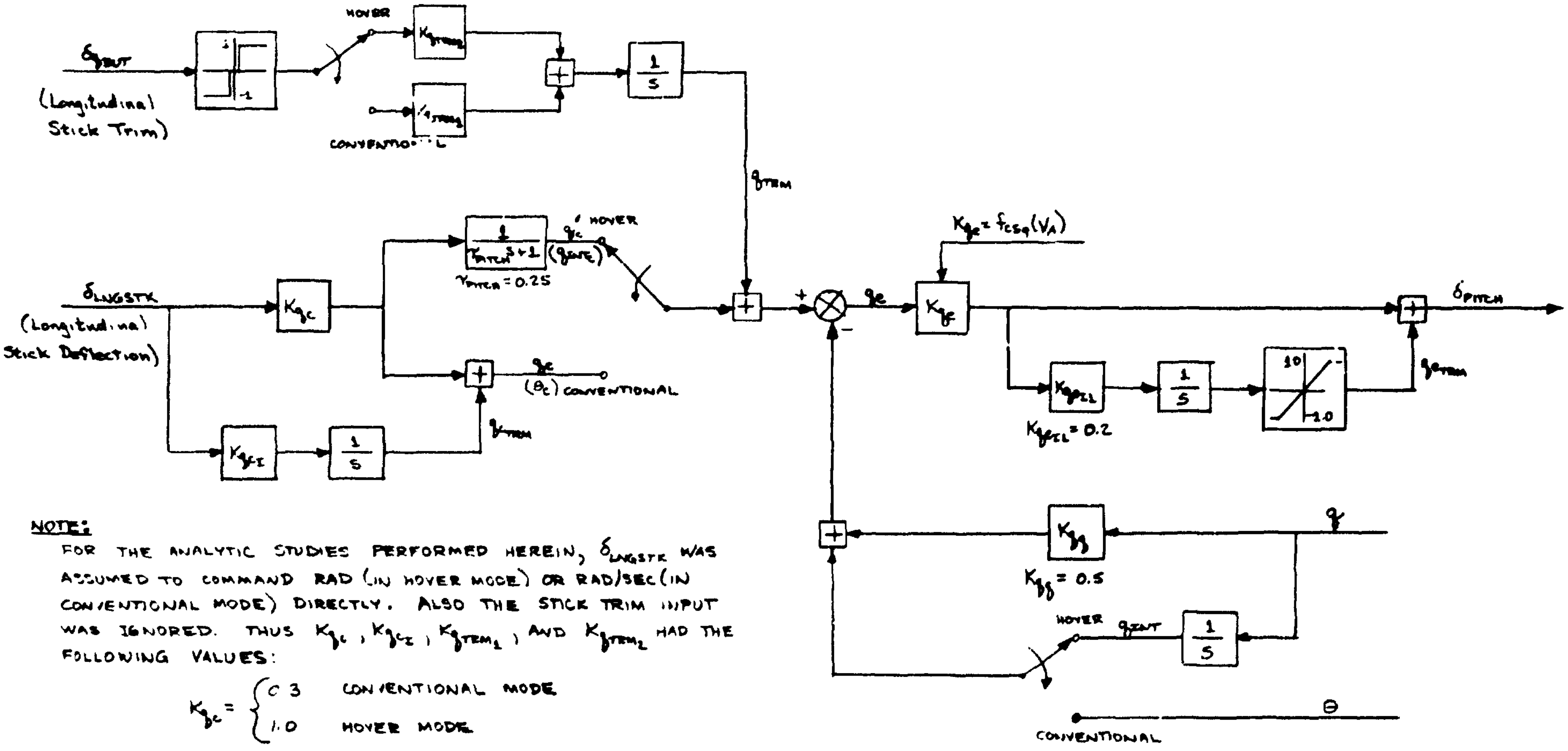

NOTE:

FOR THE ANALYTIC STUDIES PERFORMED HEREIN, δ_{LNGSTK} WAS ASSUMED TO COMMAND RAD (IN HOVER MODE) OR RAD/SEC (IN CONVENTIONAL MODE) DIRECTLY. ALSO THE STICK TRIM INPUT WAS IGNORED. THUS K_{q_c}, $K_{q_{cI}}$, $K_{q_{TRM_1}}$, AND $K_{q_{TRM_2}}$ HAD THE FOLLOWING VALUES:

$$K_{q_c} = \begin{cases} 0.3 & \text{CONVENTIONAL MODE} \\ 1.0 & \text{HOVER MODE} \end{cases}$$

$K_{q_{cI}} = 1.0$; $K_{q_{TRM_1}} = K_{q_{TRM_2}} = 0.0$

Figure 3-6. SF-121 Baseline Pitch Flight Control System

τ_{PITCH} is zeroed. Thus, δ_{LNGSTK} commands are proportional to the integral of pitch rate (q_{INT_c}) in the hover mode and to pitch rate (q) in the conventional mode. Logic for initializing the pitch rate integrator, manual trim integrator, and pitch input integrator at the FCS mode switch point is based on that indicated on figure 2-28.

The heave FCS is operative only in the hover mode. In conventional mode the pilot controls thrust directly with manual throttle. In hover mode he normally controls heave (and thus thrust) through his heave rate command lever. Manual throttle is available during hover but its use would likely be limited to emergency conditions requiring sudden large changes in thrust. Similar to the pitch FCS, the forward path of the heave FCS has a straight gain (K_{z_e}) in parallel with an integrator (gain = $K_{z_{e_I}}$) for automatic trim and low frequency gain boost. The feedback is heave rate which is compared with the heave rate command lever inputs to form the forward path error signal. It will be demonstrated in Section 3.8 that the performance of both modes of the pitch and heave FCS laws and gains developed here is adequate. Thus there was no need to iterate the laws and gains loop of the FCS design procedure (figure 3-1). Complete specification of the SF-121 baseline pitch and heave FCS gains is given in Sections 3.8.3 and 3.8.5, respectively, of Volume II.

3.7.1.1 Hover Mode System Analysis

A root locus sketch of the pitch FCS hover mode loop closure at $V_A = 10$ kt as a function of K_{q_e} is shown in figure 3-7. The zero at $s = -0.2 = -K_{q_{e_{I1}}}$ and pole at the origin result from the forward path compensation. The zero at $s = -2.0 = -1/K_{q_q}$ results from the pitch rate feedback gain and was placed to effect a good closed loop damping ratio (0.7 - 0.8) at the desired system bandwidth (approximately 3.0 rad/sec). With the exception of the elevon and pitch thrust deflection actuators both having poles at s = -20, the other open loop poles and zeros are those of the unaugmented airplane q_{INT}/δ_{PITCH} transfer function. As can be seen, the selected K_{q_e} (= 10/rad) provides dominant closed loop roots which appear to provide a larger than desired system bandwidth. As indicated by the closed loop

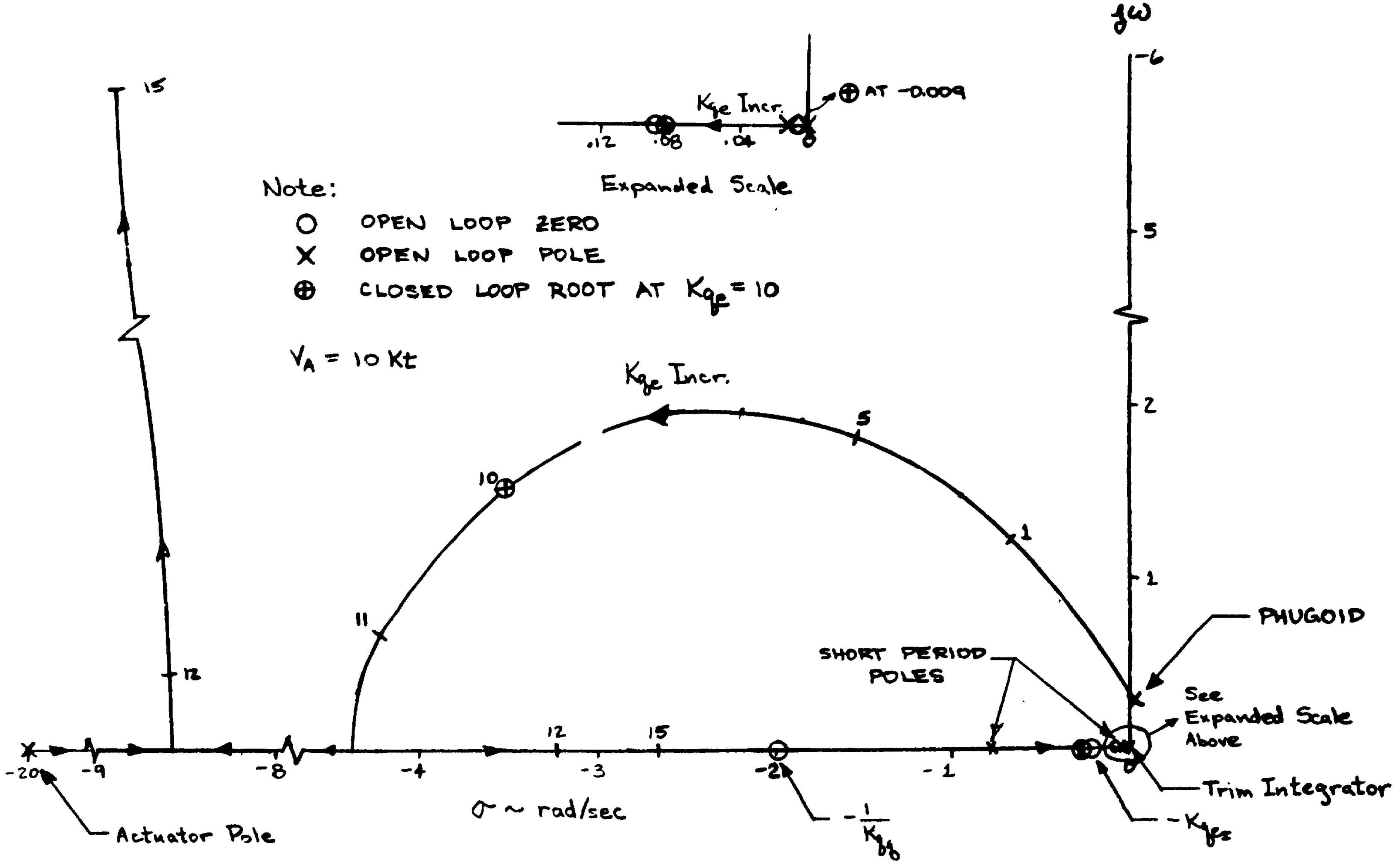

Figure 3-7. Root Locus of Pitch FCS Hover Mode Loop Closure

q_{INT}/q_{INT_c} frequency response (figure 3-9), this is not the case. The equivalent closed loop bandwidth is 2.8 rad/sec which is slightly less than desired.

A root locus sketch of the heave FCS loop closure at $V_A = 10$ kt with the pitch FCS hover mode loop closed is shown in figure 3-8. The forward path gain ($K_{\dot{Z}_e}$) varies along the locus. The zero at $s = -0.2 = -K_{\dot{Z}_{e_I}}$ and pole at the origin result from the forward path compensation. The pole at $s = -5.0$ represents the thrust dynamics at the trim thrust setting. The remaining "open loop" pole at $s = -.00905$ is the only one of the $\dot{Z}_e/\delta_{HEAVE}|q_{INT}, q \to \delta_{PITCH}$ transfer function poles not effectively cancelled by zeros. The designation, $\dot{Z}_e/\delta_{HEAVE}|q_{INT}, q \to \delta_{PITCH}$, indicates the $\dot{Z}_e/\delta_{HEAVE}$ transfer function which results when the pitch FCS loop is closed (i.e. q_{INT} and q are fedback to δ_{PITCH}). The value of $K_{\dot{Z}_e}$ selected ($=$ 500 lb/ft/sec) provides a heave rate loop bandwidth of 1.41 rad/sec which is acceptably close to the desired 1.5 rad/sec bandwidth. This is demonstrated by the closed loop $\dot{Z}_e/\dot{Z}_{e_c}$ frequency response in figure 3-10.

3.7.1.2 Conventional Mode System Analysis

A root locus sketch of the pitch FCS conventional mode loop closure at $V_A = 120$ kt as a function of K_{q_e} is shown in figure 3-11. The zero at $s = -0.2 = -K_{q_{e_{I1}}}$ and pole at the origin result from the forward path compensation. The zero at $s = -2.0 = -1/K_{q_q}$ results from the pitch rate feedback gain and was placed to obtain a closed loop bandwidth of approximately 3.0 rad/sec. With the exception of the elevon and pitch thrust deflection actuators both having poles at $s = -20$, the other open loop poles and zeros are those of the unaugmented airplane θ/δ_{PITCH} transfer function. Note the unstable short period pole which arises from the static instability designed into the SF-121. As confirmed by the θ/θ_c frequency response (figure 3-12), the selected K_{q_e} ($=$ 7./rad) provides a 3.15 rad/sec attitude bandwidth. The θ/θ_c frequency response does not include the effects of the longitudinal stick shaping network [(s + 3.33)/s] which makes the conventional mode pitch FCS a rate command-attitude hold system.

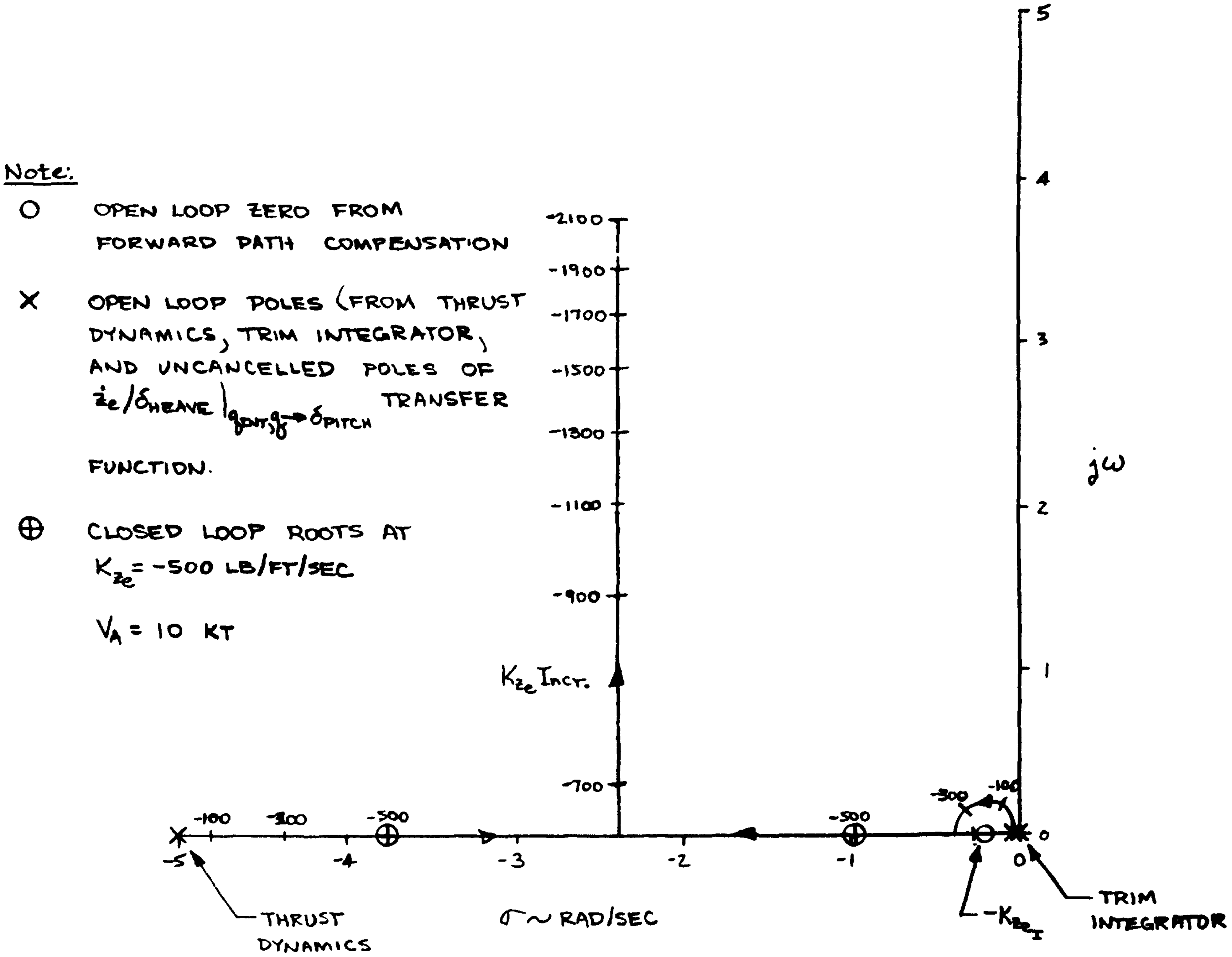

Figure 3-8. Root Locus of Heave FCS Loop Closure With Pitch FCS Hover Mode Loop Closed

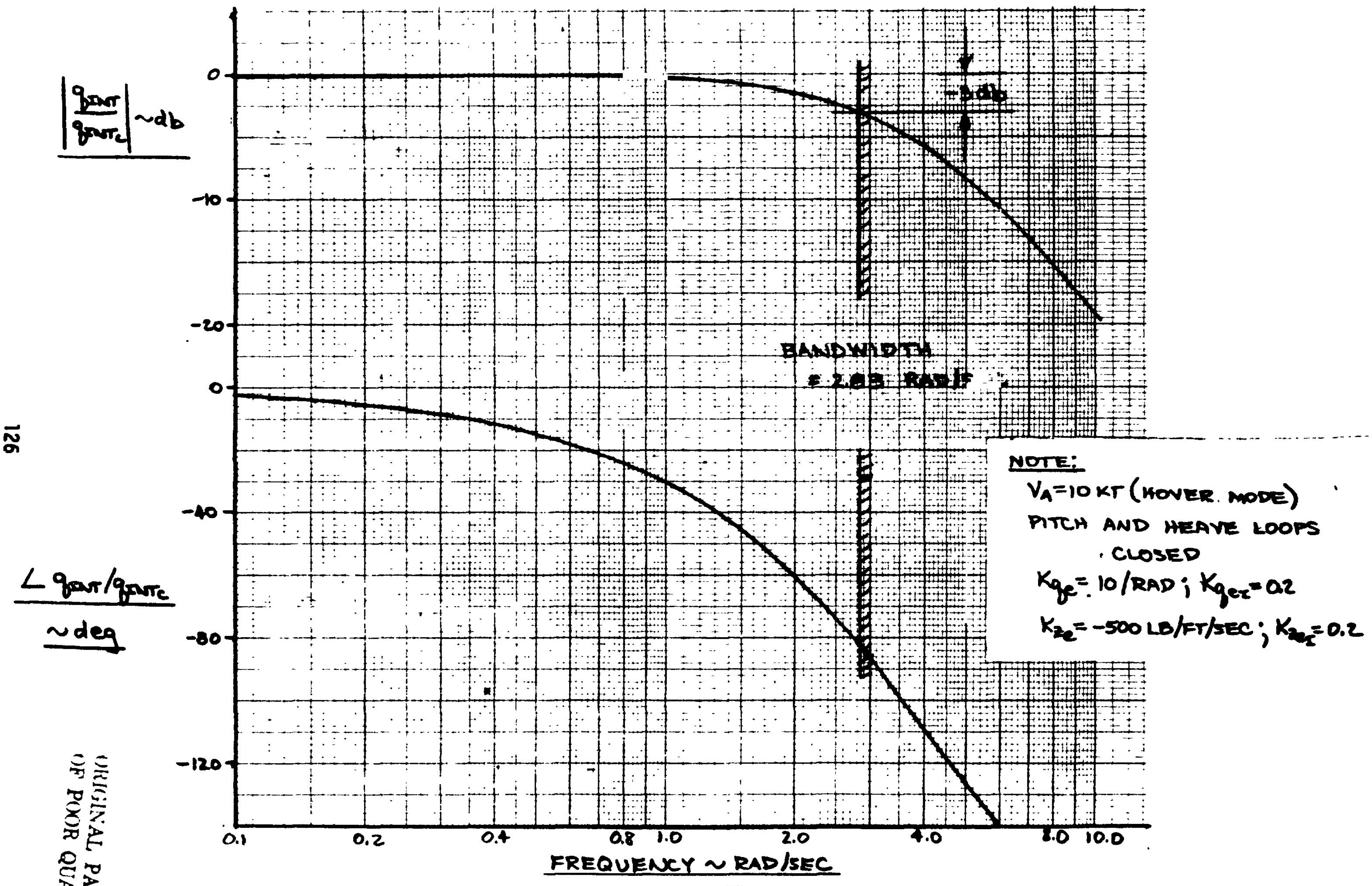

Figure 3-9. Frequency Response of Pitch FCS in Hover Mode

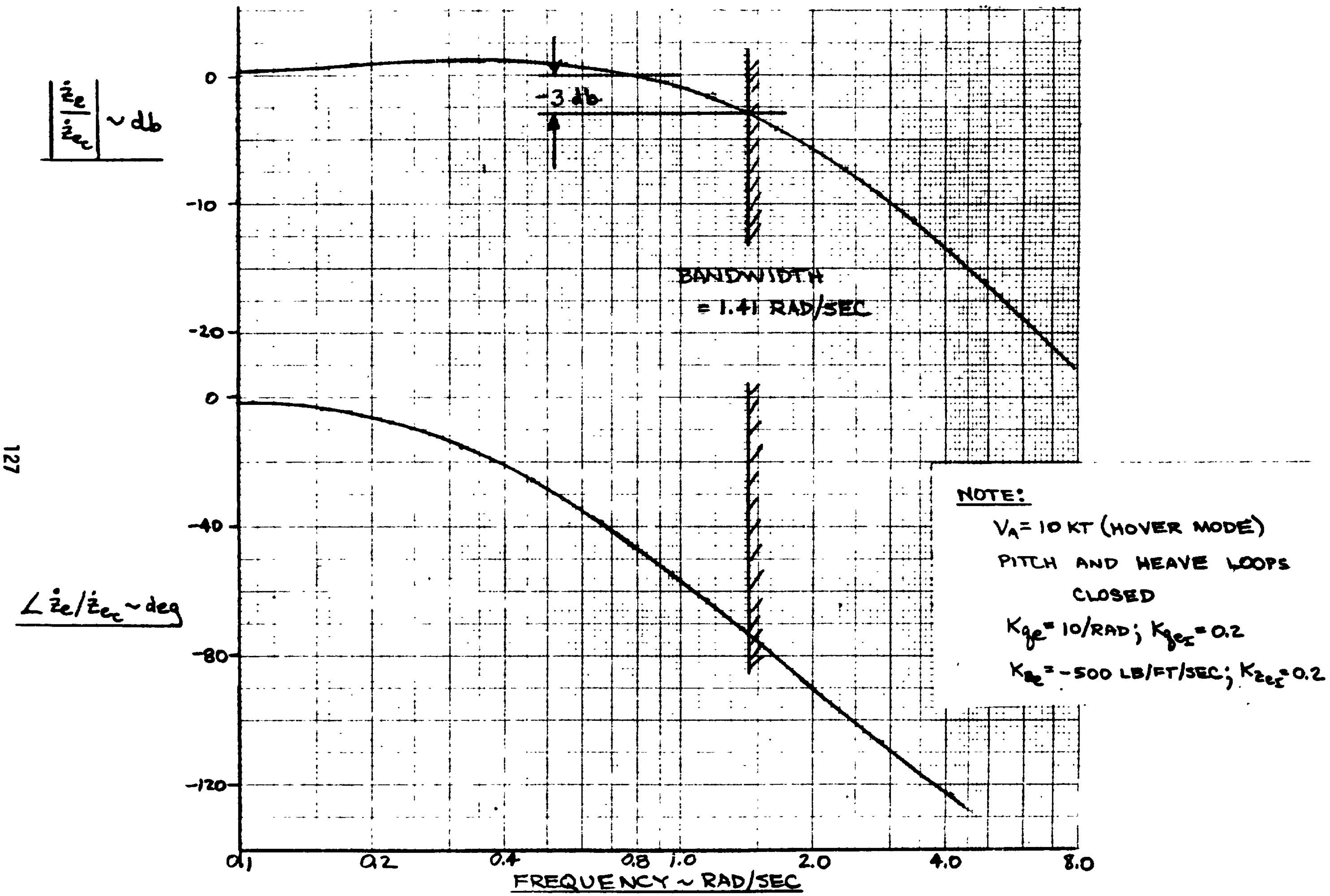

Figure 3-10. Frequency Response of Heave FCS in Hover Mode

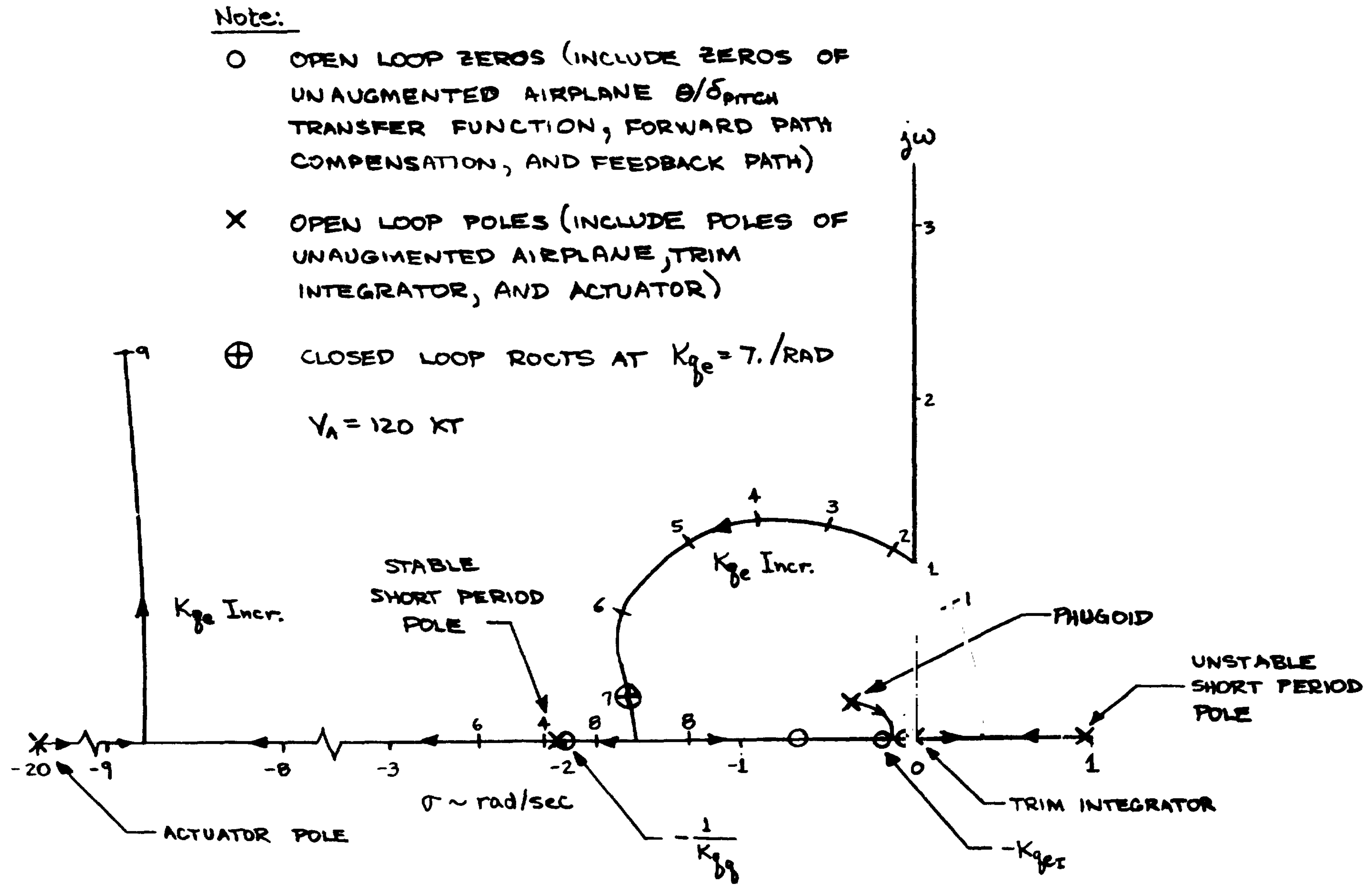

Figure 3-11. Root Locus of Pitch FCS Conventional Mode Loop Closure

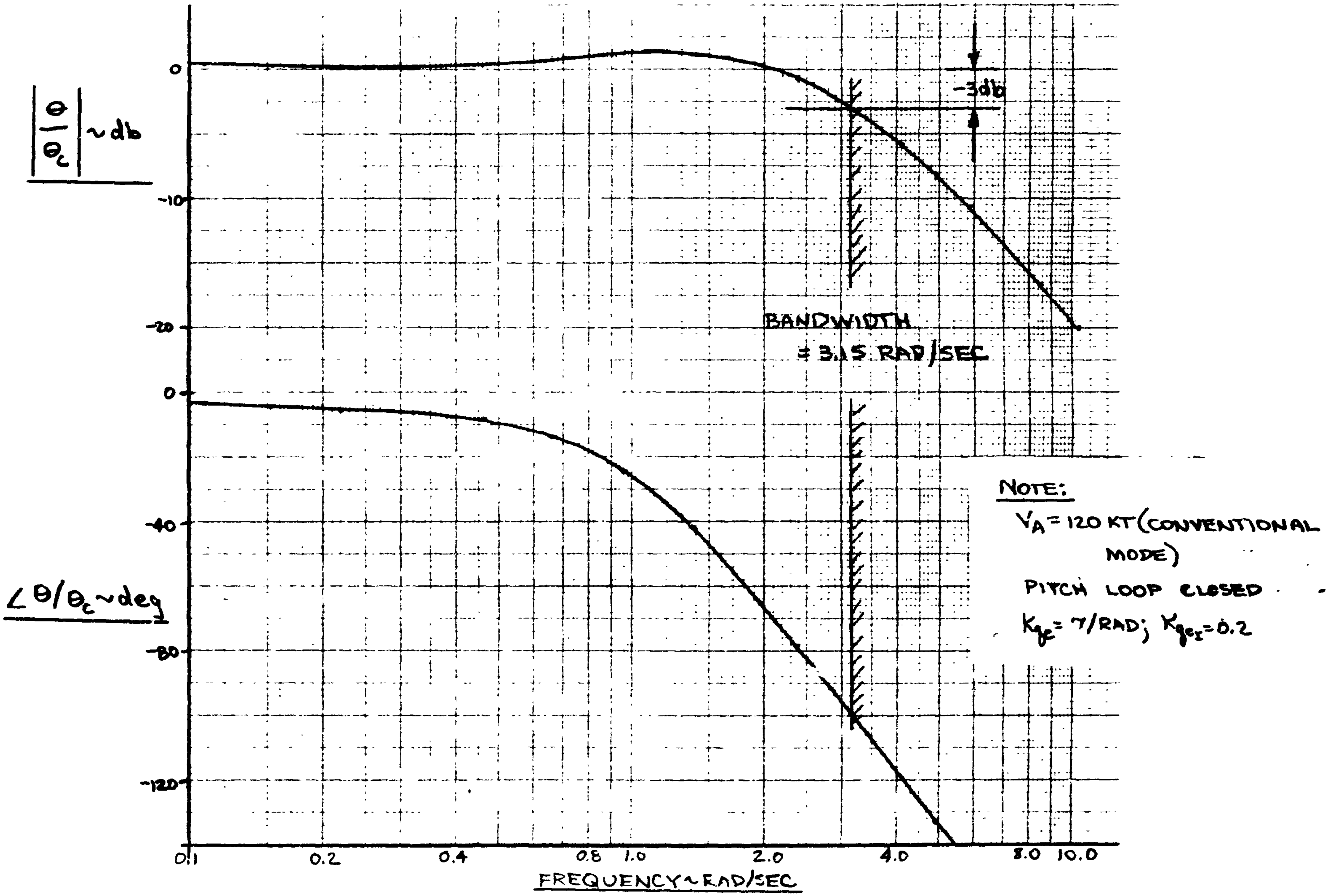

Figure 3-12. Frequency Response of Pitch FCS in Conventional Mode

3.7.2 Lateral FCS Development

Baseline configurations for the roll and yaw control systems are shown in figures 3-13 and 3-14 respectively. The values adopted for many of the generic roll and yaw control system parameters are evident in comparisons of figure 2-27 and 3-13 and of figures 2-29 and 3-14. Many features of these configurations have been discussed in Sections 3.3 and 3.7. The functional descriptions which follow are intended as a review but provide additional details where required.

The forward path of the roll FCS consists of a straight gain (K_{p_e}) and a parallel integrator (gain = $K_{p_{e_{I1}}}$) that provides automatic trim and boosts the low frequency gain of the loop. K_{p_e} is programmed as a function of airspeed while $K_{p_{e_I}}$ is a function of control system mode. The feedbacks in the hover mode include body axis roll rate through a gain (K_{p_p}) in parallel with the integral of body axis roll rate (p_{INT}). In the conventional mode the roll FCS feedbacks are stability axis roll rate through K_{p_p} in parallel with roll angle (ϕ).

The forward path of the yaw FCS is identical in function to that of the roll FCS except the gains are K_{r_e} and $K_{r_{e_{I1}}}$. Similar to the roll FCS, K_{r_e} is programmed as a function of airspeed while $K_{r_{e_{I1}}}$ is a function of control system mode. The feedbacks in the hover mode include body axis yaw rate through a gain (K_{r_r}) in parallel with the integral of body axis yaw rate (r_{INT}). The feedbacks in the conventional mode reflect requirements imposed by the bare airframe lateral characteristics of the SF-121 (Table 3-10). The airplane has a coupled roll-spiral mode and an inadequate relation between the numerator of the r_s/δ_{yaw} transfer function and the Dutch roll mode. The coupled roll-spiral mode is decoupled by a lateral acceleration (a_y) to δ_{yaw} feedback through a gain (K_{a_y}). The latter characteristic makes pure r_s feedback ineffective as a yaw damper and resulted in the adoption of a pseudo - $\dot{\beta}$ ($\hat{\beta} = (g/V_A)\,\phi - r_s$) to δ_{yaw} feedback. The use of $\hat{\beta}$ as a yaw damper as well as a turn coordinator is described in reference (e).

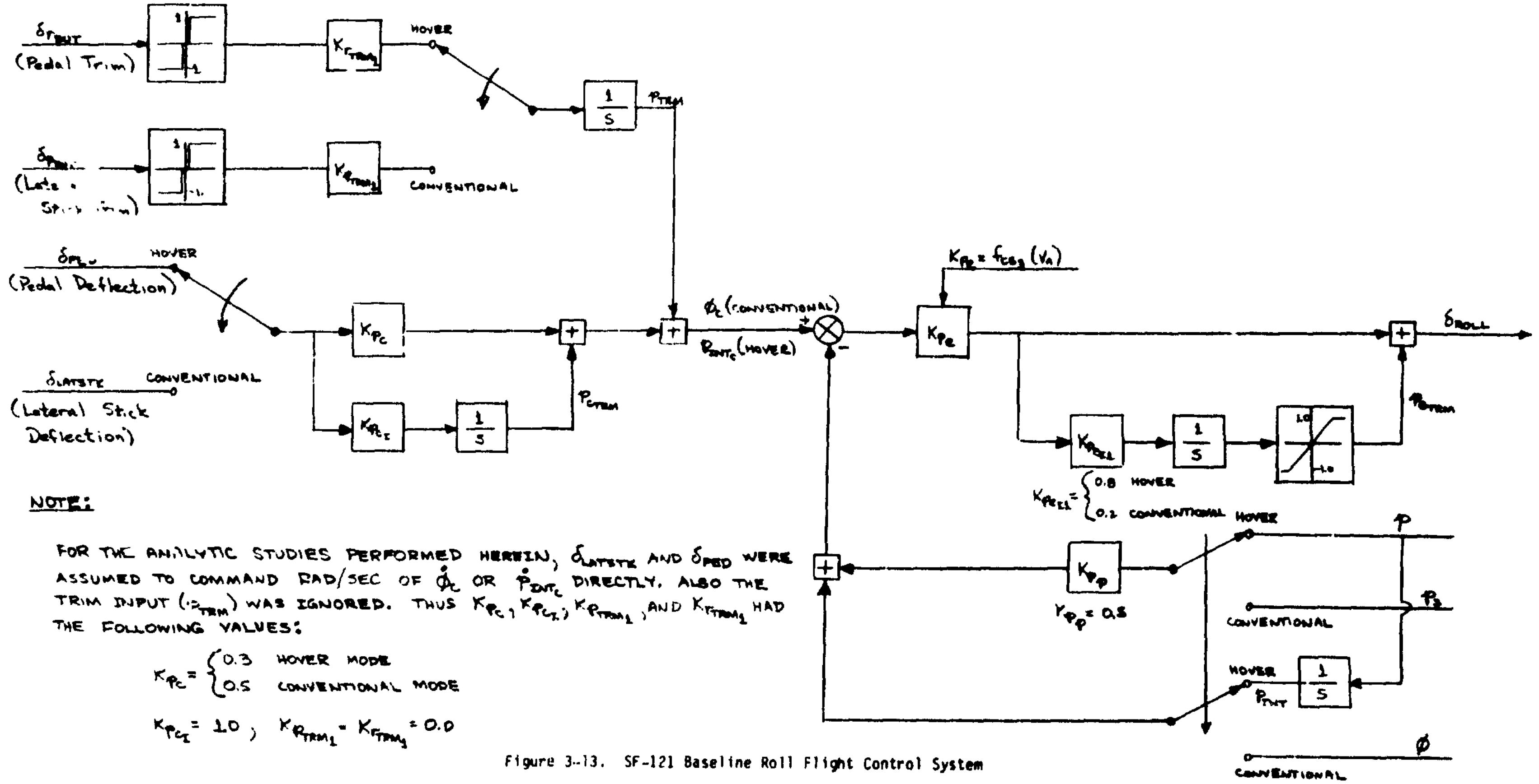

NOTE:

FOR THE ANALYTIC STUDIES PERFORMED HEREIN, δ_{LATSTK} AND δ_{PED} WERE ASSUMED TO COMMAND RAD/SEC OF $\dot{\phi}_c$ OR $\dot{P}_{INT_c}$ DIRECTLY. ALSO THE TRIM INPUT (P_{TRM}) WAS IGNORED. THUS K_{P_C}, $K_{P_{C_I}}$, $K_{P_{TRM_1}}$, AND $K_{r_{TRM_1}}$ HAD THE FOLLOWING VALUES:

$$K_{P_C} = \begin{cases} 0.3 & \text{HOVER MODE} \\ 0.5 & \text{CONVENTIONAL MODE} \end{cases}$$

$$K_{P_{C_I}} = 1.0 \,, \quad K_{P_{TRM_1}} = K_{r_{TRM_1}} = 0.0$$

Figure 3-13. SF-121 Baseline Roll Flight Control System

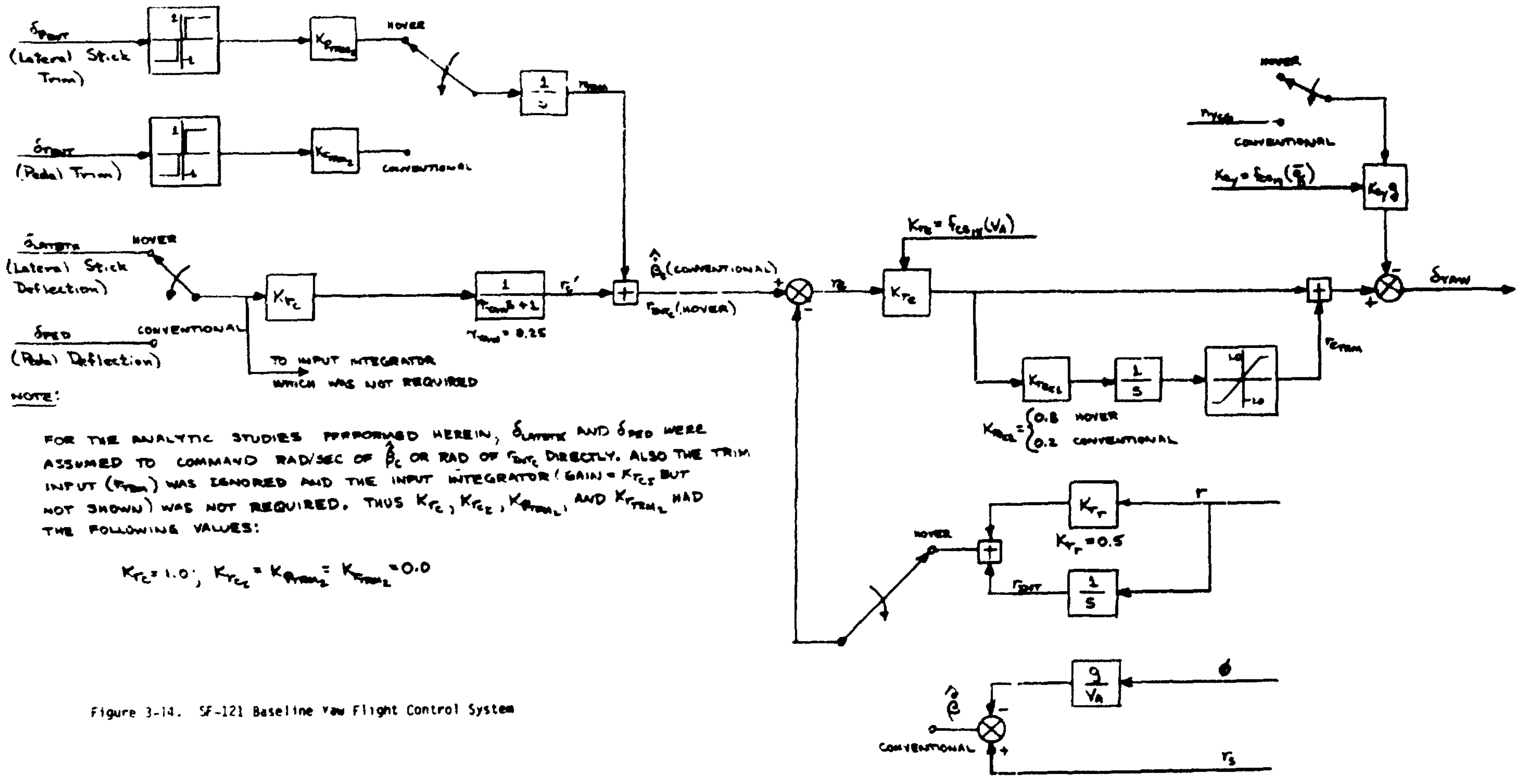

NOTE:

FOR THE ANALYTIC STUDIES PERFORMED HEREIN, δ_{LATSTK} AND δ_{PED} WERE ASSUMED TO COMMAND RAD/SEC OF $\hat{\beta}_c$ OR RAD OF r_{INT_c} DIRECTLY. ALSO THE TRIM INPUT (r_{TRIM}) WAS IGNORED AND THE INPUT INTEGRATOR (GAIN = $K_{r_{CI}}$ BUT NOT SHOWN) WAS NOT REQUIRED. THUS K_{r_C}, $K_{r_{CI}}$, $K_{P_{TRIM_2}}$, AND $K_{r_{TRIM_2}}$ HAD THE FOLLOWING VALUES:

$$K_{r_C} = 1.0; \quad K_{r_{CI}} = K_{P_{TRIM_2}} = K_{r_{TRIM_2}} = 0.0$$

Figure 3-14. SF-121 Baseline Yaw Flight Control System

The lateral FCS has four pilot controller inputs - lateral stick trim button ($\delta_{p_{BUT}}$), pedal trim ($\delta_{r_{BUT}}$), lateral stick deflection (δ_{LATSTK}), and pedal deflection (δ_{PED}). The roles of these inputs are a function of FCS mode: In the hover mode, the roll FCS receives inputs from δ_{PED} and $\delta_{r_{BUT}}$ while the yaw FCS receives inputs from δ_{LATSTK} and $\delta_{p_{BUT}}$. In the conventional mode, the controller roles are reversed - δ_{PED} and $\delta_{r_{BUT}}$ become yaw FCS inputs and δ_{LATSTK} and $\delta_{p_{BUT}}$ become roll FCS inputs. The roll FCS is rate command-attitude hold in both modes. Thus, δ_{PED} in hover and δ_{LATSTK} in conventional are interfaced with the roll FCS through a gain (K_{p_c}) and a parallel integrator (gain = $K_{p_{c_I}}$). The yaw FCS in conventional mode is a pseudo-$\dot{\beta}$ command system. The pedals are thus interfaced with the yaw FCS through a gain (K_{r_c}) and input filter (time constant = τ_{YAW}). Note that, except for deliberate sideslips, the pilot should not have to use pedals in the coventional mode. In hover mode the yaw FCS is a r_{INT_c} command system; δ_{LATSTK} is interfaced through K_{r_c} and the input filter.

Logic for initializing the yaw and roll rate integrators and the trim inputs at the FCS mode switch point is based on that indicated on figures 2-27 and 2-29. This logic helps to smooth the mode change transients. Its effectiveness is demonstrated in Section 3.8.

It will also be shown in Section 3.8 that the performance of both modes of the yaw and roll FCS laws and gains developed here is adequate. Thus there was no need to iterate the laws and gains loop of the FCS design procedure (figure 3-1). Complete specification of the SF-121 baseline yaw and roll FCS gains is given in Sections 3.8.2 and 3.8.4, respectively, of Volume II.

3.7.2.1 Hover Mode System Analysis

A root locus sketch of the yaw FCS hover mode loop closure at $V_A = 10$ kt is shown in figure 3-15. The forward path gain (K_{r_e}) varies along the locus. The zero at $s = -0.8 = -K_{r_{e_{I1}}}$ and one of the poles at the origin

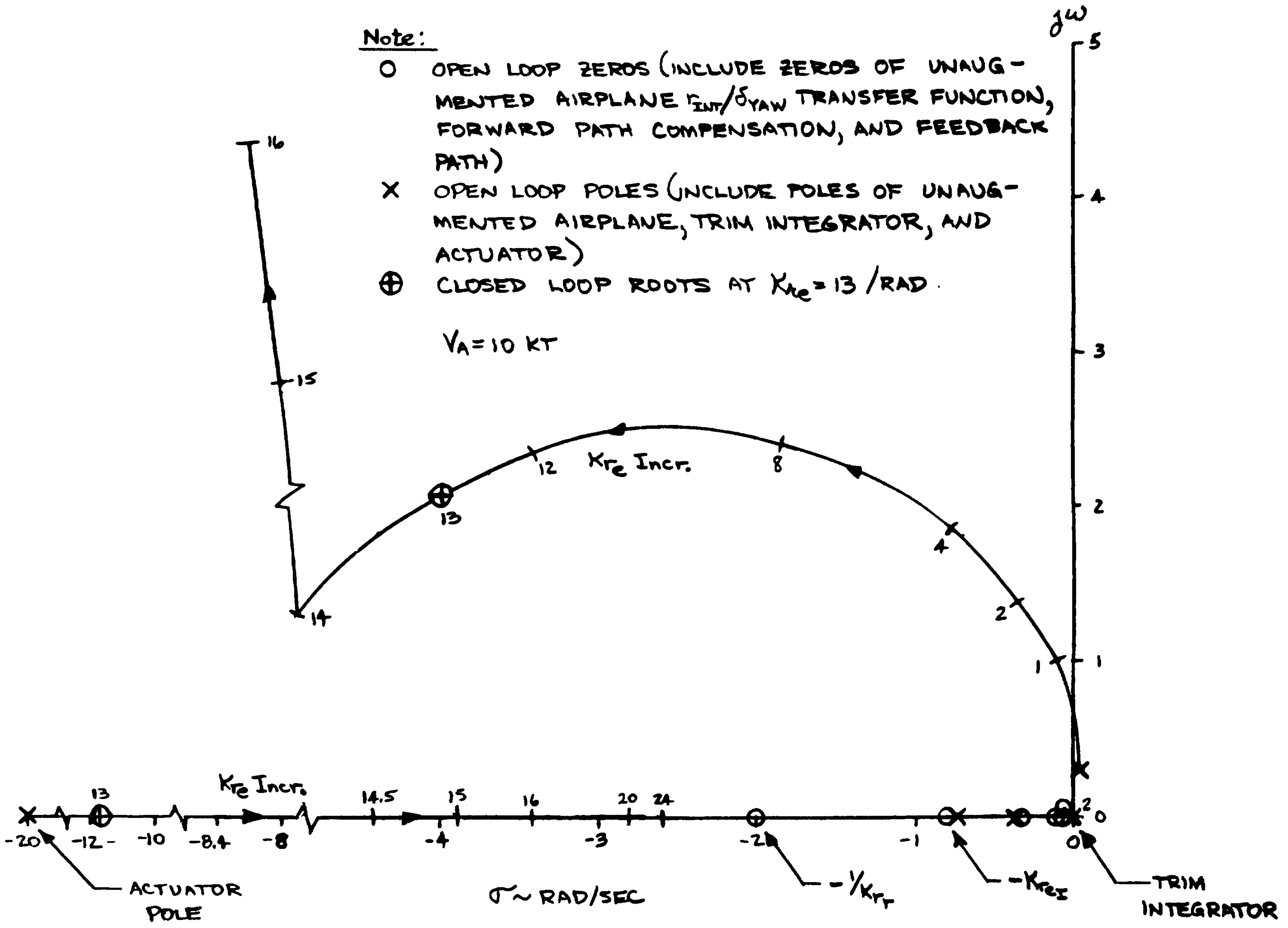

Figure 3-15. Root Locus of Yaw FCS Hover Mode Loop Closure

arise from the forward path compensation. The zero at $s = -2.0 = -1/K_{r_r}$ results from the body axis yaw rate feedback and was placed to provide good loop closure properties. The actuator pole at $s = -20.$ represents the dynamics of the rudder and yaw thrust deflection actuators. The remaining open loop poles and zeros are those of the unagumented airplane r_{INT}/δ_{YAW} transfer function. The selected closed loop gain ($K_{r_e} = 13/\text{rad}$) in combination with the roll FCS loop closure (depicted in figure 3-16) is demonstrated by the r_{INT}/r_{INT_c} frequency response (figure 3-17) to produce an attitude bandwidth of 3.24 rad/sec.

The root locus of the roll FCS hover mode closure at $V_A = 10$ kt with the yaw FCS loop closed is shown in figure 3-16. Equivalently to the yaw loop, the roll loop forward path gain (K_{p_e}) varies along the locus; the zero at $s = -0.8 = -K_{p_{e_{I1}}}$ and the pole at the origin arise from the forward path compensation; and the zero at $s = -2.0 = -1/K_{p_p}$ results from the body axis roll rate feedback. The remaining "open loop" poles and zeros are those of the $p_{INT}/\delta_{ROLL}\Big|_{r_{INT}, r \rightarrow \delta_{YAW}}$ transfer function which do not effectively cancel each other. Actuator dynamics are not indicated in the locus sketch due to their negligible influence. The selected closed loop gain ($K_{p_e} = 6/\text{rad}$) is demonstrated by the p_{INT}/p_{INT_c} frequency response (figure 3-18) to produce an attitude bandwidth of 3.32 rad/sec. This frequency response plot does not include the effects of the pedals shaping network $[(s + 3.33)/s]$ which makes the hover mode roll FCS a rate command-attitude hold system.

3.7.2.2 Conventional Mode System Analysis

As mentioned above, the SF-121 has a coupled roll-spiral mode at the airspeeds considered in this FCS development. Traditional design guidelines for lateral control law development (also the flying qualities specification) prohibit this coupling. The first task in the lateral FCS conventional mode development therefore was to decouple the roll and spiral modes. This was accomplished by a lateral acceleration (a_y) to δ_{YAW} feedback. Figure 3-19

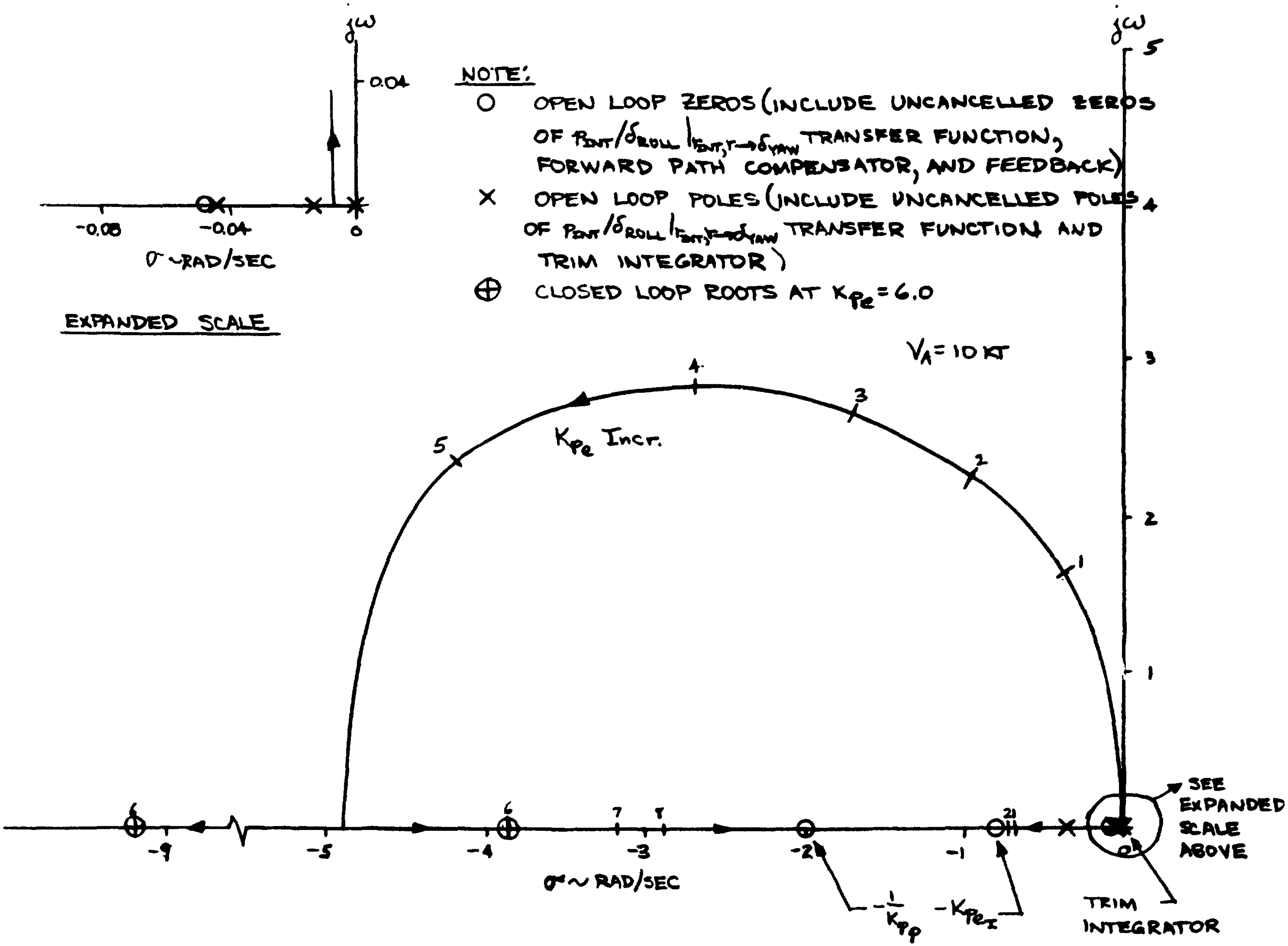

Figure 3-16. Root Locus of Roll FCS Hover Mode Loop Closure With Yaw FCS Loop Closed

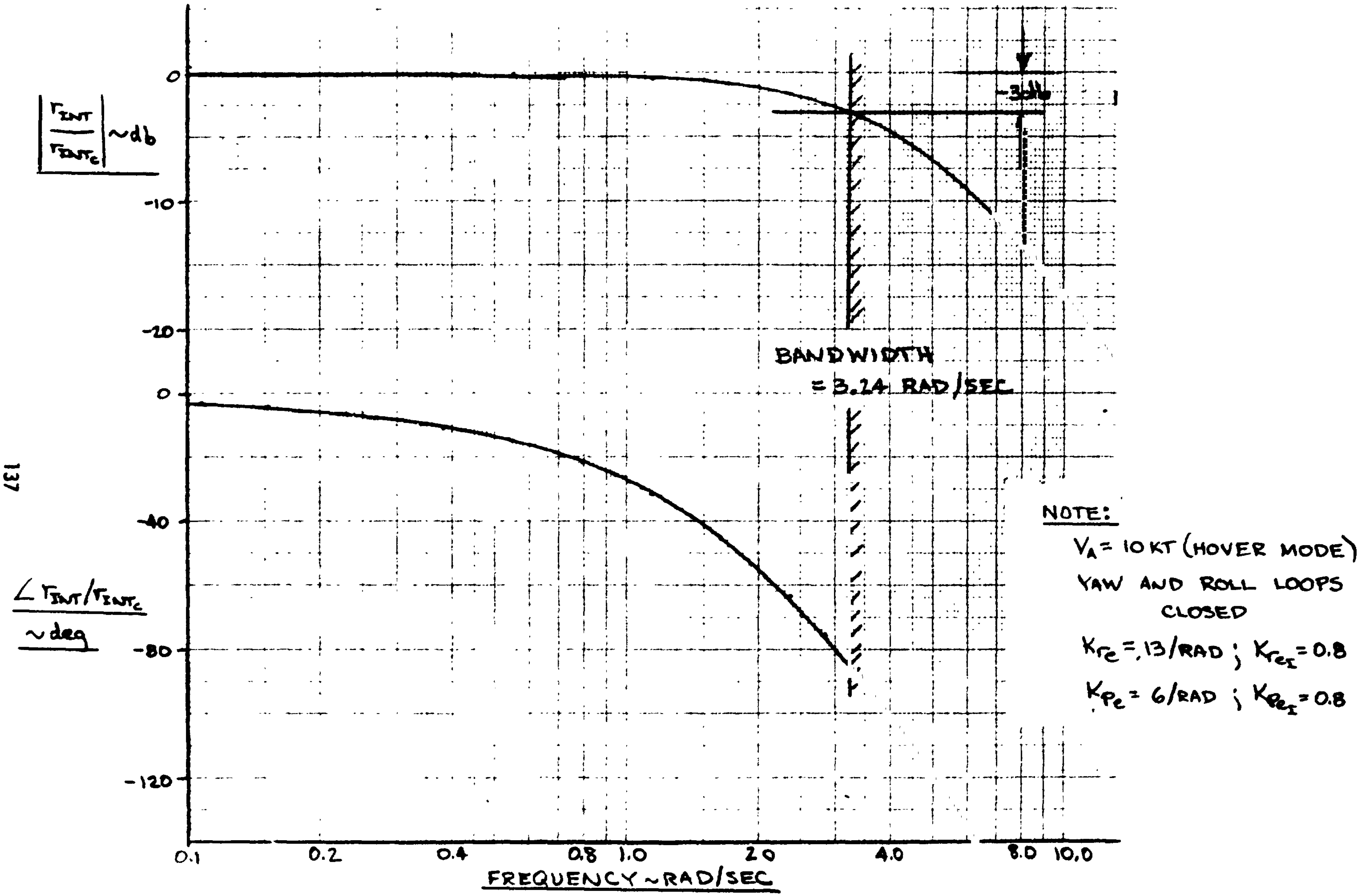

Figure 3-17. Frequency Response of Yaw FCS in Hover Mode

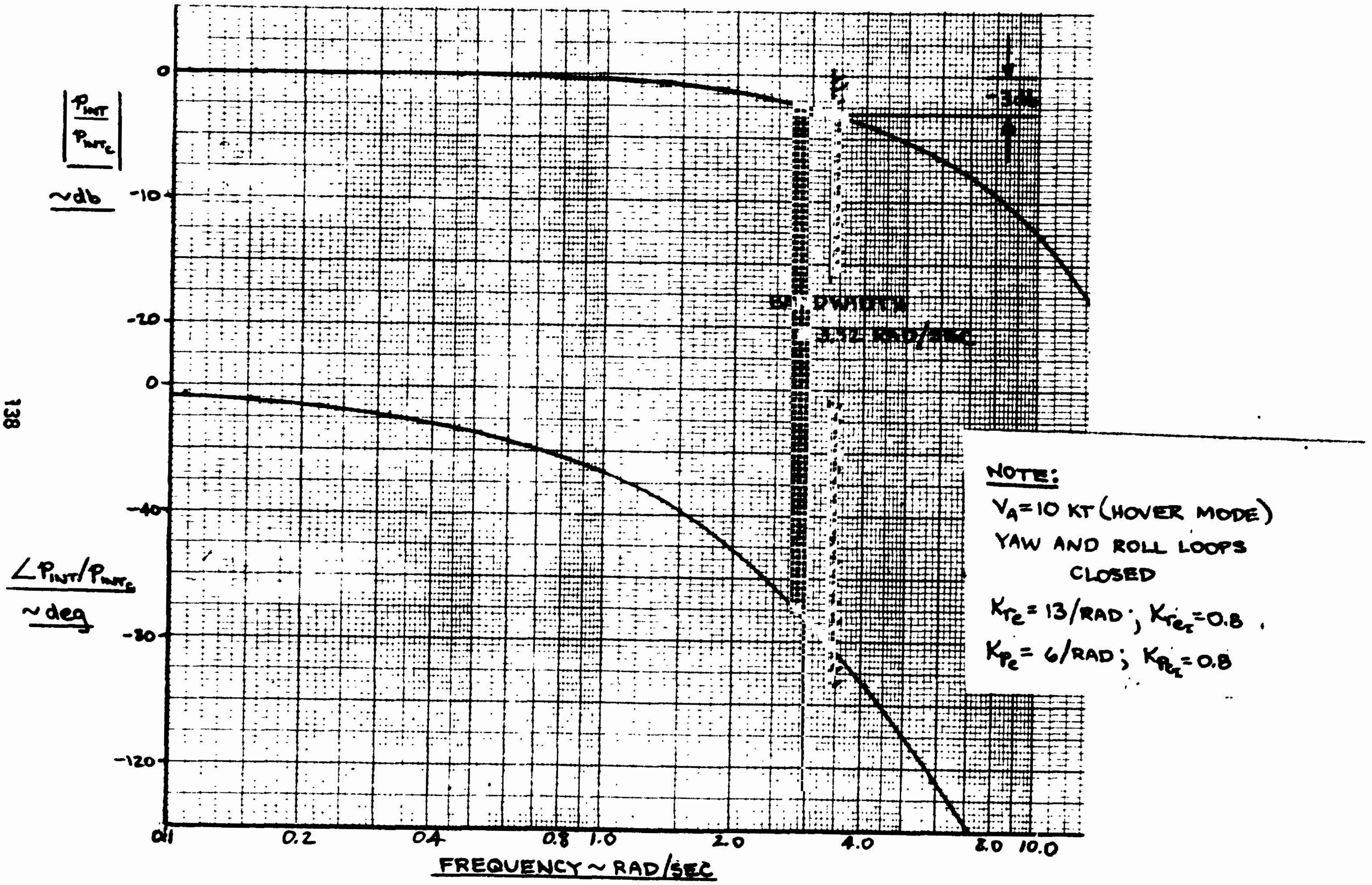

Figure 3-18. Frequency Response of Roll FCS in Hover Mode

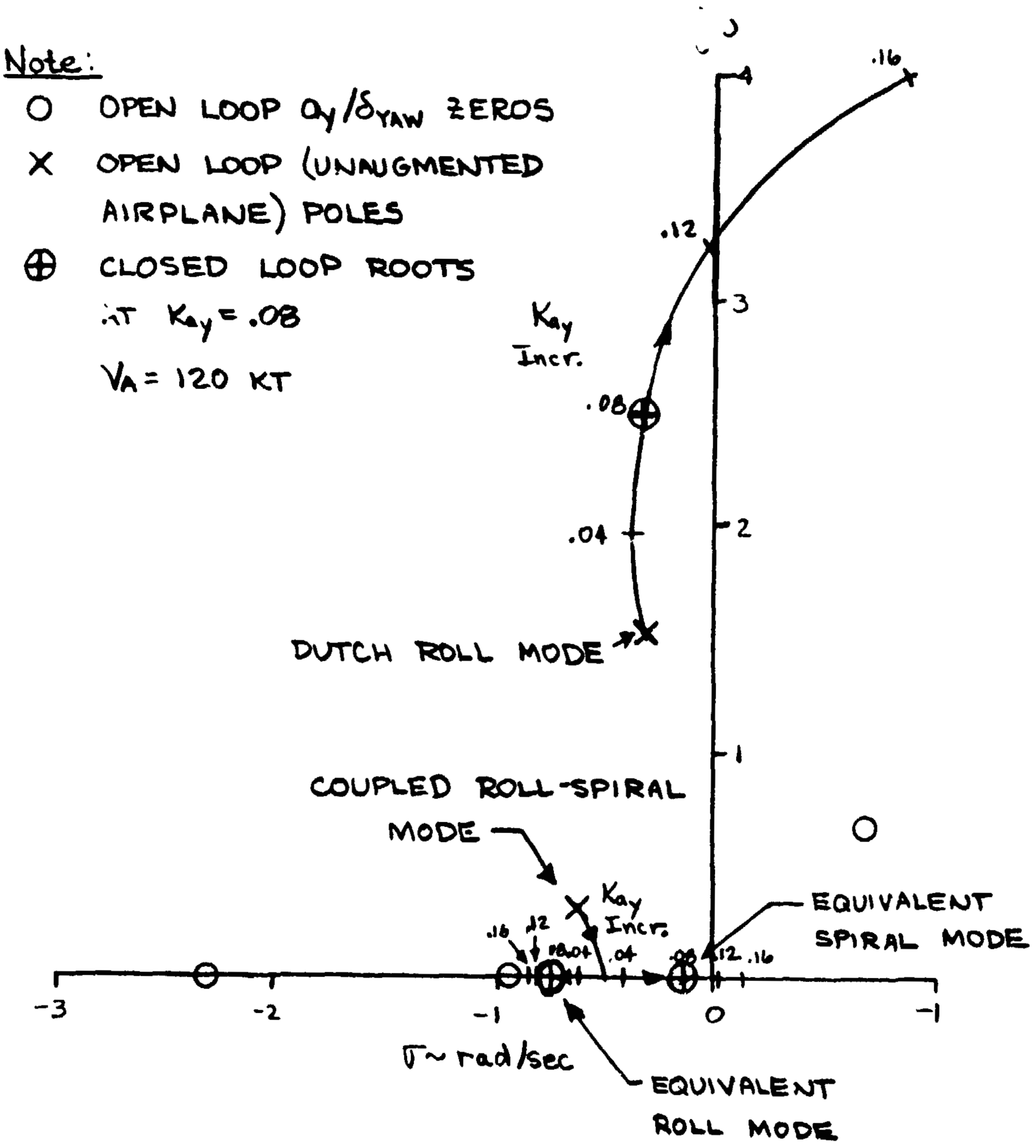

Figure 3-19. Root Locus of Lateral Acceleration to δ_{YAW} Loop Closure (V_A = 120 kt)

shows a root locus sketch of this loop closure at $V_A = 120$ kt. The lateral acceleration gain (K_{a_y}) varies along the locus. Note the formation of the decoupled equivalent roll and spiral modes and the characteristic decrease in Dutch roll damping which accompanies lateral acceleration feedback.

Also mentioned above was the application of psuedo-$\dot{\beta}$ ($\hat{\dot{\beta}} = (g/V_A)\,\phi - r_s$) feedback for increasing Dutch roll damping and providing turn coordination. Traditionally these functions are provided by a washed out stability axis yaw rate feedback. The effectiveness of this feedback depends on the relative location of the complex zeros of the r_s/δ_{YAW} transfer function numerator and the Dutch roll mode poles. If these zeros and poles are near the $j\omega$ axis or in the right half plane or the frequency of the zeros is greater than 0.4 to 0.5 that of the poles, the yaw rate feedback will be ineffective. Both these detracting conditions are displayed by the SF-121. Reference (e) develops and demonstrates how pseudo-$\dot{\beta}$ feedback is an appropriate substitute for washed out yaw rate.

Figure 3-20 provides a root locus sketch of the $\hat{\beta}$ to δ_{YAW} loop closure at 120 kt with the a_y to δ_{YAW} loop closed. The forward path gain (K_{r_e}) varies along the locus. The zero at $s = -0.2 = -K_{r_{e_{I1}}}$ and the pole at the origin are contributed by the forward path compensation. The remaining open loop zeros are the zeros of the $\hat{\beta}/\delta_{YAW}$ transfer function while the remaining poles are the equivalent lateral directional modes created by the a_y to δ_{YAW} loop closure. Note that the Dutch roll damping is increased and that an unstable low frequency mode is developed by this closure. The unstable mode will be stabilized by the roll FCS loop closure. As is demonstrated in figure 3-22, the gain selected for $\hat{\beta}$ loop closure (K_{r_e} = 1.1/rad/sec) in combination with the roll FCS loop closure (sketched in figure 3-21) produces a body axis lateral velocity ($v \approx V_A\beta$) to pedal (or $\hat{\beta}_c$) frequency response which is similar to that of an unaugmented airplane having uncoupled roll and spiral modes and a well damped Dutch roll made.

The final lateral conventional mode loop closure, the roll FCS, is depicted by the root locus sketch of figure 3-21 for $V_A = 120$ kt. The

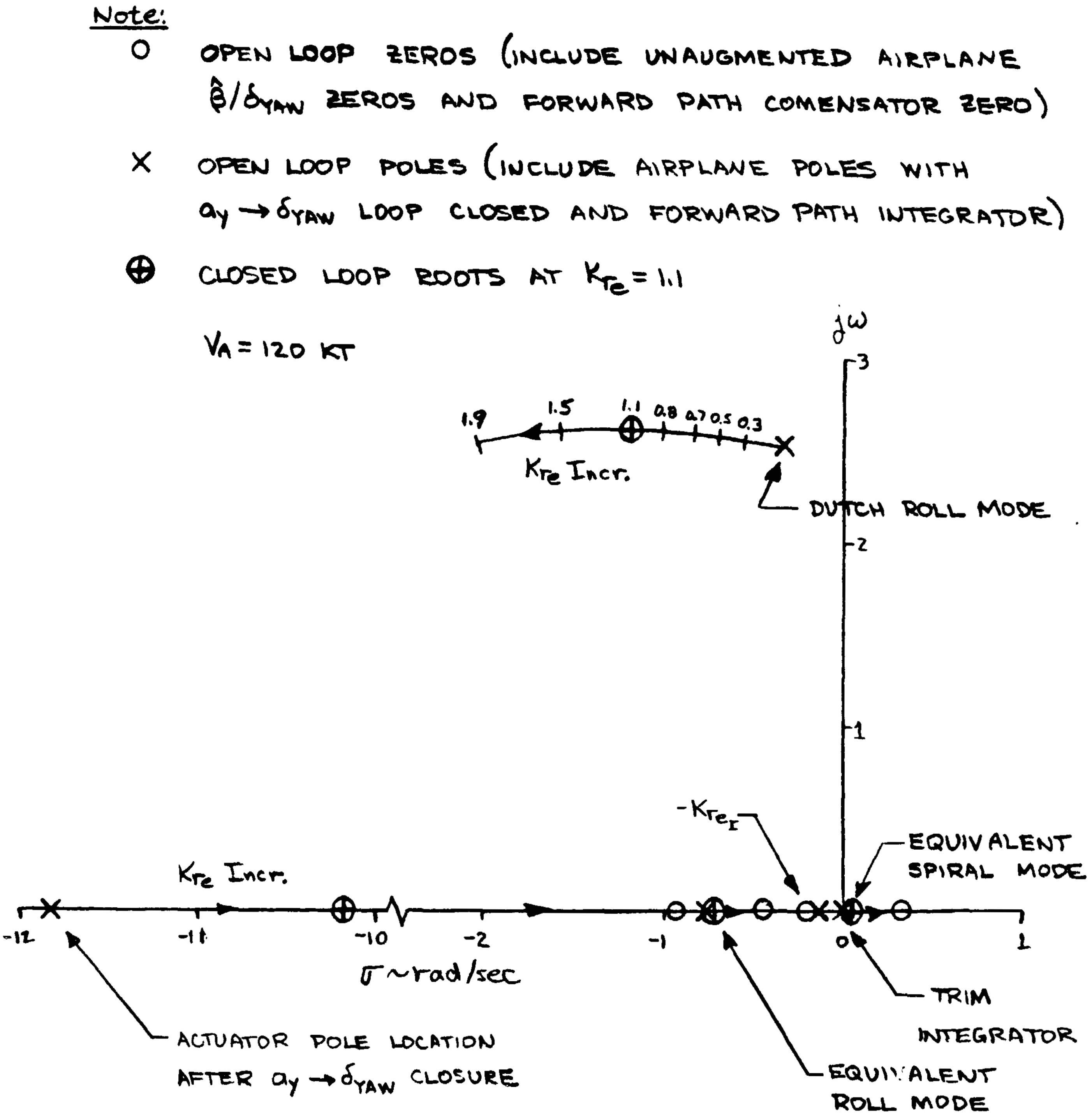

Figure 3-20. Root Locus of Pseudo-$\dot{\beta}$ to δ_{YAW} Loop Closure With a_y to δ_{YAW} Loop Closed (V_A = 120 kt)

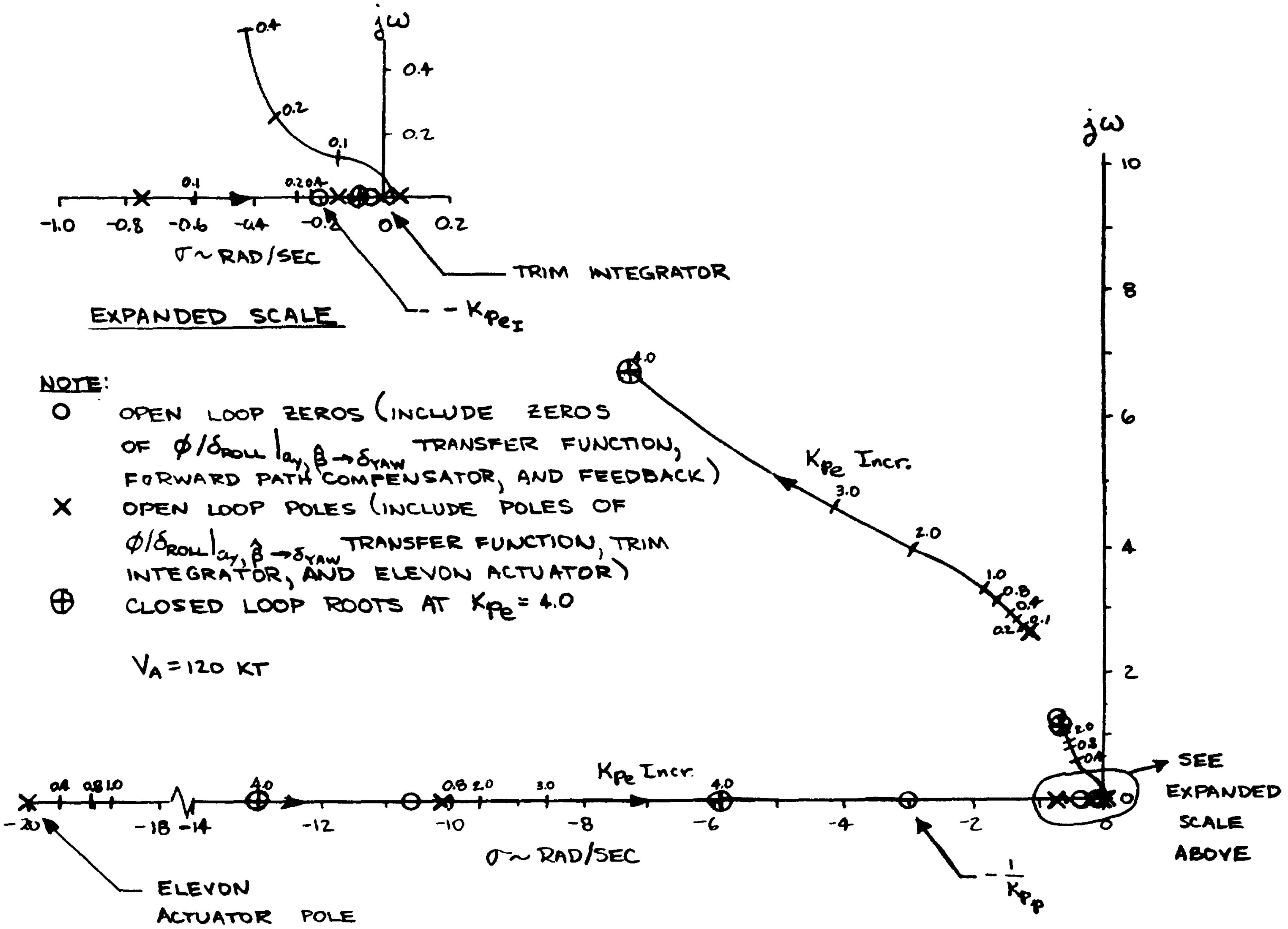

Figure 3-21. Root Locus of Roll FCS Conventional Mode Loop Closure With a_y to δ_{YAW} and $\hat{\beta}$ to δ_{YAW} Loops Closed

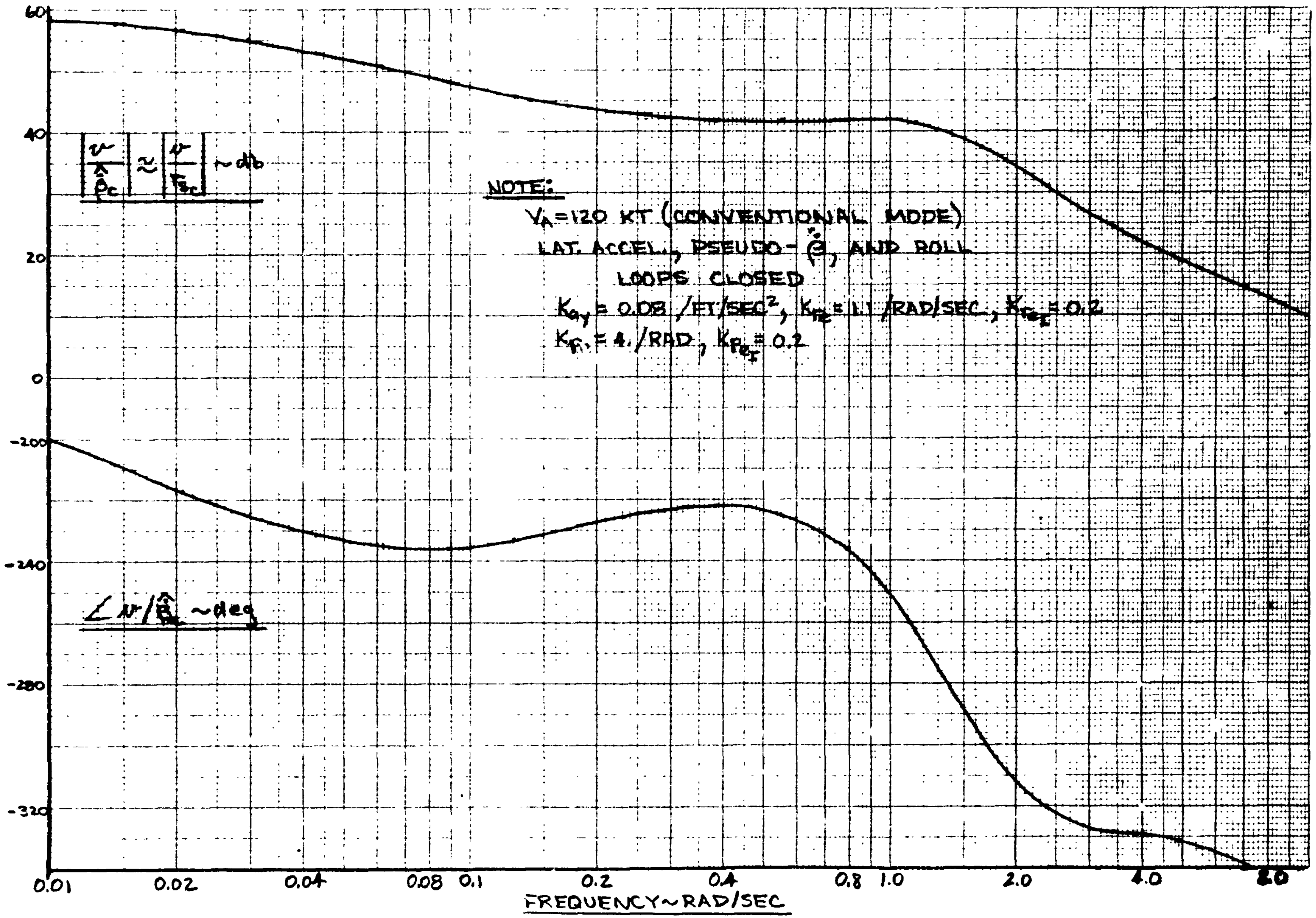

Figure 3-22. Frequency Response of Yaw FCS in Conventional Mode

forward path gain (K_{p_e}) varies along the locus. The zero at $s = -0.2 = -K_{p_{e_{I1}}}$ and the pole at the origin are contributed by the forward path compensation. The zero at $s = -3.0 = -1/K_{p_p}$ results from the stability axis roll rate feedback and was placed to effect a reasonable loop closure. The actuator pole at $s = -20$ represents the elevon actuators dynamics. The effects of the dynamics of the RCS and its actuators are negligible to this loop closure. The remaining "open loop" poles and zeros are those of the $\phi/\delta_{ROLL}\big|_{a_y,\ \hat{\beta} \rightarrow \delta_{YAW}}$ transfer function. As is demonstrated by the ϕ/ϕ_c frequency reponse (figure 3-23), the gain selected for roll FCS loop closure ($K_{p_e} = 4$/rad) produces an attitude bandwidth of 2.7 rad/sec which is slightly less than the desired 3.0 rad/sec. This frequency response plot does not include the effects of the lateral stick input shaping network [(s + 3.33)/s] which makes the conventional mode roll FCS a rate command-attitude hold system.

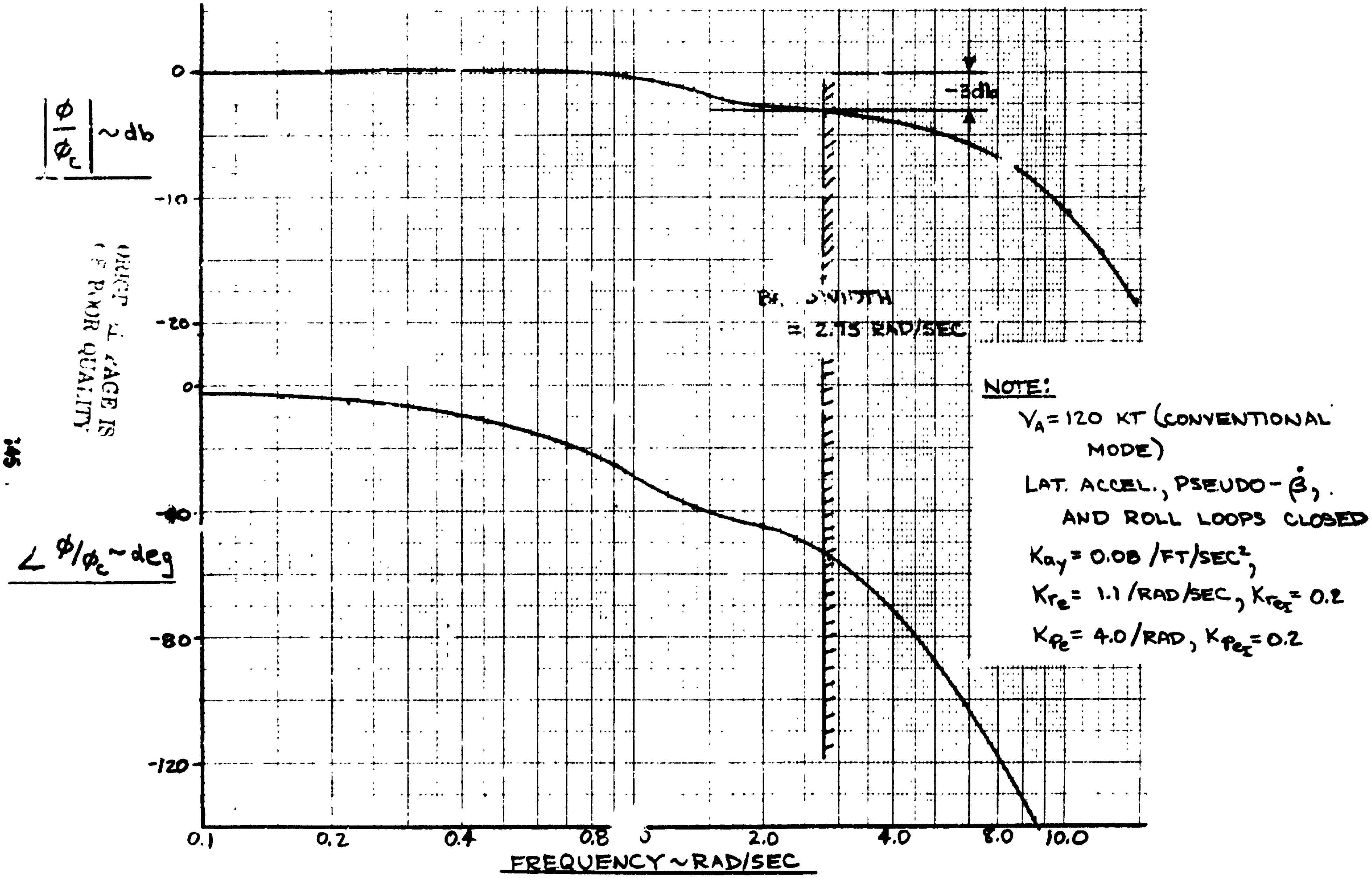

Figure 3-23. Frequency Response of Roll FCS in Conventional Mode

3.8 FCS Performance Evaluation

The control laws and gains established by the analyses described in Section 3.7 were incorporated into VATLAS. Nonlinear time reponses to various cockpit controller inputs and pseudo-pilot flown scenarios were then calculated to evaluate the FCS performance. Ten cases selected for evaluation and demonstration of this performance are as follows:

1. Longitudinal stick doublet at $V_A = 120$ kt commanding 10 deg/sec pitch rate for 0.7 sec followed by -10 deg/sec for 0.7 sec (figure 3-24)
2. Lateral stick pulse at $V_A = 120$ kt commanding 20 deg/sec roll rate for 1.4 sec (figure 3-25)
3. Pedal step at $V_A = 120$ kt commanding 4 deg/sec of pseudo $\dot{\beta}$ (figure 3-26)
4. Longitudinal stick doublet at $V_A = 10$ kt commanding 10 deg of q_{INT} for 0.7 sec followed by -10 deg for 0.7 sec (figure 3-27)
5. Lateral stick doublet at $V_A = 10$ kt commanding 10 deg of r_{INT} for 0.7 sec followed by -10 deg for 0.7 sec (figure 3-28)
6. Pedal pulse at $V_A = 10$ kt commanding 20 deg/sec roll rate for 1.4 sec (figure 3-29)
7. Heave rate controller doublet at $V_A = 10$ kt commanding -10 ft/sec heave rate for 3.0 sec followed by 10 ft/sec for 3.0 sec (figure 3-30)
8. Mode switching transient. Aircraft trimmed in a 0.1g decelerating 0.5 mile turn at $V_A = 62$ kt, then simultaneous longitudinal and lateral stick pulses of 0.7 sec duration commanding 10 deg/sec pitch and roll rates are input 0.3 sec into the run (figure 3-31)
9. Psuedo-pilot flown transition initiated at $V_A = 200$ kt (figure 3-32)
10. Pseudo-pilot flown turn over a spot (i.e. stationkeeping) in a 35 kt wind (figure 3-33)

Each case is discussed in some detail in Sections 3.8.1 to 3.8.10.

The doublet, step, and pulse inputs for cases 1 to 7 were given sufficient magnitude to induce control system saturation and/or exercise other significant system nonlinearities. As such they simulate fairly vigorous pilot use of the SF-121 and its control system. Other than the fact that 0.7 sec is approximately twice the time constant of the attitude loops there is no rationale for selecting multiples of 0.7 sec for pulse and doublet lengths. Similarly 3.0 sec for the heave rate doublet input is approximately four times the time constant of the heave rate loop. Case 8 demonstrates the system capability to maintain control in the presence of large simultaneous multi-axis pilot inputs at the mode switch speed. Cases 9 and 10 demonstrate the capabilities of the VATLAS pseudo-pilot logic and the control system for two operational scenarios for the aircraft.

3.8.1 Case 1 - Longitudinal Stick Doublet at V_A = 120 kt

The pitch rate response is essentially linear until the doublet reverses at 1.0 sec (figure 3-24). The linear response overshoots its commanded value of 10 deg/sec by approximately 20%. This is consistent with the pitch loop frequency response (figure 3-12) which indicates that the system is less than critically damped (i.e. it has a 2.5 db peak which indicates a damping ratio of approximately 0.4). At 1.0 sec the symmetrical elevon command becomes saturated due to the normalized pitch control becoming < -1.0. From this point on the response is nonlinear. The resulting response is stable and completes the doublet maneuver with considerable lag. Coupling into the lateral degrees of freedom is minimal.

3.8.2 Case 2 - Lateral Stick Pulse at V_A = 120 kt

The lateral stick pulse commands a fairly rapid entry to a 28 deg banked turn. A steady state turn rate of approximately 4 deg/sec is generated by this maneuver. The time history traces shown on figure 3-25 indicate that the 28 degree roll angle is attained with no overshoot but reduces a degree or so when the lateral stick command is released due to the overshoot in the roll rate response. Approximately 4 deg of β (adverse yaw) and -0.15g lateral acceleration are generated during the turn entry. These are rapidly driven to near zero (thus coordinating the turn) by the yaw control system when the desired roll angle is attained and held.

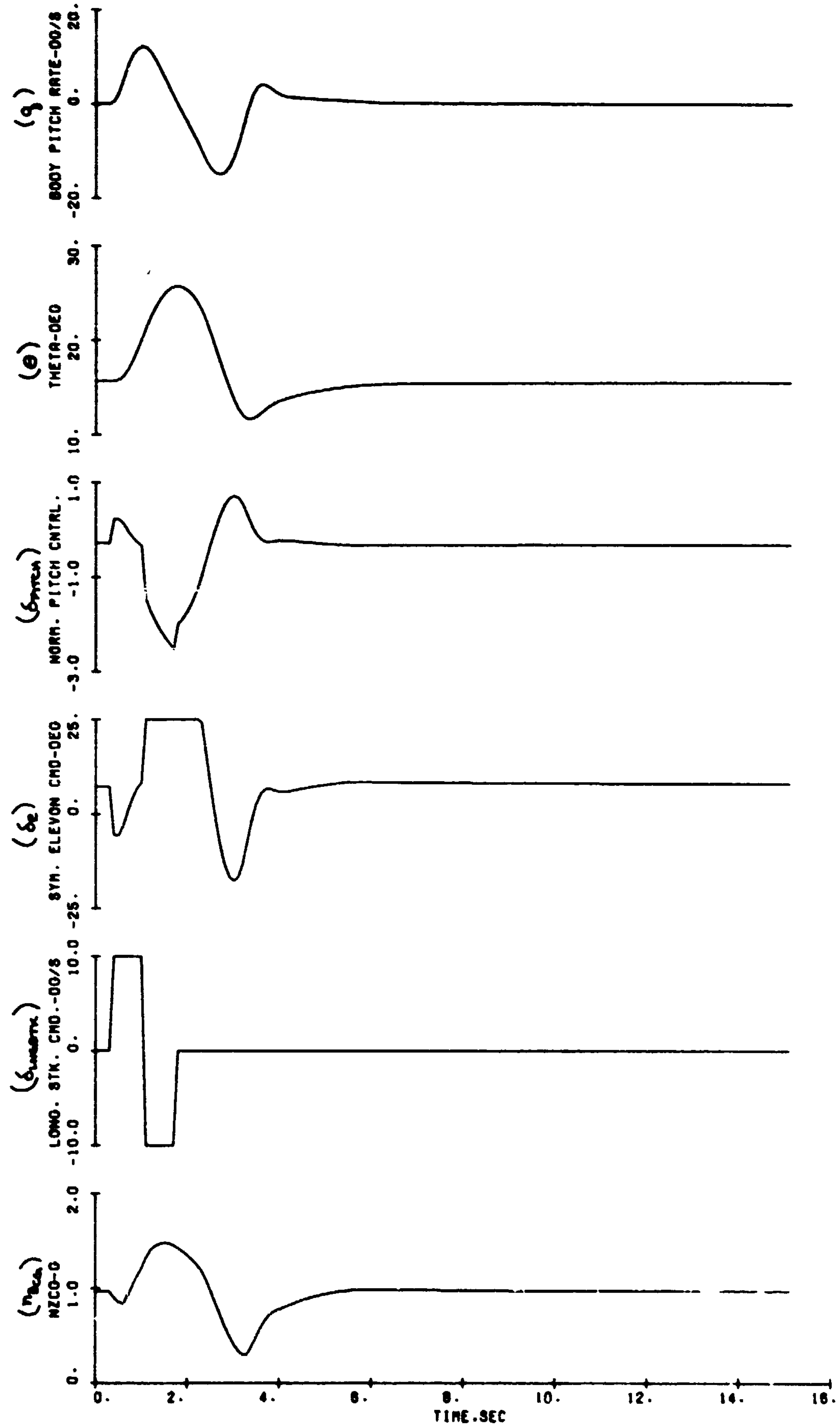

Figure 3-24. Longitudinal Stick Doublet Response at V_A = 120 kt (Sheet 1 of 3)

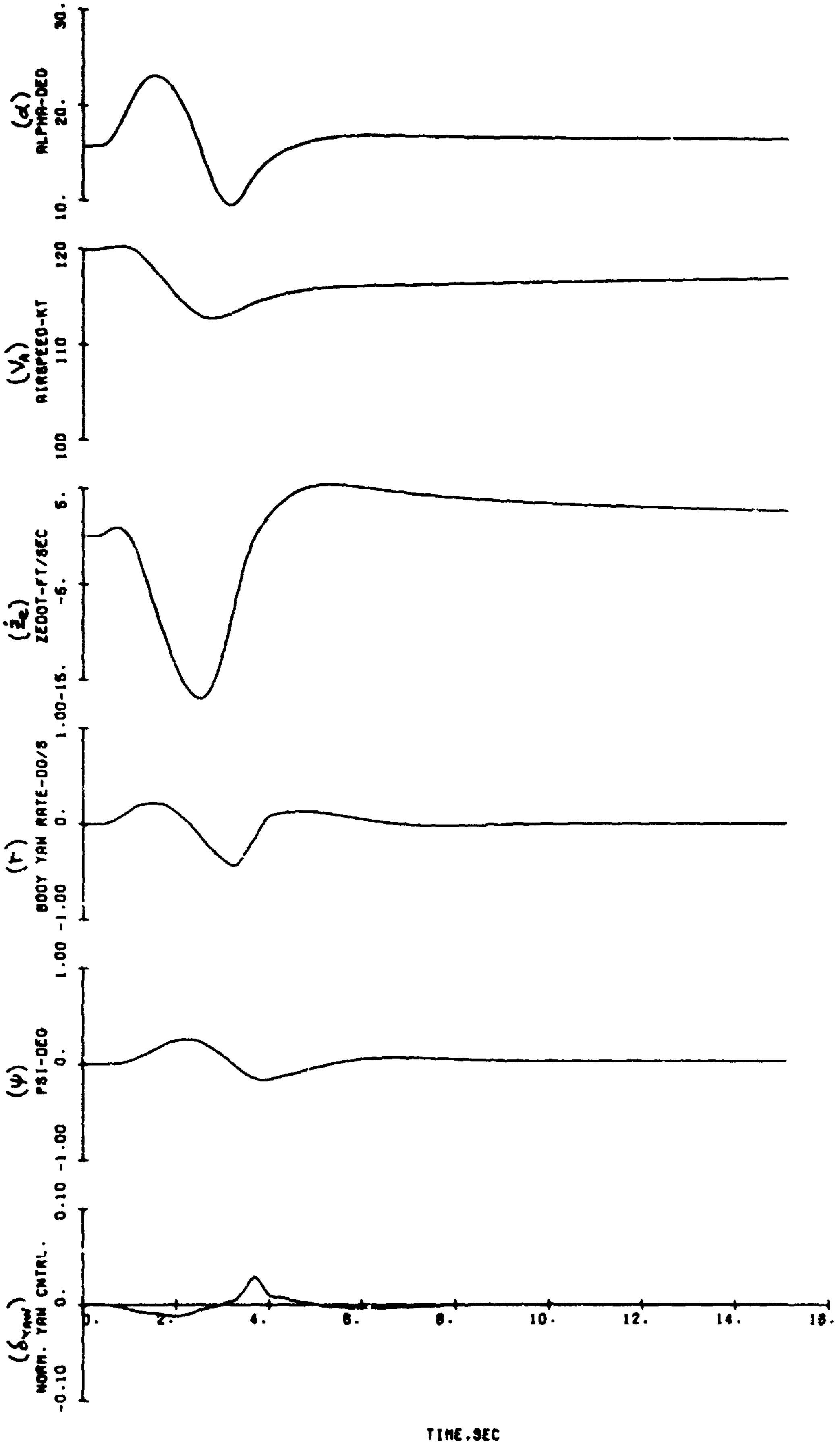

Figure 3-24. Longitudinal Stick Doublet Response at $V_A = 120$ kt (Sheet 2 of 3)

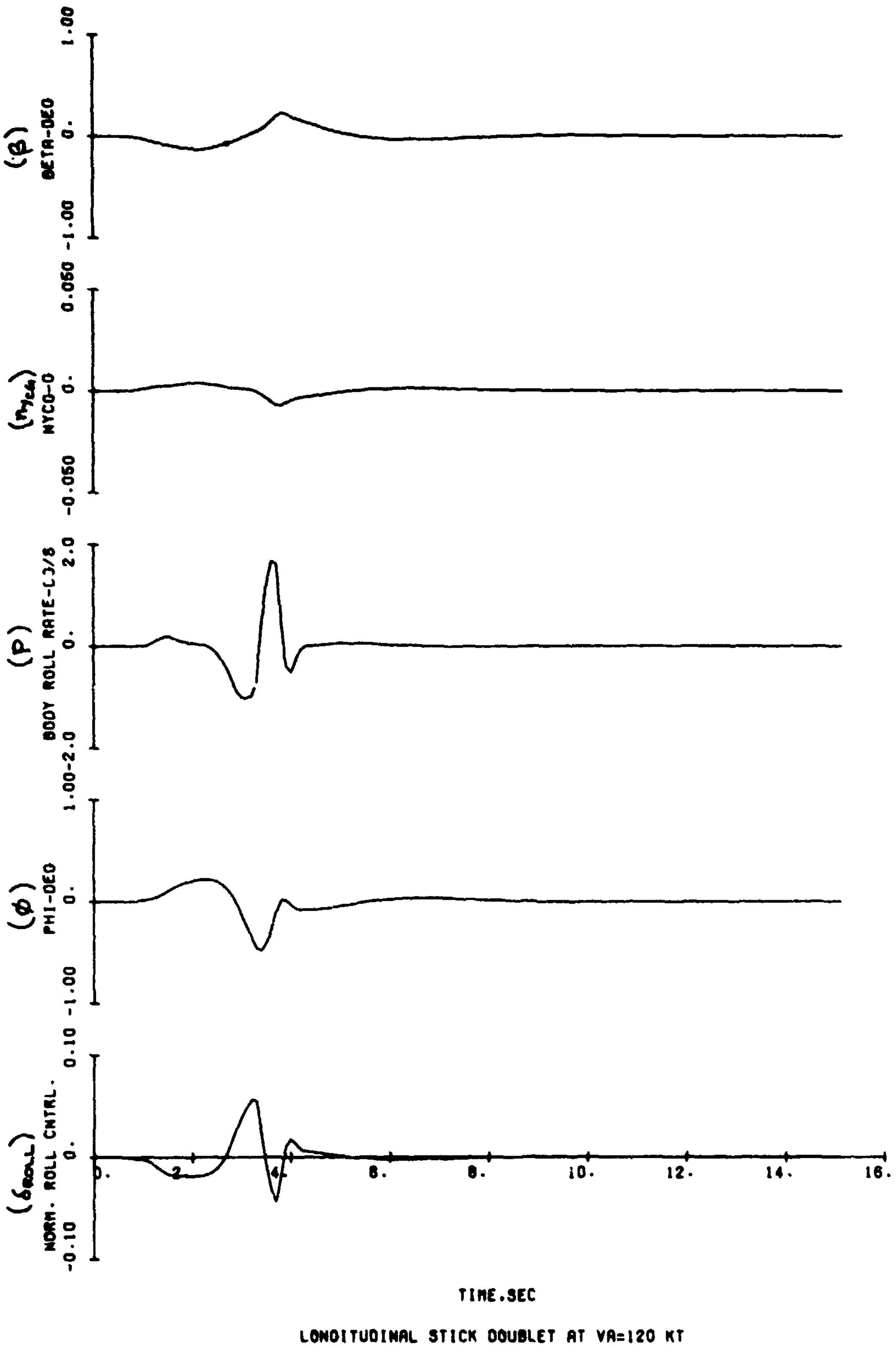

Figure 3-24. Longitudinal Stick Doublet Response at V_A = 120 kt (Sheet 3 of 3)

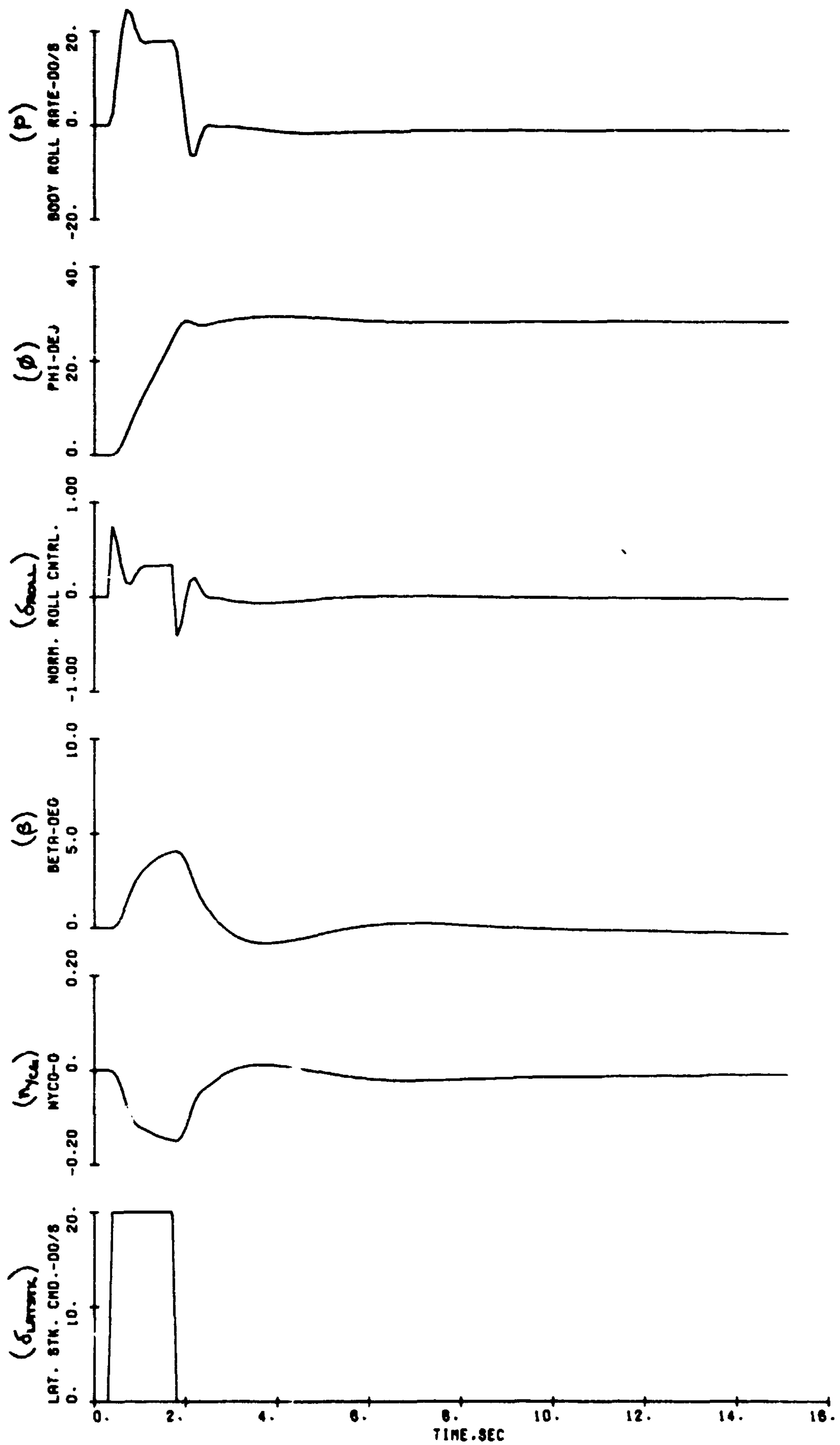

Figure 3-25. Lateral Stic. Pulse Response at V_A = 120 kt (Sheet 1 of 3)

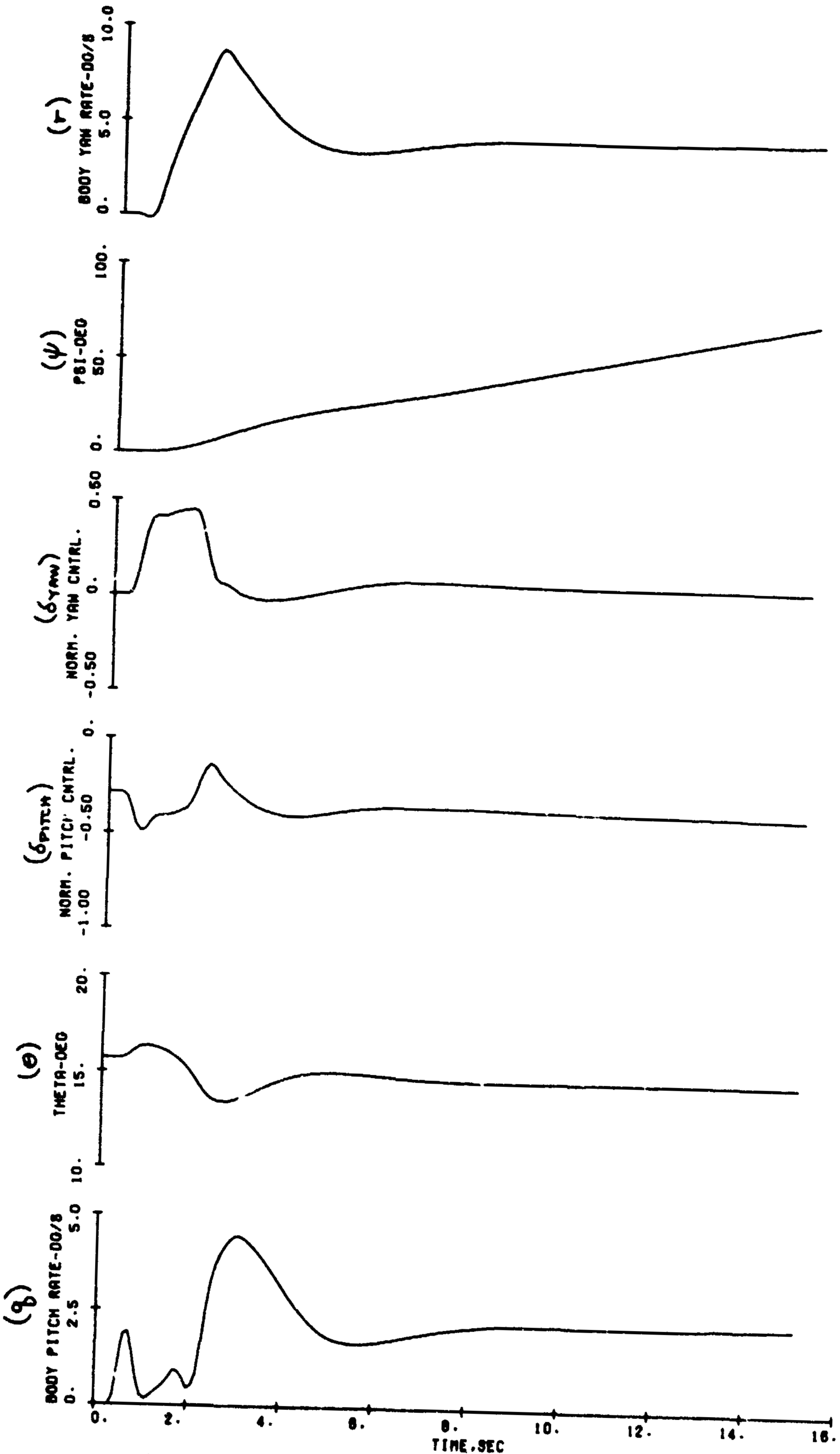

Figure 3-25. Lateral Stick Pulse Response at V_A = 120 kt (Sheet 2 of 3)

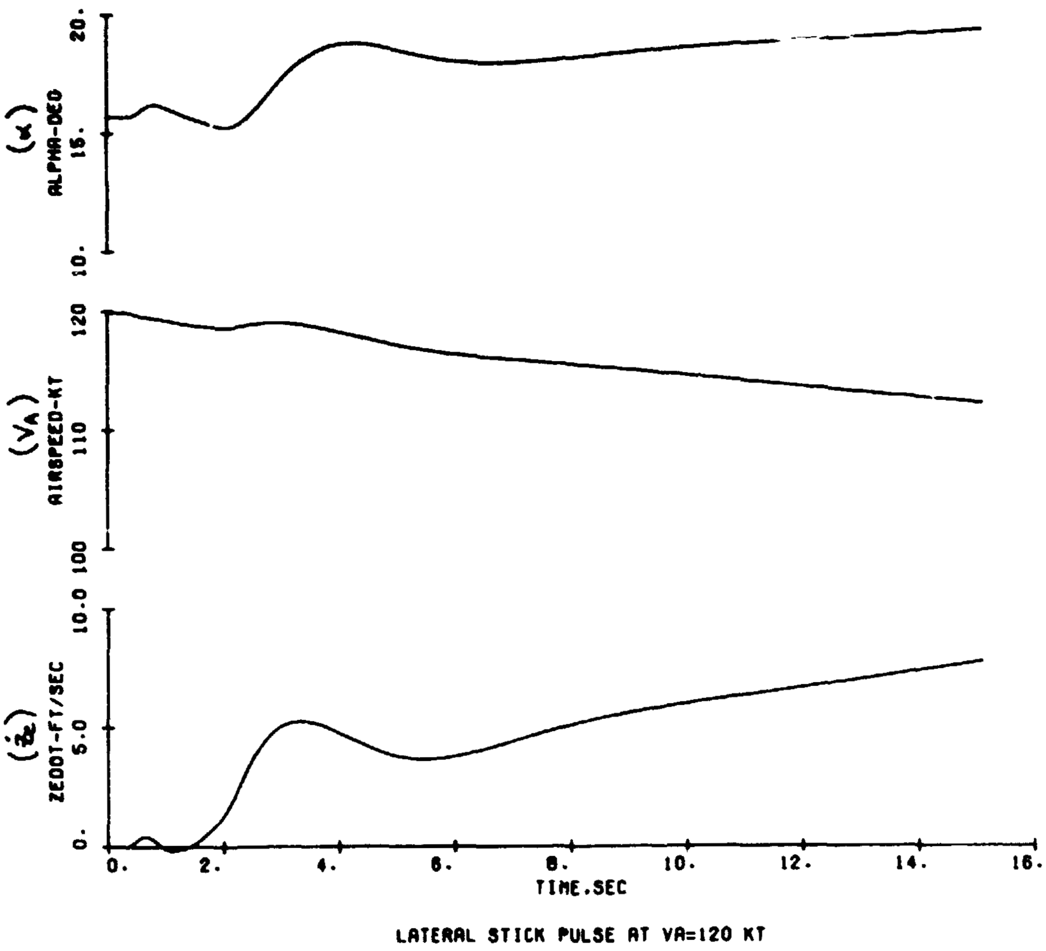

Figure 3-25. Lateral Stick Pulse Response at V_A = 120 kt (Sheet 3 of 3)

Coupling into the longitudinal degrees of freedom is apparent and was anticipated. The steady state pitch rate is required by the kinematics of the steady turn. The reduced (from trim) steady state pitch angle is due to the pitch control system error returning to zero at steady state; since both pitch rate and pitch angle are fed back and steady state pitch rate is non zero with a positive value, steady state pitch angle must reduce to keep the pitch control system error zero. Increased pitch angle during turn entry is caused by the loss of elevon effectiveness at large deflections; turn entry requires increased left elevon deflection and reduced right elevon deflection thus producing a nose up moment. A nose down moment is produced when the differential elevon deflection is removed upon attaining the desired roll angle.

Overall, there are no apparent stability or control problems or unanticipated motions in the aircraft response to the lateral stick pulse.

3.8.3 Case 3 - Pedal Step at $V_A = 120$ kt

The pedal step commands the aircraft to perform a wings level ($\phi = 0$) skidding ($\beta \neq 0$) turn ($r \neq 0$). The pedal step on figure 3-26 is labelled as a pseudo-$\dot{\beta}$ command input. This is consistent with $\hat{\beta}$ feedback of the yaw control system. Since the attitude hold feature of the roll control system keeps wings level, the yaw control system feedback becomes yaw rate and the pedal becomes a yaw rate controller.

The β response shows the effects of the two "shelf" $v/\hat{\beta}_c$ frequency response (figure 3-22). The magnitude of the frequency response has a steady state level ("shelf") of 57 db which extends to approximately 0.02 rad/sec, then the response drops to another "shelf" of 42 db which extends to approximately 1.0 rad/sec where the response starts its characteristic drop off to $-\infty$db. Thus the β time response should and does demonstrate two distinct modes; a short term response wherein β reaches approximately -4 deg in 2.5 sec superposed on a long term response which appears as a drift. The yaw rate response has a similar bimodal response.

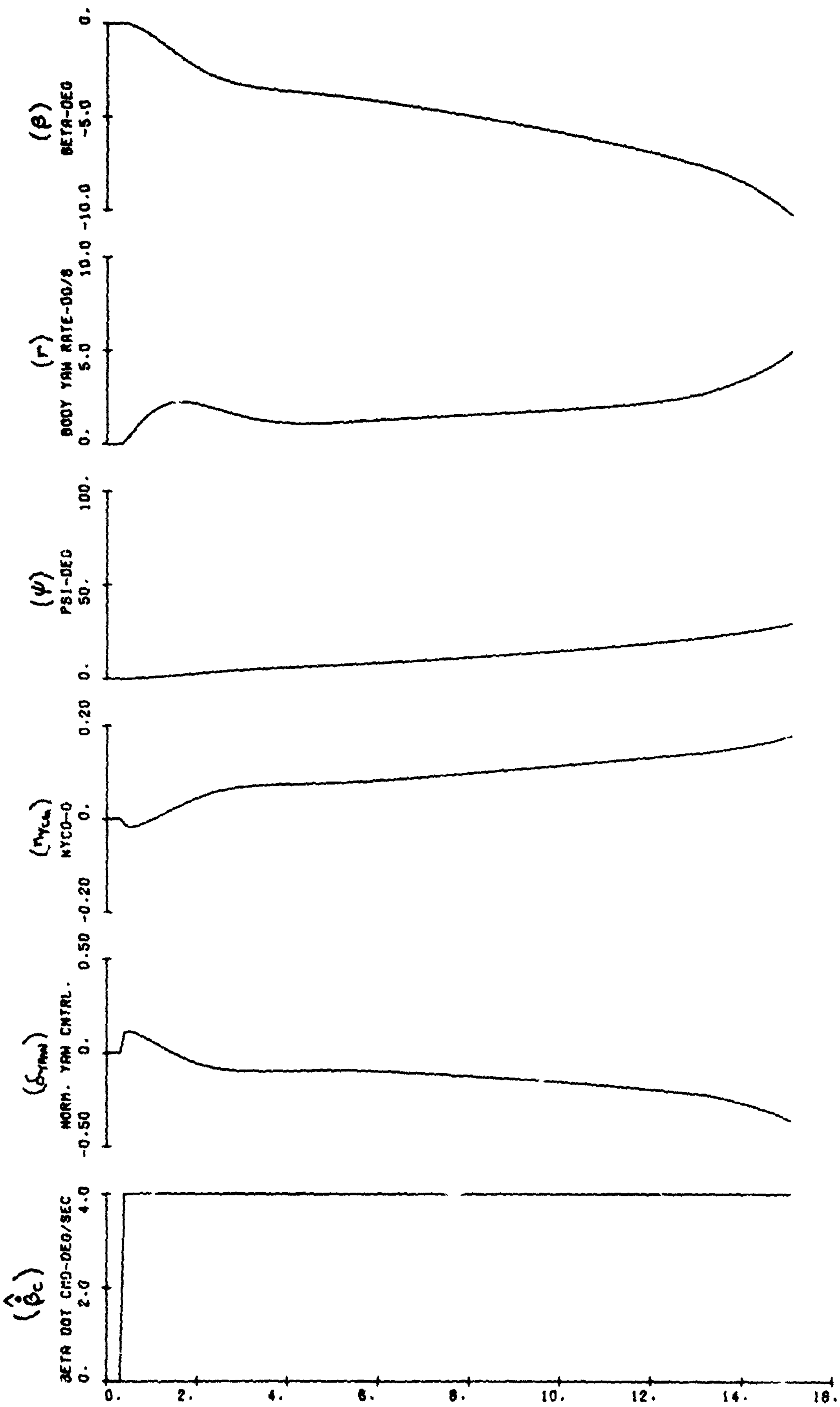

Figure 3-26. Pedal Step Response at V_A = 120 kt (Sheet 1 of 3)

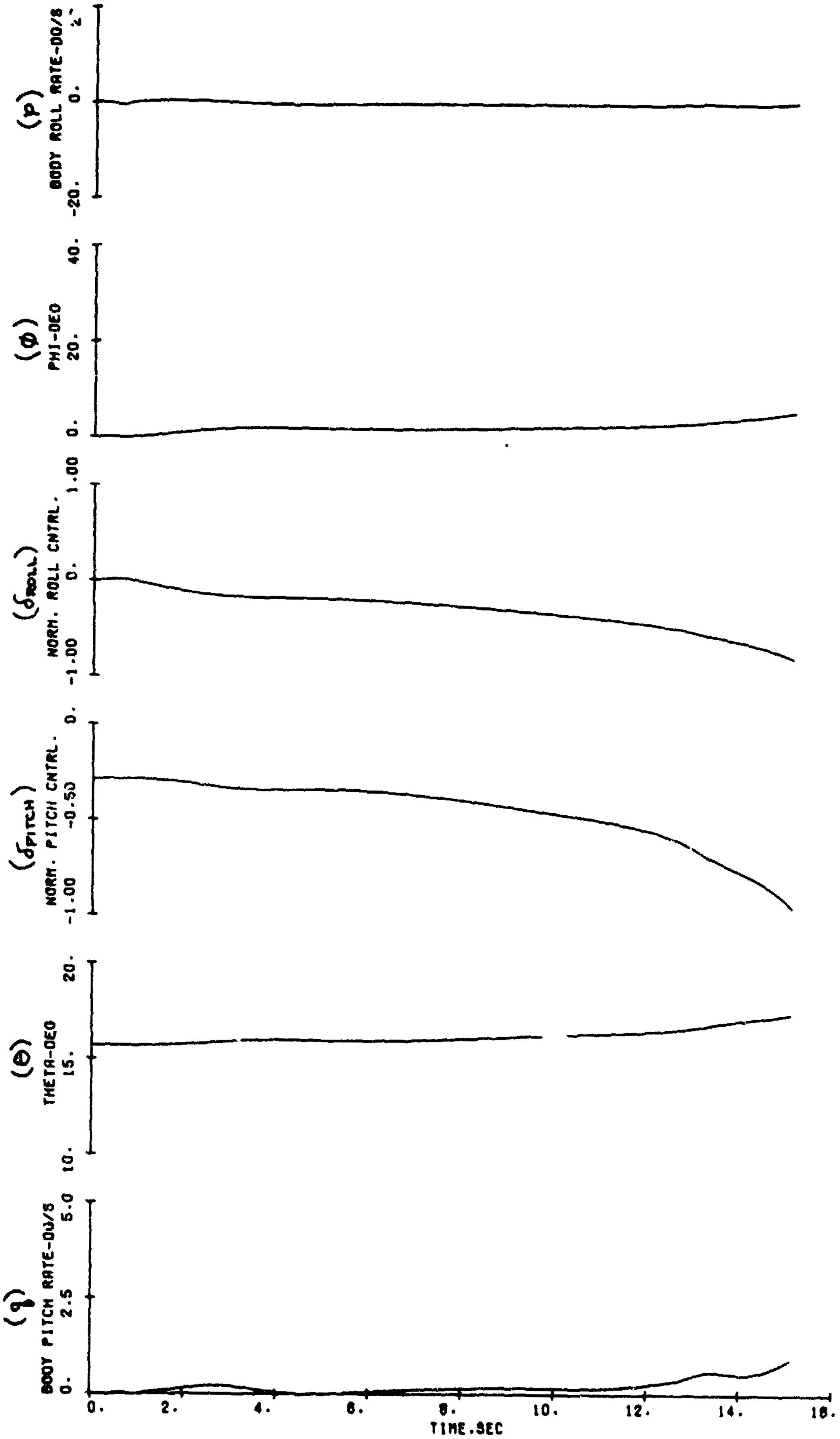

Figure 5-26. Pedal Step Response at V_A = 120 kt (Sheet 2 of 3)

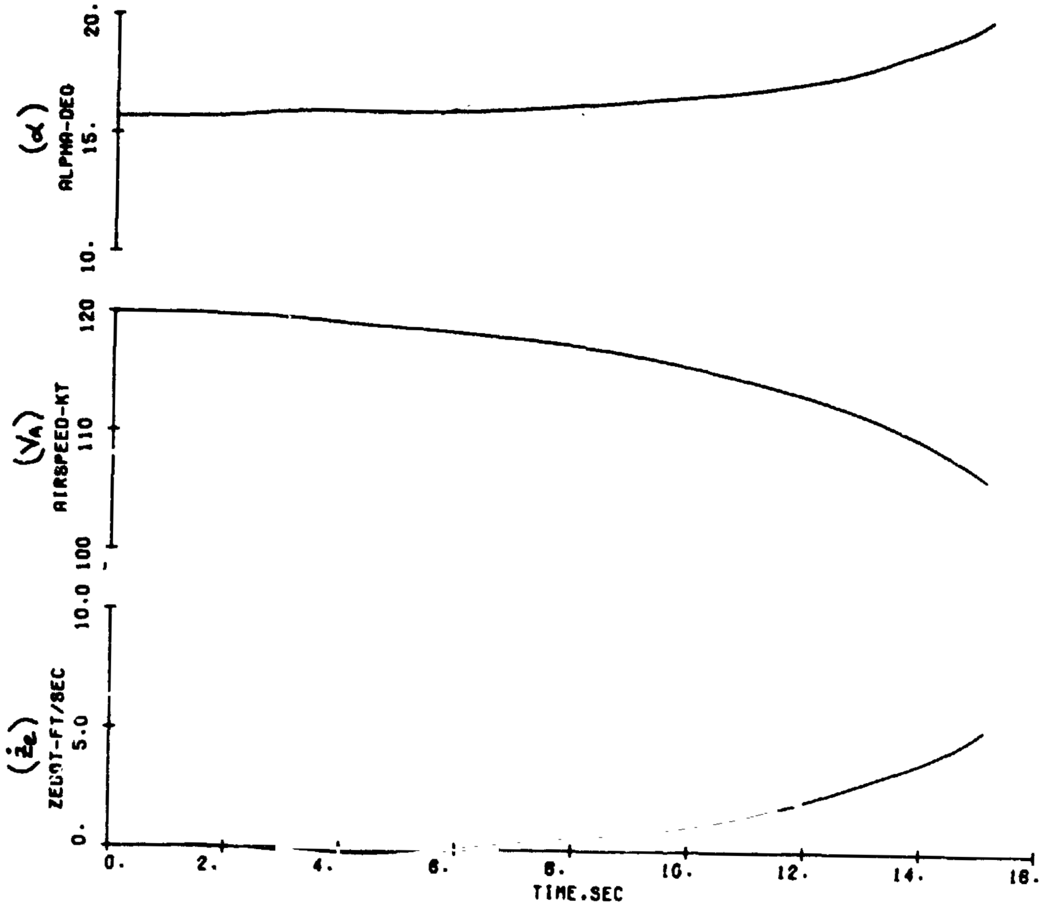

PSEUDO BETA DOT COMMAND STEP
120 KT AIRSPEED

Figure 3-26. Pedal Step Response at V_A = 120 kt (Sheet 3 of 3)

Another interesting aspect of figure 3-26 is the effect of decreased elevon effectiveness at large deflections which was discussed in Section .8.2. As β increases, the roll moment required to maintain wings level increases because of the aircraft dihedral effect (C_{l_β}). This is seen in the δ_{ROLL} trace. The pitch up due to the elevon effectiveness loss must be countered by increased nose down pitch moment as shown by the δ_{PITCH} trace. Note that the aircraft is nearly out of nose down pitch control ($\delta_{PITCH} \approx -1.0$) and running out of negative roll control at the end of the 15 sec time history. A short time more and the aircraft would be in control saturated situation. Thus figure 3-26 demonstrates a β limitation in the transition region of flight; a not uncommon characteristic of V/STOL aircraft.

3.8.4 Case 4 - Longitudinal Stick Doublet at $V_A = 10$ kt

The longitudinal stick doublet commands the aircraft to pitch through vertical tnen down through trim and then return to trim. Since $\dot{X}_e$ is controlled by pitch attitude (q_{INT}) the intent of this maneuver is to decrease $\dot{X}_e$ then increase it beyond trim $\dot{X}_e$ and then return it to near trim. Figure 3-27 shows that the desired pitch maneuver is performed with some saturation of the pitch controls; $|\delta_{PITCH}|$ exceeds 1.0 and $|\theta_T|$ is limited to 15 deg. The desired effect on $\dot{X}_e$ is not obtained and herein lies the most distinguishing flying qualities characteristic of hover control of the SF-121. (The characteristic is indigenous to any VATOL aircraft employing aft end thrust deflection for moment control.) $\dot{X}_e$ initially <u>increases</u> before proceeding to follow the desired response: i.e. the $\dot{X}_e$ and, likewise, $n_{Z_{cg}}$ response to pitch attitude are initially in the wrong direction. The reason for this is that to increase pitch angle the thrust must deflect forward (in a direction to increase $\dot{X}_e$) initially to produce a nose up pitch moment. This is a non-minimum phase control characteristic and is indicated during control system analysis by zeros of the $\dot{X}_e/\delta_{LNGSTK}$ transfer function lying in the right half of the s-plane. Thus the SF-121 has the potential for instability and PIO (pilot induced oscillations) if the pilot aggressively pursues position control of the airplane. The addition of pitch RCS jets acting as a force couple would eliminate this tendency and allow pitch thrust deflection to be used as a direct force control.

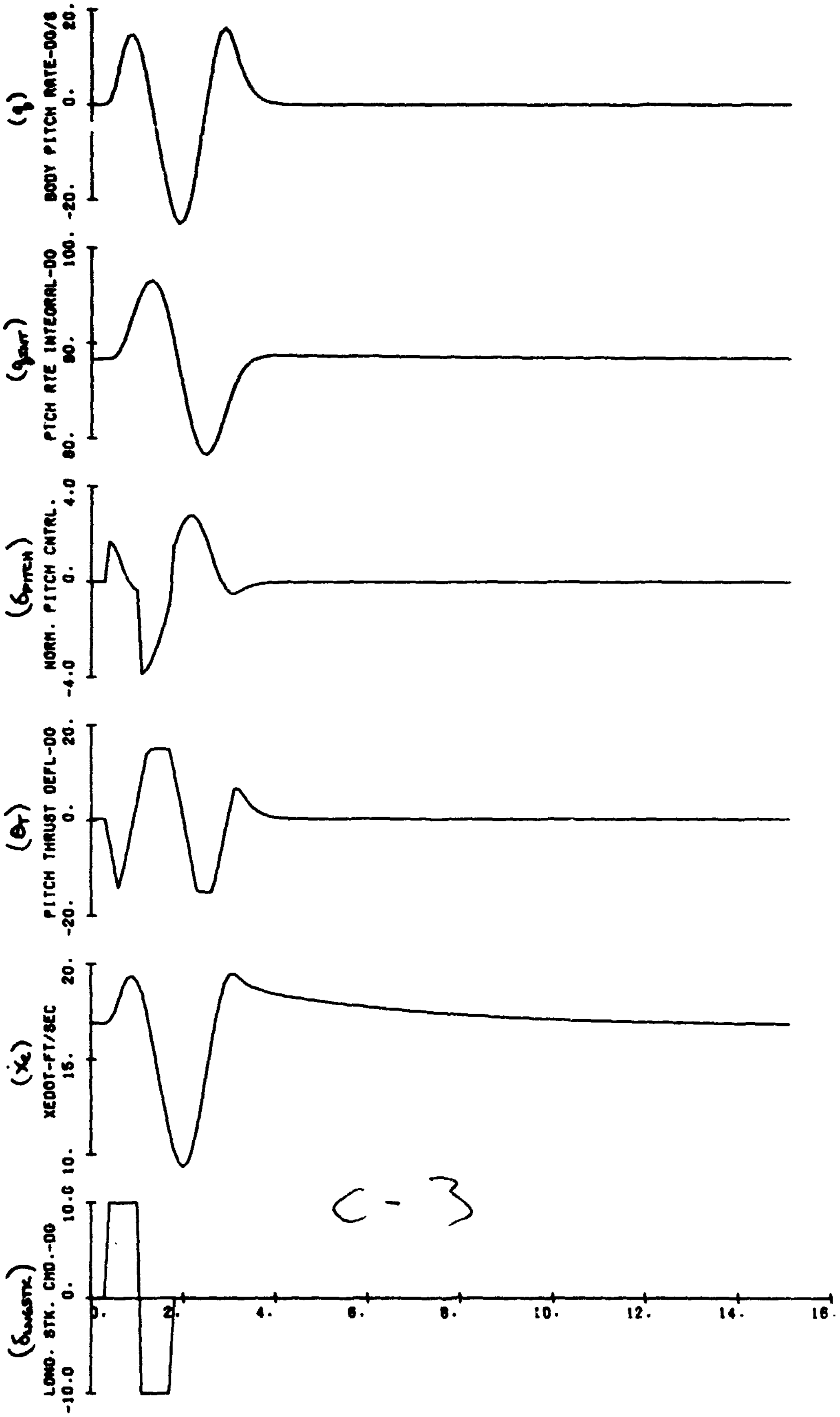

C-3

Figure 3-27. Longitudinal Stick Doublet Response at V_A = 10 kt (Sheet 1 of 3)

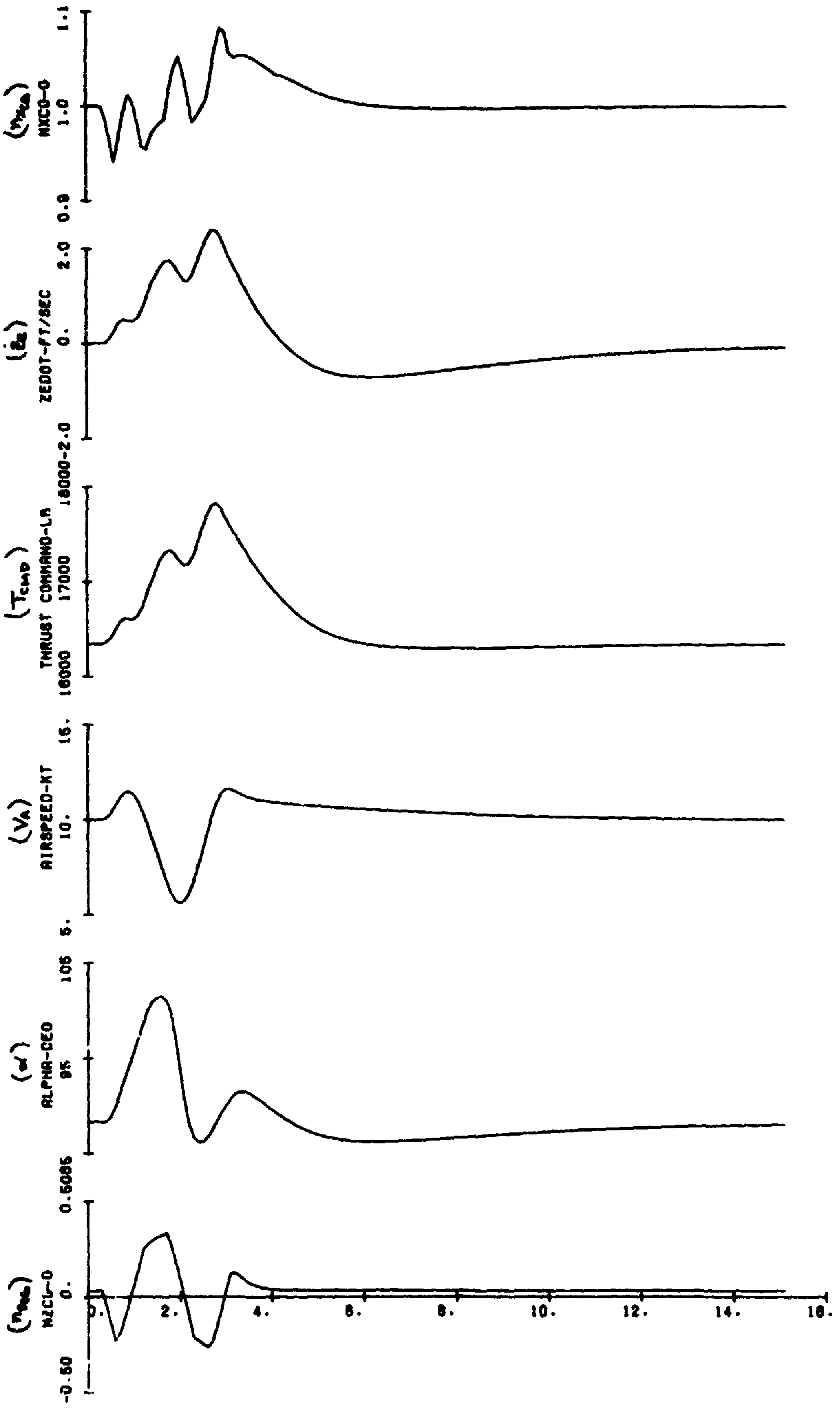

Figure 3-27. Longitudinal Stick Doublet Response at V_A = 10 kt (Sheet 2 of 3)

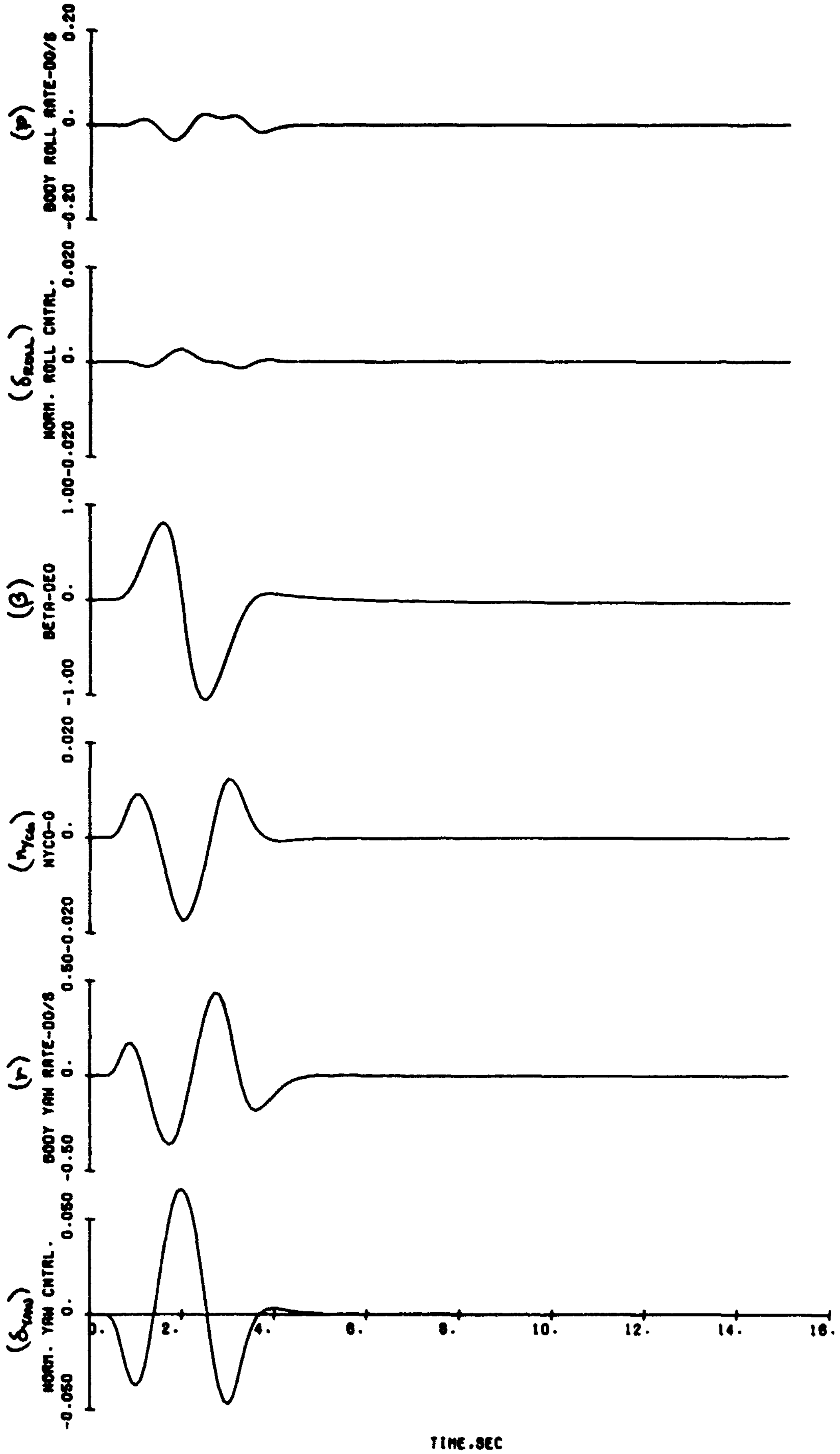

Figure 3-27. Longitudinal Stick Doublet Response at V_A = 10 kt (Sheet 3 of 3)

The longitudinal stick doublet response also demonstrates that there is a modicum of lateral coupling but fairly significant through anticipated heave coupling. Thrust deflection reduces the vertical thrust component and the aircraft begins to sink ($\dot{Z}_e > 0$). The heave control system provides appropriate thrust corrections to drive the heave rate back to trim ($\dot{Z}_e = 0$). Note that the aircraft will sink for pitch control inputs in either direction from trim. Should it prove annoying the heave coupling can be alleviated by a crossfeed from δ_{PITCH} to thrust command.

3.8.5 Case 5 - Lateral Stick Doublet at $V_A = 10$ kt

The lateral stick doublet response is the lateral dual of the longitudinal stick doublet response. The following verbal and symbology replacements inserted in Section 3.8.4 will make the discussion generally applicable as well to the time trace of figure 3-28:

$$\text{Replace}\left\{\begin{matrix}\dot{X}_e\\ \text{pitch}\\ q_{INT}\\ \delta_{PITCH}\\ \theta_T\\ \delta_{LNGSTK}\\ n_{z_{cg}}\end{matrix}\right\}\text{ in Section 3.8.4 with }\left\{\begin{matrix}\dot{Y}_e\\ \text{yaw}\\ r_{INT}\\ \delta_{YAW}\\ \psi_T\\ \delta_{LATSTK}\\ n_{y_{cg}}\end{matrix}\right\}$$

The lateral response differs as a dual from the longitudinal response only in that $\dot{Y}_e$, and subsequently β, do not return to zero (trim) at the end of the maneuver whereas $\dot{X}_e$, the longitudinal dual, does. The difference stems from the fact that the fuselage tilts to the right farther and longer than it does to the left during the maneuver (i.e. r_{INT} is positive for a longer time than it is negative and attains larger positive magnitudes). Since $\dot{Y}_e$ is proportional to the integral of r_{INT} it should, and does, have a positive value at the end of the maneuver. Since the aircraft is now moving obliquely through the air mass, it also has a steady state β.

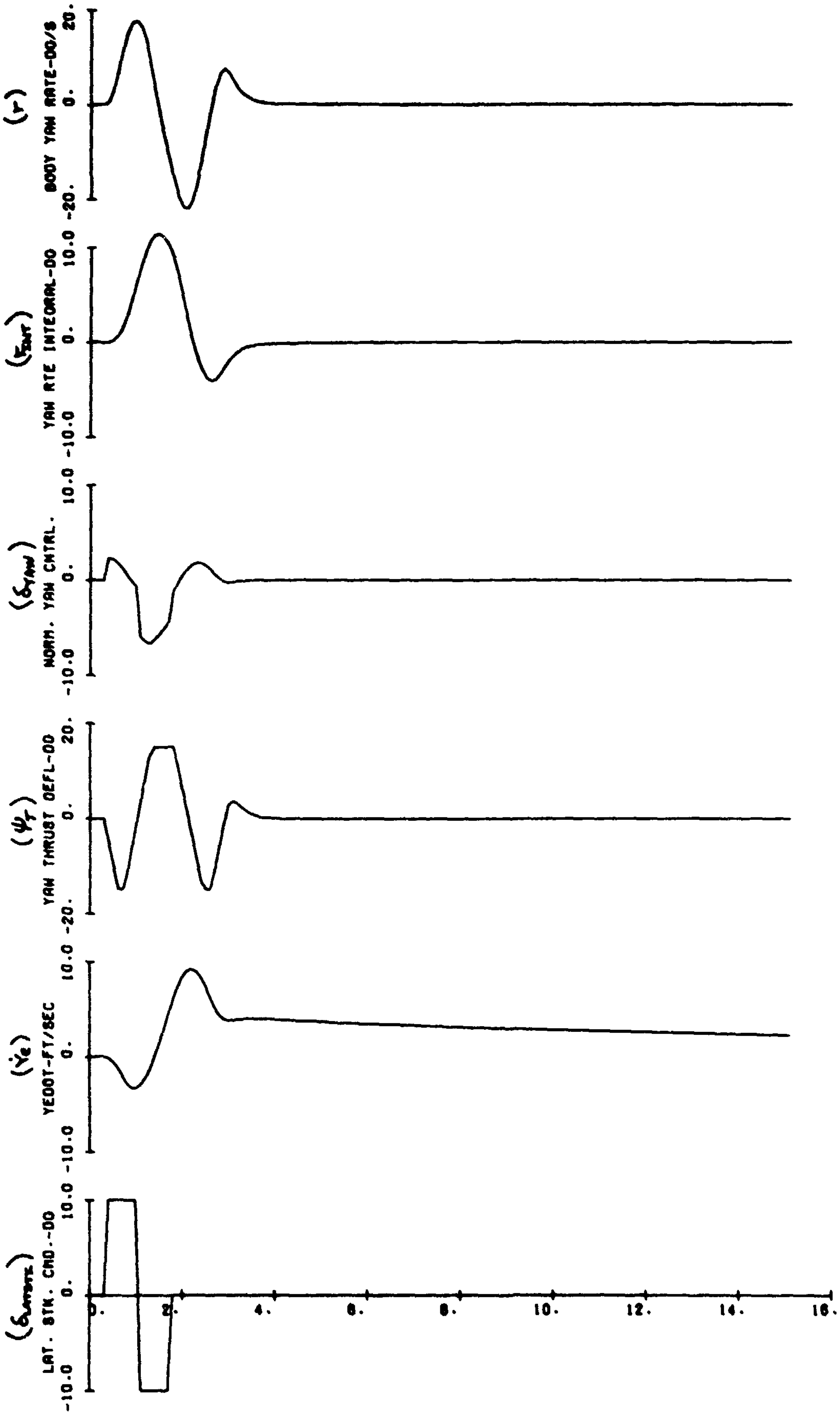

Figure 3-28. Lateral Stick Doublet Response at V_A = 10 kt (Sheet 1 of 3)

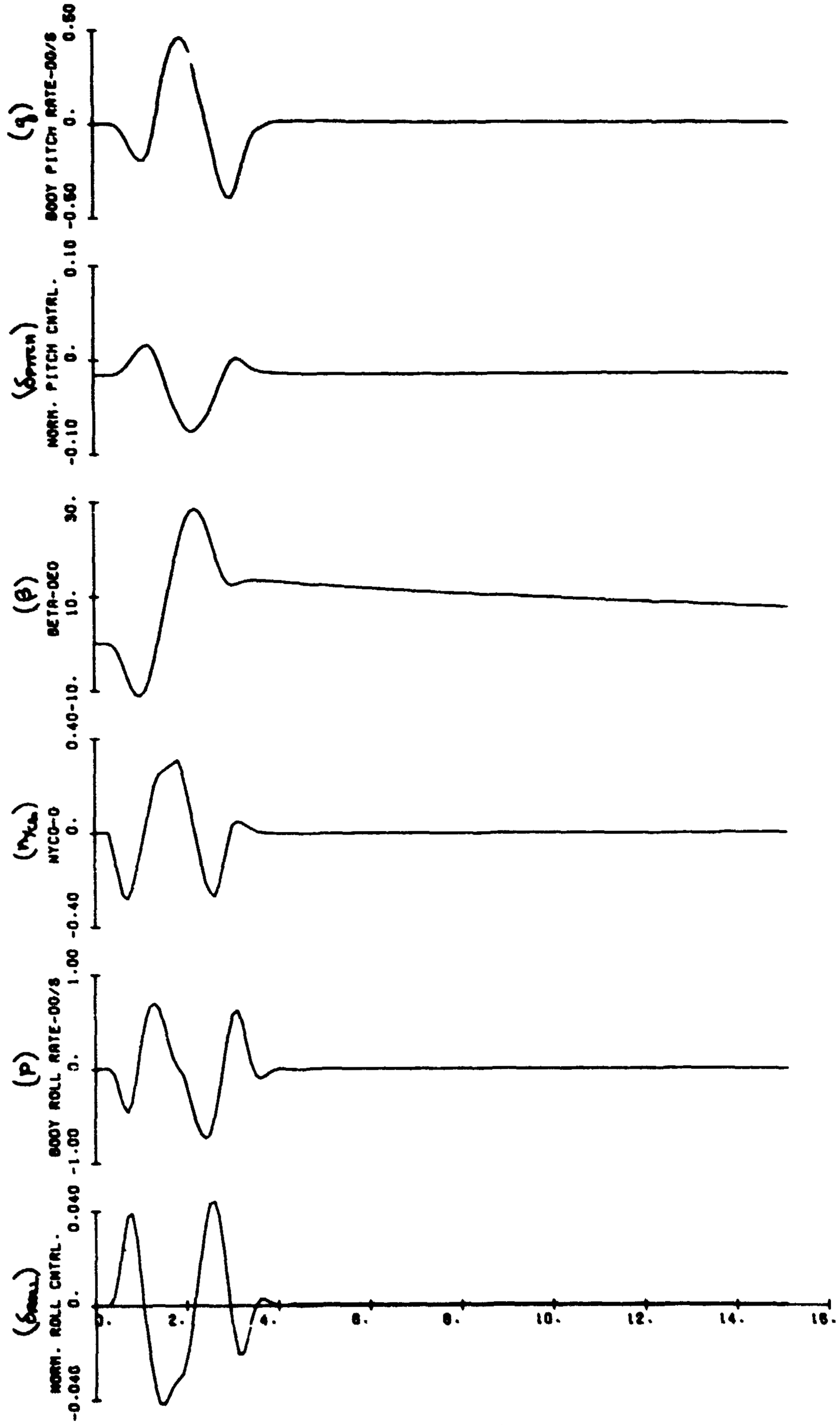

Figure 3-28. Lateral Stick Doublet se at V_A = 10 kt (Sheet 2 of 3)

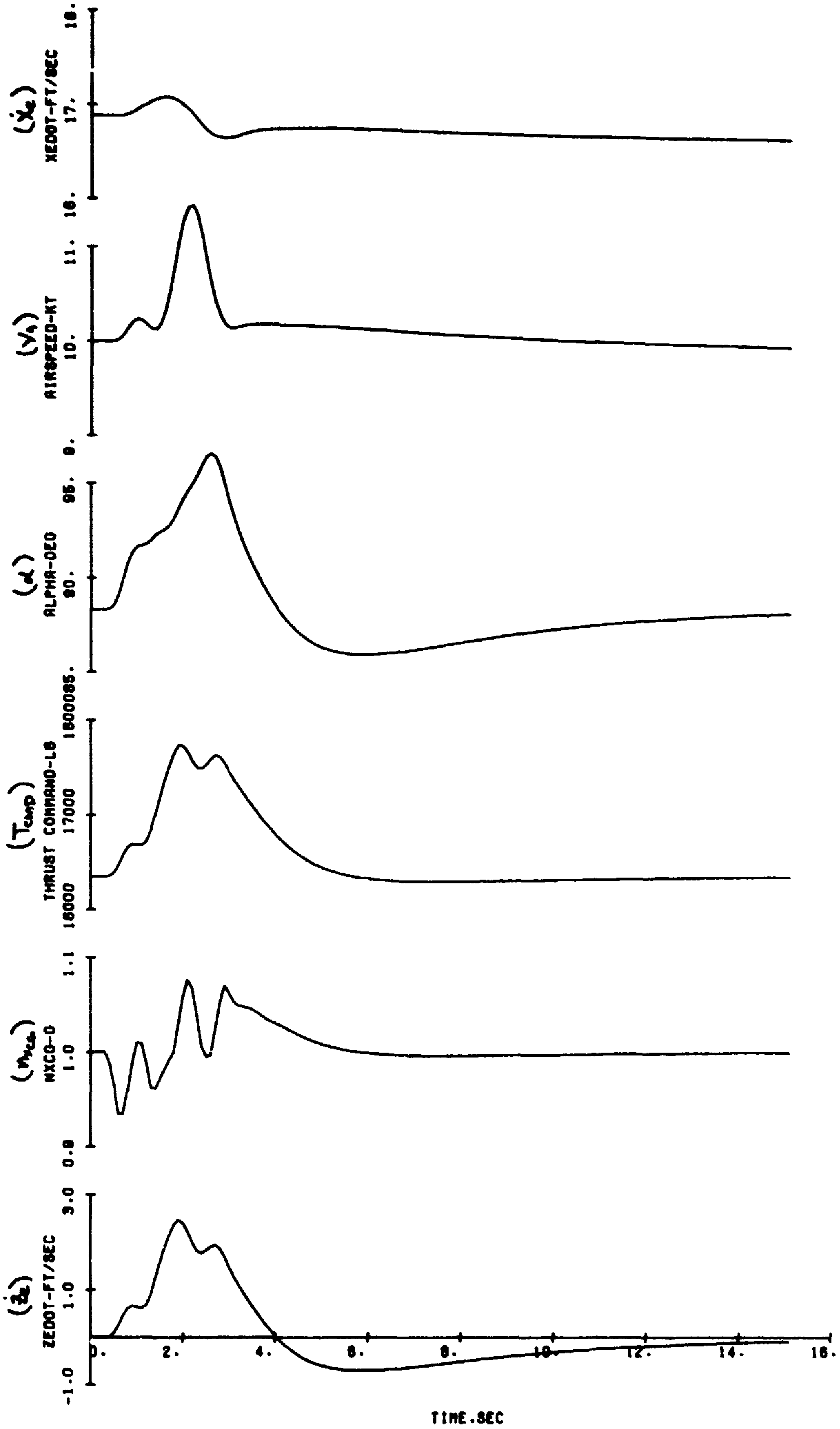

Figure 3-28. Lateral Stick Doublet Response at V_A = 10 kt (Sheet 3 of 3)

3.8.6 Case 6 - Pedal Pulse at $V_A = 10$ kt

The pedal pulse commands the airplane to rotate 28 deg around the X_B axis at a rate of approximately 20 deg/sec. This maneuver appears to the pilot as a cockpit yaw to the left. As indicated by figure 3-29, the maneuver is performed with no control saturation, negligible coupling in the yaw degree of freedom, and noticeable, but expected, coupling in the heave, surge, and pitch degrees of freedom. The roll control power for this maneuver is provided by the RCS jets. The RCS has a demand bleed arrangement and thus, when roll control power is required, thrust will decrease. In addition the RCS jets are located aft of the cg and thrust along the airplane positive X_B axis such that a nose up moment and small positive surge force (negative $n_{z_{cg}}$) are generated. The reduction in thrust produces a decrease in $n_{x_{cg}}$ and establishes a sink rate ($\dot{Z}_e > 0$). The $\dot{Z}_e$ is corrected by the heave control system. Similarly the pitch moment effects are cancelled by the pitch control system. The surge force is not controlled and the airplane drifts to a slightly higher airspeed following completion of the maneuver. Note that the direction of heave, surge, and pitch coupling is the same regardless of the direction of roll control power application.

In general, the longitudinal coupling displayed by the pedal pulse response is typical of RCS - equipped airplanes. Should it prove annoying, the culprit can be eliminated or alleviated by one or more of the following modifications:

1. Alleviate pitch coupling by relocating the RCS jets nearer the cg or by a δ_{ROLL} to δ_{PITCH} crossfeed.
2. Eliminate heave coupling by a continuous bleed RCS but at the expense of reduced thrust capability.
3. Alleviate heave coupling by a crossfeed of δ_{ROLL} to thrust command.

3.8.7 Case 7 - Heave Rate Controller Doublet at $V_A = 10$ kt

The heave rate controller doublet commands the airplane to establish a 10 ft/sec rate of climb ($\dot{Z}_e = -10$ ft/sec) followed by a 10 ft/sec sink rate

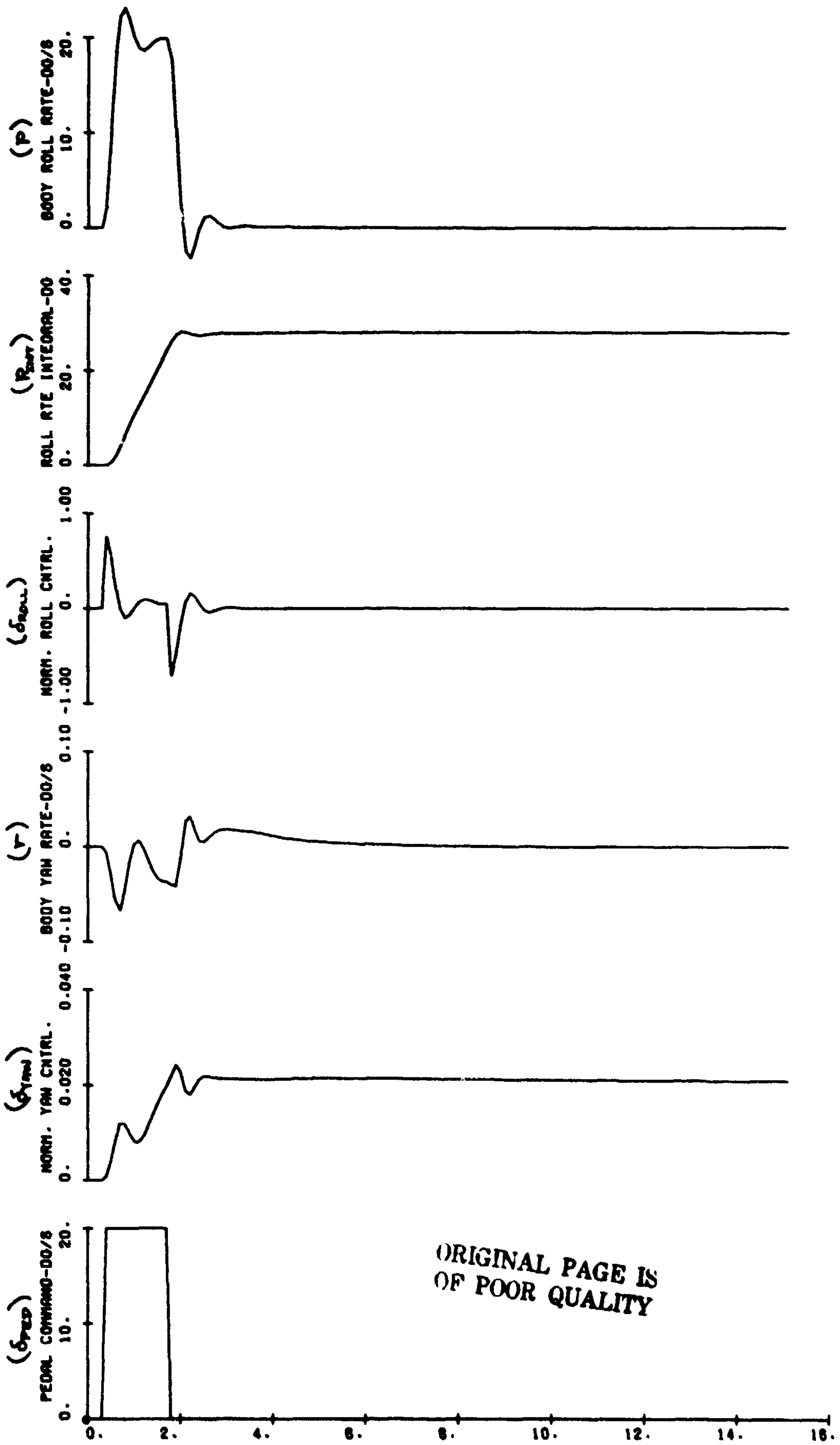

ORIGINAL PAGE IS
OF POOR QUALITY

Figure 3-29. Pedal Pulse Response at V_A = 10 kt (Sheet 1 of 3)

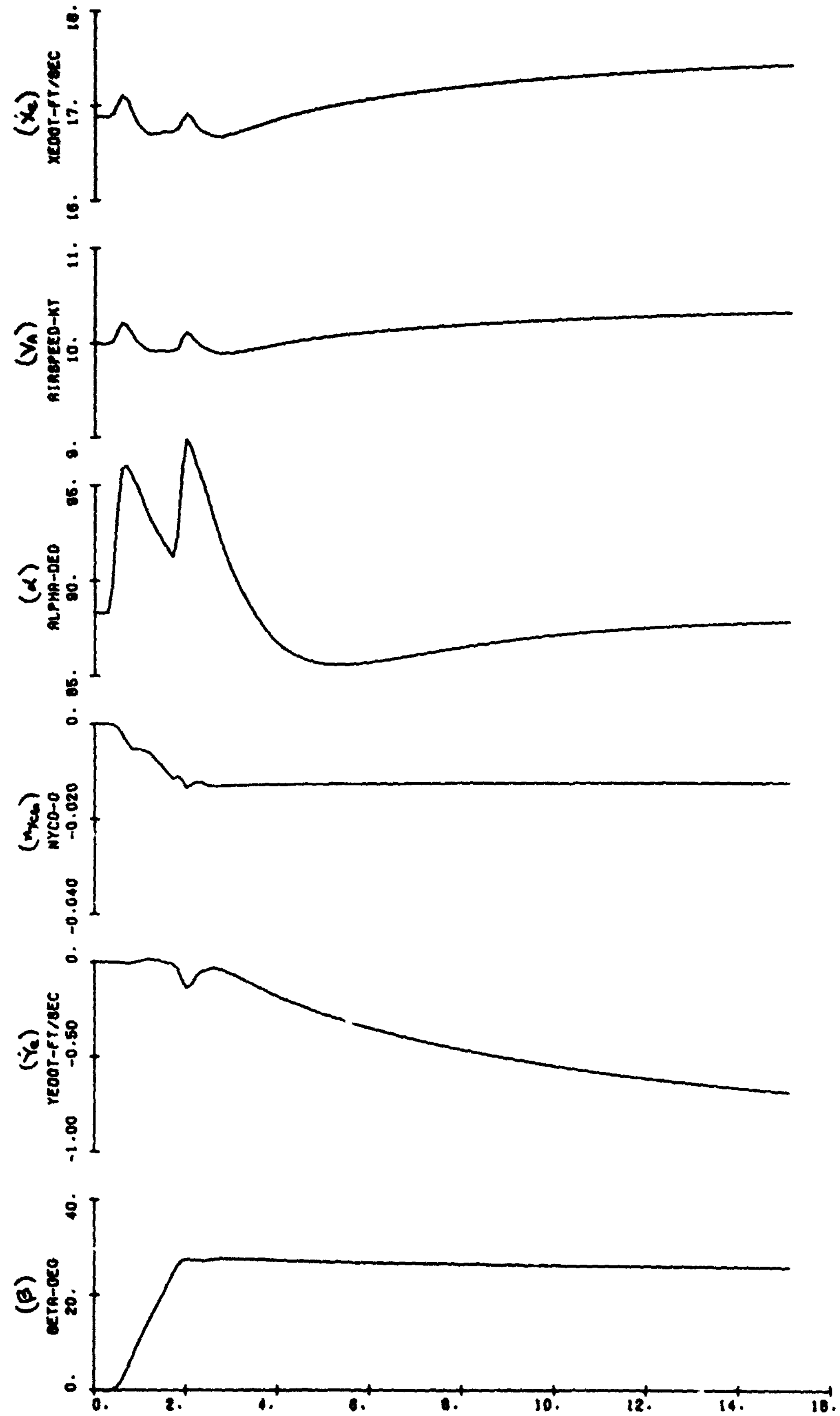

Figure 3-29. Pedal Pulse Response at V_A = 10 kt (Sheet 2 of 3)

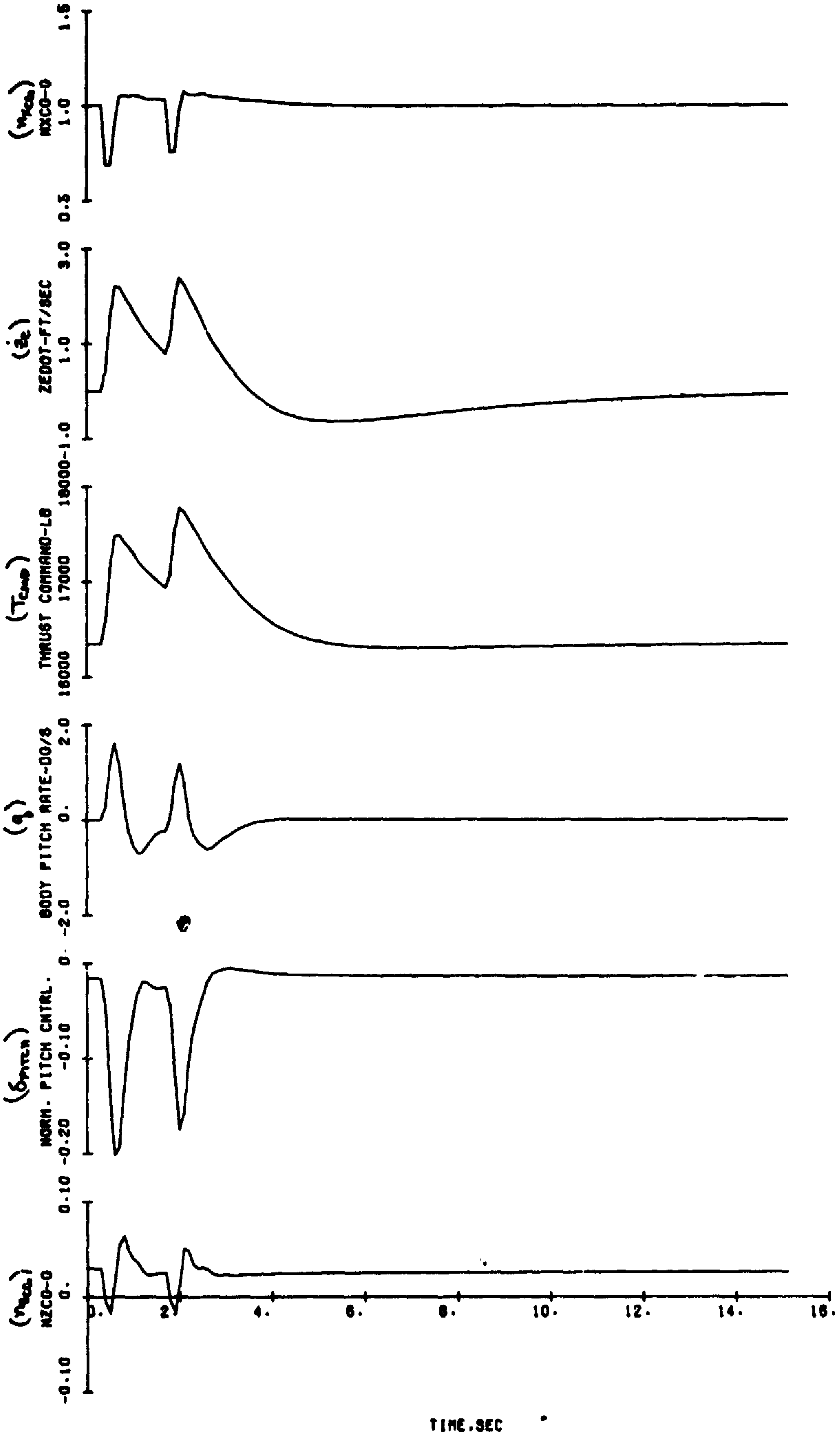

Figure 3-29. Pedal Pulse Response at V_A = 10 kt (Sheet 3 of 3)

($\dot{Z}_e = 10$ ft/sec) and return to trim (figure 3-30). The most significant feature of this response is the thrust dynamics shown by the trace of the thrust before (B4) correction for RCS coupling. Since time constant increases and the deceleration limit decreases as thrust level decreases the thrust response is slower when, at the same trim speed, establishing a sink rate, arresting a climb, or changing from climb to sink than it is when establishing a climb, arresting a sink, or changing from sink to climb.

Coupling into the lateral degrees of freedom was negligible during the maneuver and not worth showing in the traces. Coupling into the surge and pitch degrees of freedom is small but noticeable; the appropriate traces have been included. Overall, the response is smooth, stable, and essentially single degree of freedom.

3.8.8 Case 8 - Mode Switching Transient

To investigate the transients which occur at the switch at 60 kt airspeed from conventional to hover FCS modes, the airplane was trimmed at 62 kt in a 0.5 mi radius right turn while decelerating at 0.1g along a constant altitude flight path. At 0.3 sec into the time history the stick was deflected aft and right to impose simultaneous 10 deg/sec positive pitch and roll rate commands on the airplane. These stick commands were held for 0.7 sec and released and should increase airplane pitch and roll angles by approximately 7 degrees each. The traces for this maneuver are shown in figure 3-31.

The ϕ and θ traces show that the desired maneuver was performed and not cancelled or altered by changing FCS modes. Control saturation is displayed only by δ_{PITCH}. It exceeds -1.0 for a short time following the release of the stick input. The mode switch occurs approximately 1.3 sec into the run. It is marked by rapid changes in δ_{ROLL}, δ_{YAW}, δ_{PITCH}, $n_{y_{cg}}$, and thrust command (i.e. the heave control system is activated) with those in δ_{YAW}, $n_{y_{cg}}$, and thrust command being fairly large. The pilot will likely notice the $n_{y_{cg}}$, which reverses from -.05g to .05g, and δ_{YAW}, which commands a yaw acceleration step approximately -0.5 rad/sec^2 to be applied to the airplane, since these are unexpected accelerations. He will

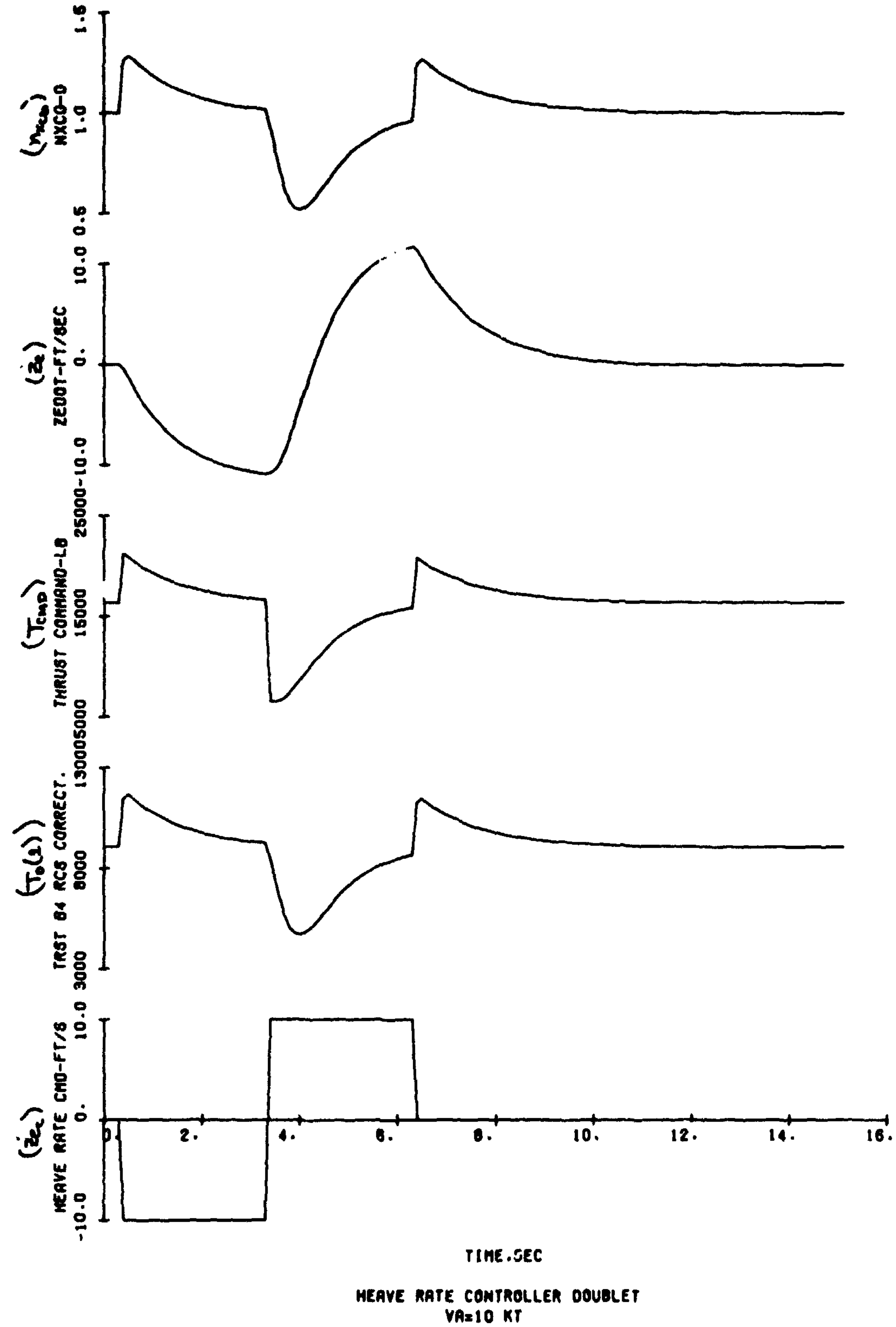

Figure 3-30. Heave Rate Controller Doublet Response at V_A = 10 kt (Sheet 1 of 2)

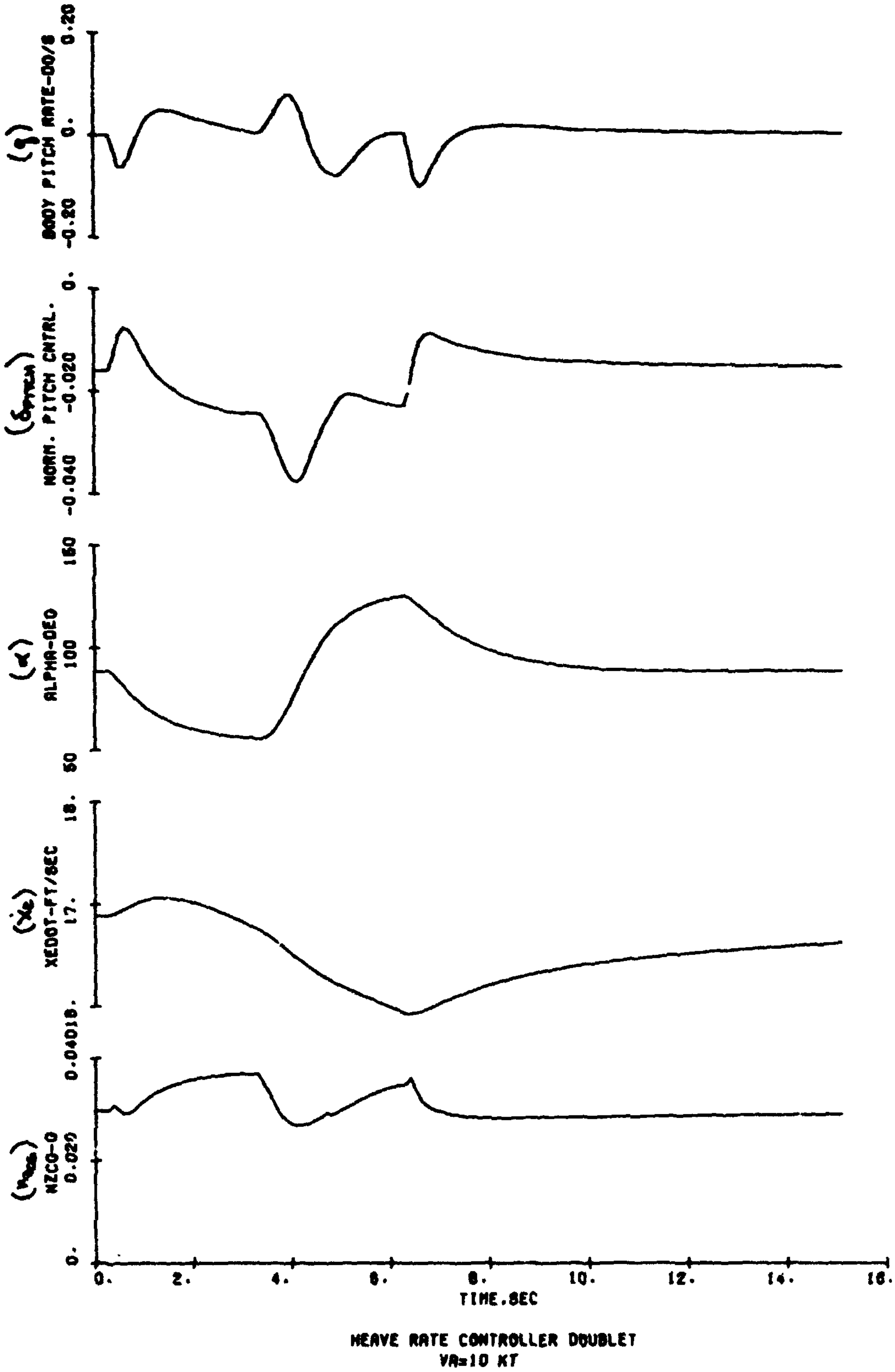

Figure 3-30. Heave Rate Controller Doublet Response at V_A = 10 kt (Sheet 2 of 2)

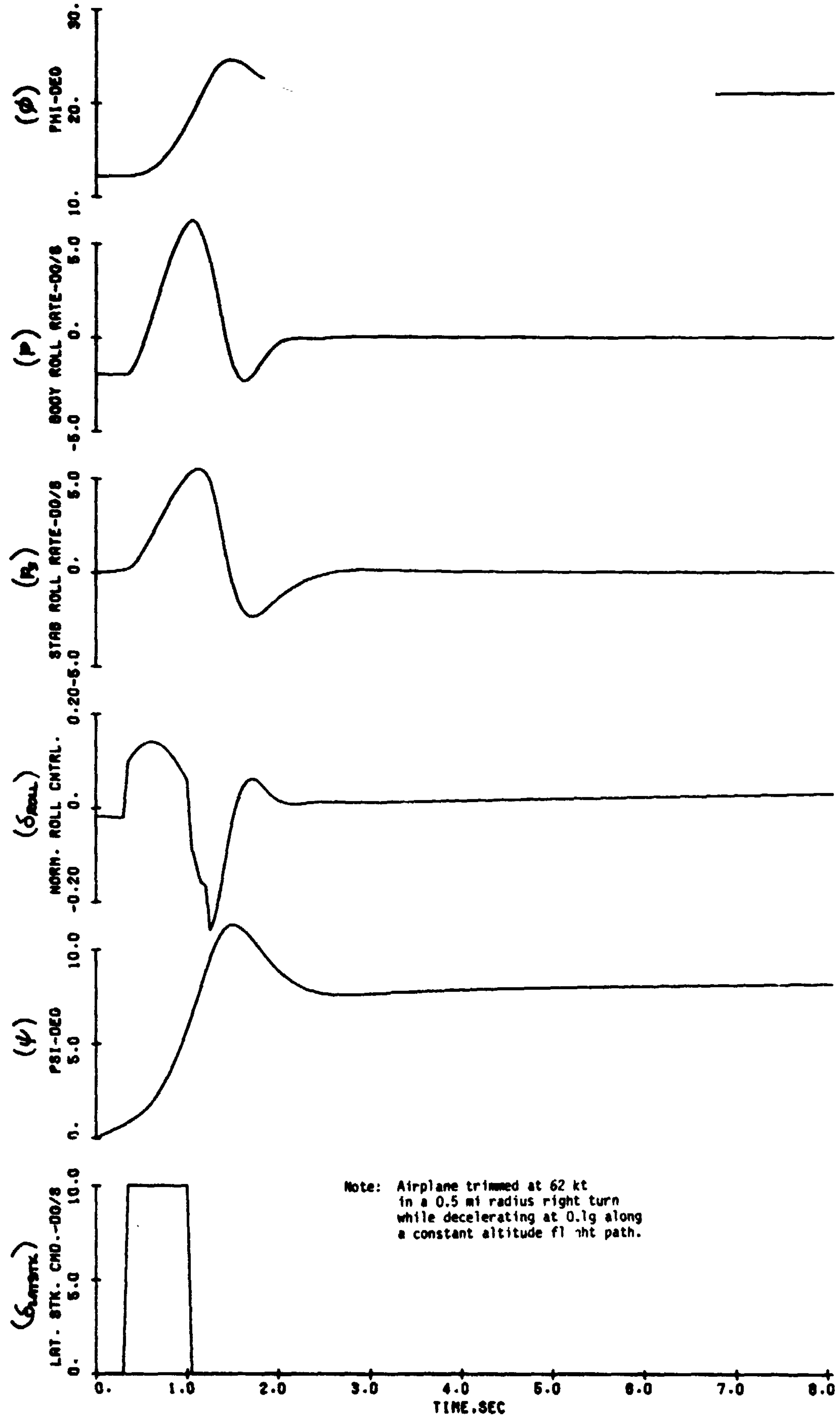

Note: Airplane trimmed at 62 kt
in a 0.5 mi radius right turn
while decelerating at 0.1g along
a constant altitude flight path.

Figure 3-31. Mode Switching Transient (Sheet 1 of 4)

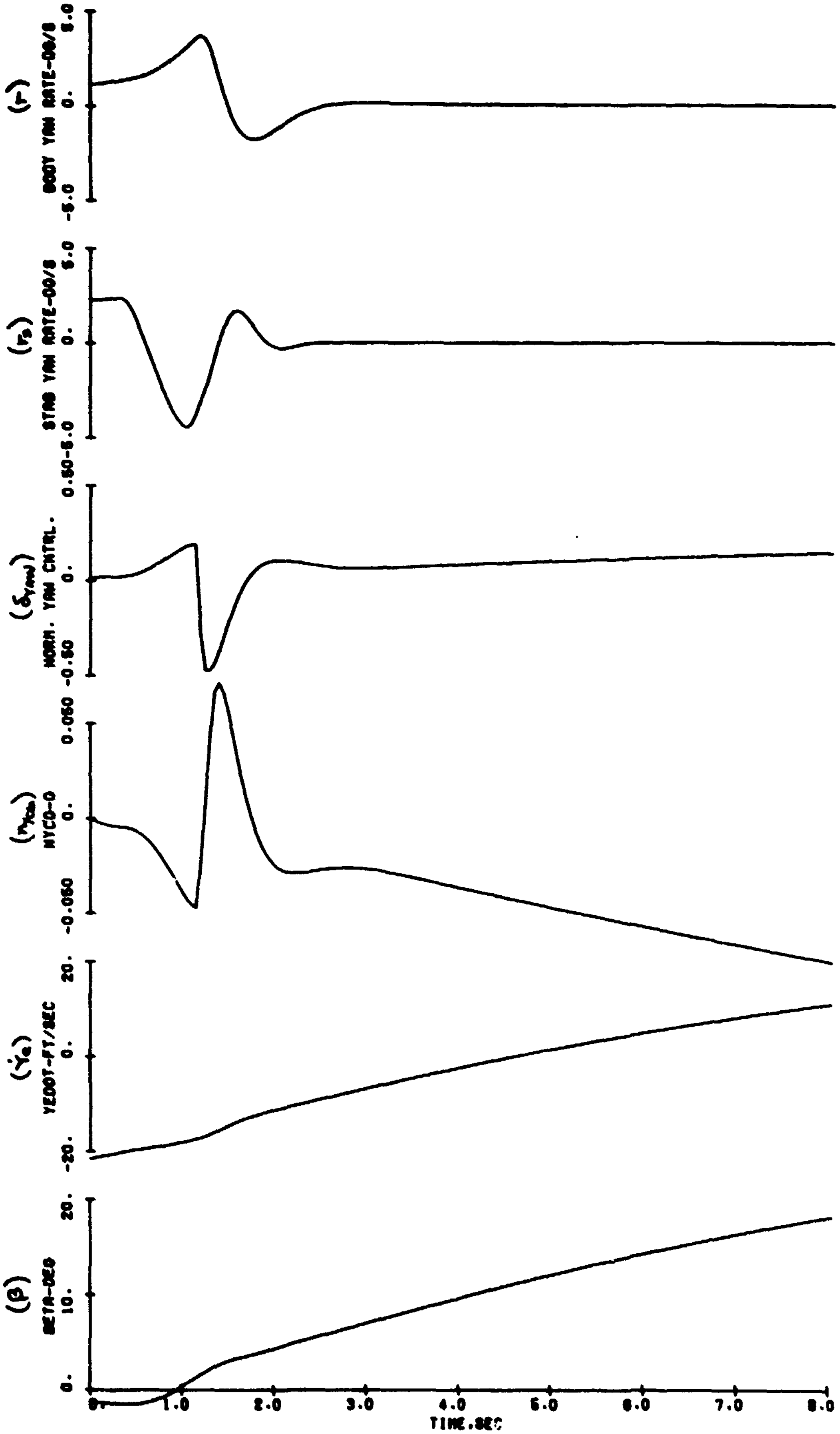

Figure 3-31. Mode Switching Transient (Sheet 2 of 4)

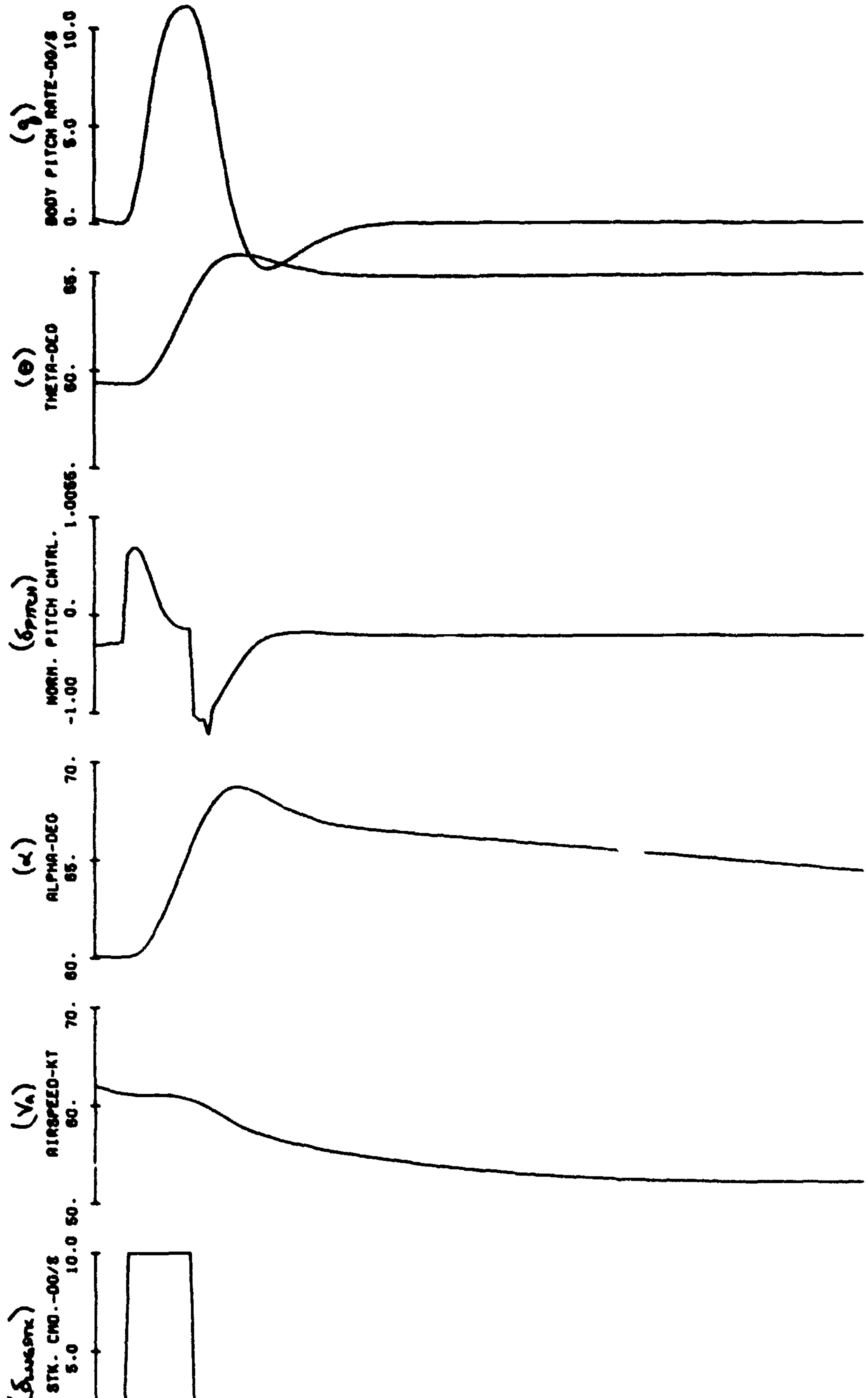

Figure 3-31. Mode Switching Transient (Sheet 3 of 4)

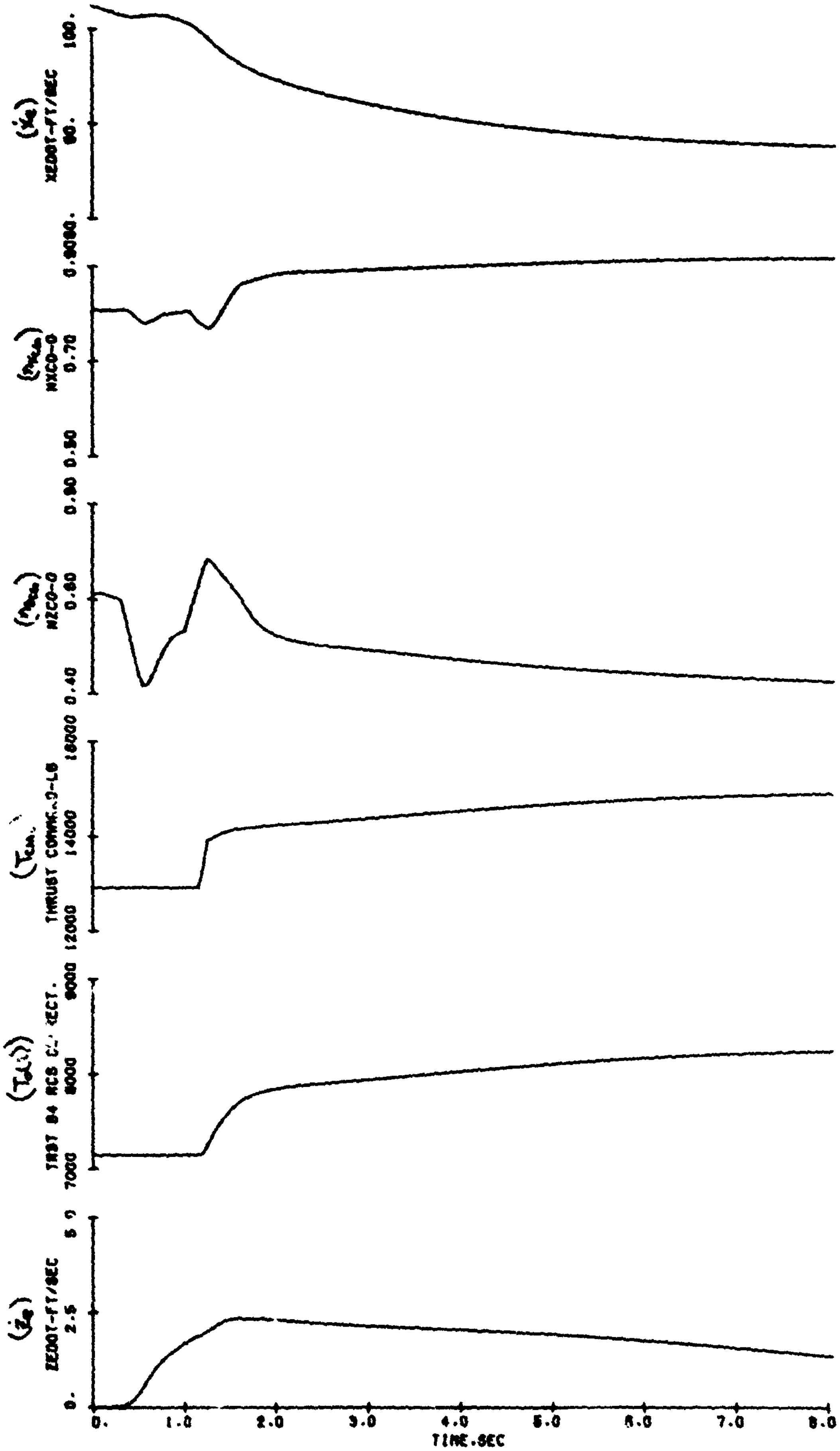

Figure 7-31. Mode Switching Transient (Sheet 4 of 4)

also notice the thrust increase to arrest the sink rate established by the stick inputs. Piloted simulation studies should determine whether these switch transient effects are annoying. For now it sufficies to say that the transients are stable, controllable, and, with the few exceptions noted above, relatively smooth and predictable.

3.8.9 Case 9 - Pseudo-Pilot Flown Transition

The pseudo-pilot flown transition (figure 3-32) demonstrates the capabilities of the pseudo-pilot transition equations detailed in Section 2.10.2 and provide further substantiation of the stability and controllability of the airplane through the mode switch region. The transition is initiated by retarding the throttle to idle. Psuedo-pilot's longitudinal stick commands are basically open loop in that they are calculated with the aid of a table of trim pitch angles vs airspeed. The stick commands are initially proportional to pitch rate and become proportional to pitch angle at the mode switch point. Psuedo-pilot's throttle variations are similarly open loop being determined from a table of trim throttle settings vs airspeed. Even though pseudo-pilot has no inputs to the roll or yaw control systems, the transition is well behaved laterally. It can thus be inferred that the baseline FCS will enable the transition to be flown with low pilot workload.

The mode switch, which occurs approximately 56 sec into the transition, is accompanied by noticeable rapid changes in δ_{PITCH}, δ_{YAW}, δ_{ROLL}, and $n_{y_{cg}}$. The change in δ_{PITCH} is expected because of the change of command function of the longitudinal stick while those in δ_{YAW}, δ_{ROLL}, and $n_{y_{cg}}$ are unexpected. Thrust command, and consequently, $n_{x_{cg}}$, also change rapidly, not unexpectedly, because the heave control system has been activated and immediately attempts to arrest the 10 ft/sec sink rate which has developed. As discussed in Section 3.8.8 any annoyance related to these switch transient effects can best be judged during a piloted simultion.

3.8.10 Case 10 - Pseudo-Pilot Flown Turn Over a Spot in a 35 kt Wind

The pseudo-pilot flown turn over a spot in a 35 kt wind (figure 3-33) demonstrates the capability of the pseudo-pilot stationkeeping control laws

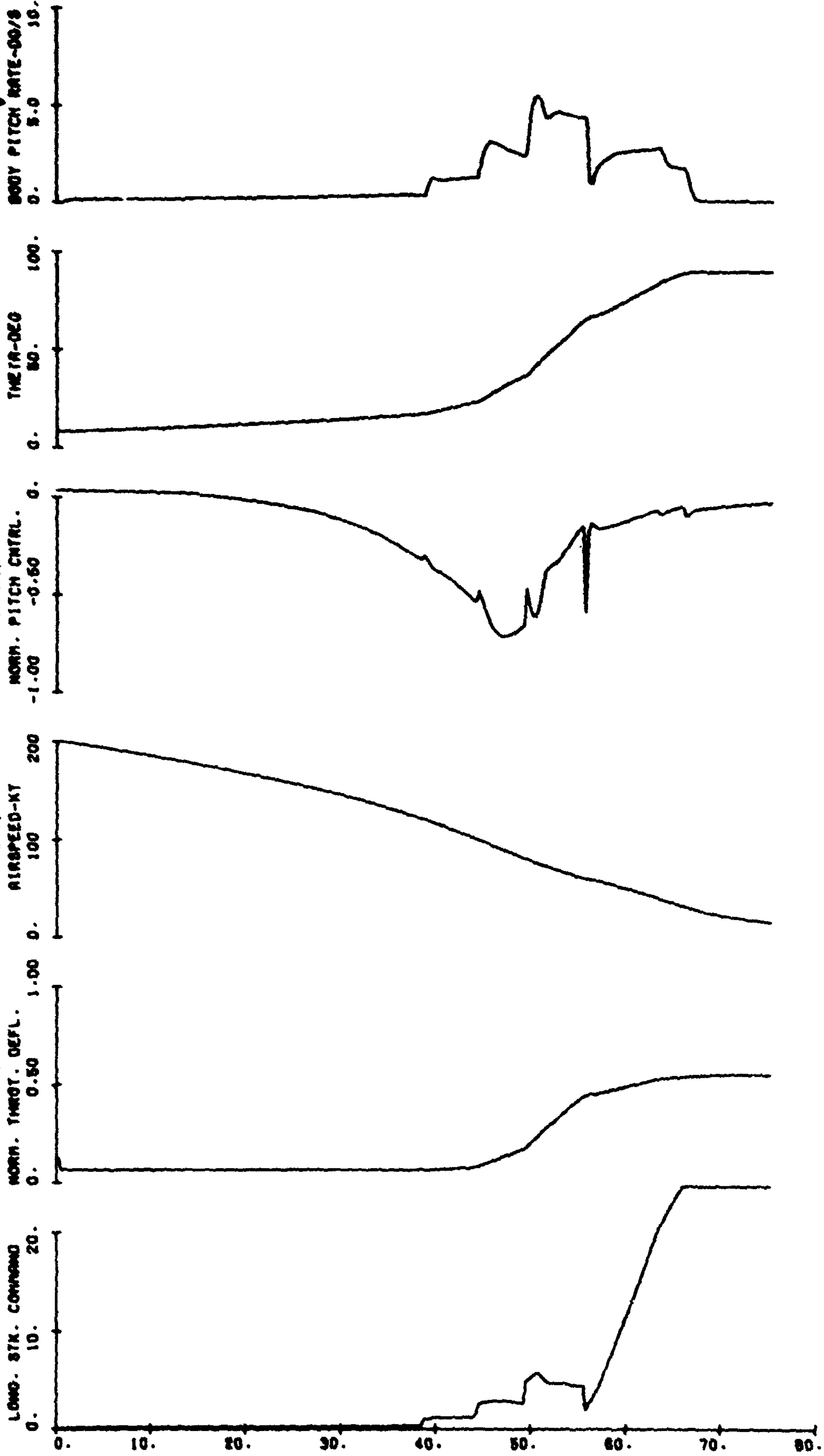

Figure 3-32. Pseudo-Pilot Flown Transition (Sheet 1 of 3)

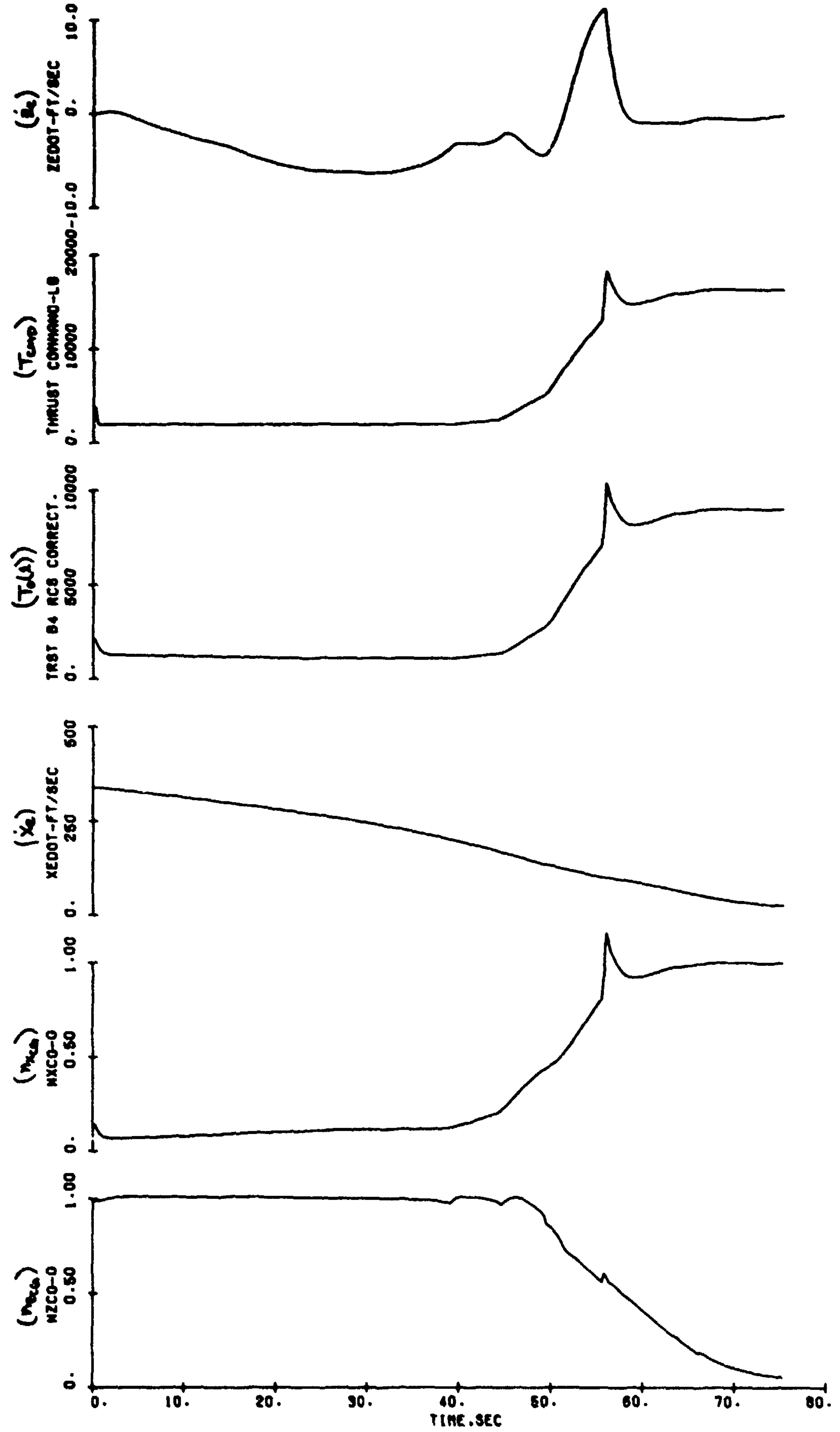

Figure 3-32. Pseudo-Pilot Flown Transition (Sheet 2 of 3)

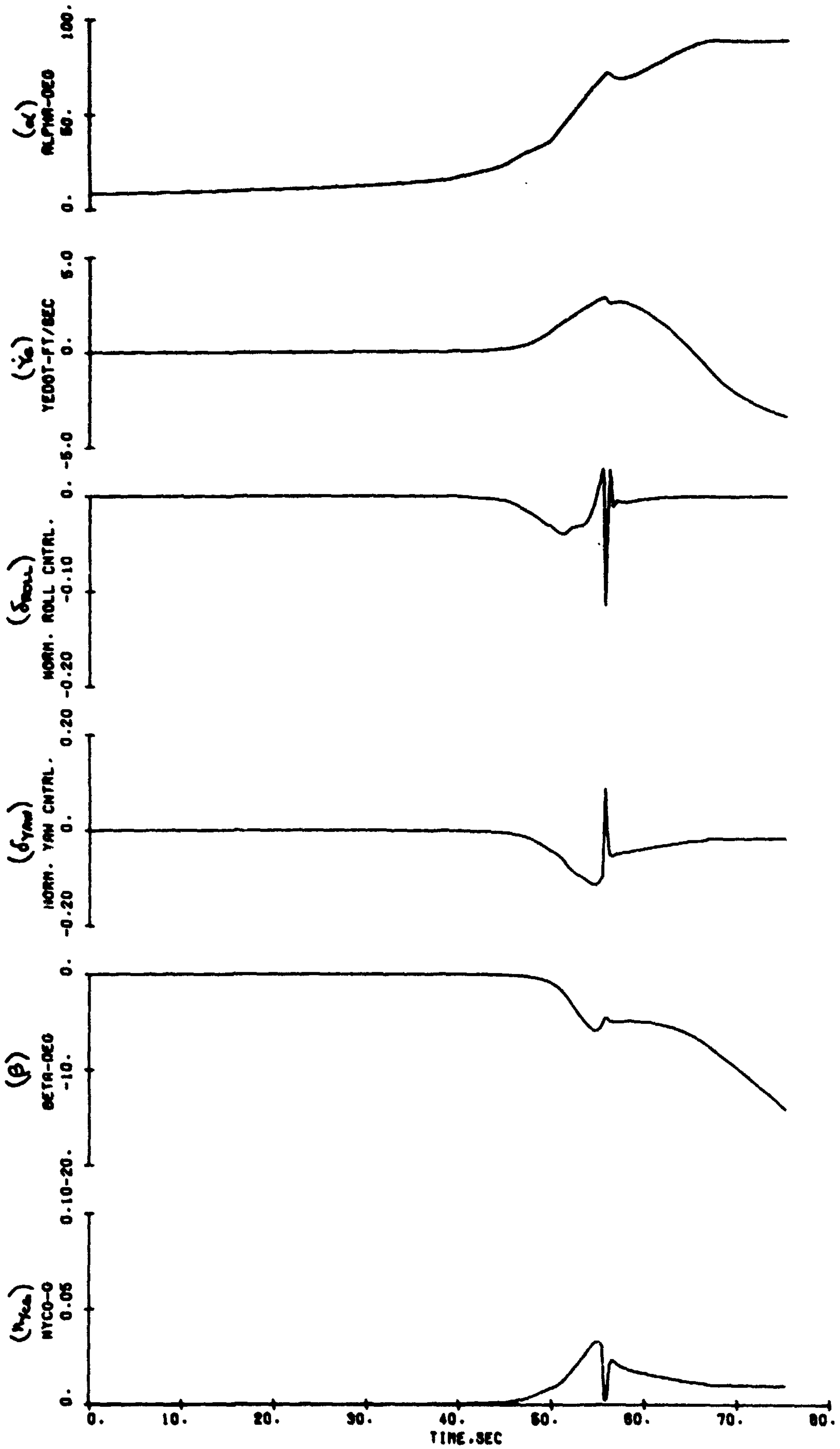

Figure 3-32. Pseudo-Pilot Flown Transition (Sheet 3 of 3)

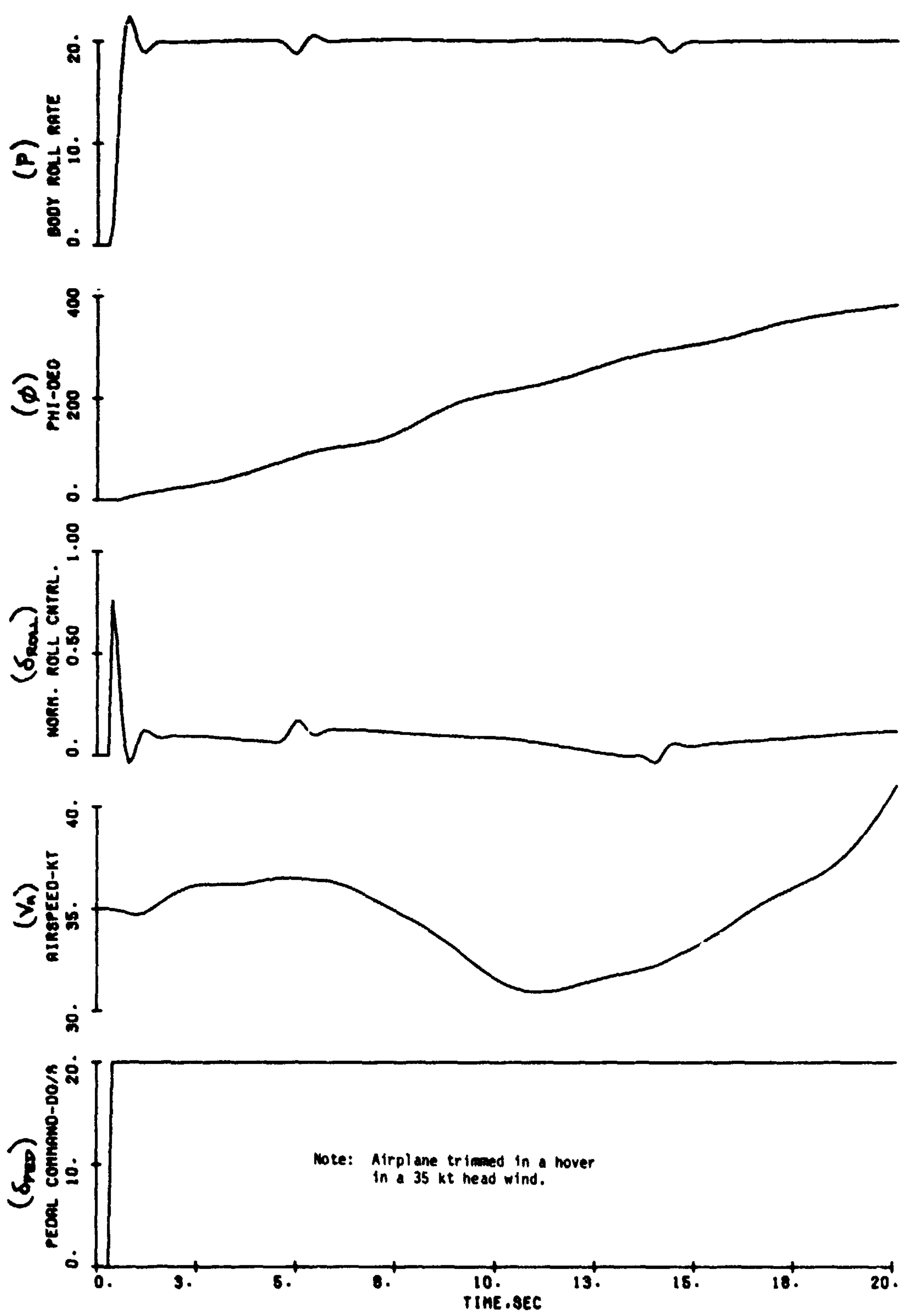

Figure 3-33. Pseudo-Pilot Flown Tu.n Over a Spot in a 35 kt Wind (Sheet 1 of 5)

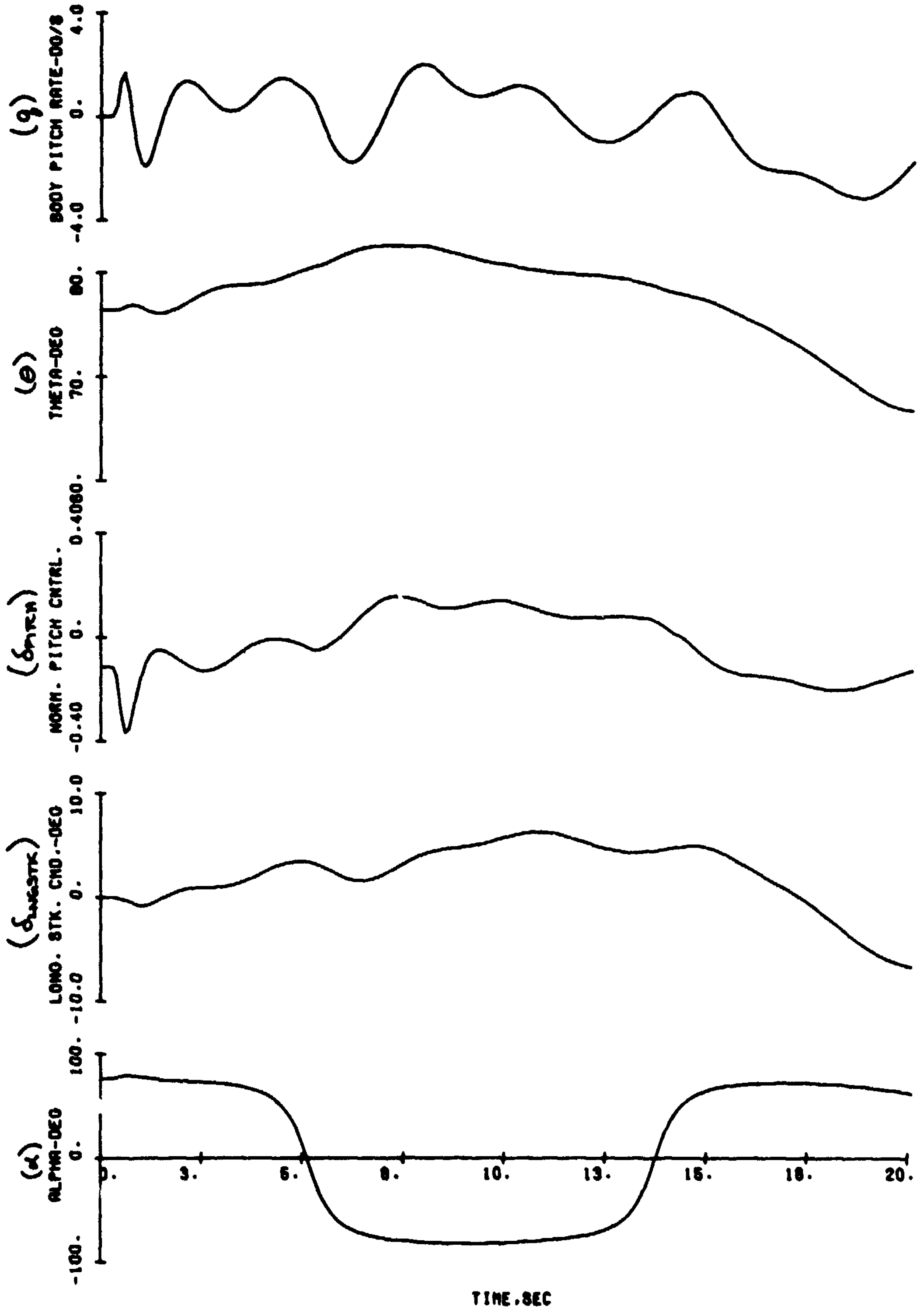

Figure 3-33. Pseudo-Pilot Flown Turn Over a Spot in a 35 kt Wind (Sheet 2 of 5)

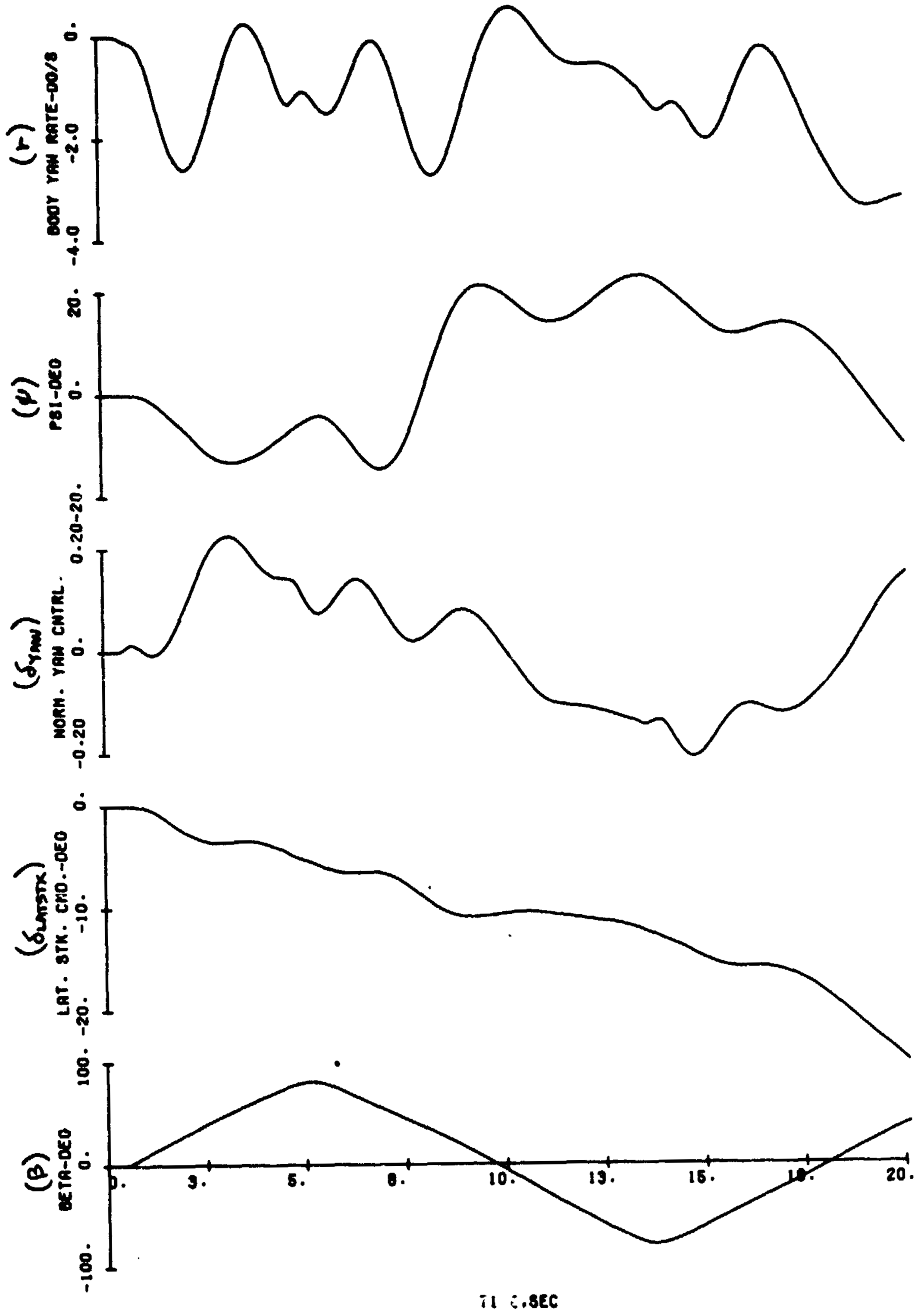

Figure 3-33. Pseudo-Pilot Flown Turn Over a Spot in a 35 kt Wind (Sheet 3 of 5)

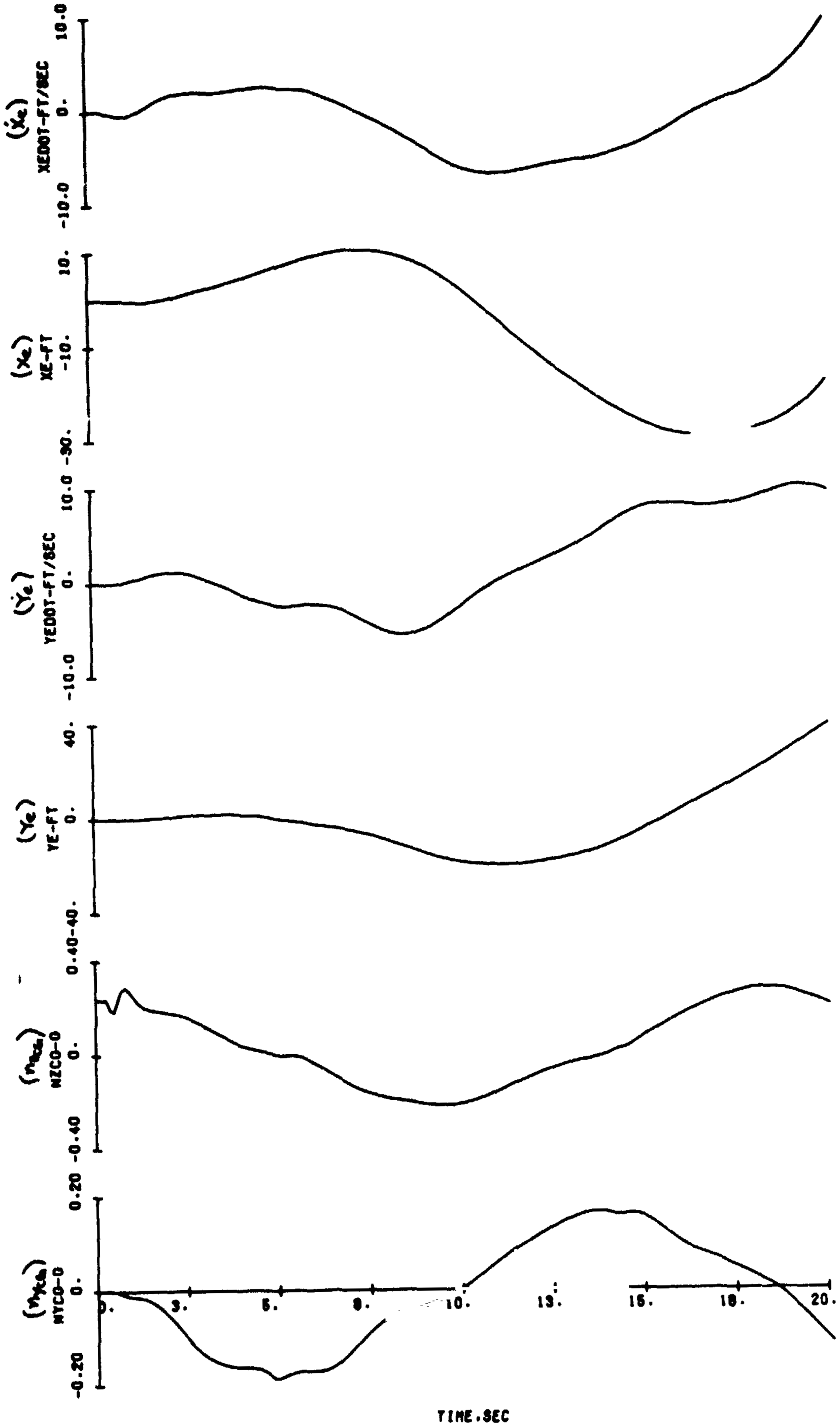

Figure 3-33. Pseudo-Pilot Flown Turn Over a Spot in a 35 kt Wind (Sheet 4 of 5)

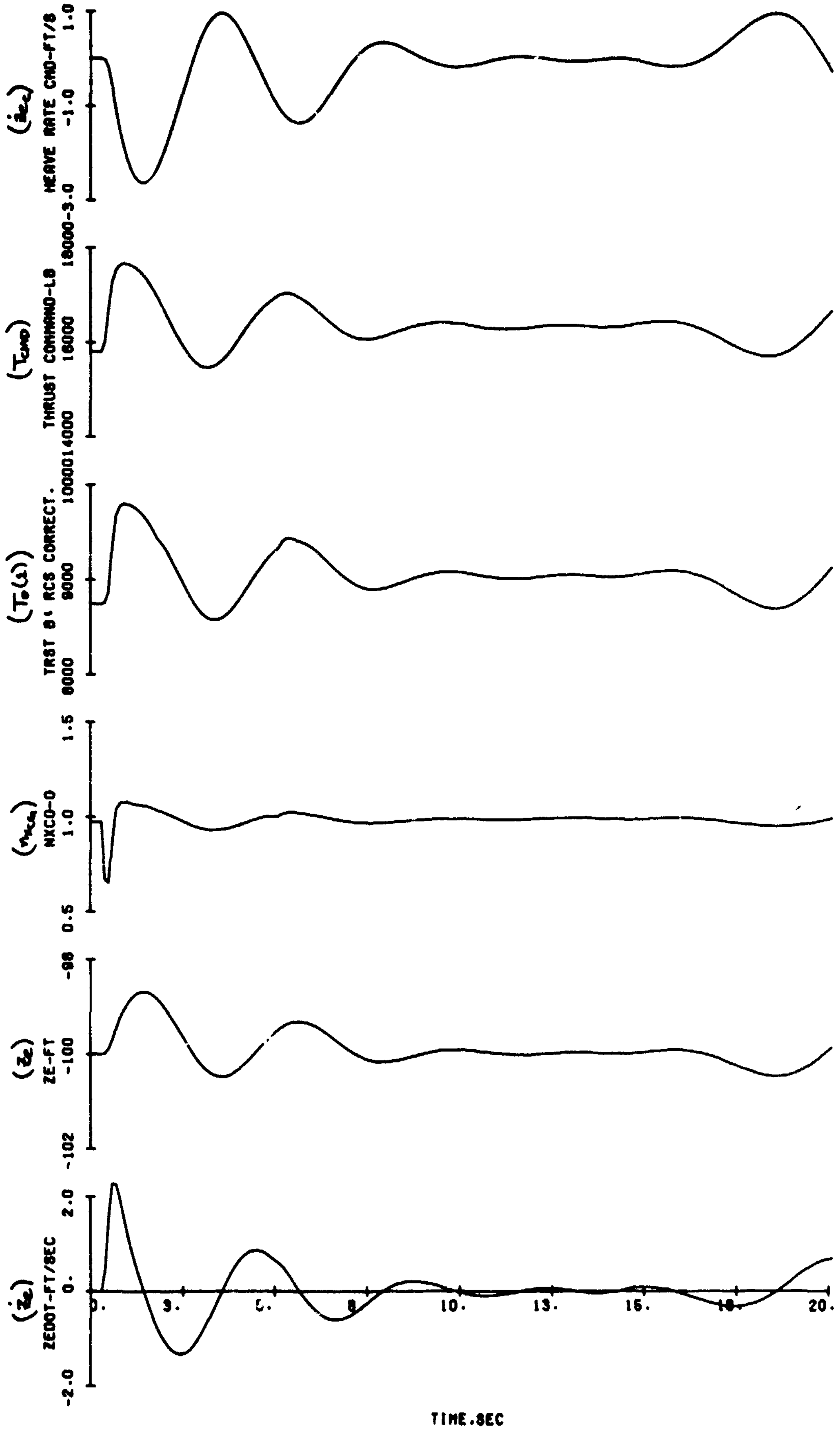

Figure 3-33. Pseudo-Pilot Flown Turn Over a Spot in a 35 kt Wind (Sheet 5 of 5)

depicted in figure 2-32. Prior to calculating the time history of the turn, a linear analysis was performed of pilot-closed position loops in a headwind to establish the pseudo-pilot stationkeeping gains. Because of the non-minimum phase characteristics of surge and sway control of the airplane, the gains had to be chosen carefully to avoid position loop instability. The gains established by the analysis and used to generate the traces of figure 3-33 are as follows:

$K_{z_{e_s}} = -0.005$ units δ_{LNGSTK}/ft; $K_w = 5.0$ ft/ft/sec;

$K_{y_{e_s}} = 0.005$ units δ_{LATSTK}/ft; $K_v = 5.0$ ft/ft/sec;

$K_{x_{e_s}} = 2.0$ ft/sec/ft; $K_u = 0$.

The airplane handling characteristics are functions of wind direction but, as noted, pseudo-pilot gains were established only for headwind conditions. For this reason plus the fact that wind direction changed fairly rapidly during the turn it was expected that pseudo-pilot would have a difficult task to maintain X_e and Y_e at the desired $X_e = Y_e = 0$ reference point. This was indeed the situation. In the time of one complete turn (approximately 18 sec), the airplane had drifted in X_e from 10 ft forward to 3 ft aft of the reference and was correcting back towards the reference while in Y_e it had drifted from 10 ft left to 40 ft right of the reference and was not yet correcting back towards the reference. Psuedo-pilot had the stick properly placed - forward and left - at the completion of the turn for correcting both situations. Because there was no wind component along the Z_e axis, pseudo-pilot did an excellent job, maintaining Z_e within 1.5 ft of the $Z_e = -100$ ft reference.

Piloted simulation studies will be beneficial to evaluate the airplane and control system performance demonstrated here. At this point it can only be concluded that turns over a spot at fairly high turn rates are controllable with modest control power usage and have predictable performance.

The roll rate and δ_{ROLL} traces of figure 3-33 demonstrate unexpected small one cycle oscillations at 5 and 14 seconds into the maneuver. These are postulated to be related to the high α and large β flow conditions which occur at these times. Time was not available to study completely this anomaly. Fortunately it does not detract from the overall utility of the test case but should be studied further to assess its root cause.

3.8.11 Summary of Results of Performance Evaluation

The following results are the most significant of the FCS performance evaluation:

1. No stability or controllability problems were actually encountered in the test cases. The following potential problems, however, were indicated:

   a) Sideslip limitation due to roll and/or pitch control power limitations at $V_A = 120$ kts. (Case 3)
   b) Potential PIO situation due to inherent non-minimum phase control characteristics when the pilot attempts tight horizontal plane position control in hover. (Cases 4 and 5)

2. There are noticeable uncommanded mode switching transients particularly in the lateral degrees of freedom. (Cases 8 and 9)
3. There is noticeable coupling into the longitudinal degrees of freedom when the RCS is used. (Case 6)
4. The pseudo-pilot transition and stationkeeping control logic works. (Cases 9 and 10)
5. An unexpected oscillation in roll rate occurs under conditions of high α, large β, and relatively high steady state roll rate. Time was not available to determine the root cause of this peculiarity. The fact that its effect is minor and occurs under seemingly unique conditions place it among items recommended for future study. (Case 10)

The conclusion drawn from the FCS performance evaluation is that the baseline FCS provides an adequate starting point for piloted simulation studies and that, consequently, the design does not have to be iterated through the performance loop of the FCS design procedure (figure 3-1).

4.0 CONCLUSIONS AND RECOMMENDATIONS

The following conclusions are supported by the developments and analyses described herein:

1. A useful capability has been developed for conducting both piloted and non-piloted simulations of the terminal operations of VATOL airplanes. This simulation capability can be, but is not restricted to being, applied at conceptual design phases where relatively few configuration - specific data are available. It will highlight handling qualities characteristics which are indigenous to the various designs.
2. The aerodynamics math model is deterministic, functions with DATCOM - type data, and can adequately represent the low speed high angle of attack, large sideslip aerodynamic characteristics of VATOL airplanes.
3. The Vought SF-121 airplane, as modeled herein, has adequate control power for meeting the trim and maneuvering requirements of the MIL-F-83300 and AGARD 577 flying qualities specifications with some residual for gust regulation.
4. The baseline FCS developed for the SF-121 provides an adequate starting point for piloted simulation studies.
5. The most distinguishing flying qualities characteristic of the SF-121 airplane (and similarly thrust deflected controlled VATOL airplanes) is a strong non-minimum phase control characteristic (i.e. initial acceleration in wrong direction) which will become apparent when the pilot attempts tight horizontal plane position control in hover.

The developments and analyses herein have provided background for the following recommendations for possible math model modifications and areas of emphasis for piloted simulations:

1. Evaluate the use of rotated inertial axis system coupled with Euler angles to orient the airplane body axes (Section 2.9). This alternative to the direction cosine formulation will circumvent the singularity in the standard Euler transformation at $\theta = 90$ deg. and

provide continuous attitude references for attitude control loops throughout the operating range of VATOL airplanes. If the approach has merit, incorporate the appropriate relations into the math model.

2. Determine and correct, if necessary, the mechanism for the small oscillation in roll rate which appears to occur under conditions of simultaneous high angle of attack rates, large sideslips, and relatively high steady state roll rates (Section 3.8.10).
3. Piloted simulation studies should consider at least the following issues regarding terminal operations of VATOL airplanes:

   - Non minimum phase control characteristics and their impact on pilot comfort, workload, and ability to effect precise position control in hover and on the need for additional moment controls (e.g. independent pitch and yaw RCS).
   - Cockpit and/or pilot rotation during transition. First consider its necessity. If required, then consider whether switching of cockpit controller roles and pilot/cockpit angle control should be automatic or manual functions.
   - Transition control system considerations - control system type (rate command, rate command/attitude hold, attitude command, etc), automatic or manual mode switching, mode blending, annoyance level of uncommanded motions during mode switching, cockpit controller authorities and sensitivities, pilot input command shaping requirements, system bandwidths, gust regulation capabilities.

5.0 REFERENCES

(a) Clark, Jr. J.W., Low-Speed V/STOL Stability and Control Prediction - Volume I: Model Description and Validation, NADC Report 76323-30, 11 January 1977.

(b) Anonymous, USAF Stability and Control DATCOM, Air Force Flight Dynamics Laboratory, U.S. Air Force, October 1960 (April 1978 Revision).

(c) Driggers, Herbert H., Study of Aerodynamic Technology for V/STOL Fighter/ Attack Aircraft, NASA CR-152132, May 1978.

(d) Bender, D. D., V/STOL Type B Engine Data: Engine MFTF-2800-25-1 for VATOL Concept, Vought Report DIR 2-53200/7DIR-105, 30 November 1977.

(e) Stapleford, R. L., Clement, W. F., Booth G. C. Fortenbaugh, R. L., Flight Control/Flying Qualities Investigation for Lift Cruise Fan V/STOL: Volume I. Analytical Development, Volume II, Piloted Simulation, Volume III. Simulator Model, NADC Report 77143-30, August 1979.

(f) Heimbold, Richard L., Yi, C. James, Miller, Ronald J., Flight Propulsion Control Coupling and Dynamic Interaction Investigation, Phase III, AFFDL-TR-77-41, June 1977.

(g) Beatty, T. D., Kress, S. S., Prediction Methodology for Propulsive Induced Forces and Moments of V/STOL Aircraft in Transition/STOL flight, NADC Report NADC-77229-30, July 1979.

(h) Fortenbaugh, R. Schonowski, J., USN/FMOD FRG VAK-191B Joint Flight Test Program: Volume 9, Flight Controls and Hydraulics, NAVAIR-9R-76, August 1976.

(i) Vetter, H. C., "Effect of a Turbojet Engine on the Dynamic Stability of an Aircraft", Journal of the Aeronautical Sciences, Volume 20, November 1953, pp 797-798.

(j) Hillman, G. W., New Subroutines for Use in Off-Line Simulation, Vought Report 2-53362/3AVO-75, 9 May 1973.

(k) Bihrle, Jr., William and Heyman, Arthur C., The Spin Behavior of Aircraft, GAEC Report No. 394-68-1, December 1967.

(l) Neal, T. P. and Smith, R. E.: An Inflight Investigation to Develop Control System Design Criteria for Fighter Airplanes, AFFDL-TR-70-74, Volume I and Volume II, June 1970.

(m) Chalk, C. R., DiFranco, D. A., Lebacqz, J. V., Neal, T. P., Revisions to MIL-F-8785B (ASG) Proposed by Cornell Aeronautical Laboratory Under Contract F33615-71-C-1254, AFFDL-TR-72-41, April 1973.